UNIVERSITY OF ASTON IN BIRMINGHAM

"A STUDY OF THE ELASTIC SCATTERING OF 2-3 Mev NEUTRONS IN SULPHUR AND CALCIUM"

Thesis submitted for the Degree of

Doctor of Philosophy

by

Mark C. Janicki, B.Sc.

Department of Physics

November 1977

SUMMARY

"A Study of the Elastic Scattering of 2-3 Mev Neutrons in Sulphur and Calcium"

Mark Charles Janicki

Doctor of Philosophy

1977

In the present work an associated particle time-of-flight spectrometer has been designed and used to study the elastic scattering of neutrons with energies of 2.99 Mev and 2.18 Mev.

The $^{2}H(d,n)^{3}He$ reaction was used as the source of neutrons. The time of origin of the neutron was determined by detecting the associated helium particle. Problems related to detecting the ^{3}He particles and resolving them from a large number of other charged particles produced at the same time, have been overcome by using thin deuterated polyethylene targets. For the production of neutrons with an energy of 2.18 Mev the neutron yield was monitored by counting the associated ^{3}He particles. Due to the incomplete resolution of the ^{3}He particles the neutron yield at an energy of 2.99 Mev was determined by monitoring the proton yield from the competing $^{2}H(d,p)^{3}H$ reaction.

Differential elastic scattering cross-sections were measured for calcium and sulphur at neutron energies of 2.99 Mev and 2.18 Mev respectively. Measurements were limited to scattering angles up to 80^{o} for calcium and 100^{o} for sulphur. The measurements obtained for calcium were compared with the results of Reber and Brandenburger at an energy of 3.29 Mev and with the results of Abramson et al at a neutron energy of 2.83 Mev. The results obtained for sulphur were comparable with the measurements of Holmqvist and Wiedling for a neutron energy of 2.47 Mev. The elastic scattering angular distributions were analysed using the optical model computer code RAROMP.

In addition an associated particle time-of-flight system was investigated for the $^{2}H(d,n)^{3}He$ reaction at the lower incident deuteron energy of 130 Kev which is more generally available.

Neutron/Elastic/Scattering/Cross-sections/Experimental

ACKNOWLEDGEMENTS

I would like to express my gratitude to Dr. A. J. Cox, my supervisor, for his continued help and guidance throughout the research project. I wish to acknowledge Professor S. E. Hunt in whose department this project was carried out and to thank the Science Research Council for providing the research grant.

I wish also to thank Mr. F. Lane and the Physics Workshop staff for invaluable help in the design and construction of much of the apparatus.

At Birmingham University I wish to acknowledge the help of Mr. D. Bassett and the Radiation Centre staff.

To my Mother and Father

CONTENTS

CHAPTER 1

GENERAL INTRODUCTION

1.1 Introduction

Knowledge of the interaction between a nucleon and nucleus is a prior requisite to an understanding of nuclear structure and reactions.

When a nucleon interacts with a nucleus the behaviour of the system is determined by all the possible interactions between the nucleons present and the incident nucleon. There are two possible methods for determining the nucleon-nucleus potential, either by theoretically summing all individual nucleon-nucleon potentials, or by determination from experimental data. Individually these methods have been found inadequate but together they are able to give a good account of the interaction. To elucidate on this inadequacy, the nucleon-nucleon potential represents a complex many body problem and analytic solution presents serious difficulties, whereas it has been found that experimental data can be fitted satisfactorily with many potentials optimised to fit the data, none of these can be distinguished experimentally.

Combining these two methods, by assuming a shape of the potential from nucleon-nucleon considerations and then iterating the relevant parameter values to obtain a fit to the experimental data, the nucleon-nucleus potential can be determined. The model established to predict the potential thus accounts for the gross behaviour of the system rather than considers individual nucleon-nucleon interactions.

The simplest model of the nucleon-nucleus interaction takes no

account of the structure of the nucleus and replaces it by a simple real potential well specified by a radius and depth. The consequences of such a model were studied by Bethe[1]. This theory was unable to predict neutron capture cross-sections, wide spacing of the resonances and slow changes of the cross-sections with energy which were observed experimentally.

The compound nucleus model[2] superseded this model and accounted successfully for the observed large capture cross-sections and the closely spaced resonance levels. According to this model the reaction proceeds via a comparatively long-lived intermediate stage involving one or more highly excited states of the compound nucleus. This strong absorption model, however could not account satisfactorily for the variation of cross-sections with increasing energy and the marked forward peaking evinced by elastic scattering distributions at some energies. This latter consideration indicated a direct interaction was taking place between the nucleon and nucleus, a mechanism wherein the compound nucleus formation was bypassed. In the direct interaction process the incident nucleon is considered to interact with a single nucleon or group of nucleons within the nucleus. For incident nucleon energies above about 10 Mev the direct interaction model predicts cross-sections which are in agreement with experiment. However, for energies below this the model is unable to account for the nature of some differential cross-section measurements i.e. isotropic distributions, which are more readily explained by the compound nucleus model.

Although the compound nucleus and direct interaction models were not entirely successful in describing the behaviour of cross-sections, each model seemed to have its validity. An intermediate model, the optical model, was proposed where the many body nuclear interaction was replaced by a two body complex nucleon-nucleus

potential. Both the real and imaginary parts of the potential are responsible for elastic scattering and the imaginary part is responsible for absorption. The consequences of this model were investigated by Fernbach et al[3][4] for neutron interactions.

The optical model has found remarkable success in describing the behaviour of certain cross-sections, notably in the differential cross-sections for elastic scattering, and in describing the gross behaviour (averaged over individual resonances) of the total reaction cross-section.

1.2 Neutron Scattering

The neutron as a result of its lack of charge possesses advantages over other charged projectiles in the study of nucleon-nucleus interaction processes. This is particularly apparent in the study of heavy nuclei, where energetic charged particles would be required to surmount the coloumbic potential barrier.

When a neutron collides with a nucleus several different processes may take place. At low ($<$10 Mev) energies the neutron can be elastically scattered by the nuclear potential or it may be absorbed to form a compound nucleus. The former process is called shape elastic scattering or potential scattering. In the latter process the nucleus is assumed to be formed in an excited state and can decay by emitting particles until it reaches the ground state. If few reactions are energetically allowed a neutron may be emitted from the compound nucleus with the same energy as the incident neutron, this process is called compound elastic scattering. At incident energies above about 6 Mev more reaction channels are available and the probability of a neutron being emitted in the entrance channel rapidly decreases with increasing neutron energy.

The optical model which has been successful in representing neutron elastic scattering has the potential form:-

$$U_{OP}(r) = U_R(r) + iW_I(r) + U_S(r) \qquad \ldots\ldots 1.1$$

where $U_R(r)$ and $i\,W_I(r)$ are the real and imaginary parts respectively and $U_S(r)$ represents the spin orbit potential. The real radial form factor is usually assumed to be the Woods - Saxon type i.e:-

$$U_R(r) = -V_R \left\{ 1 + \exp\left(\frac{r - R}{a}\right) \right\}^{-1} \qquad \ldots\ldots 1.2$$

Here R is the nuclear radius and a is the diffuseness parameter of the nuclear surface. The imaginary potential may take a number of different forms, Woods - Saxon for volume absorption, and a derivative Woods - Saxon or Gaussian for surface absorption being the most common forms.

To calculate the cross-sections for two particles interacting through the potential described in equation 1.1, Schrödinger's wave equation is applied to the system, viz:-

$$\frac{\hbar^2}{2m} \nabla^2 \psi + (E - U_{OP})\psi = 0 \qquad \ldots\ldots 1.3$$

where U_{OP} is the potential, E is the total energy available in the centre of mass system, m is the reduced mass of the incident and target nuclei, and $\hbar = h/2\pi$ where h is Plands constant.

The optical model potential U_{OP} defined in equation 1.1 depends only on the position of the incident particle, the wave function ψ can be expanded in spherical harmonics to give a series of radial wave function equations. These radial wave equations are then solved by numerical integration from the origin to a point

where the nuclear potential is negligibly small. The solutions of these radial wave equations have both real and imaginary components as the potential defined in equation 1.1 is complex. The solutions enable the elastic scattering and reaction cross-sections to be calculated. Comparison with experimental data allow the parameters of the potential to be obtained more precisely.

Difficulty can be encountered in comparing theory with experiment, in that whereas the total cross-section is both calculable and measurable, its individual components cannot necessarily be compared. The total cross-section can be calculated from:-

$$\sigma_T = \sigma_{SE} + \sigma_R \qquad \ldots\ldots 1.4$$

where σ_{SE} is the shape elastic cross-section and σ_R is the reaction cross-section predicted by the optical model. For neutron energies (<6 Mev) where compound elastic scattering is a predominant mode of decay of the compound nucleus, the predicted reaction cross-section contains both the compound elastic cross-section σ_{CE} and the non-elastic cross-section σ_{NE}, viz:-

$$\sigma_R = \sigma_{CE} + \sigma_{NE} \qquad \ldots\ldots 1.5$$

The measurable components of the total cross-section are the elastic cross-section σ_{EL} and the non-elastic cross-section, hence:-

$$\sigma_T = \sigma_{EL} + \sigma_{NE} \qquad \ldots\ldots 1.6$$

and

$$\sigma_{EL} = \sigma_{CE} + \sigma_{SE} \qquad \ldots\ldots 1.7$$

For neutron energies where compound elastic scattering is not negligible measured values must be compensated for this contribution if calculated and measured quantities are to be

compared meaningfully.

Uncertainty about the compound elastic cross-section makes it difficult to apply the optical model in the low energy region. Experimentally compound elastic scattering is indistinguishable from shape elastic scattering but in the optical model it is included in the decay of the compound nucleus. The amount of compound elastic scattering may be estimated in several ways none of them completely satisfactorily. Beyster et al[5] compensated the experimental data for compound elastic scattering by subtracting a variable isotropic component from the observed differential cross-section until the optical model fit was optimised. This is not reliable because the lack of fit may be due to inadequacies of the model. Other methods have been described which are either limited to specific elements[6] or are dependent on parameters generated by the optical model[4][7].

This latter technique can yield accurate results if the optical model potential employed represents accurately differential elastic scattering cross-sections at neutron energies where compound elastic scattering can be neglected. The model can be used to predict with a good degree of confidence data for lower neutron energies. The discrepancy between measured and calculated values can be used to determine the compound elastic contribution.

This method was employed by Perey and Buck[8] in fitting a single energy-independent non-local optical potential to elastic scattering data for neutron energies between 4 Mev and 25 Mev. The model gave good agreement between theoretical and experimental angular distributions and was used to predict differential elastic scattering cross-sections and compound elastic cross-sections for neutron energies down to 1 Mev. The non-local potential not only depends on the centre of the incoming particle

but also accounts for the dispersive nature of the nuclear matter. This leads to increased complexity in computing and Wilmore and Hodgson[9] calculated an equivalent local potential i.e. the potential depended only on the centre of the incoming particle. This model was then used to analyse differential elastic cross-sections for medium and heavy weight nuclei for neutron energies between 1 Mev and 15 Mev. Compound elastic cross-sections were also calculated from the discrepancy between calculated and experimental results.

1.3 The Research Programme

The aim of the research programme was to study differential neutron elastic scattering cross-sections at neutron energies between 2 Mev and 3 Mev. The availability of data on angular distributions for elastic scattering in this neutron energy range is as yet limited to a number of nuclei only. This region is of interest as the neutron energies correspond approximately to neutron energies produced by a fission reactor. However, only recently has it been possible to build apparatus with sufficient resolution to enable measurements to be made.

As it was beyond the scope of the present work to obtain information on a large number of elements, attention was focused on medium weight nuclei ($30<A<50$). The reasons for this are that the optical model has been found more successful for medium and heavy nuclei as these approach the limit of uniform nuclear matter. In addition, with heavy nuclei the excited states of the nucleus tend to be closely spaced, this can present problems when resolving elastic and inelastic contributions from low lying states.

From the literature survey undertaken at the beginning of the work limited data only was available for the differential elastic

scattering cross-sections and for the optical model analysis on calcium and sulphur for the neutron energies under consideration.

For calcium, differential elastic cross-sections had been measured at neutron energies of 2.83 Mev by Abramson et al[10] and at 3.29 Mev by Reber and Brandenburger[11]. No optical model analysis had been performed for the former energy. An analysis was made at the latter energy, but the optical model and parameters obtained appeared to be inadequate to describe the angular distributions at neutron energies where compound elastic scattering was negligible, and to predict values which were in agreement with the measured values at the neutron energy of 3.29 Mev. This may have been due to inadequacies in the model or inaccurate determination of the compound elastic scattering contribution.

There was also an absence of data available on differential elastic cross-sections for sulphur for neutron energies below 2.4 Mev and a lack of optical model parameters.

The aim of the present work was to provide data on the angular distributions for calcium at a neutron energy around 3 Mev and for sulphur at an energy below 2.4 Mev. Relevant optical model analysis could then be performed by correcting the experimental data for compound elastic scattering cross-sections obtained by Wilmore and Hodgson.

To obtain the desired elastic scattering data a time-of-flight spectrometer is described. The design, construction and calibration of the spectrometer constituted a major part of the research programme.

1.4 Time-of-flight Technique

In recent years neutron scattering measurements have been enhanced by the development of nano-second time-of-flight

spectrometers. These spectrometers essentially measure the transit time of a neutron over a defined path. The constituents of a scattered neutron beam can then be analysed in terms of their relative velocities i.e. the difference in their arrival times at the end of a defined flight path. When a neutron collides with a nucleus either elastic or inelastic scattering may occur, the latter process is possible provided the neutron energy is higher than the first excitable state of the nuclei. If scattering studies are the motive for the resarch then the resolution of the spectrometer is important in order to resolve both elastic and inelastic contributions.

Time-of-flight techniques require the establishment of two time signals relating to neutron production and detection. An essential part of the time-of-flight measurement is therefore the precise determination of the time of origin of the particles. Time-of-flight methods for neutron energies above 1 Mev involve either pulsed beam techniques or the associated particle method. These methods differ in the way the time of origin of the neutron is obtained, the neutron source is a nuclear reaction induced by ion bombardment.

In the pulsed beam techniques, methods are concerned with producing the neutrons in short bursts, the time duration of the neutron bursts is one of the factors determining the spectrometer resolution. Neutron bursts are produced by pulsing the ion beam used to induce the reaction, the time structure of the ion bursts then determines the time of origin of the neutron. Because of the finite time duration of the pulse an uncertainty is introduced in the time of origin of the neutron, this time uncertainty can be reduced by time compression of the ion beam pulses by either a Mobley magnet system or a Klystron bunching system. Compression

also increases the peak current of the ion beam pulses. The pulsed charged particle beam technique can be used for a wide range of neutron producing reactions.

This pulsed beam technique was first applied to neutron energy measurements by Cranberg and Levin[12]. This technique has been used by others [13-15] to discriminate between elastically scattered neutrons and gamma rays, and is now widely used.

The main alternative to pulsed beam techniques for energetic time-of-flight measurements is the associated particle method. This system was the first time-of-flight method to be used to investigate the scattering of monoenergetic fast neutrons[16][17]. The source of neutrons is either the $^{3}H(d,n)^{4}He$ or $^{2}H(d,n)^{3}He$ reactions. The time of origin of the neutron is determined by detecting the associated charged particle which can be detected with 100% efficiency. By selection of the angle at which the recoil particle is detected, the angle of emission and thus to some extent the energy of the emitted neutron can be determined. The advantages of this system are that the timing depends only on the characteristics of the charged particle and neutron detectors and their associated electronics. In addition, a collimated neutron beam can be obtained simply by collimation of the associated charged particles. This leads to a reduction in the shielding requirements, with the pulsed beam method time related neutrons are produced in all directions.

The associated particle technique has not been exploited with the $^{2}H(d,n)^{3}He$ reaction until recently due to technological problems. These problems are mainly related to performing accurate spectrometry on the associated charged particles. However, recent developments with semi-conductor detectors and in electronics has enabled some of the problems to be overcome. As a result there

are only a few spectrometers producing neutrons from this time-of-flight technique.

As neither space nor facilities were available for the development of a pulsed beam system, the associated particle system was developed for the production of neutron beams with energies between 2 Mev and 3 Mev from the $^{2}H(d,n)^{3}He$ reaction.

In the present work two accelerators, a Dynamitron and a S.A.M.E.S. accelerator, were available to produce incident deuteron beams with energies between 1 Mev and 3 Mev for the former and up to 140 Kev for the latter accelerator. For deuteron energies up to 140 Kev an experimental time-of-flight spectrometer has been reported for the production of 14 Mev neutrons from the $^{3}H(d,n)^{4}He$ reaction, the associated particle technique was employed[18]. One of the aims of the research programme was to determine the feasibility of producing neutrons with energies between 2 Mev and 3 Mev from the $^{2}H(d,n)^{3}He$ reaction at the same facility. This study was motivated as the S.A.M.E.S. is a more economical accelerator and hence is more readily available to research establishments.

In addition an associated particle time-of-flight system is described for the production of neutrons within the same energy range for the Dynamitron accelerator, this aspect is considered in Chapters 2-4.

CHAPTER 2

ASSOCIATED PARTICLE TIME-OF-FLIGHT SYSTEM FOR THE $^{2}H(d,n)^{3}He$ REACTION FOR USE ON THE DYNAMITRON ACCELERATOR

Neutrons with an energy between 2 Mev and 3 Mev were produced from the associated particle reaction $^{2}H(d,n)^{3}He$. There are technical difficulties encountered in applying the time-of-flight technique to this reaction. These problems and the methods used to overcome them are discussed in the subsequent sections.

The incident deuteron beam was furnished by a Dynamitron accelerator which was located at Birmingham University.

2.1 The Dynamitron Accelerator

The Dynamitron accelerator is a variable energy potential drop device capable of terminal potentials from about 800 Kv to 3 Mv. It is powered by an R.F. oscillator operating at 130 kHz. The power is fed to two large semi-cylindrical plates (the dees) inside the pressure vessel which are capacitively coupled to semicircular rings about the acceleration column. These rings (the corona rings) are seperated by 64 solid-state rectifier modules which form a chain from the base of the machine to the terminal. The rectification of the R.F. over these stages produces the D.C. potential on the terminal. The solid-state rectifiers were installed in the December of 1975, previously thermionic rectifiers had been used which limited the minimum terminal potential to 1 Mv. The machine can accelerate electrons or positive ions. In the positive mode up to 2 mA of protons can be produced at 3 Mv. The beam produced is not entirely monoenergetic; there is a ripple of 1 kv at 1 Mv and increases to 3 kv at 3 Mv. Over a period of 1.5 hours the terminal potential can drift from a

set value by about 0.2 kv. The acceleration column is shown in Figure 2.1.

Ions are produced in a duoplasmatron ion source, and either hydrogen or deuterium can be used. In order to separate the different ions produced, the source is placed at an angle to the acceleration column and the ions deflected into the plane of the accelerator by a permanent magnet. Adjustment of the potential used to extract the ions from the source prior to entry into the magnetic field, selects the mass through the analyser.

The Dynamitron is stabilised using the current drawn through a resistor chain connecting the terminal in the machine to earth. The resistor chain is about 10^{10} ohm and the current produced is measured on a DVM reading across a 500 ohm resistor in the control panel. The current passes onto a control circuit which feeds back to the oscillator. The target current is monitored on a Keithley electrometer.

When the beam emerges from the base of the accelerator column it enters a magnet room. In order to transport the beam into the Low Scatter (Upper) Cell used in the present experiments, the beam passes into a first bending magnet, the H-magnet, which steers the beam through 45°. It then enters a second magnet, the C-magnet, which can steer the beam through a further 45° into the beam room.

2.1.1 Data Acquisition Facilities

Data acquisition is accomplished using a Hewlett-Packard computer system, which comprises three data collecting stations. A standard system has a teletype, display and an ADC which has 4096 data channels. The software to drive the stations is usually the Hewlett-Packard 5406B nuclear data package but the system which organises the links between the satellite processors and the central

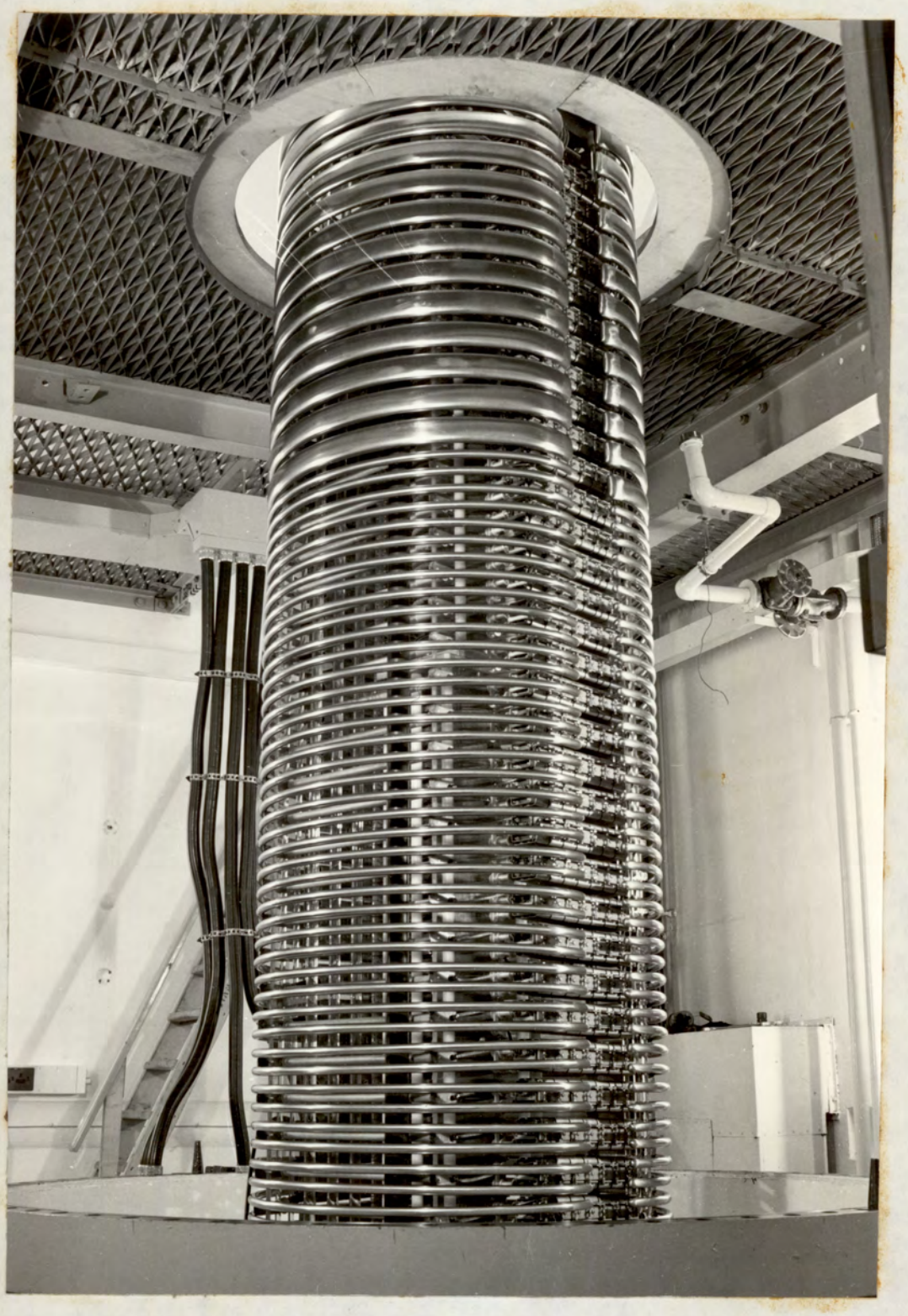

Figure 2.1 The Dynamitron acceleration column

computer enables the user to call any operating system previously configured.

The central computer operates a real-time executive package (RTE) which handles most types of basic peripherals. Several levels of programme can co-exist simultaneously in the core and Fortran programmes can be run. The satellite computers can initiate programmes in the central computer and enable data to be transferred.

2.2 Kinematics

In the $^{2}H(d,n)^{3}He$ reaction the interaction process can be considered as a two body inelastic collision, figures 2.2(a) and 2.2(b) show the reaction in the laboratory and centre of mass systems. The equations relevant to the reaction are given in appendix A.1. In order to allow both particles to be detected the angle and energy for the ^{3}He are considered for a defined neutron angle and incident deuteron energy.

For neutron emission at a laboratory angle Ψ the corresponding energy E_3 in the laboratory can be found from equation A1.2. In order to calculate the laboratory values for the energy and angle of the associated ^{3}He, the centre of mass angle ϑ for neutron emission is required, this can be evaluated using equation A1.7. The relationship between the neutron and ^{3}He centre of mass angles is given by:-

$$\phi = 180 - \vartheta \text{ (degrees)} \qquad \ldots\ldots 2.1$$

where ϕ is the ^{3}He centre of mass angle.

The value of ϕ is then substituted into A1.4 to obtain the laboratory energy of the ^{3}He, E_4. The laboratory angle ζ for ^{3}He emission corresponding to a neutron angle of Ψ is obtained from equation A1.6. Results were obtained in this manner for the maximum and minimum (2.5 Mev and 1 Mev) deuteron energies under consideration.

a) Laboratory system

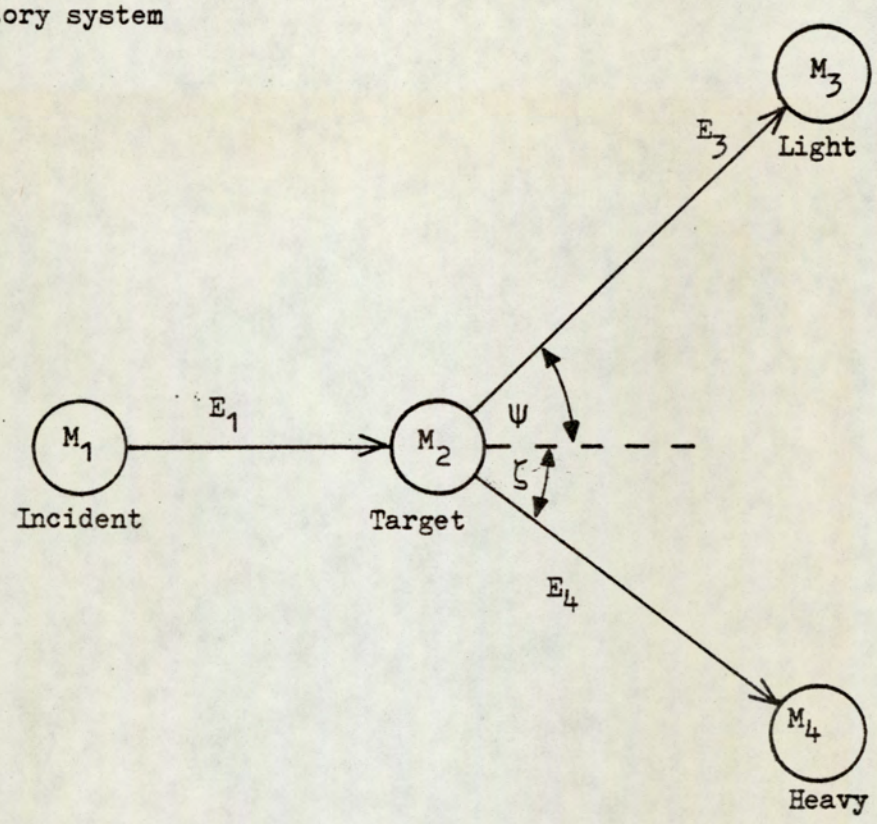

b) Centre of Mass system

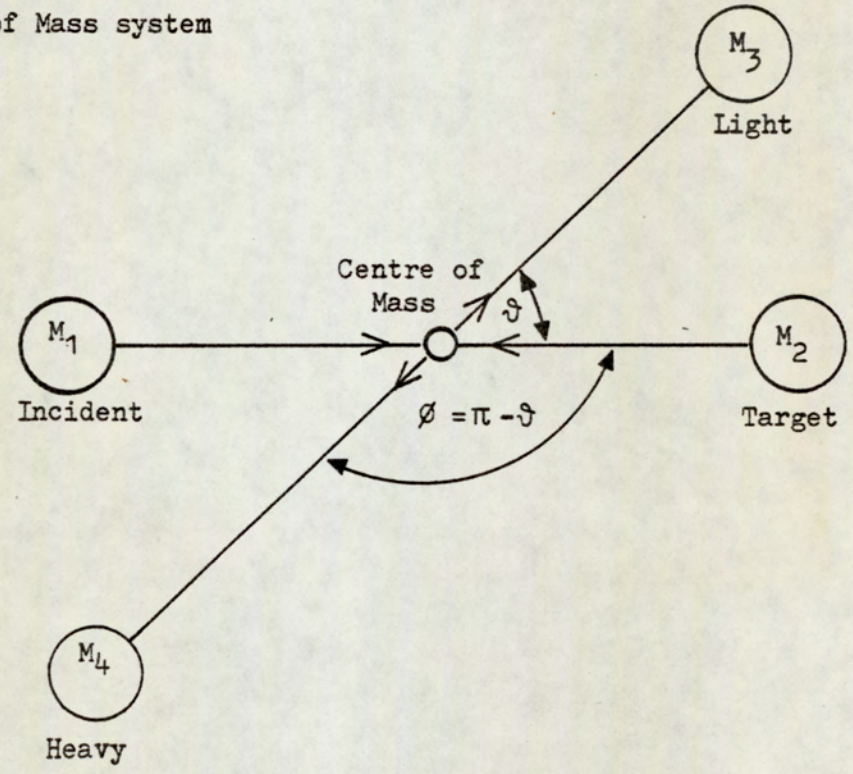

Figure 2.2 Kinematics of a nuclear reaction.

Figure 2.3 shows the variation of the energies of the ^{3}He and neutron particles as a function of neutron angle, while figure 2.4 gives the variation of ^{3}He angle with neutron angle. Also shown in figures 2.3 and 2.4 are the results obtained for a deuteron energy of 0.1 Mev, these results are shown to highlight problems encountered in applying techniques used in establishing associated particle systems at low deuteron energies ($\simeq$ 100 Kev) at the higher deuteron energies under consideration. These and related problems are discussed in more detail in this section.

By the use of the method described and the graphs shown, the required kinematic positions for the two detectors to produce an associated system can be obtained.

However, in applying the associated particle technique to this particular reaction considerable experimental problems are encountered. The main difficulties arise in resolving the ^{3}He particles from a large number of other charged particles produced at the same time. This resolution is important if the associated ^{3}He particles are to be detected unambiguously.

The main particles produced in addition to ^{3}He by the deuteron bombardment of a deuterium target are protons and tritons from the competing $^{2}H(d,p)^{3}H$ reaction, deuterons elastically scattered by the coulombic field of the target nucleus and neutron capture γ-rays produced in the surrounding materials.

The main problem is encountered when considering the scattered deuteron flux, which is 10^{5} times higher than the flux of ^{3}He particles. If these deuterons are not prevented from reaching the detector they will saturate the detector electronics. The cross-sections for the $^{2}H(d,n)^{3}He$ and $^{2}H(d,p)^{3}H$ reactions are comparable and vary with energy in a similar way, therefore the protons and tritons produced contribute only slightly to the pulse pile up.

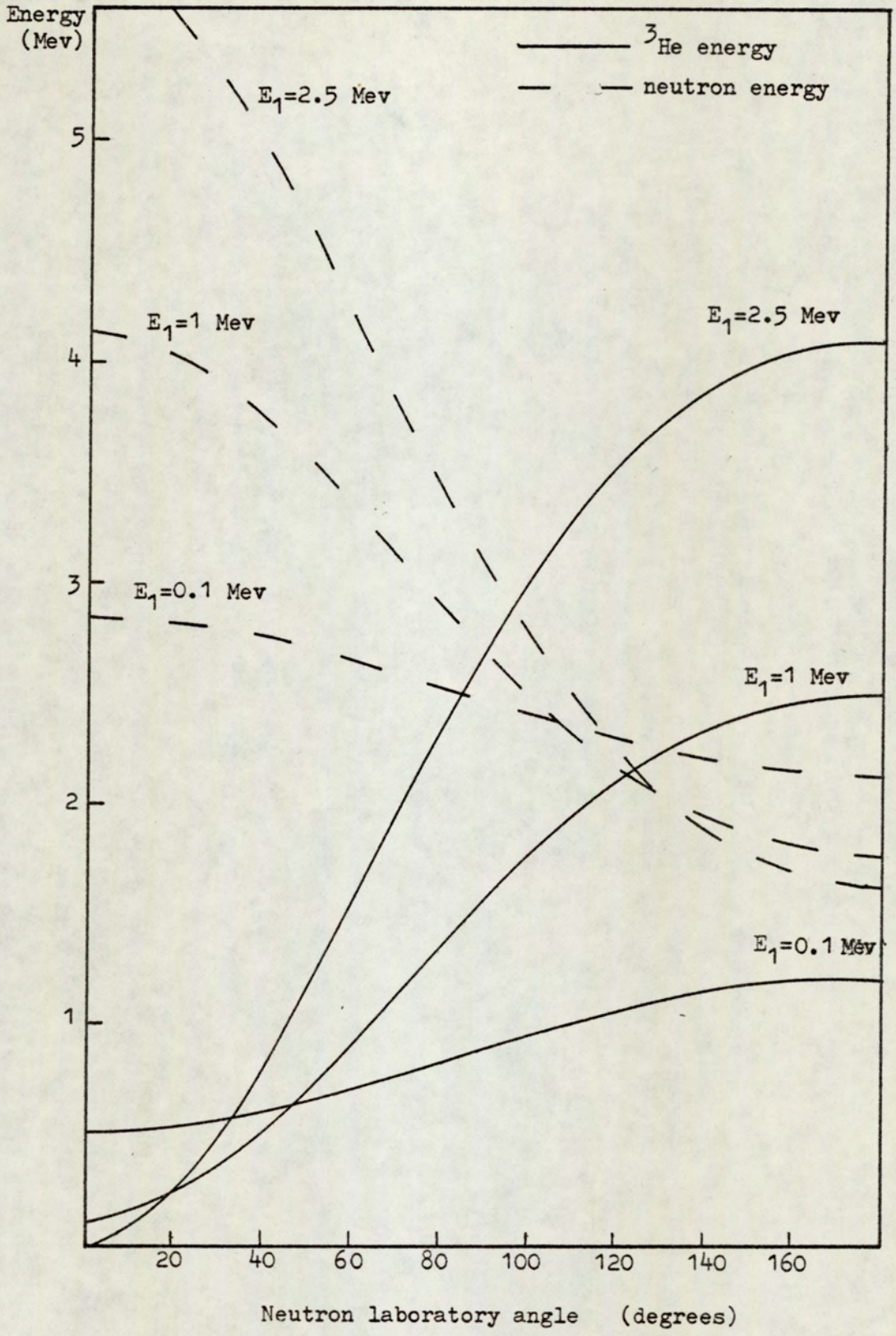

Figure 2.3 Variation of neutron and associated ^{3}He energy with neutron angle at various incident deuteron energies.

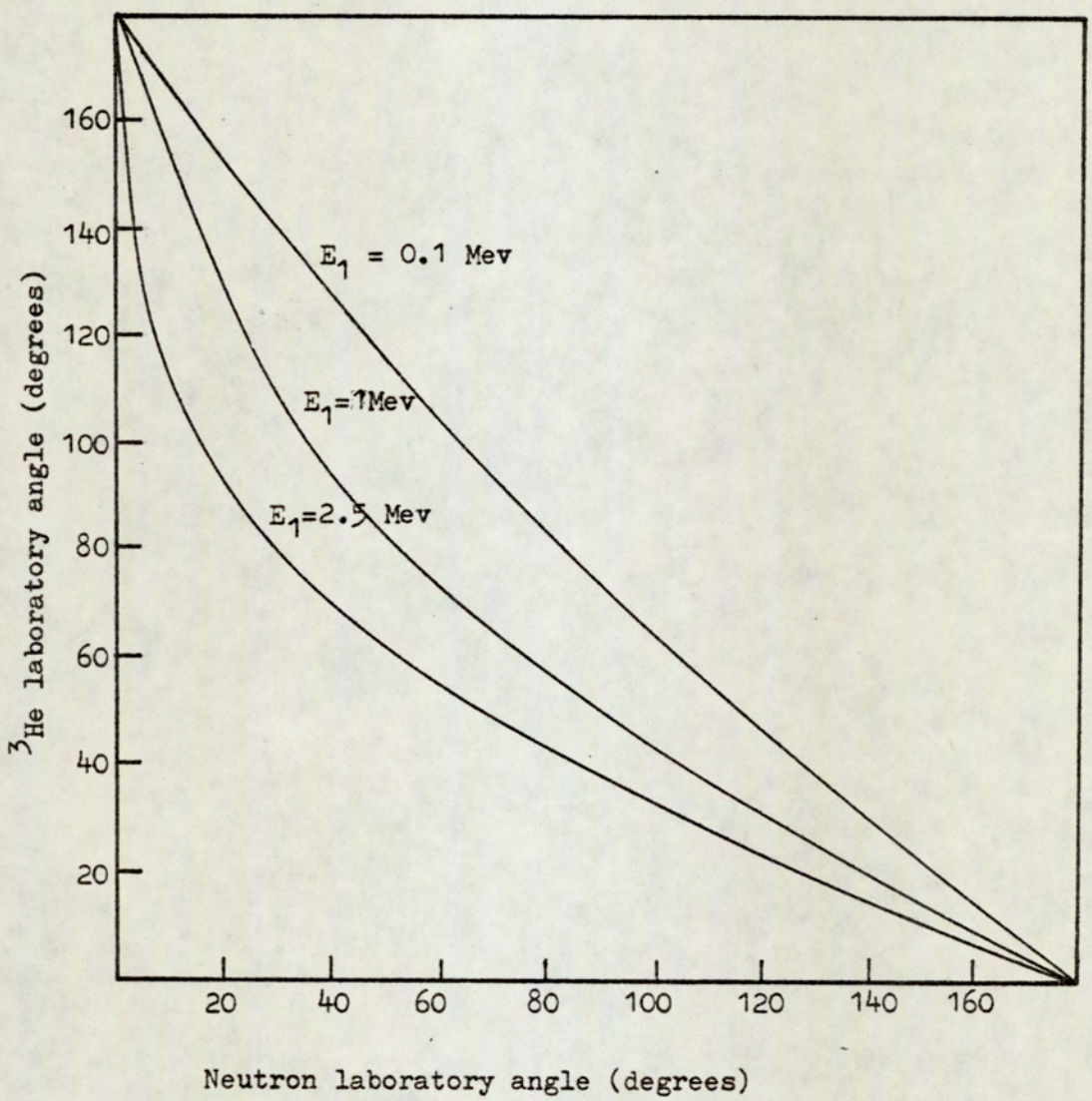

Figure 2.4 Relation between ^{3}He and neutron laboratory angles at various incident deuteron energies

The energy of the scattered deuterons is considered in order to determine whether discrimination can be employed to limit or stop them entering the ^3He detection system. Figure 2.5 is a vector diagram relating the centre of mass and laboratory systems for an elastic collision.

The laboratory energy of the scattered particle E_1 is given by:-

$$E_1 = \frac{E_o M_1^2}{(M_1+M_2)^2} \left\{ \cos\Psi + \left[\left(\frac{M_2}{M_1} \right)^2 - \sin^2\Psi \right]^{\frac{1}{2}} \right\}^2 \quad \ldots\ldots 2.2$$

where E_o is the energy of the incident particle of mass M_1 and M_2 is the target nucleus mass. For the condition where the incident particle and target masses are the same i.e. deuteron-deuterium elastic scattering, equation 2.2 reduces to:-

$$E_1 = E_o \cos^2\Psi \quad \ldots\ldots 2.3$$

If the deuterium is present in a target containing other constituent atoms then from equation 2.2 the energy of the scattered deuteron will depend on the target nucleus mass and the angle of scatter, Ψ.

The maximum energy of a scattered deuteron produced in the target will be equal to the incident beam energy, E_o. If the target is thick to the incident beam (i.e. the incident deuteron loses all its energy in the target) the scattered deuterons will have a maximum energy distribution between E_o and zero.

At low incident deuteron energies (< 300 Kev) the energy of the ^3He is higher than the maximum energy of the scattered deuterons, in figure 2.3 the ^3He energy variation with neutron angle is shown for E_o = 0.1 Mev. Discrimination can be employed to remove the scattered deuterons before they reach the detector. This is accomplished by an absorber placed between the detector and target.

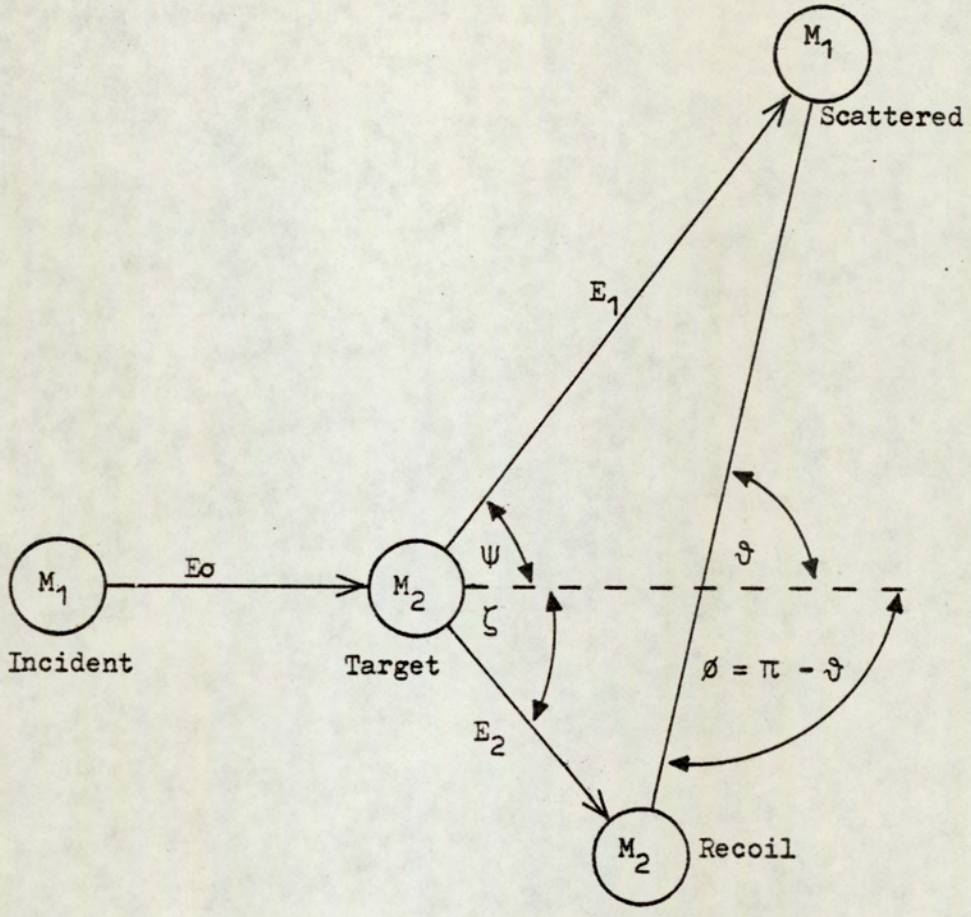

Figure 2.5 Kinematics of nuclear scattering in laboratory and centre of mass systems

Dixon et al[19] and Bell et al[20] working at incident deuteron energies of 100 Kev used a CsI(Tl) crystal for ^{3}He detection. The scattered deuterons and light emitted from the target were prevented from reaching the detector by a 225 $\mu g\ cm^{-2}$ thick aluminium coating evaporated onto the face of the crystal. Although a thin crystal (.51 mm) was employed, neutron capture γ radiation still reached the detector.

However at higher incident deuteron energies (above 1 Mev) an absorber capable of stopping the deuterons will also stop the ^{3}He particles.

Other methods of discrimination against scattered deuterons have been applied at low bombarding energies (<300 Kev). In a target containing constituent atoms where the mass of these target nuclei are greater than the deuteron mass, deuterons can be elastically scattered in all directions. However, for deuteron-deuterium elastic scattering no deuterons can be scattered beyond 90°. Franzen et al[21] established an associated particle system by using a deuterium gas target at 90° to the incident beam. The disadvantages of this system at higher incident energies are that it is difficult to obtain both good angular resolution and a high intensity of neutrons. Experimental problems are also encountered in designing a system employing a gas cell, as the cell must be isolated from the main accelerator pumping system by either differential pumping or by the use of thin windows to seal the gas cell.

Put et al[22] operating at an incident energy of 280 Kev, applied electrostatic analysis to seperate the ^{3}He particles from the scattered deuterons. Although this method is feasible at higher energies the longer path lengths cause a large spread in the time of detection for ^{3}He particles of different energies, since the variation in flight time of ^{3}He particles of different energies is proportional to path length.

A method of reducing the intensity of deuterons scattered in the backward angle is to use a target of low atomic mass. Monier et al[23] used heavy ice targets at an incident energy of 50 Kev. The intensity of deuterons observed at 105° was reduced sufficiently to prevent electronic saturation and allow the ^{3}He particles to be partially resolved from the deuteron. Although detection at backward angles, for low mass targets, affords a method of resolving the ^{3}He from scattered deuterons, difficulty is encountered when applying this technique to higher incident energies. The energy of the ^{3}He detected at backward angles decreases with increasing deutron energy (figures 2.3 and 2.4) the low energy of the ^{3}He makes the detection process difficult for incident deuteron energies above 1 Mev.

A further problem is encountered in considering the energies of the products from the competing $^{2}H(d,p)^{3}H$ reaction (Q value of 4.04 Mev). The kinematic equations used to describe the $^{2}H(d,n)^{3}He$ reaction can also be applied to the $^{2}H(d,p)^{3}H$ reaction. The energy of the triton for a particular angle of ^{3}He detection is comparable to the energy of the ^{3}He. The scattered deuterons, ^{3}H and ^{3}He all undergo energy loss in escaping from the target as a result of collisions with the target nuclei. With 'thick' targets this results in a large energy distribution of the particles emerging from the target and it is impossible to prevent ^{3}H and deuterons overlapping in energy with the ^{3}He particles.

From the preceding discussion it can be seen that the methods of discrimination used at low deuteron energies are not applicable at higher incident energies. Clearly a different technique is required if the ^{3}He particles are to be resolved from other charged particles.

Tripard et al[24] working at an incident energy of 2 Mev employed thin self-supporting targets of deuterated polyethylene,

$(CD_2)_n$. The advantages of these targets are that, both the scattering from and the energy degradation in the targets is sufficiently small that the associated particle detector can be exposed directly to the flux of particles coming from the target. However, the scattered deuteron flux was still sufficiently large to mask the ^3He pulses in the detector energy spectrum. The ^3He energy spectrum was resolved from surrounding groups by gating the ^3He pulses with pulses from a neutron monitor mounted in the associated neutron beam. This has obvious problems when a sample is placed in the neutron beam for scattering experiments. Also by gating the ^3He spectrum with neutron pulses the ^3He count becomes dependent on the efficiency of the neutron detector.

Schuster et al[25] using deuteron energies up to 14 Mev used similar targets but with thin backing materials of titanium and carbon. The backing material allowed an increase in the target currents due to the larger thermal capacity of the targets, but the ^3He, ^3H and scattered deuterons suffered a large energy loss in emerging from the targets. The ^3He spectrum was gated with the neutron pulses to resolve the ^3He peak from overlapping energy groups.

In the associated particle system the resolution of the ^3He peak is important as it enables the defined neutron beam to be monitored. If a scattering sample is placed such that it intercepts the defined neutron beam, the number of neutrons incident on the sample can be obtained from the detected ^3He count. If the ^3He peak is unresolved an alternative method to determine the neutron yield is to monitor a peak in the energy spectrum well resolved from surrounding groups. The proton produced in the competing $^2H(d,p)^3H$ is of high energy and is well separated from lower energy groups. The proton yield is then related to the ^3He yield hence neutron flux produced[26].

The use of thin films of deuterated polyethylene provides an acceptable solution to the problems inherent in applying the associated particle technique to the $^{2}H(d,n)^{3}He$ reaction. By using these targets the intensity of deuterons can be reduced sufficiently for an adequate neutron flux to be produced. The problem encountered with targets which are thick to the incident deuteron beam, namely that of a large distribution of pulse sizes for each particle type produced, can be overcome to some extent in the choice of a target of suitable thickness.

The present experimental system makes use of these thin targets where the "thickness" is chosen to give a compromise between the neutron yield and the energy loss of the particle groups formed in the target. In the following section consideration is given to the reaction kinematics for the present system so that the difference in energy between the scattered deuterons, triton and the ^{3}He can be maximised, in order to reduce the number of background events overlapping with the ^{3}He peak.

2.2.1 Kinematic Considerations for the Experimental Geometry

The experimental system limited the neutron production angles to 30°, 75° and 120° from the incident beam direction. Considering these neutron emission angles, the corresponding ^{3}He angles and energies were calculated for increasing incident deuteron energies. The ^{3}He angle obtained was then used to compute the energies of the proton and triton particles produced in the competing reaction. The energies of the deuterons scattered from carbon and deuterium in the target were calculated from equations 2.2 and 2.3. Figures 2.6, 2.7 and 2.8 give the variation of the energies of the particles emerging from the target as a function of increasing deuteron energy for the three neutron emission angles.

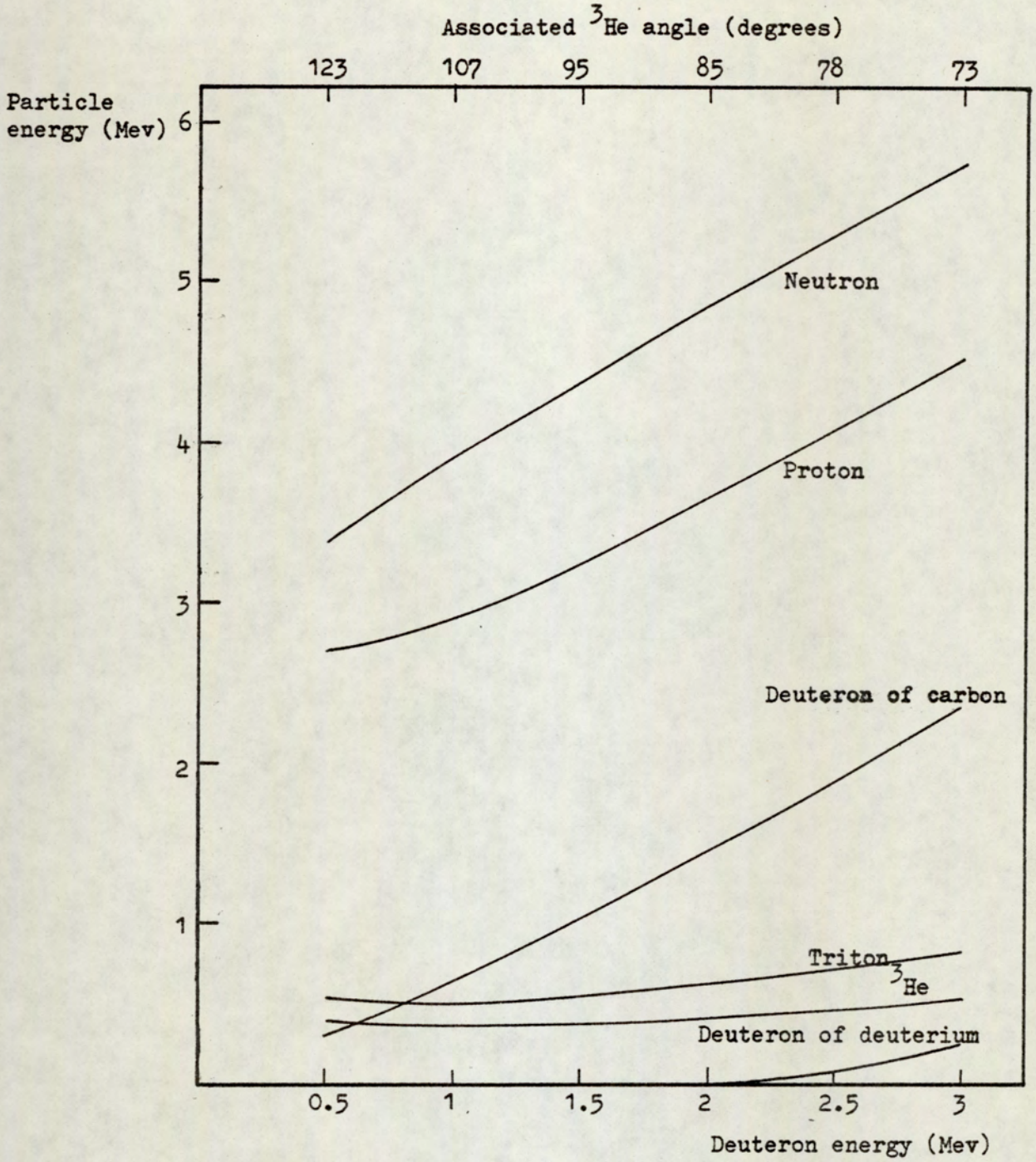

Figure 2.6 Energy of particles produced at an angle defined by an associated neutron laboratory angle of 30°

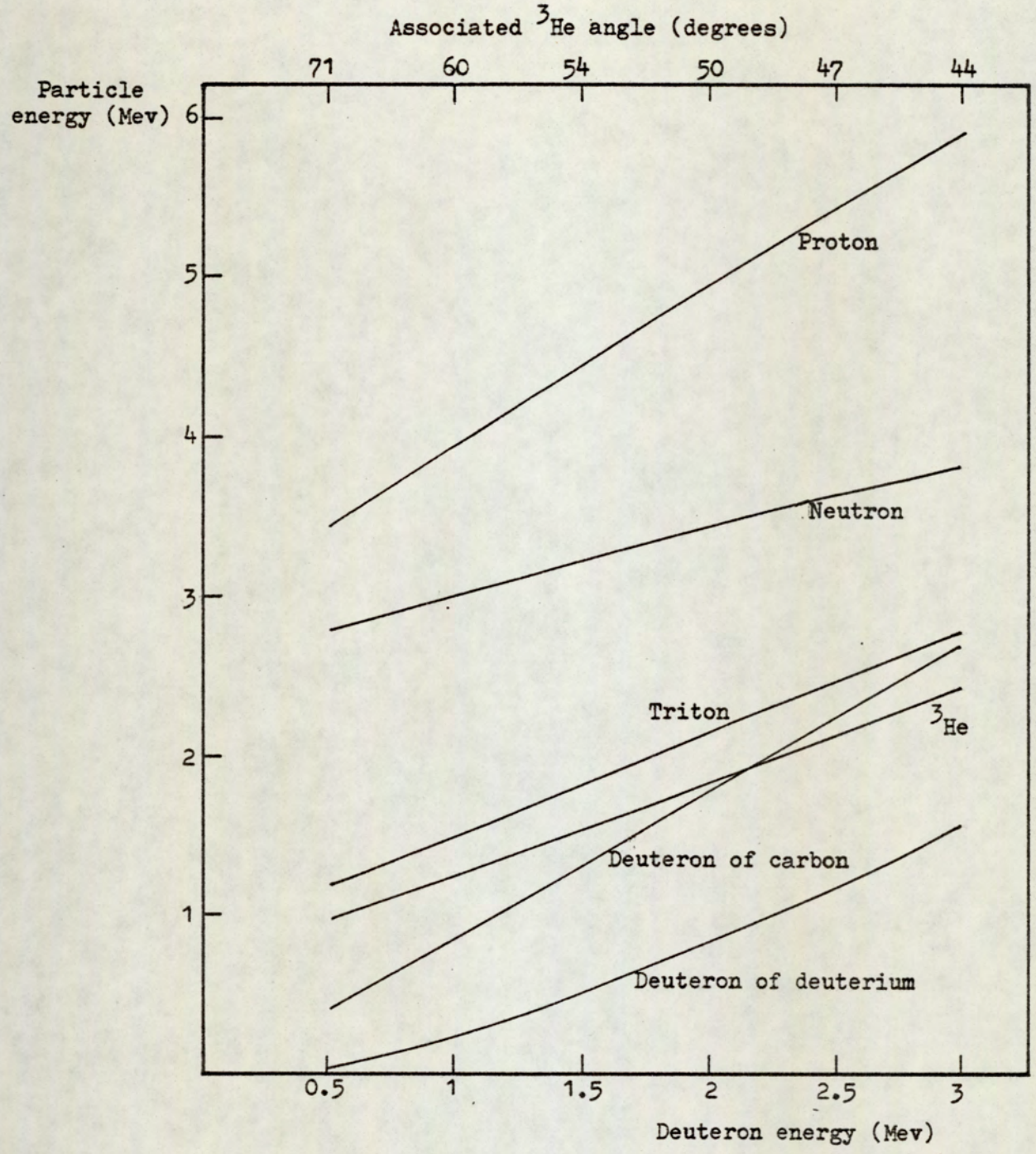

Figure 2.7 Energy of particles produced at an angle defined by an associated neutron laboratory angle of 75°

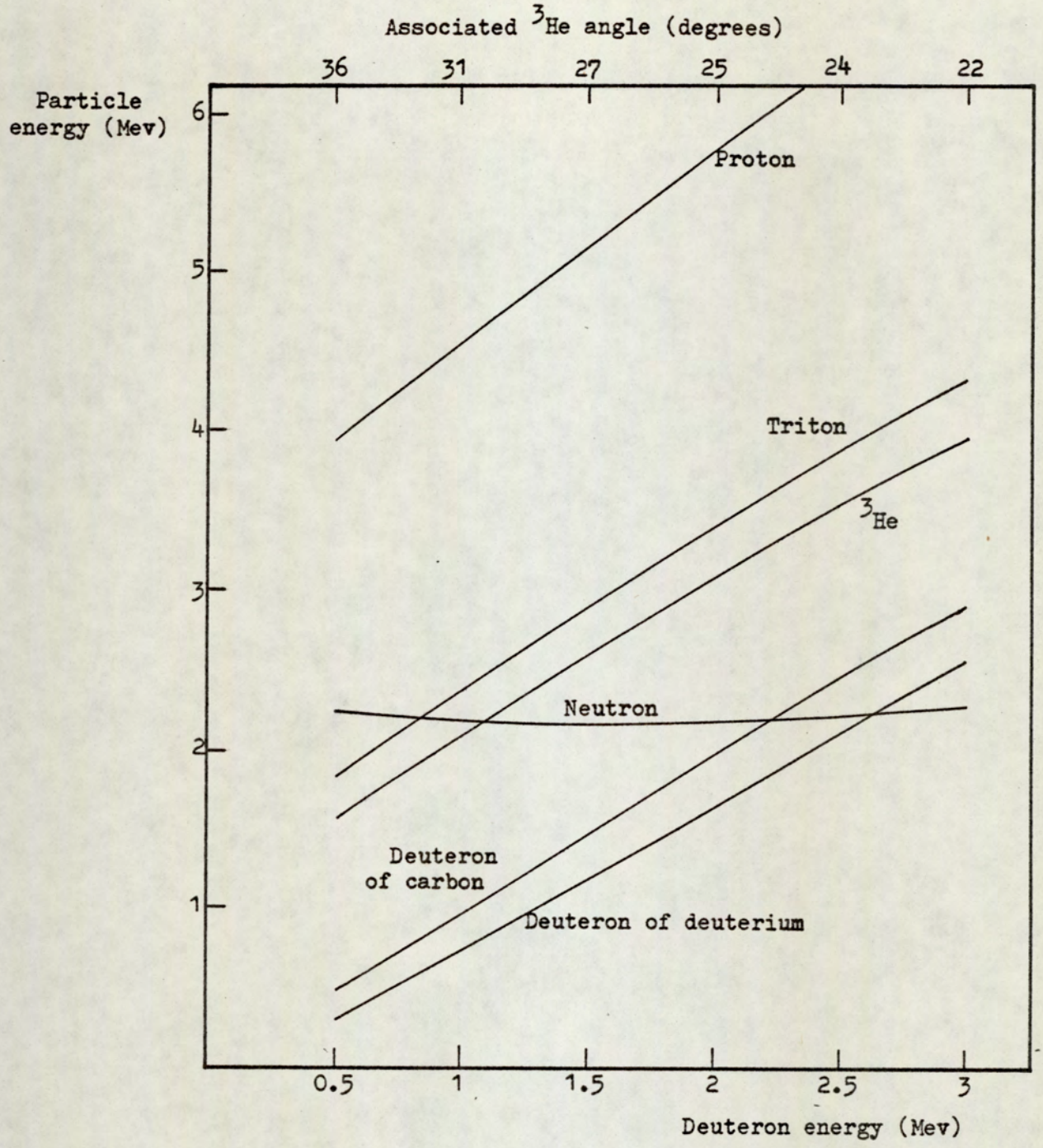

Figure 2.8 Energy of particles produced at an angle defined by an associated neutron laboratory angle of 120°

There are many factors which can influence the angle at which the associated particle detector is placed and the choice of incident beam energy, those considered of importance are discussed below. The energy difference between the ^{3}He and triton, and ^{3}He and the deuteron energy groups was maximised. This was to ensure a minimum number of unrelated events in the ^{3}He energy range, enabling the ^{3}He pulses to be used directly for timing purposes, eliminating gating with the neutron pulses. The charged particle detector was limited to angles below 25° to the incident beam direction. The reason for this was the differential cross-section for the elastic scattering of deuterons from carbon and deuterium increasing rapidly above 25°. The ^{3}He energy was chosen to be as large as possible, thus ensuring a minimum of energy spread for the ^{3}He in emerging from a thin target. The neutron energy produced must also be within the energy range of 2 - 3 Mev for use in the scattering experiments.

In figure 2.6 the energies of the particles are shown for a neutron production angle of 30°. In this arrangement the neutrons produced have energies between 4 Mev and 5 Mev depending on the incident deuteron energy. Also the deuterons scattered from carbon have energies greater than the ^{3}He particles. Considering the other two neutron angles 75° and 120° the neutron and associated ^{3}He energies are more favourable. At 75°, figure 2.7, the optimum operating energy is 1 Mev. At this energy the neutron energy is 3.02 Mev. With increasing deuteron energy the neutron energy will also increase, while the energy difference between the ^{3}He and scattered deuteron decreases. For a neutron angle of 120°, figure 2.8, the ^{3}He energy remains about 1 Mev higher than the scattered deuteron, although a high incident energy is favoured in terms of a high ^{3}He energy, this must be considered against the neutron yields produced. Over the incident deuteron energy range (1 Mev

to 2.5 Mev) the neutron energy varies between 2.18 Mev and 2.24 Mev.

Considering limitations imposed on the experimental system, neutron energies and in resolving the ^{3}He peak, only the neutron emission angles of 75° and 120° were considered for the development of the associated particle systems. The optimum deuteron energy for neutron emission at 75° was 1 Mev, however for neutron emission at 120° an incident deuteron energy of 2.5 Mev was favoured for resolving the ^{3}He peak.

In the following section the neutron yields are calculated as a function of target thickness for deuterated polyethylene targets. Considering the yields the optimum incident energy is determined for neutron emission at 120°.

2.3 Neutron Yields

The total neutron yield due to a deuteron of incident energy E_o, losing all its energy in a target containing nd deuterium atoms per cm^3 is given by:-

$$Y_t = \frac{nd}{\rho} \int_0^{E_o} \frac{\sigma_T dE}{dE/dx\ (E)} \qquad \ldots\ldots 2.4$$

where σ_T is the total reaction cross-section in barns, dE/dx is the energy loss of the deuteron at an energy E expressed in units of Mev g^{-1} cm^2 and ρ is the target density (g cm^{-3}). The yield of neutrons per steradian produced by a deuteron interacting in a thin target element is represented by:-

$$Y = \frac{nd}{\rho} \int_{E_2}^{E_1} \frac{d\sigma/dw(E)}{dE/dx\ (E)}\ dE \qquad \ldots\ldots 2.5$$

where $d\sigma/dw$ is the laboratory differential cross-section of the

reaction, in the units of barns/steradian, at an energy E, E_1 and E_2 are the incident and emergent deuteron energies on the thin element.

The target element thickness Δx, producing a yield Y from equation 2.5 can be found from:-

$$\Delta x = \frac{1}{\rho} \int_{E_2}^{E_1} \frac{dE}{dE/dx} \qquad \ldots\ldots 2.6$$

The yield was calculated as a function of target thickness for an incident energy of 1 Mev at the neutron production angles of 75° and 120°. Also considered, at the latter angle, is the yield due to a 2.5 Mev incident deuteron energy.

The calculation was performed by numerical integration of equation 2.5 to give the yield and equation 2.6 to give the corresponding target thickness. In order to perform the integrations, values for the energy loss of deuterons in deuterated polyethylene and the differential cross-section for the $^{2}H(d,n)^{3}He$ reaction were required as a function of deuteron energy.

2.3.1 Energy Loss of Deuterons in Deuterated Polyethylene

The deuterated polyethylene $(C_2D_4)_n$ used as target material contained 98% deuteron atoms, the remaining 2% consist of impurity hydrogen atoms bonded, in place of deuterium, to the carbon atoms. There were no experimental energy loss values available for charged particles in $(C_2D_4)_n$ but Rich and Madey[27] have calculated theoretical values for deuterons with an energy greater than 2 Mev in CD_2. Energy loss values are considered for CD_2 as this is the repeat unit in the polymer.

No information was available for lower deuteron energies, however experimental measurements have been made for the energy loss of protons in carbon[28][29][30] and atomic hydrogen[30][31][32].

The energy loss values for deuterons in atomic nuclei can be scaled to those obtained for protons. For particles of the same charge, the rate of energy loss is a function only of the velocity of the particle, the energy loss of deuterons then scales to proton data by:-

$$\left(\frac{dE}{dx}\right)_p (E) = \left(\frac{dE}{dx}\right)_d (2E)$$

The average energy loss of deutrons in deuterium in Mev mg^{-1} cm^2 is equal to onehalf the energy loss in hydrogen in Mev mg^{-1} cm^2, as the charge on the target nuclei are the same but the atomic mass of deuterium is twice that of hydrogen.

The energy loss of deuterons in CD_2 was calculated from Bragg's law, which states that the stopping cross-section of a compound is the sum of the cross-sections of the constituents. The stopping cross-section S is usually in units of eV - cm^2 $atom^{-1}$ and is related to the energy loss by:-

$$S = \frac{1}{n} \frac{dE}{dx}$$

The constant n is the number of nuclei of the constituent per cm^3. Considering the energy loss values in Mev mg^{-1} cm^2 and by applying Bragg's law to available data, the energy loss of deuterons in CD_2 is given by:-

$$\left(\frac{dE}{dx}\right)_{CD_2} = \frac{12}{12+2Nd+NH}\left(\frac{dE}{dx}\right)_C + \frac{2Nd}{12+2Nd+NH}\left(\frac{dE}{dx}\right)_D + \frac{NH}{12+2Nd+NH}\left(\frac{dE}{dx}\right)_H \quad \ldots\ldots 2.7$$

The hydrogen energy loss term must allow for the 2% impurity content, Nd and NH are respectively the number of deuterium and

hydrogen atoms per carbon.

Considering 98% deuteration i.e. 1.96 deuterium atoms per carbon, equation 2.7 becomes:-

$$\left(\frac{dE}{dx}\right)_{CD_2} = 0.7519\left(\frac{dE}{dx}\right)_C + 0.2456\left(\frac{dE}{dx}\right)_D + 0.0025\left(\frac{dE}{dx}\right)_H \quad \ldots. 2.8$$

Gorodetzky et al[28] have measured the energy loss of protons in carbon at incident energies between 0.4 Mev and 6 Mev, the values obtained being accurate to 3.5%. Between 0.012 Mev and 0.067 Mev proton energies, Ormrod et al[29] obtained values with an uncertainty of 3.5%. Of interest are the results of Reynolds et al[30], the stopping cross-sections of protons in organic compounds were measured between 0.03 Mev and 0.6 Mev. By applying Bragg's law to the results (i.e. by subtracting the hydrogen contribution from the stopping cross-section of the hydrocarbons) several values for the stopping cross-sections of protons in carbon were calculated at each energy. Above energies of 0.2 Mev the values agree within the experimental error, comparison with the results of Gordetzky et al[28] and Ormrod et al[29] on atomic nuclei show good agreement. The values obtained for deuterons in carbon, scaled up from proton data, are shown in figure 2.9(a).

Energy loss values for protons in atomic hydrogen were obtained from Reynolds et al[30], Weyl et al[31] and Dalgarno et al[32], the latter report is a theoretical analysis at low proton energies. The values were in good agreement, down to incident energies of 0.2 Mev, with derived values obtained from Reynolds[30] by subtracting the carbon contribution from the stopping cross-sections of the hydrocarbons. Figures 2.9(b) and 2.9(c) show the energy loss of deuterons in deuterium and hydrogen.

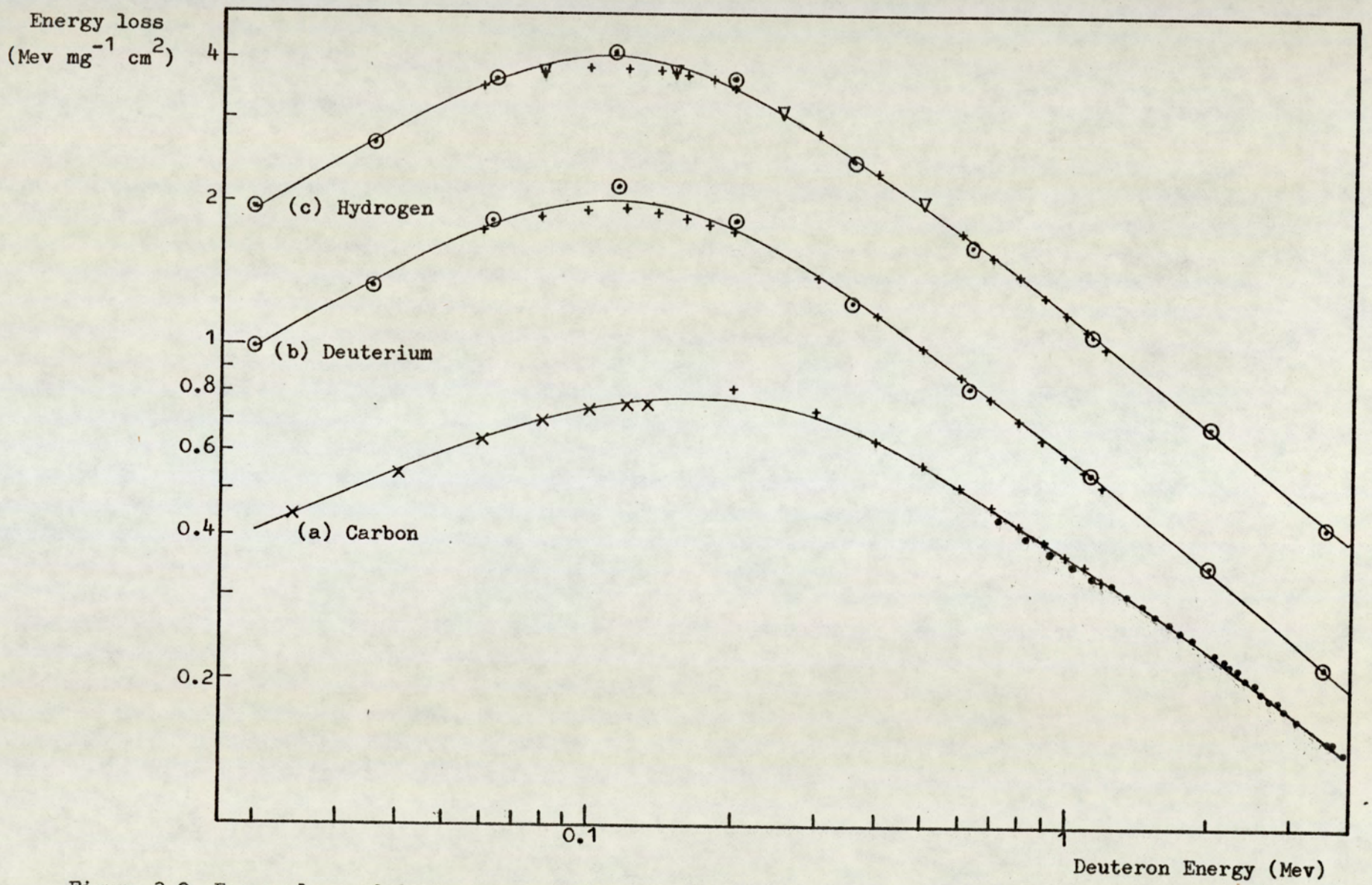

Figure 2.9 Energy loss of deuterons in Carbon, Deuterium and Hydrogen: Scaled from proton data
References for experimental points: • (28); × (29); + (30); ∇ (31); ⊙ (32)

The solid lines through the experimental points in 2.9(a), (b) and (c) are a smooth fit to the data, the maximum deviation from the curves is 6% for carbon and 4% for 2.9(b) and (c). Analysis of the theoretical and experimental values for atomic hydrogen obtained by Reynolds[30] show Bragg's law valid down to energies of 0.2 Mev, the results for carbon also give supporting evidence. The energy loss values for deuterons in carbon, hydrogen, deuterium and CD_2 are given in table 2.1, the values for CD_2 were obtained from equation 2.8 and are shown in figure 2.10.

The amount by which Bragg's law fails at low energies is uncertain, Platzman[33] has shown deviations of 5% in compounds containing C, N, O and F. By analysis of the results of Reynolds[30], much greater deviations are found for compounds containing only carbon and hydrogen at energies below 0.1 Mev. The energy loss values for deuterons in CD_2 are considered accurate to within $\pm$ 8% above 0.3 Mev, below this energy the error in the values could be as high as $\pm$ 20%.

2.3.2 Differential Cross-section for the $^2H(d,n)^3He$ Reaction

There were no comprehensive data sets available on either laboratory or centre of mass differential cross-sections for the $^2H(d,n)^3He$ reaction. However, an analysis of total cross-section measurements and Legendre coefficients has been carried out by Liskien et al[34], the recommended values were obtained by smoothing and analysing existing published results, these are shown in figures 2.11 and 2.12. The differential cross-section in the centre of mass, $d\sigma/dw^1$ at an angle ϑ can be represented by a Legendre polynomial thus:-

$$\frac{d\sigma}{dw^1}(\vartheta) = \frac{d\sigma}{dw^1}(0^\circ) \sum_i A_i P_i(\vartheta) \qquad \ldots\ldots 2.9$$

TABLE 2.1

Energy Loss of Deuterons in Carbon, Deuterium, Hydrogen and CD_2

Deuteron Energy Mev	$(dE/dx)_C$ Mev $mg^{-1}cm^2$	$(dE/dx)_D$ Mev $mg^{-1}cm^2$	$(dE/dx)_H$ Mev mg^{-1} cm^2	$(dE/dx)_{CD_2}$ Mev $mg^{-1}cm^2$
0.03	0.485	1.23	2.44	0.673
0.04	0.456	1.43	2.83	0.769
0.05	0.593	1.61	3.21	0.849
0.06	0.635	1.77	3.52	0.921
0.07	0.670	1.89	3.76	0.977
0.08	0.702	1.97	3.92	1.021
0.09	0.73	2.02	4.05	1.055
0.1	0.745	2.06	4.10	1.076
0.12	0.768	2.04	4.10	1.089
0.14	0.780	2.00	3.97	1.088
0.16	0.788	1.93	3.82	1.076
0.18	0.782	1.85	3.66	1.051
0.2	0.780	1.78	3.50	1.032
0.3	0.732	1.40	2.81	0.901
0.4	0.640	1.16	2.33	0.772
0.5	0.566	1.00	1.99	0.676
0.6	0.510	0.87	1.75	0.601
0.7	0.465	0.78	1.56	0.545
0.8	0.428	0.70	1.40	0.497
0.9	0.395	0.64	1.28	0.457
1.0	0.370	0.59	1.18	0.426
1.5	0.280	0.43	0.87	0.318
2.0	0.229	0.34	0.68	0.257

Continued ....

2.5	0.197	0.29	0.57	0.220
3.0	0.174	0.25	0.49	0.193
3.5	0.158	0.22	0.44	0.173
4.0	0.143	0.20	0.39	0.157

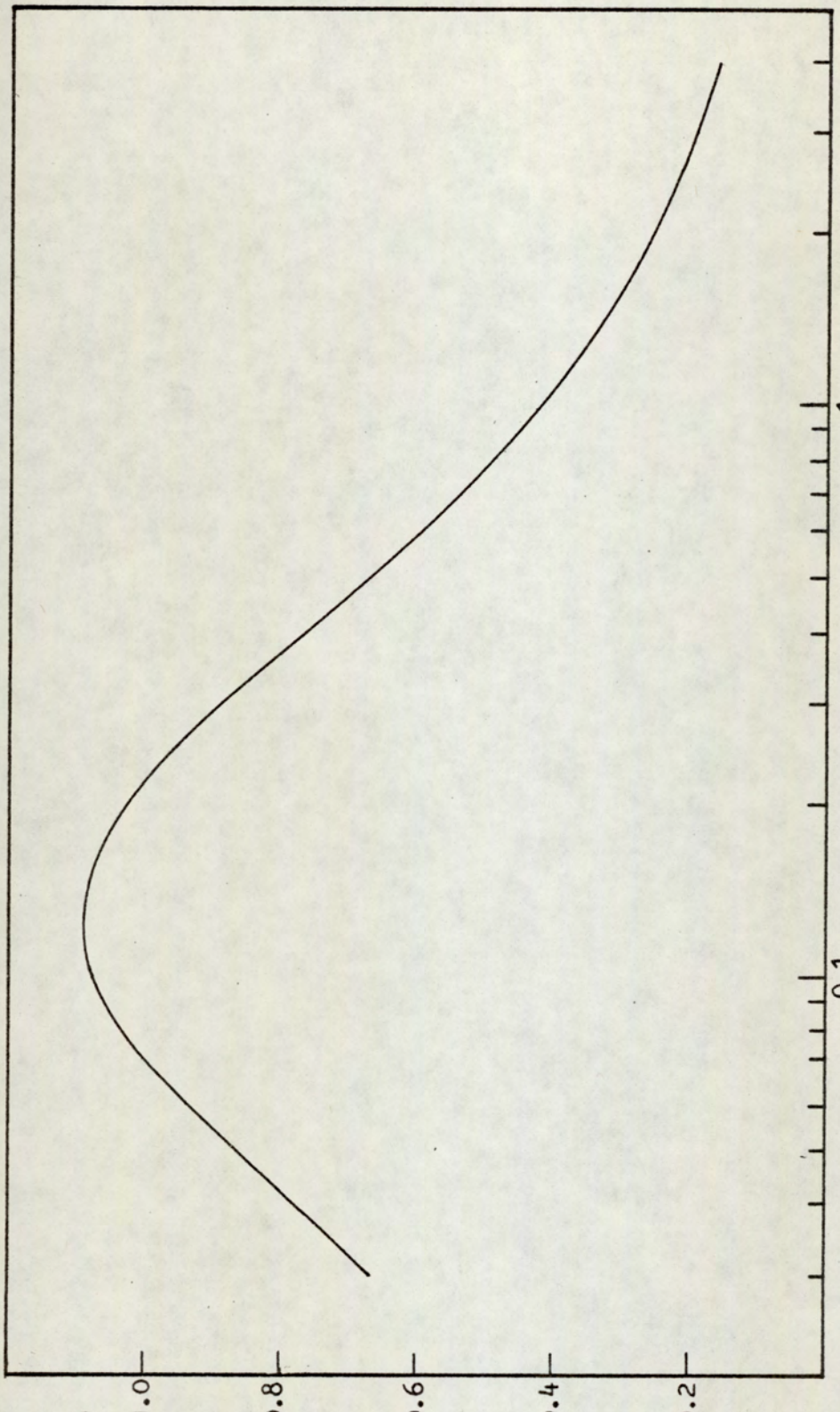

Figure 2.10 Calculated Energy loss of deuterons in deuterated polyethylene

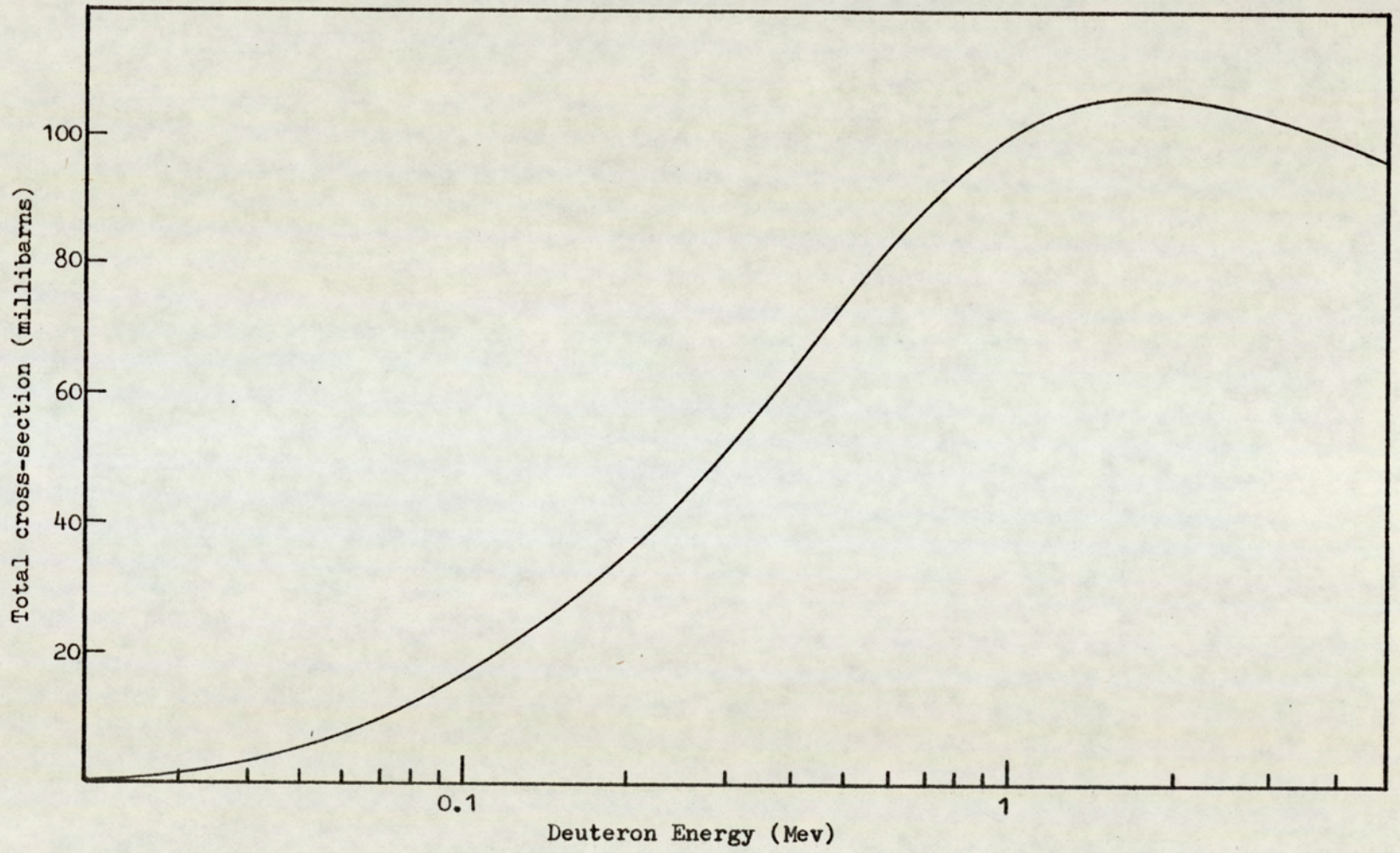

Figure 2.11 Total cross-section for the $^{2}H(d,n)^{3}He$ reaction, from Liskien and Paulsen[34]

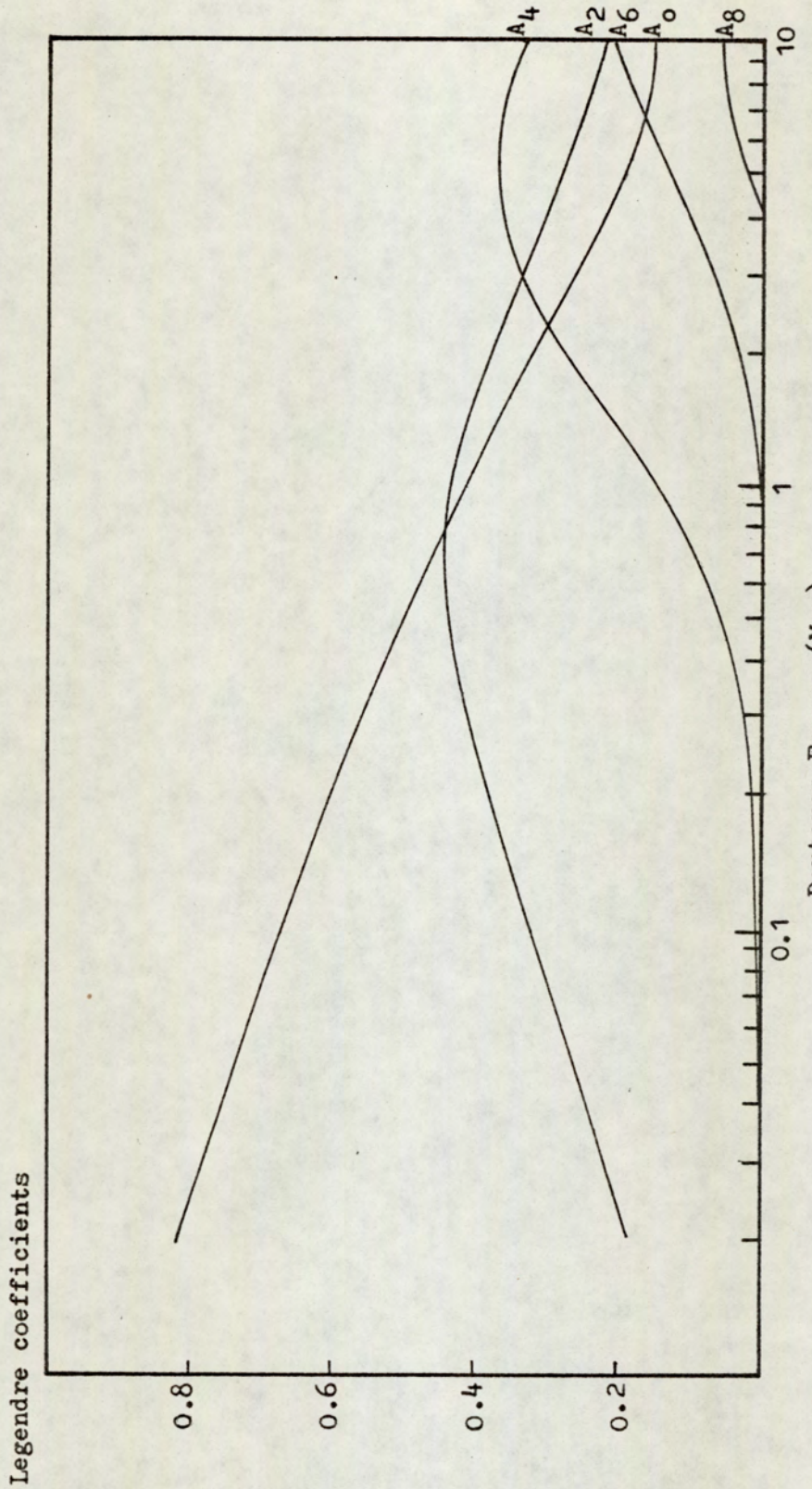

Figure 2.12 Legendre coefficients for the $^{2}H(d,n)^{3}He$ reaction from ref.(34)

where $A_i P_i(\vartheta)$ is the i^{th} term in the Legendre expansion and $d\sigma/dw^1\ (0^o)$ is the 0^o differential centre of mass cross-section which is isotropic and can be found from:-

$$\frac{d\sigma}{dw^1}(0^o) = \frac{\sigma_T}{4\pi A_o} \qquad \ldots\ldots 2.10$$

where A_o is the first coefficient in the Legendre expansion. Combining equations 2.9 and 2.10 the differential cross-section at an angle ϑ is given by:-

$$\frac{d\sigma}{dw^1}(\vartheta) = \frac{\sigma_T}{4\pi A_o} \sum_i A_i P_i(\vartheta) \qquad \ldots\ldots 2.11$$

The centre of mass and laboratory cross-sections are related by:-

$$\frac{d\sigma}{dw} = \frac{d\sigma}{dw^1}\frac{dw^1}{dw} \qquad \ldots\ldots 2.12$$

where $d\sigma/dw$ is the laboratory differential cross-section and dw^1/dw is the anisotropy factor i.e. rate of change of the centre of mass solid angle to the laboratory angle.

The centre of mass cross-sections were computed using equation 2.11, the values were then converted to the laboratory system using equation 2.12. The differential cross-sections in the laboratory system for an angle of 75^o as a function of deuteron energy are shown in figure 2.13.

2.3.3 Density of CD_2

To calculate the yields the number of nuclei cm^{-3}, nd,of deuterium atoms in CD_2 was required. Due to the small quantities and high cost of the CD_2 available the density was calculated from data available on polyethylene. The density of polyethylene $(CH_2)_n$ can vary between 0.91 g cm^{-3} and 0.967 g cm^{-3}, depending on the

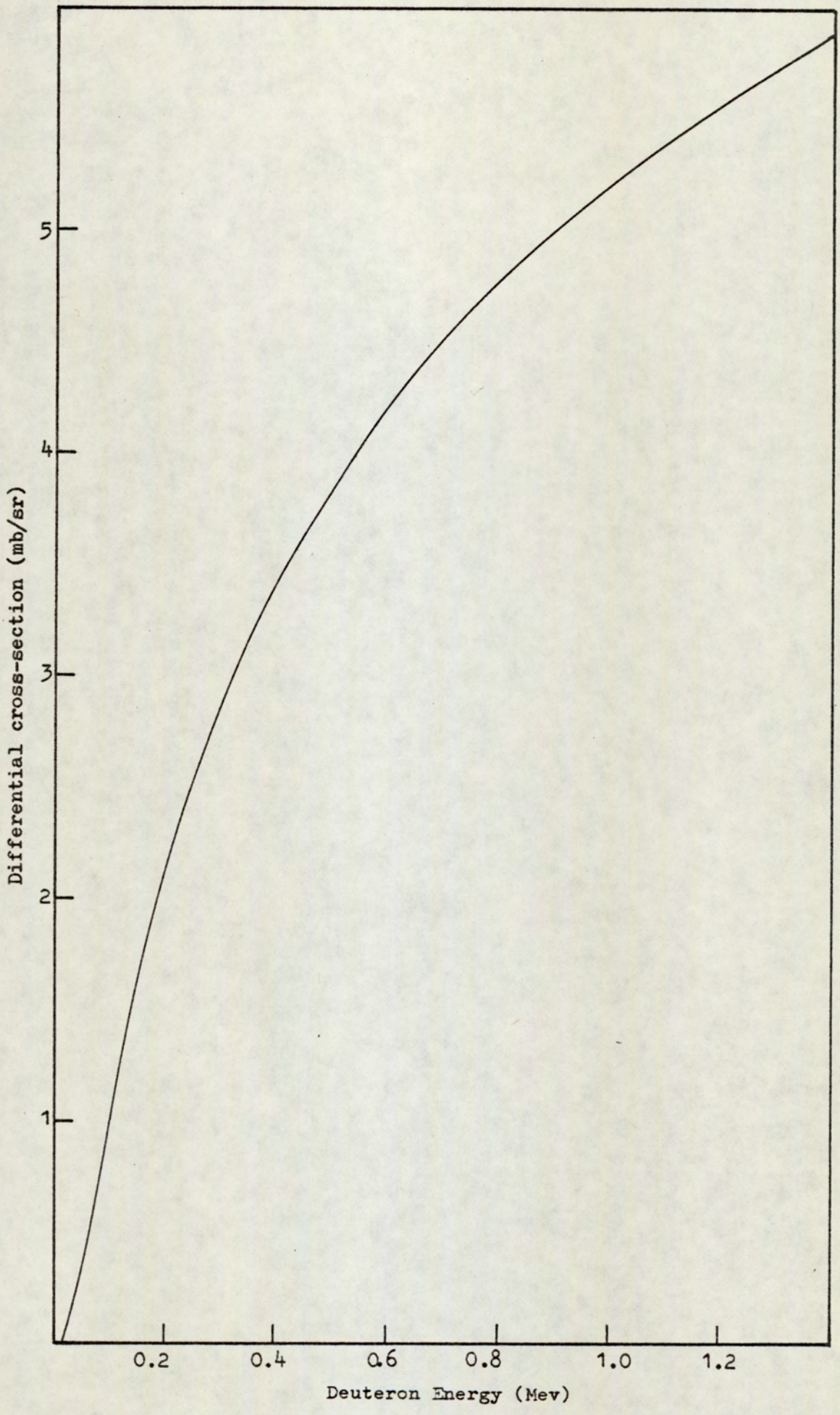

Figure 2.13 Differential cross-section for a neutron laboratory angle of 75°

method of preparation of the polymer. The average value was used to calculate ρ , the density of the deuterated polyethylene, by assuming a 1.143 increase in the mass of the polymer due to the deuterium atoms. The value of ρ was calculated at 1.073 ($\pm$0.033) g cm^{-3}. The number density was then found to be 7.93($\pm$ 0.24) x 10^{22} atoms cm^{-3}.

2.3.4 Neutron Yield Values

Values under the integral in equation 2.5 were found for different deuteron energies, the results for a neutron angle of 75° are given in figure 2.14. This curve was integrated in steps of ΔE using the trapezoidal method, the neutron yield was then given in increments of ΔY. The target thickness Δx corresponding to ΔE was obtained from equation 2.6. The neutron yield increments were then summed such that:-

$$Y = \sum_{E=E_2}^{E=1.0} \Delta Y$$

where E_2 represents the emergent deuteron energy after a 1 Mev deuteron has traversed a distance x in the target. The distance x was found from:-

$$x = \sum_{E=E_2}^{E=1.0} \Delta x$$

The yield of neutrons at 75° as a function of target thickness is shown in figure 2.15. The neutron yield is in units of the number of neutrons μC^{-1} sr^{-1} and the target thickness in μm.

The neutron yields at 120° were considered in a similar manner, figure 2.16 shows the calculated yields for incident deuteron energies of 1 Mev and 2.5 Mev. Only a part of the yield for 2.5 Mev

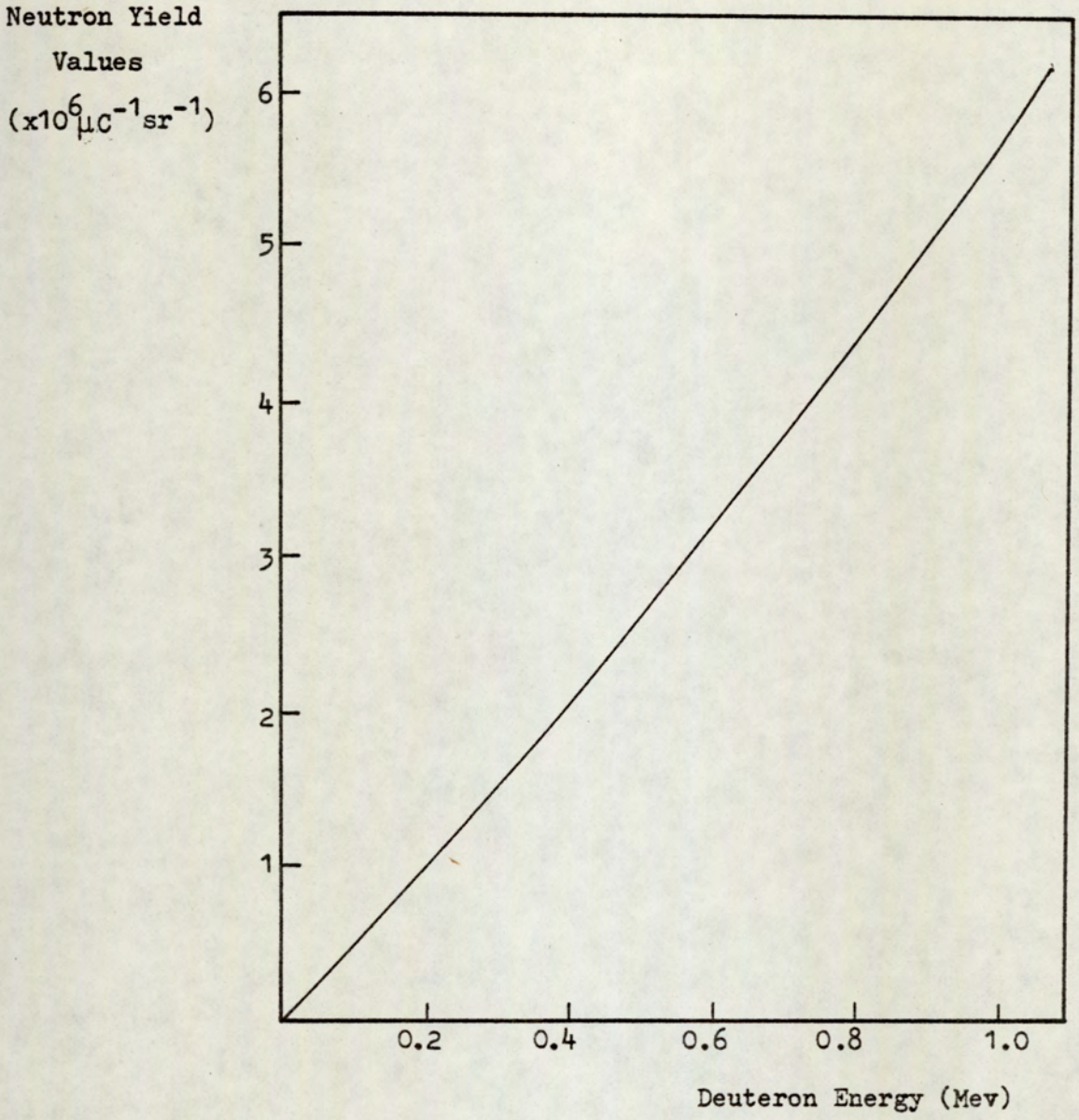

Figure 2.14 Calculated Neutron yield values for a laboratory angle of 75°

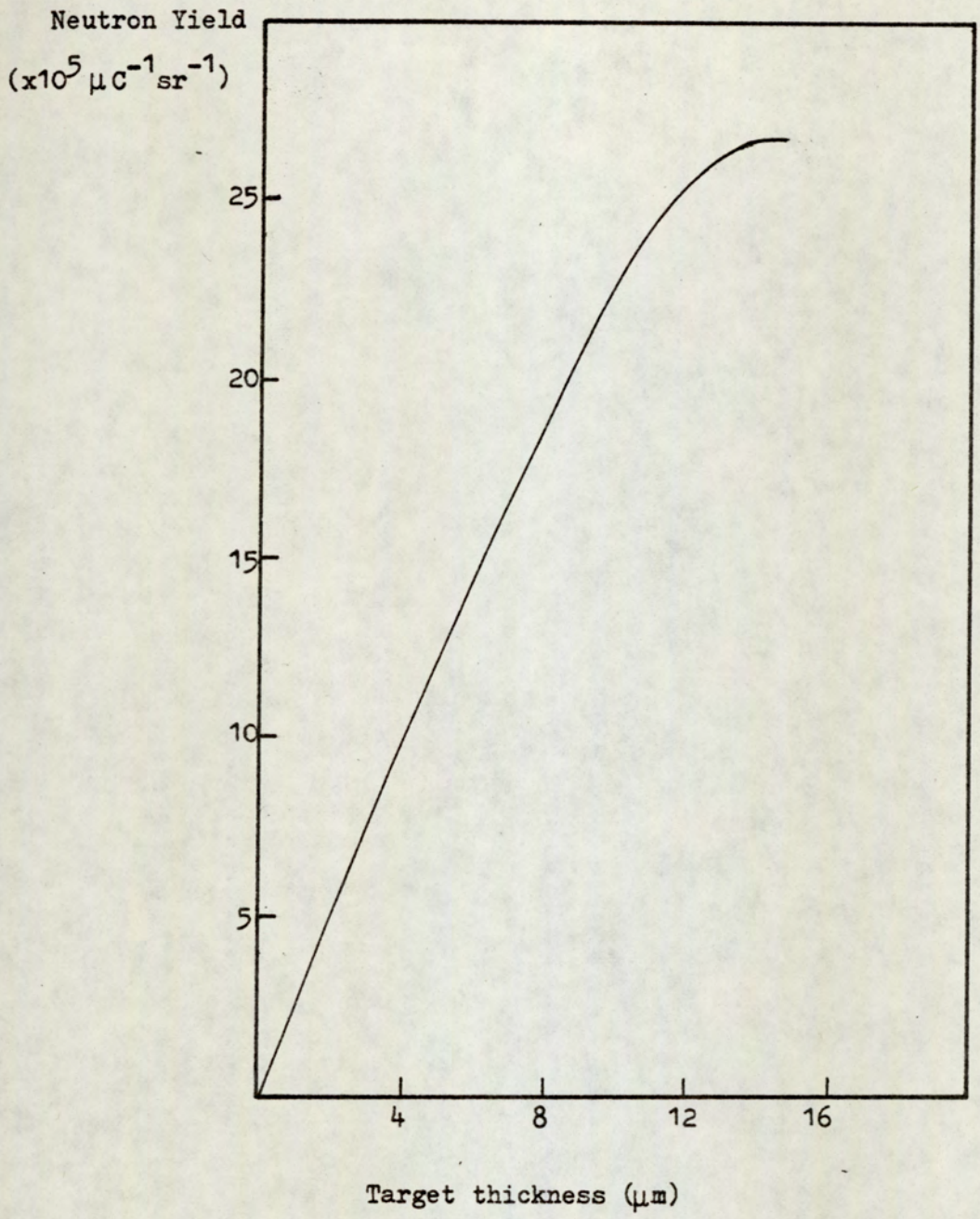

Figure 2.15 Calculated neutron yield for a laboratory production angle of 75°, as a function of target thickness, for an incident deuteron energy of 1 Mev.

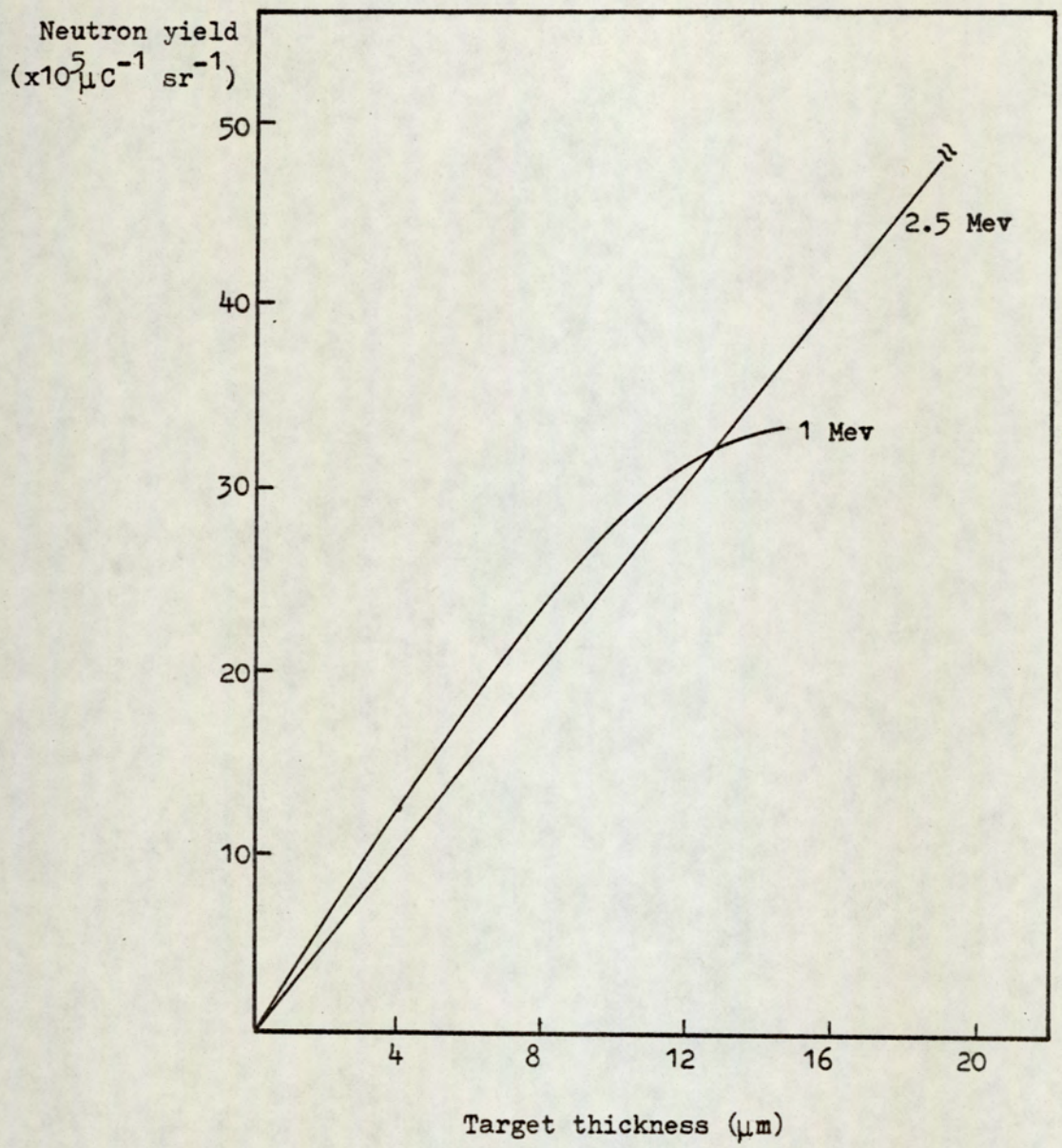

Figure 2.16 Calculated neutron yields for a laboratory production angle of 120°, as a function of target thickness, for incident deuteron energies of 1 Mev and 2.5 Mev

deuterons is shown, the target thickness, for a deuteron losing all its energy is 85 μm. By comparison of the yields at the two energies it can be seen that for the same yields a target thickness greater than at 1 Mev is required for 2.5 Mev deuterons. Due to the requirement of minimum target thickness and high neutron yields an incident energy of 1 Mev was chosen for both neutron production angles.

For a target thickness of less than 10 μm the yields were considered accurate to ± 15% a greater thickness would give rise to errors of ± 25%. The target thickness employed in the experimental system was governed by the spread in energy of the emitted particles. This aspect is now considered.

2.4 Target Thickness

Considering a deuteron beam incident onto a target of finite thickness, the charged particles produced will have an energy spread. The maximum target thickness will be limited by the energy spread of the ^{3}He, ^{3}H and scattered deuteron energy groups.

In this section target thickness is considered for neutron emission at 75°, for a 1 Mev incident deuteron energy the angle of the associated particle detector is 60°. From figure 2.7 the energies of the particles in the vicinity of the 1.25 Mev ^{3}He peak are 1.5 Mev for the ^{3}H and 0.845 Mev for the elastically scattered deuterons from carbon. For neutron emission at 120° (figure 2.8) the ^{3}He angle is 30° and the resulting charged particles have higher energies for this kinematic system.

To minimise the energy loss of the charged particles in emerging from the target, it is necessary after formation for the particles to traverse the minimum thickness of target before reaching the detector. The path length travelled by the incident

beam must also be minimised to limit the energy spread of the interacting deuterons. The ideal situation is with the target surface normal to both the incident beam and detector positions. However, this cannot be realised experimentally, to compromise for the larger energy loss of the ^3He and ^3H the target was placed at 45° to the incident beam. The target surface was then at 75° with respect to the charged particle detector positions at 60° and 30°, with the charged particles emerging on the target surface opposite to the incident beam direction. Figure 2.17 is a schematic representation of detection of charged particles at 60°. In the diagram b is the target thickness and r^1 and r are the thicknesses traversed by the charged particles and incident deuterons respectively.

For a certain target thickness the limiting energies for the energy spread of the charged particles are obtained when, (i) the incident deuteron E_D interacts at the target surface A, the charged particle is produced and undergoes energy loss and emerges with an energy E_{OUT} (ii) the deuteron interacts after losing energy in the target, interaction occurs at the opposite target surface B with an energy E^1_D, the resulting charged particle undergoes no energy loss and emerges with an energy E^1_{OUT}.

In considering the first case the energies of the particles are found after they have traversed a distance r^1, r is zero and interaction is due to a 1 Mev deuteron. To obtain the ranges of the ^3He and ^3H the energy loss values are now considered. The specific case for the energy loss of deuterons in CD_2 was discussed in section 2.3.1, the energy loss values for the ^3He and ^3H can be obtained by scaling this data. For ^3He the scaling was obtained by:-

$$\left(\frac{dE}{dx}\right)(^3He)\ \frac{3}{2}\ E = 4\left(\frac{dE}{dx}\right)(D)\ E$$

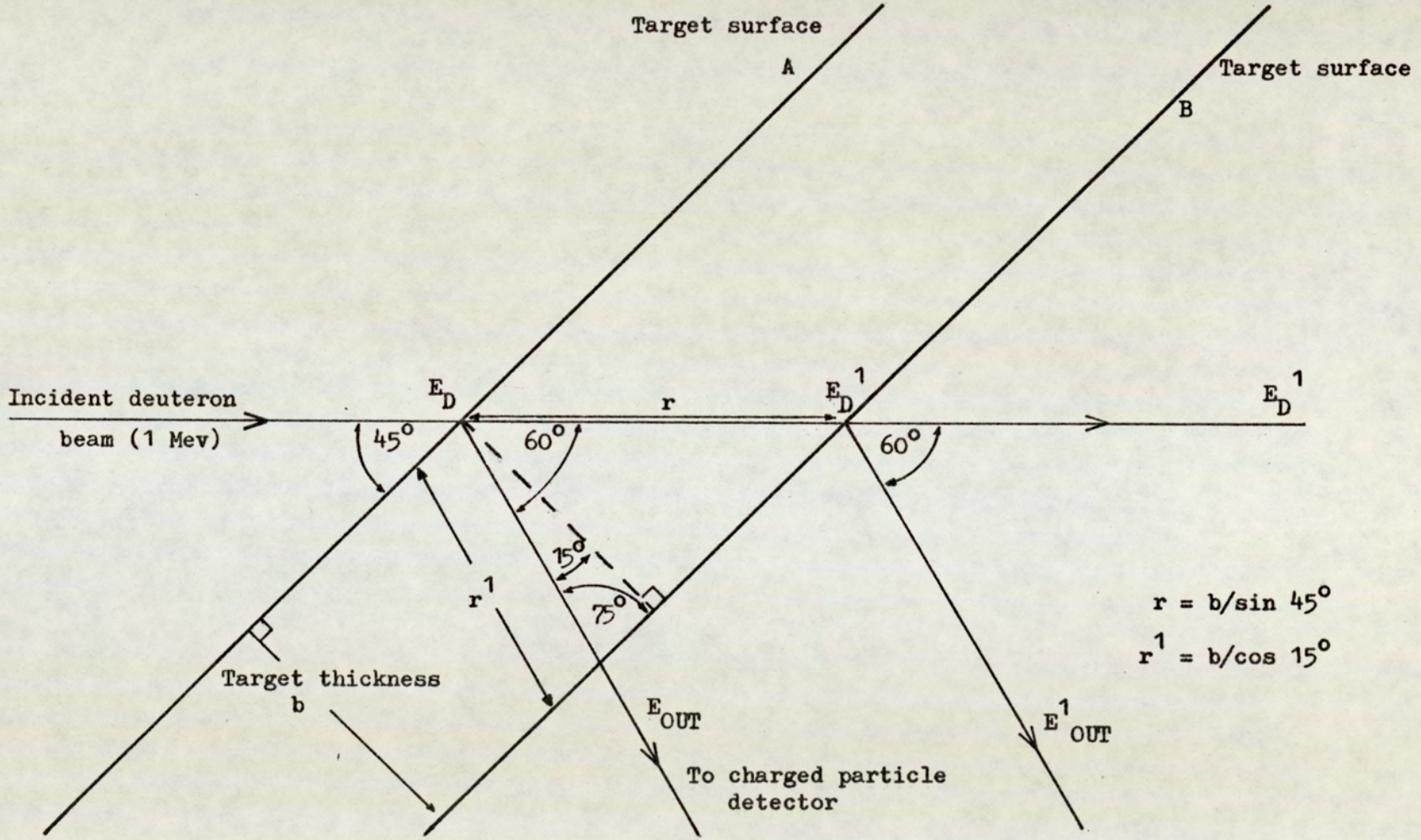

Figure 2.17 Schematic representation of charged particle detection at 60°

The energy loss of ^3He in CD_2 is shown in figure 2.18. The emergent energy, after traversing a distance r^1, for a ^3He of initial energy 1.25 Mev was then found for increasing target thickness. The energy loss curve was integrated in steps of ΔE from 1.25 Mev to 0 Mev, the corresponding target thickness could be found from:-

$$\Delta x = \frac{\Delta E}{dE/dx}$$

the values of Δx were summed such that:-

$$x = \sum_{E=E_{OUT}}^{E=1.25} \Delta x$$

where E_{OUT} is the emergent energy of the ^3He after passing through a target thickness x. Similar consideration was given for the 1.5 Mev triton. Figure 2.19 gives the emergent energies of the ^3He, ^3H and deuteron scattered from carbon for increasing target thickness (in μm). The abscissas values of x are for the thickness values of r^1.

In the second case the particles have energies defined by kinematics for an interacting deuteron of energy E^1_D. The energy E_D^1 is due to the incident deuteron losing energy in the target, after traversing a distance r, before interaction. The minimum interacting energy can be obtained from figure 2.19, the abscissa distance x will be the same as for the distance r.

Figure 2.20 shows the energy spreads of the charged particles as a function of increasing target thickness b, also given is the interacting deuteron energy spread. From this it can be seen that if the ^3He pulses are to be resolved then a target thickness of less than 2 μm is required. Above this the ^3He pulses will be

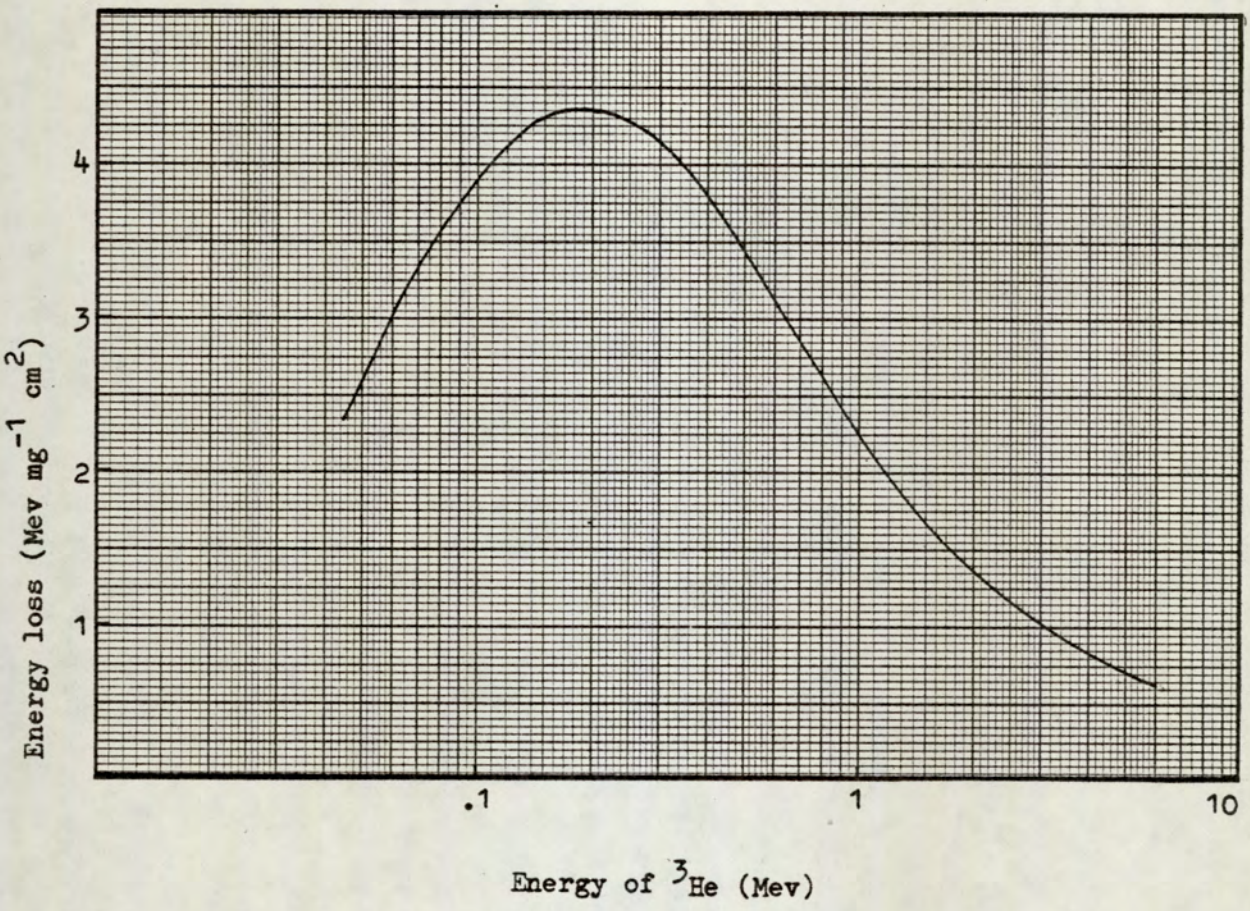

Figure 2.18 Calculated energy loss of ^{3}He in CD_2

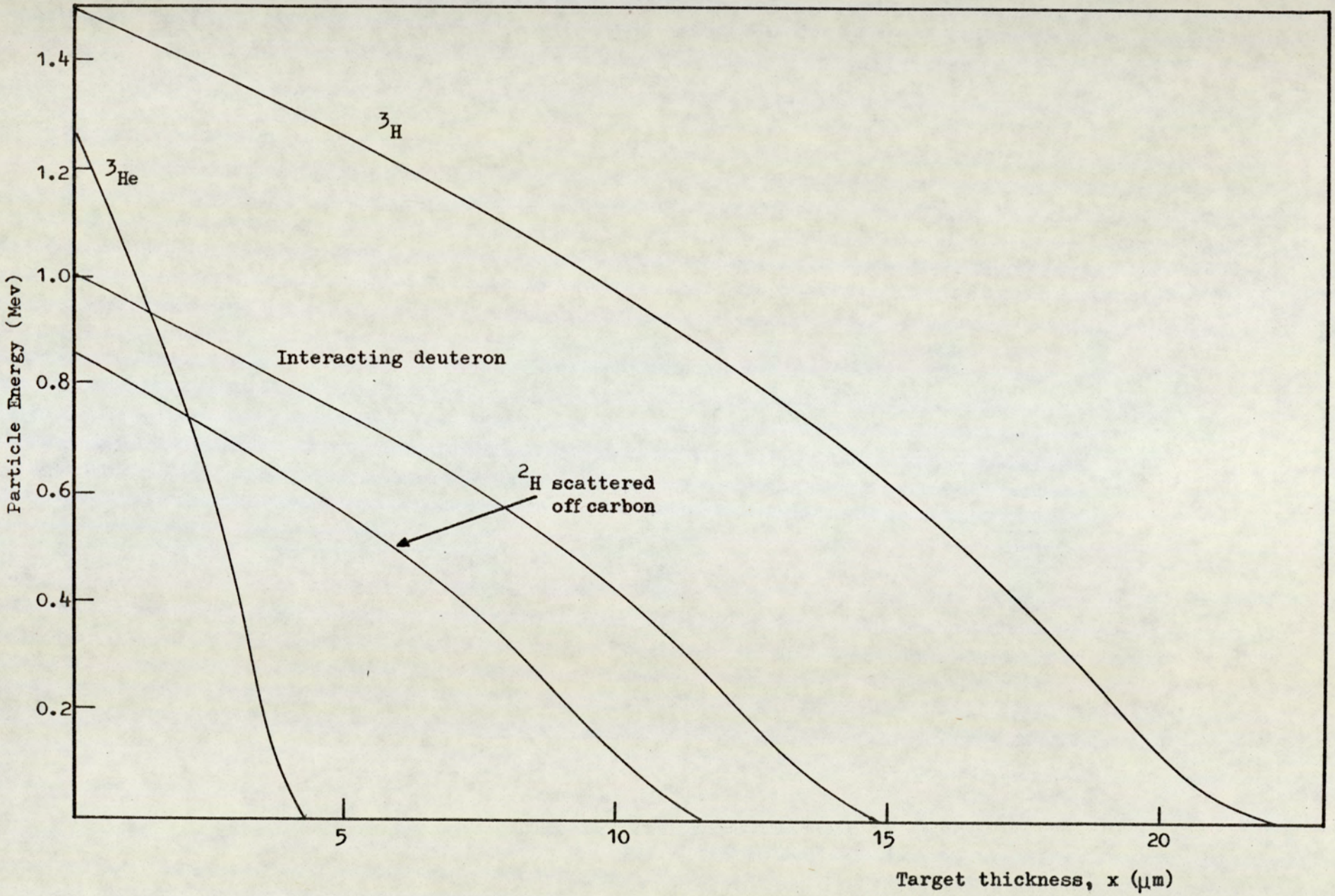

Figure 2.19 Emergent energies of charged particles from a CD_2 target as a function of target thickness

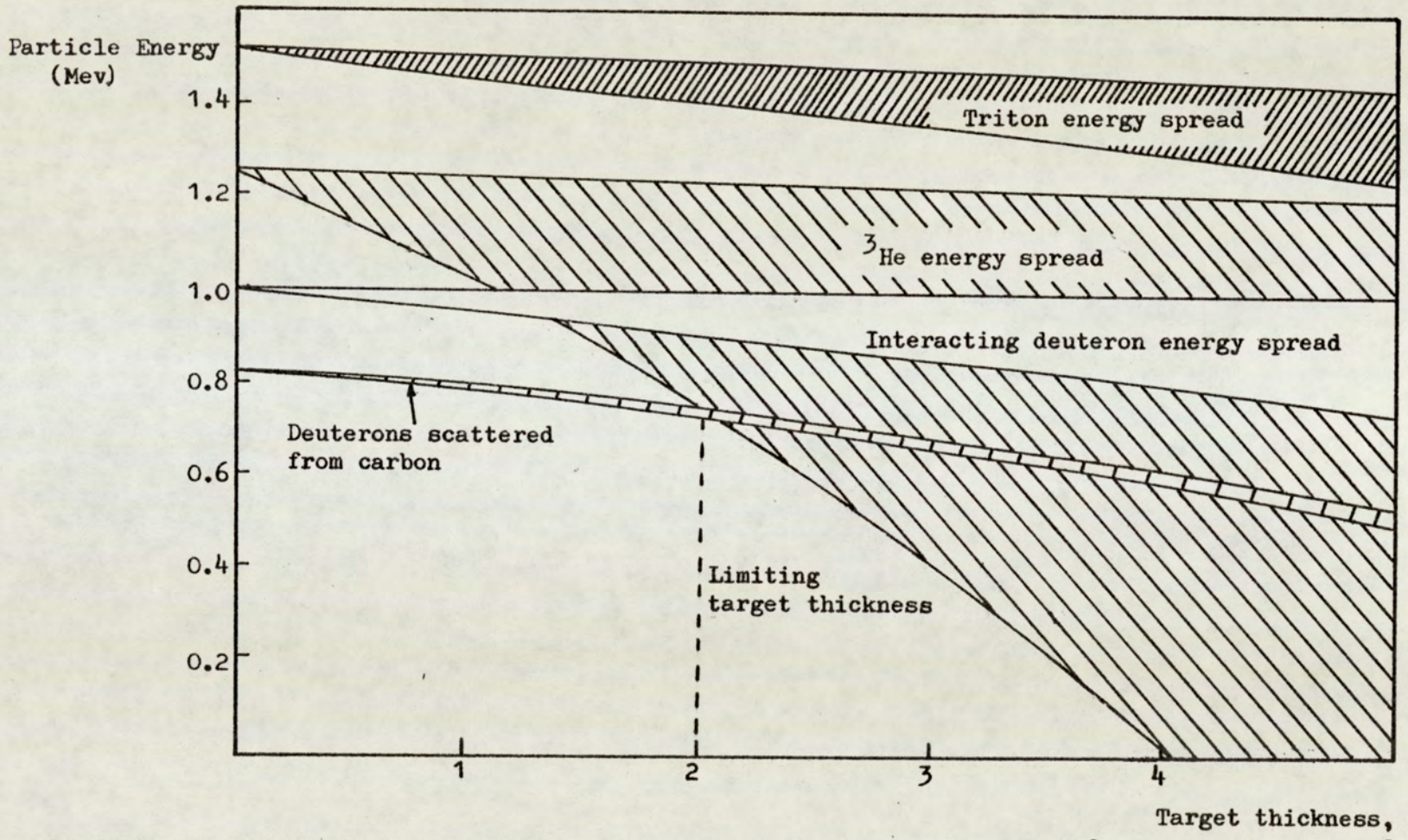

Figure 2.20 Calculated Energy spreads of charged particles emerging at 60° from a target at 45° to the incident deuteron beam direction.

indistinguishable from the scattered deuterons.

In addition to restrictions on the maximum target thickness the angular spread of the neutron cone was also limited. Consideration is given to the ^{3}He detection angular spread required to produce the associated neutrons within the defined angular range.

2.5 Charged Particle Detector and Incident Beam Collimation

Due to the physical geometry of the laboratory and available apparatus the neutron angular spread was limited to $\pm 7.5^\circ$ at both 120° and 75° central neutron production angles. The required neutron cone was obtained by consideration of target thickness, associated particle detector collimation and incident deuteron beam size.

As discussed in section 2.4 the maximum target thickness which could be employed was 2 μm. As the target is at 45° to the incident beam direction, this gives a path length of 2.8 μm for the incident deutron to traverse, from figure 2.20 the incident deuteron beam can interact with an energy between 1 Mev and 0.87 Mev. The variation of neutron angle with associated ^{3}He angle as a function of reacting deuteron energy, within this energy range, is shown in figure 2.21. A neutron angular spread of $\pm 7.5^\circ$ gives rise to a ^{3}He angular spread of $\pm 5^\circ$ centred at 61.3° for neutron production at 75° and $\pm 4^\circ$ centred at 31.2° for production at 120°.

The charged particle detector angular spread is derived from the angle subtended at the target spot, α. The effect of finite target spot size on the ^{3}He angle is shown in figure 2.22.

The maximum angle subtended by the detector collimation at the beam spot is given by:-

$$\pm \alpha = \pm \tan^{-1}\left(\frac{D + x}{2y}\right) \qquad \ldots\ldots 2.13$$

where D is the detector collimator diameter, x is the maximum beam

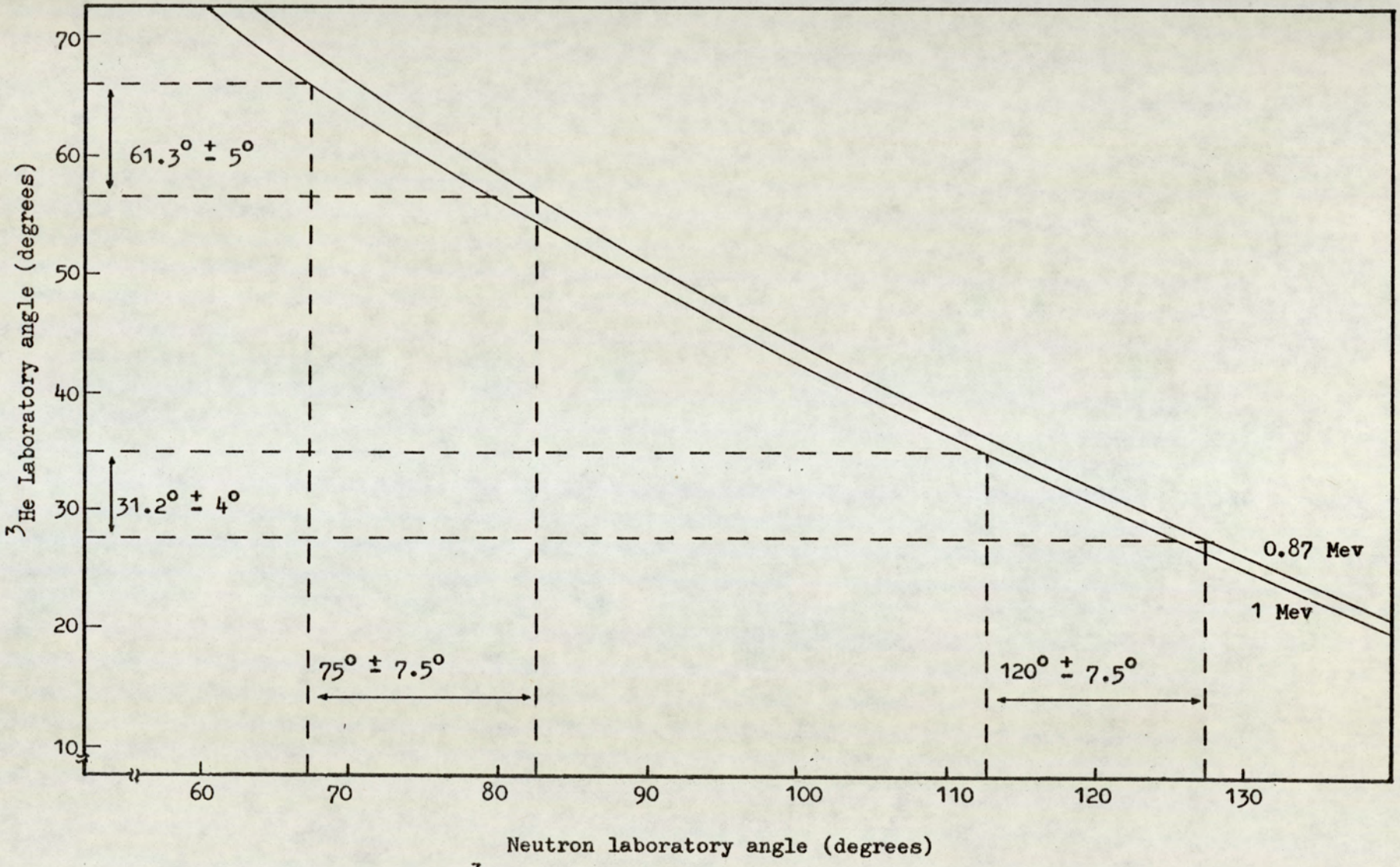

Figure 2.21 Related neutron and ^{3}He angles of emission for incident deuteron energies of 1 Mev and 0.87 Mev

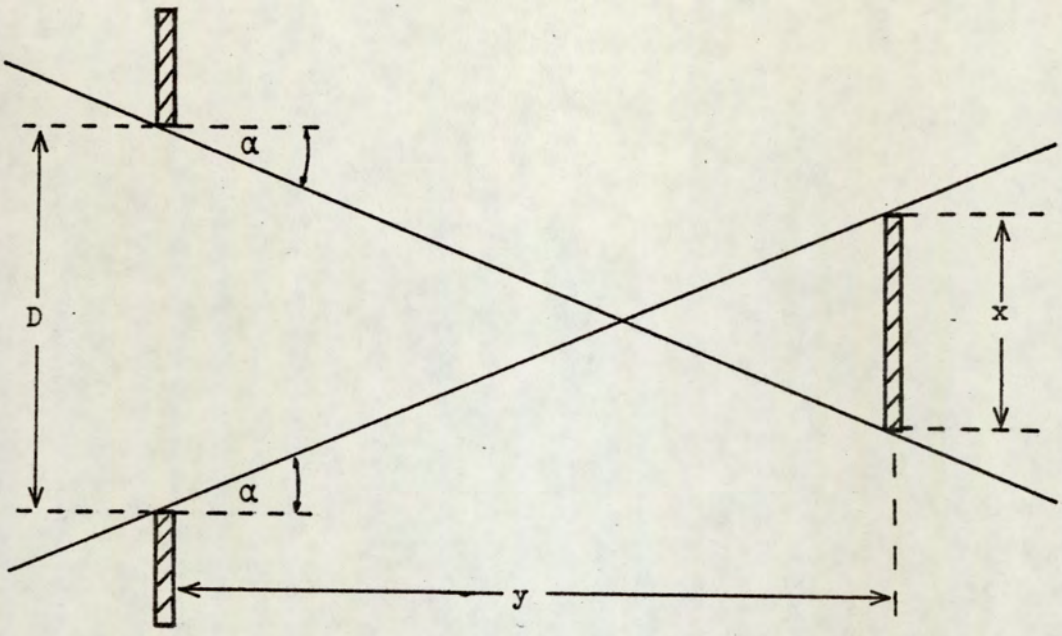

Figure 2.22 Charged particle detector angular spread

size and y is the separation. To maximise the yield of associated neutrons produced it was considered important to have the beam size smaller than the detector collimation. If this is not the case a fraction of the neutrons produced in the defined angular range will have no associated ^{3}He particles. Although this problem is always apparent in considering finite beam geometry an attempt was made to keep this background neutron yield to a minimum. Small beam collimation was therefore favoured, a 1 mm diameter collimator was considered an optimum for beam transportation.

Considering a parallel beam incident on the collimator an elliptical beam spot will be produced on the target. The projected beam spot on the target has major axis length of 0.7 mm and a minor axis length of 0.5 mm. For ^{3}He detection centred at 61.3° the value of y, the separation distance, was 50 mm and from equation 2.13 a ^{3}He collimation of 3.9 mm radius gives the required neutron cone in the horizontal plane, in the vertical plane the angle α is $\pm$ 4.7°. So far, consideration has been given to a parallel incident beam and this represents ideal beam transportation conditions.

The main beam limiting collimators used in the accelerator beam line and their respective separations are shown in figure 2.23. The maximum angular divergence of the beam on the target is governed by the 15 mm diameter (A) and the 1 mm diameter (B) collimators. Consideration of the geometry of these two apertures gives the largest possible excursion of the beam over the target. Collimator A is an integral part of the beam line, the position of which is accurate to within $\pm$ 3mm. Collimator B was integral to the experimental system and could be aligned to within $\pm$ 0.5 mm of the beam centre line axis. By consideration of the possible errors in alignment and transportation the beam could have a maximum excursion of $\pm$ 3.4 mm from the target centre. To maintain the same neutron angular spread a ^{3}He collimation of 3 mm diameter is required.

To allow for the uncertainties in beam size a 3 mm diameter collimater was used for the charged particle detector. For neutron production at 120°, to limit the neutron beam the same ^{3}He collimation was used but the seperation was increased to 60 mm.

2.6 Beam Collimation

The 1 mm diameter beam collimator, made from tantalum foil was electrically insulated from the main beam line and target chamber. The tantalum foil in the form of a disc was mounted in an annular aluminium holder; this was peforated with six equally spaced holes to maintain efficient pumping of the target chamber. To electrically isolate the collimator from both the beam line and target chamber the aluminium holder was mounted in the face of a roughing-out port used in evacuating the experimental system. Figure 2.24 is a schematic diagram showing the position of the collimator and the vacuum seal between the roughing-out port and connecting pipe of the target chamber. A vacuum seal between the two components was

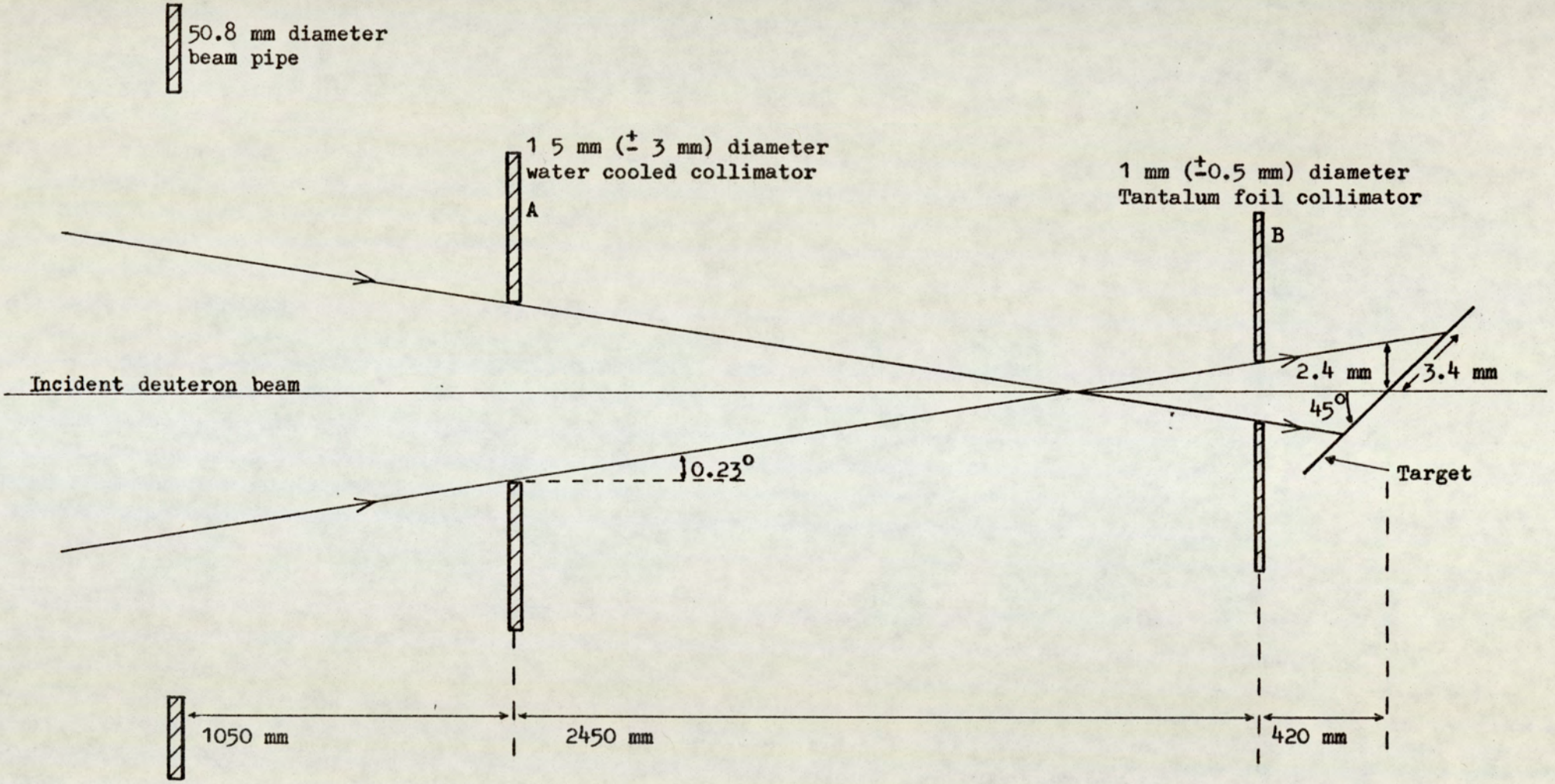

Figure 2.23 Beam line collimators

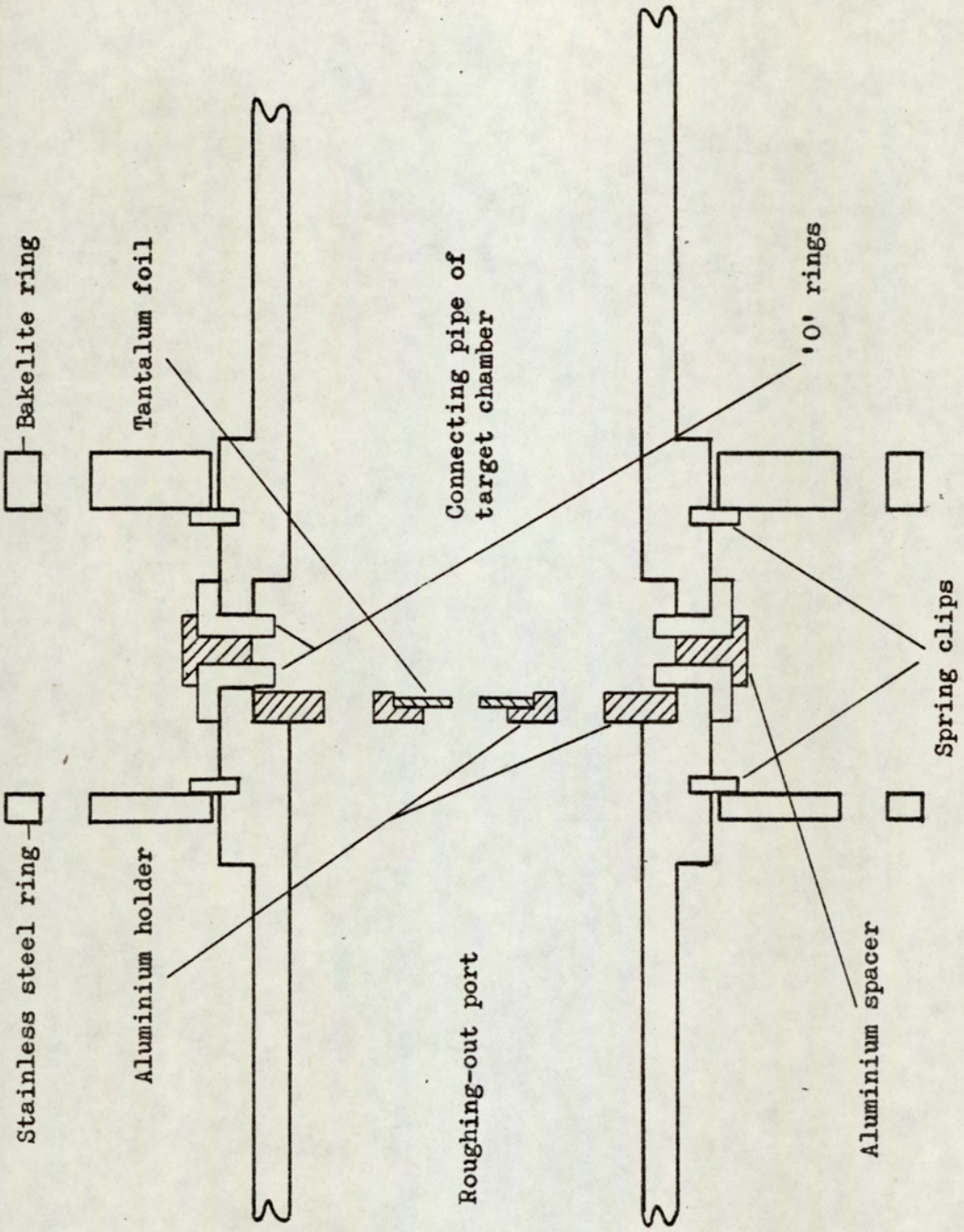

Figure 2.24 Location of the 1 mm beam collimator

achieved by the use of an 'O' ring seated on each face of the components, an aluminium spacer separated the two 'O' rings. The two components were held together by a stainless steel ring on the roughing-out port bolted to a bakelite ring on the target chamber connecting pipe.

The viton 'O' rings and bakelite flange prevent electrical contact between the two faces. The roughing-out port was electrically isolated from a liquid nitrogen cold trap by a similar process. The complete beam line and experimental assembly is shown in figure 2.25.

2.7 Target Preparation

There are several techniques for producing thin films of deuterated polyethylene. White[35] has described the preparation of thin polyethylene films between 900 Å and 2500 Å thick by vacuum evaporation. One of the disadvantages of this technique is that a large fraction of the evaporated polyethylene is lost in the vacuum system.

Arnison[36], Tripard et al[37] and Bartle et al[38] have all described similar techniques in which the polyethylene is dissolved in boiling xylene, the solution is then evaporated on glass slides. The films are floated off the slides in water and can be picked up directly onto metal frames.

Bartle et al[38] modified this slightly by precoating the slides with a parting agent to make the detachment process easier to accomplish. This technique was adapted slightly in the present work and used to prepare targets of 1.5 μm thickness.

A parting agent was made by dissolving 3 cm^3 of industrial cleaning agent, either TOT* or TEPOL** were found suitable, in 1.5

* Supplied by DEB Chemical Proprietaries Ltd., Belper, Derbyshire

** Shell produce, distributed by BDH Chemicals Ltd., Poole, Dorset.

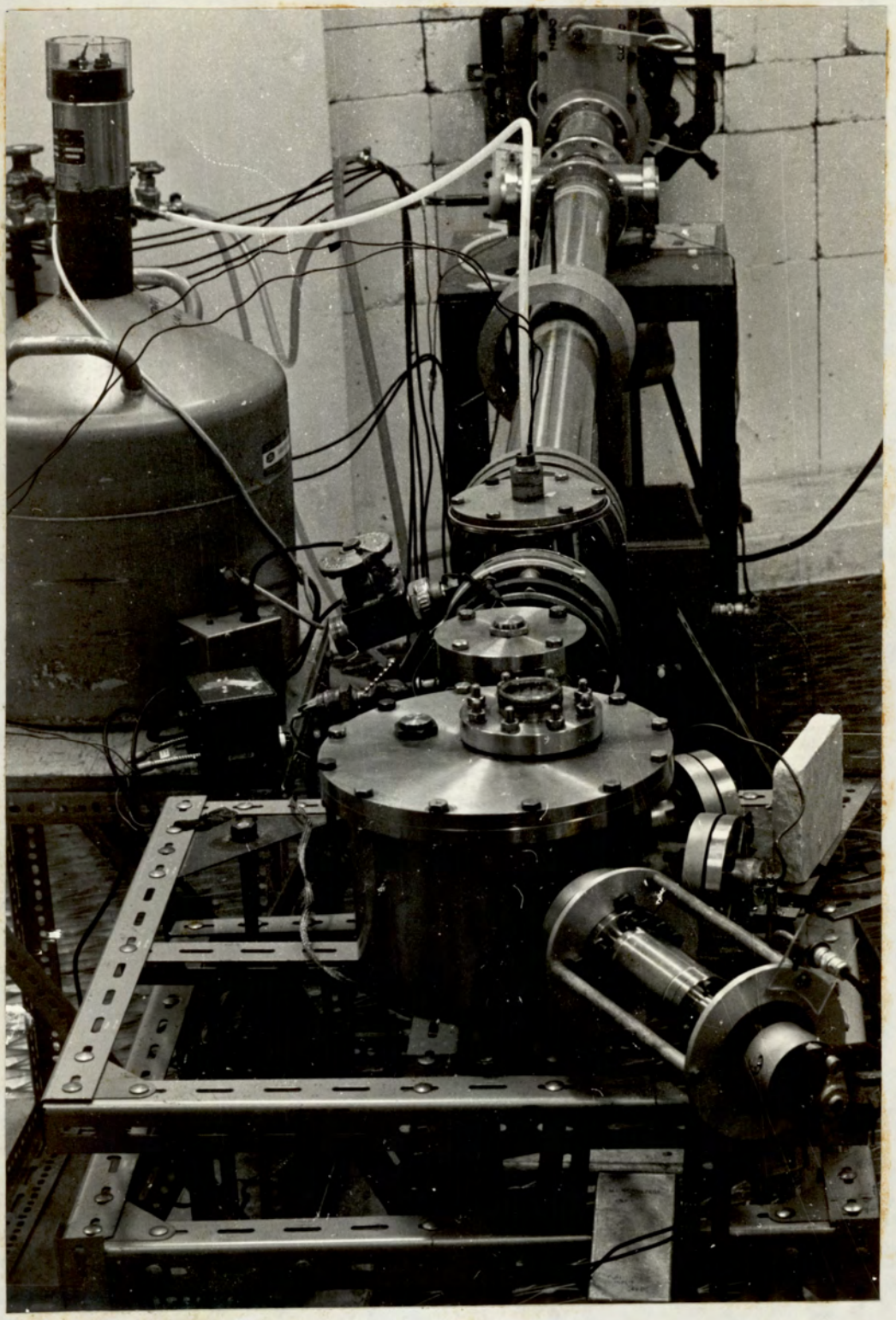

Figure 2.25 Beam line and experimental assembly

litres of distilled water. A glass slide (5 cm x 5 cm) was immersed in the solution and dried on a hot plate kept at a temperature of approximately 95°C. Films of 1.5 μm thickness were produced by adding 3.8 mg of deuterated polyethylene to 3 cm^3 of xylene. The solution was heated on a hot plate to the boiling temperature of the solution (~145°C). The solution was allowed to boil for several minutes until all the polyethylene had dissolved. The solution was removed, allowed to cool slightly, and poured carefully onto the glass slide which was positioned on the first hot plate kept at 95°. The evaporation rate of the xylene, which is normally very rapid, is slowed down by covering the slide in the evaporation stage. A petridish was inverted over the slide and one edge of the dish was raised by about 0.3 cm. The slide was left for approximately 5 minutes until the xylene had evaporated, leaving a clear polymerised layer. Next the slide was removed and allowed to reach room temperature. To release the film, the slide was slowly immersed in water until the foil floated free, the best rate of separation was obtained when the slide was immersed at 45° to the water surface. The film was then lifted onto stainless steel rings with a centre hole of 2.86 cm. diameter, initially the film was lifted by one corner, the foil and frame were then drawn from the water at an acute angle to the water surface.

The best method found for assessing the quality of the foils was to observe the uniformity of the film surface. A badly prepared foil would show irregular flow marks and areas of greater thickness. The thickness of each foil was measured by first weighing the dried glass slide precoated with the parting agent, then reweighing the slide after the polymerisation. Normally about 20 targets were produced at the same time and the maximum deviation in the thickness of a foil was usually ± 0.5 μm.

Stationary targets have a limited life-time during bombardment. They show a marked degradation in the neutron yield as a function of time and are soon punctured by the incident beam. The energy deposited in the target by the incident deuteron beam was manifested in the form of heat. Because of the low thermal conductivity of the targets the heat was dissipated over a large surface area by rotating the targets. The method used to rotate the targets to increase target lifetimes and maintain a stable neutron yield is discussed in the next section.

2.8 Target Chamber

The internal lay-out of the target chamber is shown in figure 2.26. The chamber with internal diameter of 22.9 cm was constructed from stainless steel. Three 5.08 cm diameter ports were mounted on one side of the chamber at 30°, 75° and 120° to the incident beam direction, the beam entered the chamber through a 10.2 cm diameter connecting pipe. A 1 cm diameter aperature was placed in the connecting pipe, before the main chamber, this was to restrict secondary electrons emitted at the 1 mm collimator entering the chamber.

The rotating target assembly was mounted at 45° to the incident beam in the chamber. An AEI RM2* rotary drive assembly was mounted in the 30° port and was geared to drive the target assembly. The thin plastic films were mounted on stainless steel rings, as described in section 2.7, which located in a recess in the assembly, the rings were held in position by clets to allow for minimum target handling in removal and positioning. The target assembly was mounted in the chamber by two adjustable 'bullets', these located into datum

* This rotary drive was changed in the course of the work to a Vacuum Generator's RD5 rotary drive and is shown in figures 2.25, 2.26 and 2.27.

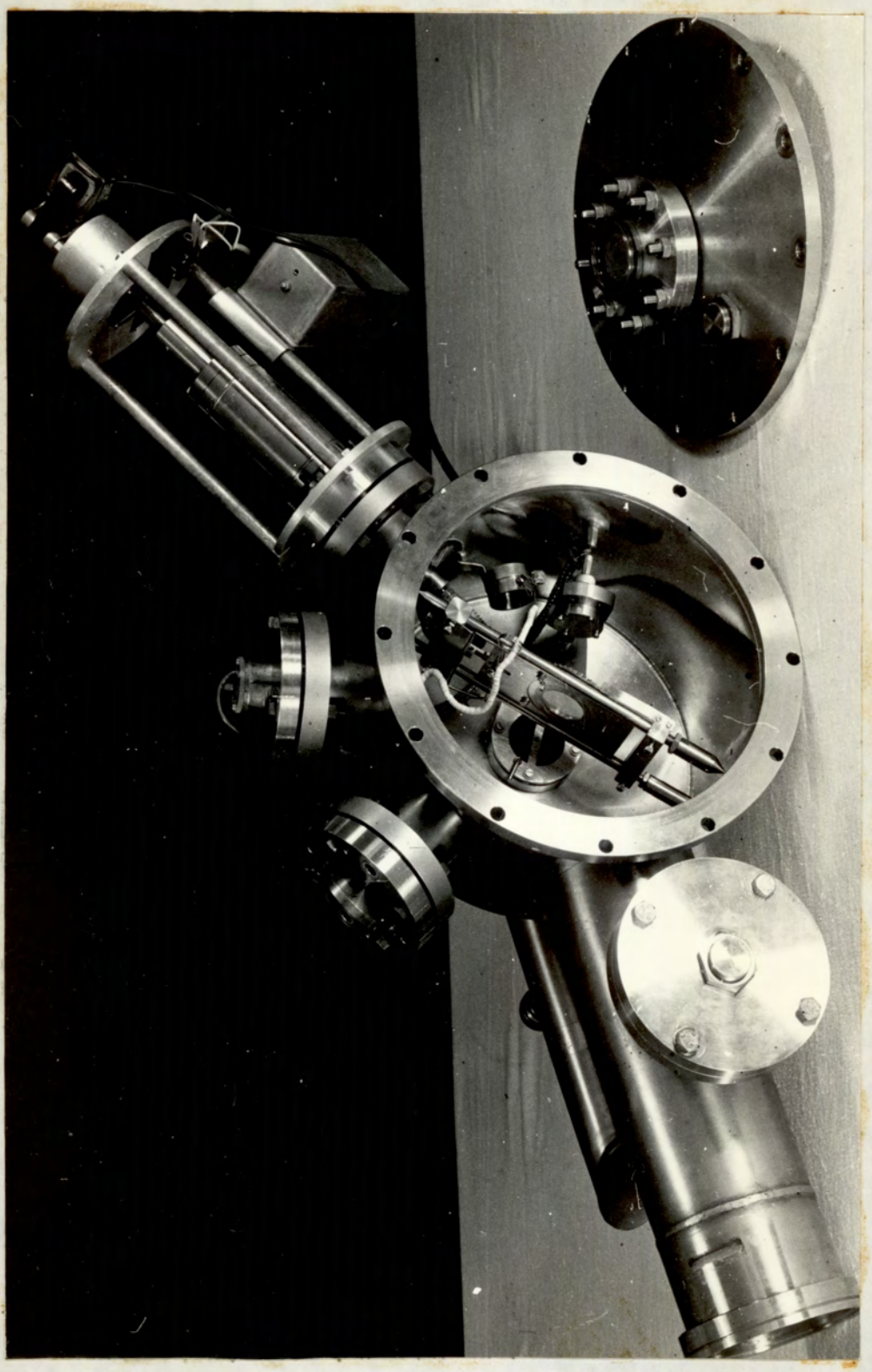

Figure 2.26 Internal lay-out of target chamber for neutron production at 120°

points in the side of the chamber. The whole assembly could be easily removed and replaced. The rotary drive was powered by a 240v A.C. motor, the primary gear of which rotated at 50 Hz, this was then geared down to the required drive. The mains supply for the motor was switched using a reed-relay, the coil voltage being supplied from a 24v D.C. supply in the control room.

To use the maximum target area, the target rotated in a circular mode as well as describing a radial scan. The beam would first scan across the target from the target centre to the edge, the assembly then rotated the annular target ring through 6° and reset to the target centre, the scan would then restart. Allowance was made in the scan length for the finite beam width at the target edge, the radial travel was therefore limited to 1 cm. The rotating assembly was constructed from stainless steel and a slow rotation was used to prevent unnecessary friction in the moving assembly. Typically the assembly would traverse the 1 cm in 60 sec, this gave a total target lifetime of 6 hrs., after which the target was replaced.

The incident deuteron beam passed through the thin targets and the beam current was monitored by a copper Faraday cup. The cup was insulated from the chamber and the output was wired to a vacuum feedthrough mounted on one of the side ports. At an incident energy of 1 Mev the maximum current, as measured on the Faraday cup, was 25 nA before visible damage to the target occurred.

To minimise attenuation of the neutrons when emerging from the chamber a 1 mm stainless steel window was used on the neutron production port. This window and the feedthrough flange could be interchanged depending on the neutron production angle being used for the experiments. The experimental configuration for neutron production at 120° is shown in figure 2.27, the position of the

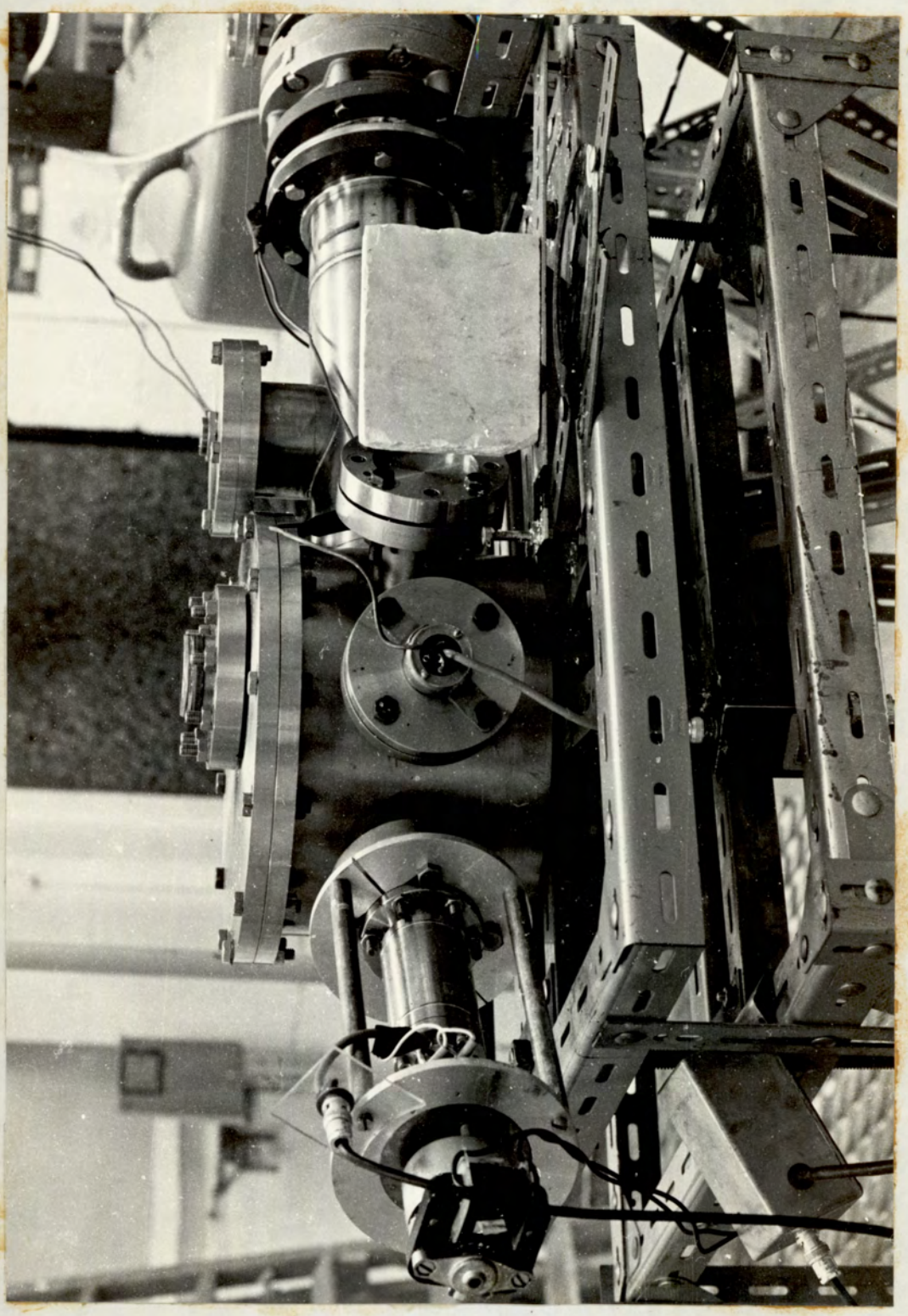

Figure 2.27 Experimental configuration for neutron production at 120°

scattering sample is also shown.

2.9 Neutron Beam Profiles

With the information obtained so far on the experimental system, it was possible to calculate the neutron beam profiles, i.e. the relative yield of neutrons with associated ^{3}He particles as a function of neutron angle. The relative neutron yield per steradian at a neutron angle Ψ_n, due to an incident deuteron energy of E Mev, is given by:-

$$Y(\Psi_n, E) \propto \frac{d\sigma/dw \quad (E, \Psi_n)}{dE/dx \quad (E)} \qquad \ldots\ldots 2.14$$

Due to the variation of the laboratory differential cross-section $d\sigma/dw$ with both energy and neutron angle, the neutron beam profile was calculated in several stages. The limiting case of a maximum diverging beam incident on the target as calculated in section 2.5 was considered.

Firstly, the beam profile which would have been measured by a point neutron detector was calculated assuming an infinitely thin target. It was also assumed that the deuteron flux was incident uniformly over the target spot and that $d\sigma/dw$ was constant over the angular range. In this case the relative yield of neutrons with associated ^{3}He particles in a given direction was proportional to the area of the charged particle detector which was seen from that direction to overlap with the elliptical target spot.

In the next stage of the calculations the finite target thickness was introduced. As the incident deuterons lose energy in traversing the target, neutrons are produced with central angles and yields corresponding to E between 1 Mev and 0.87 Mev. The thin target yields for deuteron energies of 1 Mev, 0.95 Mev, 0.9 Mev and 0.87 Mev were calculated from equation 2.14. The energy loss

dE/dx is only a function of E and was therefore a constant for each energy and only the variation of $d\sigma/dw$ with Ψ_n determined the neutron yield variations for each thin element. The neutron beam profiles were then obtained by multiplying the yield at each neutron angle by the fraction that the target and recoil detector overlapped. The thin target profiles for ^{3}He detection at 61.3° are shown in figure 2.28.

The neutron beam profile for a target thickness of 2 μm was obtained by summing these thin target profiles. The horizontal neutron beam profiles produced for ^{3}He central production angles of 61.3° and 31.2° are shown in figures 2.29 and 2.30, the f.w.h.m. (full width at half maximum) for the two profiles are 8.8° and 10° respectively.

2.10 Neutron Line Shapes

The energy spread for each of the defined neutron cones are of interest in determining the energy resolution of the neutron beams produced, and are found by considering the neutron line shapes. In the previous section the relative yield of neutrons with associated ^{3}He particles at a particular deuteron energy E and for a particular neutron emission angle of Ψ_n was found by using equation 2.14. The yield of neutrons was plotted as a function of neutron emission angle (figures 2.29 and 2.30).

At a deuteron energy E the neutron energy was calculated from equation A1.2 for a given neutron angle. The thin target yield profiles obtained previously were plotted as a function of neutron energy and are shown in figure 2.31 for neutron emission centred at 75°. The thin target profiles were then summed to give the relative yield of neutrons at a neutron energy, figure 2.32 and 2.33 give the neutron line shapes for neutron emission angles centred at 75°

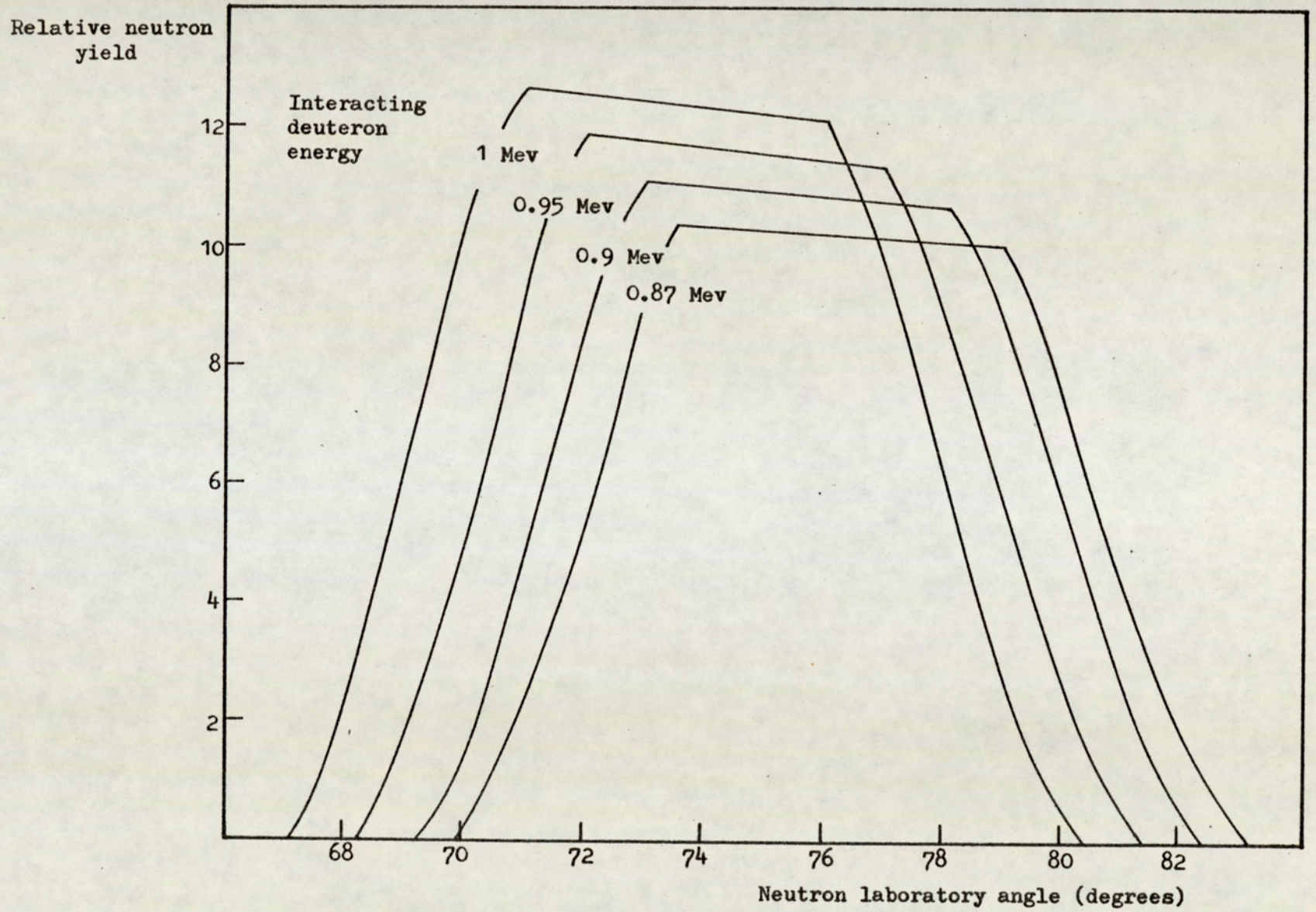

Figure 2.28 Calculated thin target neutron yield (horizontal) profiles associated with ^{3}He detection centred at 61.3°

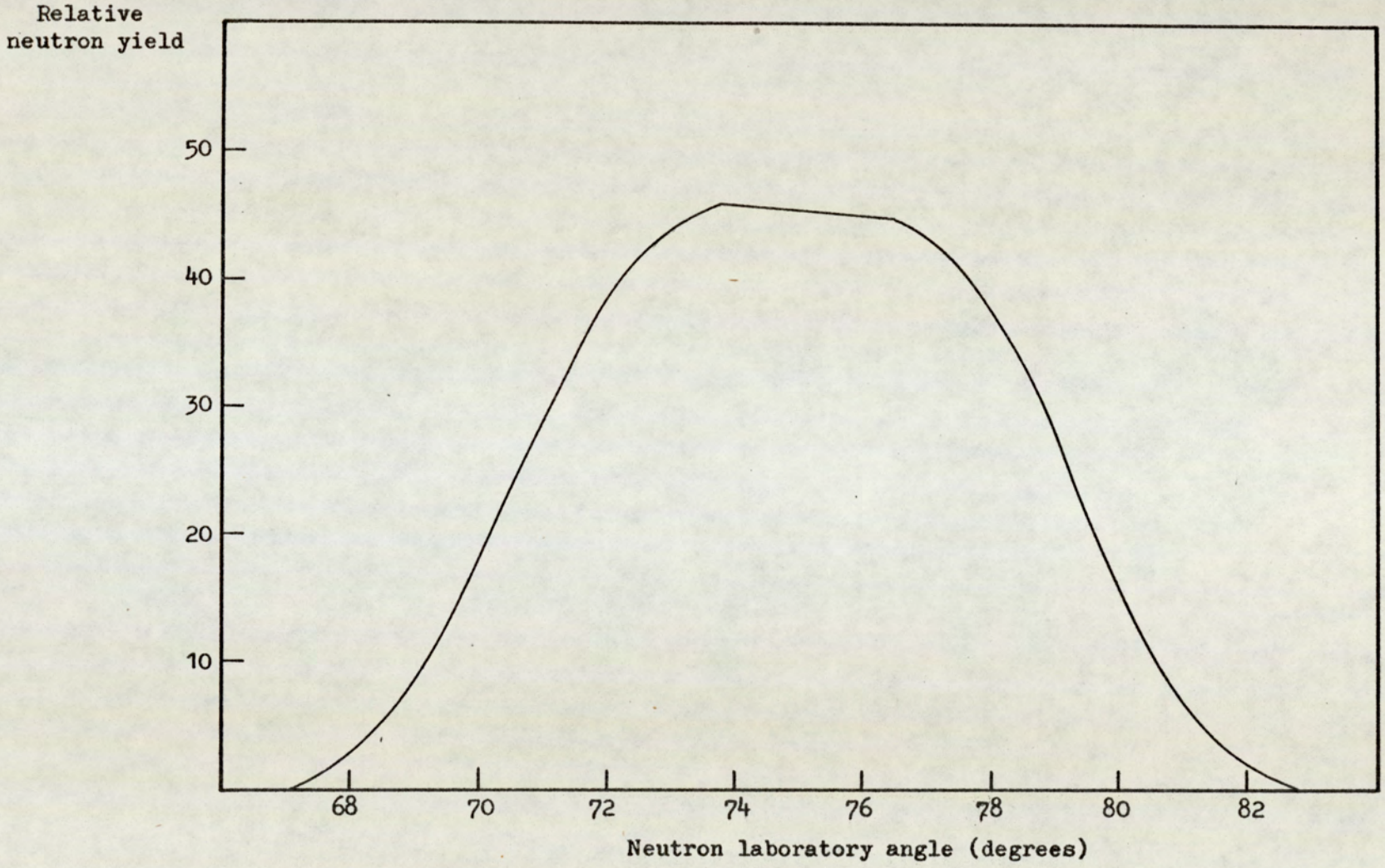

Figure 2.29 Calculated horizontal neutron yield profile associated with ^{3}He detection centred at 61.3°.

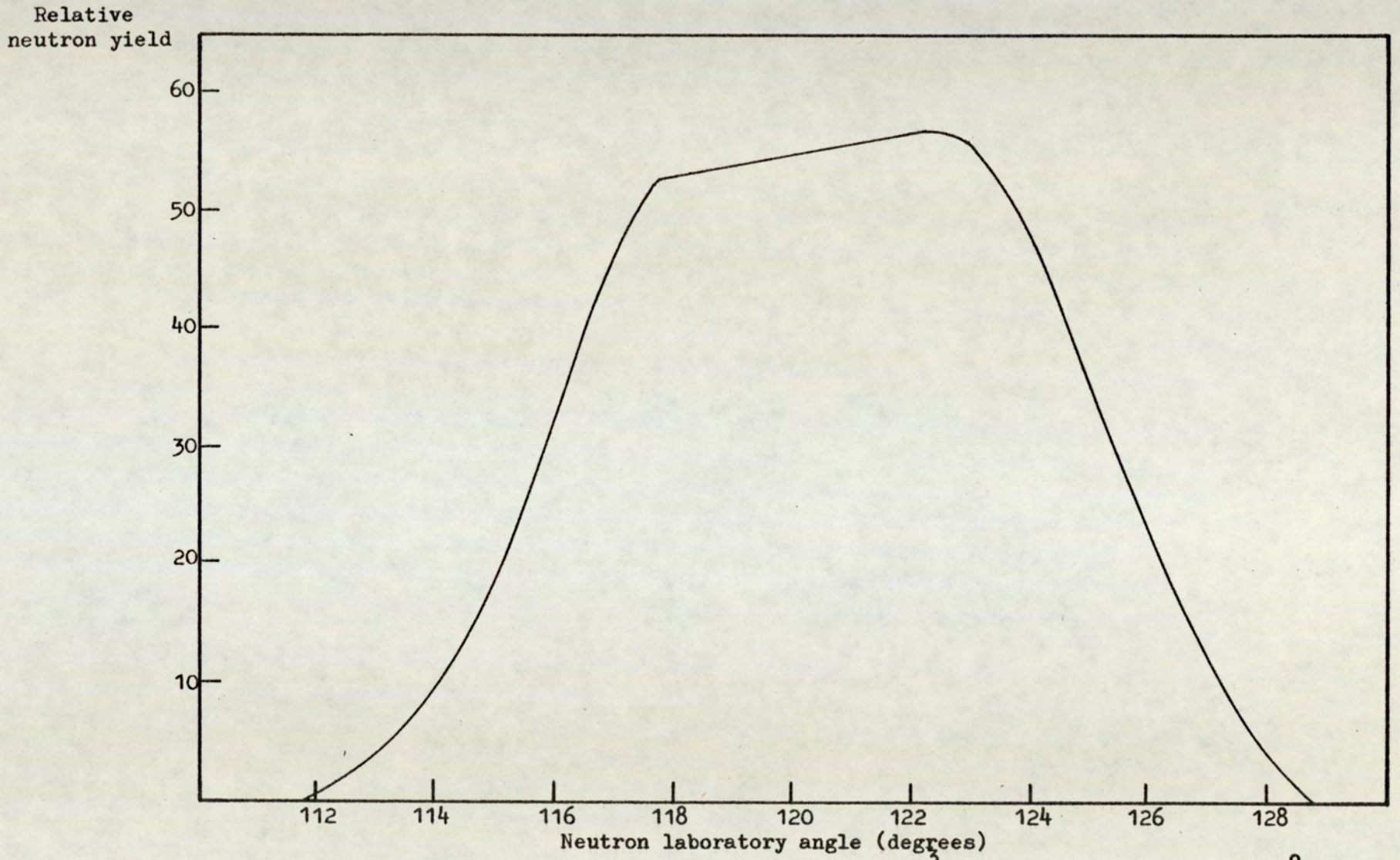

Figure 2.30 Calculated horizontal neutron yield profile associated with ^{3}He detection centred at 31.2°.

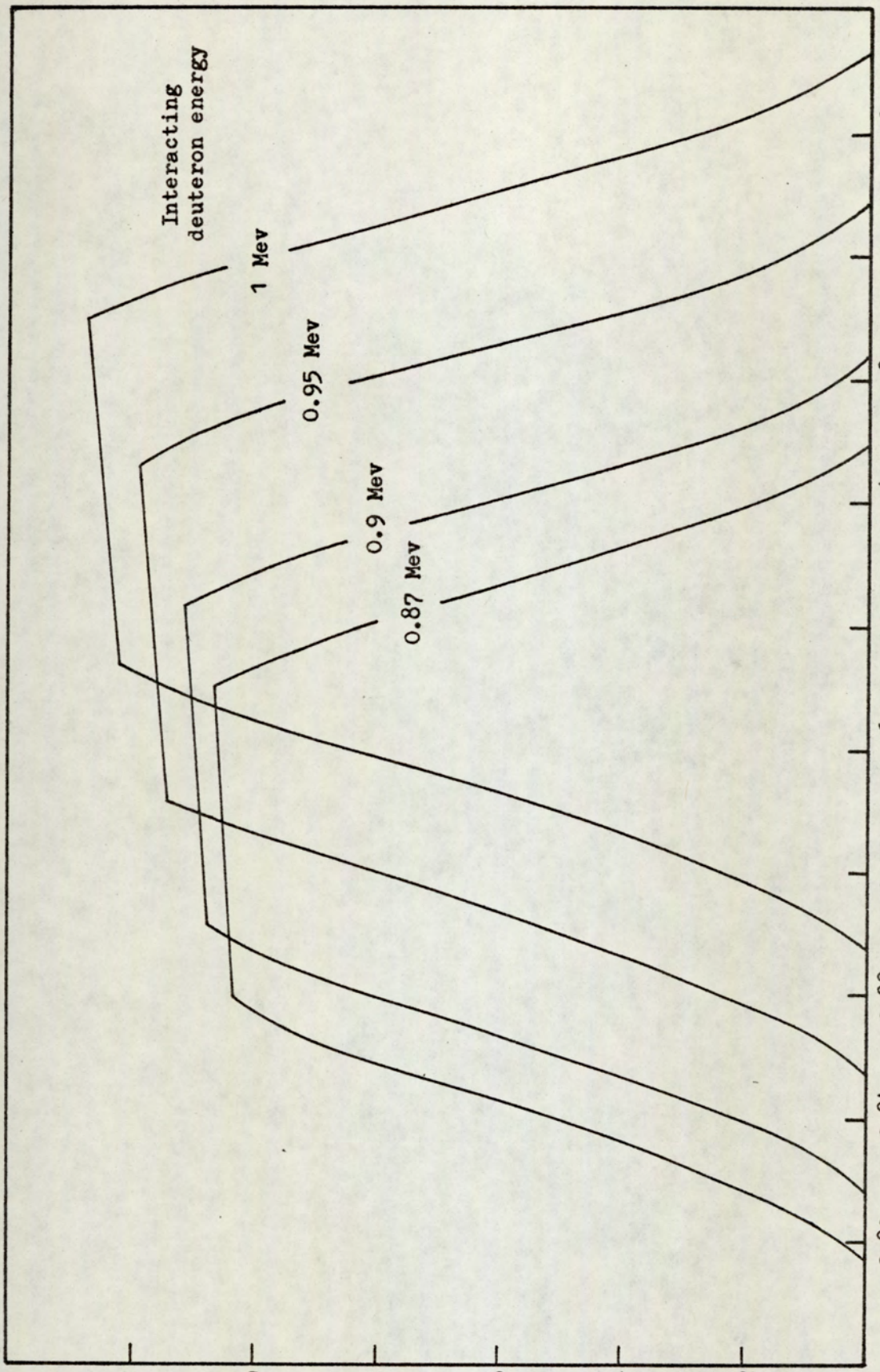

Figure 2.31 Calculated neutron line shapes, for thin target elements, corresponding to ^{3}He detection centred at 61.3°

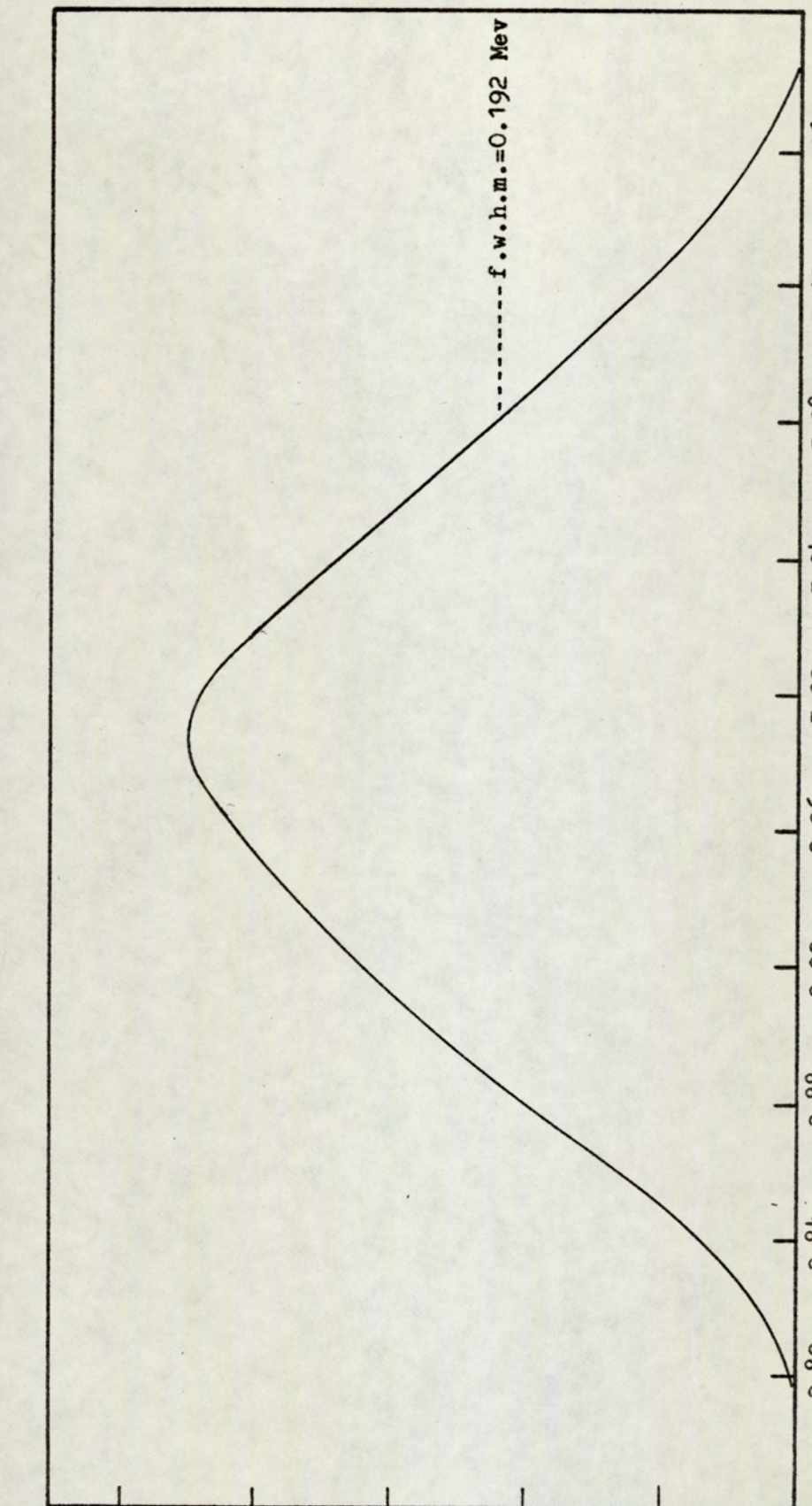

Figure 2.32 Calculated neutron line shape for a neutron production angle of $75^{\circ} \pm 7.5^{\circ}$

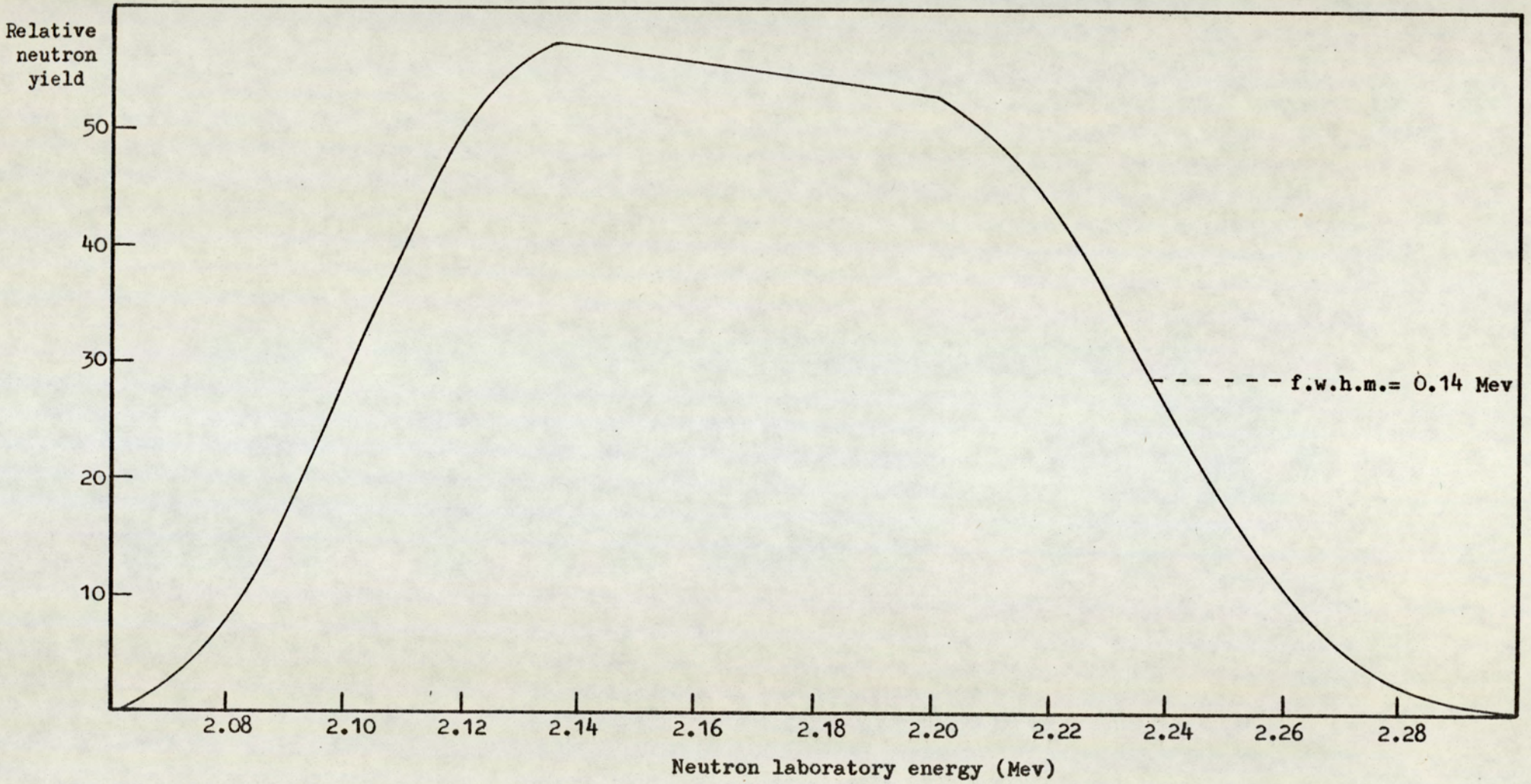

Figure 2.33 Calculated neutron line shape for a neutron production angle of $120^{\circ} \pm 7.5^{\circ}$

and 120° respectively.

The resulting neutron energies are 2.99 Mev at 75° and 2.18 Mev at 120°, the respective neutron beams have f.w.h.m. of 0.19 Mev and 0.14 Mev. This energy spread is attributed to the variation of neutron energy with angle and interacting deuteron energy. The method of neutron detection used for these energies and the efficiency of the process is discussed in the next Chapter. Also discussed is the method of charged particle detection.

CHAPTER 3

NEUTRON AND CHARGED PARTICLE DETECTION

3.1 Neutron Detection

The neutron, due to its lack of charge cannot be detected directly. Unlike charged particles they produce negligible ionisation in a detecting medium. A neutron being uncharged can readily penetrate the electron cloud of an atom and collide with the nucleus, interaction can then occur either through scattering or reaction. In either process the neutron produces charged particles which can then be detected. At high energies the usual method and the one adopted here, for neutron detection is to use a scintillator containing hydrogen, the neutrons elastically scatter from the hydrogen to produce detectable recoil protons in the scintillator.

Organic scintillators containing only carbon and hydrogen are the most convenient method of obtaining a high concentration of hydrogen. The scintillator used in the present work was NE 102A, which provided light output pulses with a rise time of approximately 1 ns and an exponential decay with a time constant of 2.4 ns. The scintillator was 5 cm thick which led to a timing uncertainty with 2 Mev neutrons of 2.55 ns.

The efficiency of the neutron detector was calculated as a function of energy, this aspect is considered in the following sections.

3.2 Scintillator Efficiency

The efficiency of an organic scintillator is defined as the ratio of the number of recoil protons produced to the number of incident neutrons.

The number of recoil protons produced in a crystal of length x by N neutrons of energy E incident along the direction of the scintillator axis is given by:-

$$N_1(E) = \frac{N\ n_H\ \sigma_H(1 - e^{-ax})}{a} \qquad \ldots\ldots\ 3.1$$

where $a = n_H \sigma_H + n_c \sigma_c$

n_H = number of hydrogen atoms cm^{-3}

n_c = number of carbon atoms cm^{-3}

σ_H = neutron-proton scattering cross-section at an energy E

σ_c = neutron-carbon scattering cross-section at an energy E

The number density n_c and cross-section for carbon are used in equation 3.1 to take account of the neutron collisions with the carbon which produce no recoil protons. The exponential term allows for the attenuation of the neutron beam in passing through the scintillator. From the definition of efficiency and considering only single collisions, the efficiency can be found from:-

$$\varepsilon_1(E) = \frac{n_H\ \sigma_H(1 - e^{-ax})}{a} \qquad \ldots\ldots\ 3.2$$

The efficiency curve obtained by applying equation 3.2 to NE 102A is shown in figure 3.1 as the solid curve. The values of n_H and n_c as quoted by the manufacturers, were 5×10^{22} atoms cm^{-3} and 4.75×10^{22} atoms cm^{-3} respectively.

Only single neutron collisions with hydrogen have been considered and this represents a simplification of the overall interaction processes. Double scattering from hydrogen can occur

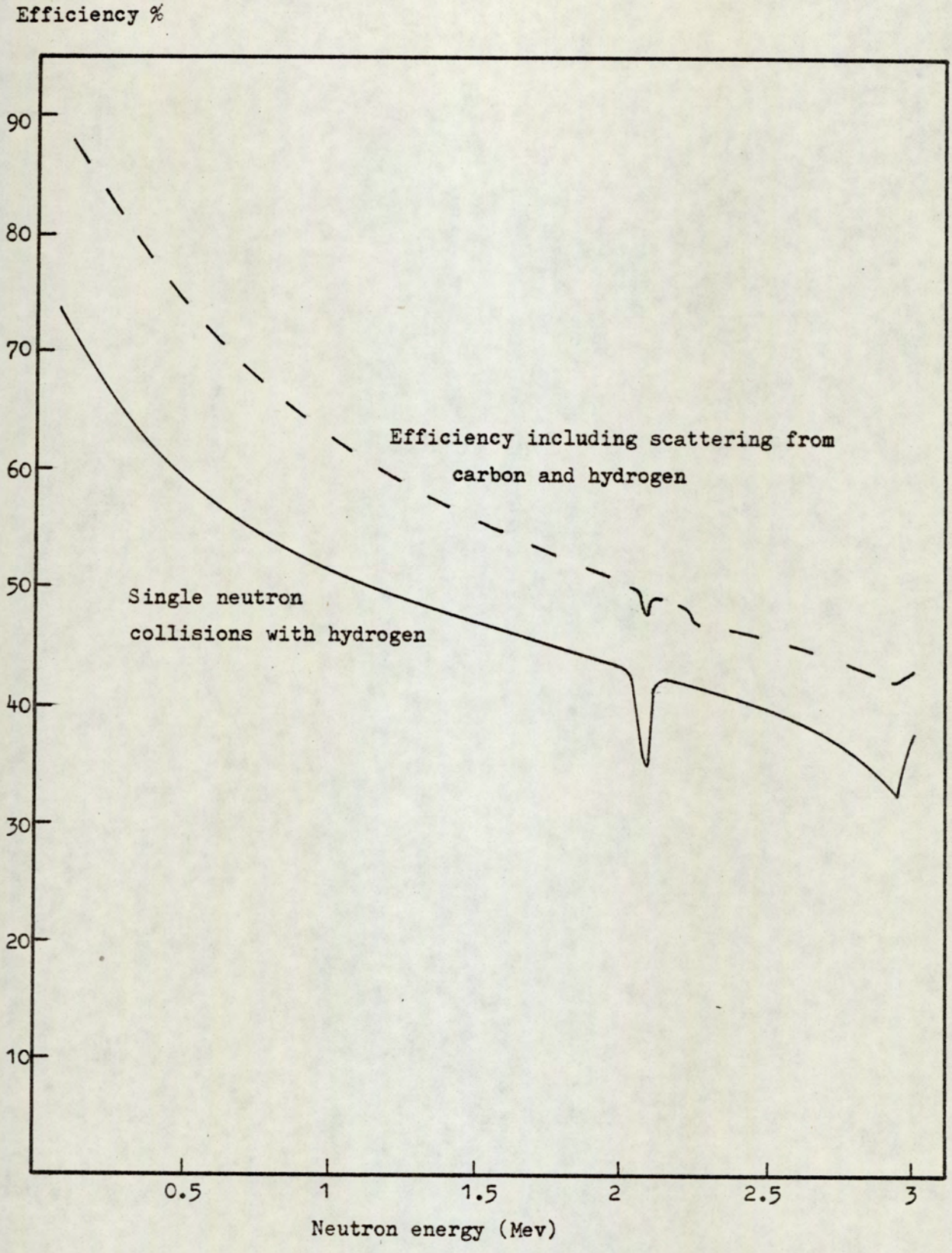

Figure 3.1 Calculated efficiency of 5 cm. NE 102A scintillator.

which results in the production of two recoil protons at almost the same instant of time which will be recorded as a single event. Also, neutrons originally scattered from carbon were assumed to be removed from the incident beam. However, the neutrons scattered from carbon can produce recoil protons by secondary collisions.

To compensate for the increase in the number of recoil protons, hence increase in efficiency due to multiple scattering a Monte Carlo type calculation should be performed. However, in this case the experimental arrangement allowed the multiple scattering contribution to be estimated sufficiently accurately. This is discussed below.

3.2.1 Scattering by Carbon and Hydrogen

As stated previously some of the neutrons scattered from the incident flux by collisions with nuclei can produce recoil protons in a second scattering event. The number of neutrons scattered once by carbon in length x can be found from:-

$$N_c = \frac{N\, n_c\, \sigma_c\, (1 - e^{-ax})}{a} \qquad \ldots\ldots 3.3$$

The average energy of these scattered neutrons is $0.85E$[39][40], where E is the incident neutron energy. If the neutrons are assumed to travel an average path x_1 in the scintillator before collision with hydrogen the number of recoil protons produced is given by:-

$$N_{2c} = \frac{N_c\, n_H\, \sigma_{H_1}\, (1 - e^{-a_1 x_1})}{a_1} \qquad \ldots\ldots 3.4$$

where the values of σ_{H_1} and a_1 are calculated for the average neutron energy. A value for x_1 which has been shown to give good agreement between theoretically determined and experimental efficiencies is

when x_1 is equal to half the thickness of the scintillator[39][40], i.e. 2.54 cm.

After second scattering the total number of recoil protons is $N_1 + N_{2c}$, where N_1 is the number of recoil protons calculated in equation 3.1. The resulting efficiency is given by:-

$$\varepsilon_2(E) = \frac{N_1 + N_{2c}}{N} = \varepsilon_1(E) \left[1 + \frac{N_{2c}}{N_1} \right] \quad \ldots\ldots 3.5$$

where $\varepsilon_1(E)$, defined as N_1/N, is calculated from equation 3.2. The efficiency calculated which included scattering by carbon and hydrogen in equation 3.5 is shown in figure 3.1 as the dashed line.

To reduce the background count in the neutron detector it was found necessary to discriminate against pulses due to low energy background neutrons, γ-rays and photomultiplier noise

The discrimination results in some of the proton pulses being rejected. The effect of the discrimination on the efficiency of the detector is now considered.

3.2.2 Recoil Proton Energy Spectrum

The energy of the recoil proton Ep produced by a neutron of energy E can be found by considering the kinematics of the elastic collision. As the mass of the incident and recoil particles are very similar equation 2.3 can be used to obtain the energy of the recoil proton:-

$$Ep = E \cos^2 \Psi \quad \ldots\ldots 3.6$$

where Ψ is the laboratory angle of the recoil particle.

In the centre of mass system the differential cross-section for the $(n, {}^1_1H)$ reaction is isotropic to within 3% up to neutron energies of 5 Mev[41]. Barshall et al[42] have shown that the energy distribution of recoil particles in the laboratory system is the

same as the angular distribution of neutrons scattered in the centre of mass system. Therefore all proton energies given by equation 3.6 are equally probable from Ep = E to Ep = 0. The recoil energy spectrum will be rectangular and is shown in figure 3.2.

3.2.3 Non-linear Response of NE 102A

Under appropriate conditions the photomultiplier output is directly proportional to the luminous output of the scintillator. However, the luminous output produced is not proportional to the energy which the proton loses in the scintillator.

The luminous output of the scintillator for charged particles is well represented by the semi-theoretical formula of Birks[43], viz:-

$$\frac{dS}{dx} = \frac{A\ dE/dx}{1 + kB\ dE/dx} \qquad \ldots\ldots\ 3.7$$

where S and x are respectively the luminous output and path length of the particle in the scintillator, E is the particle energy, and A and kB are empirical constants.

To avoid dependence on specific units for S, it is convenient to represent the crystal output by the variable P = S/A, equation 3.7 can be rewritten as:-

$$\frac{dP}{dE} = A^{-1}\frac{dS}{dE} = \left(1 + kB\frac{dE}{dx}\right)^{-1} \qquad \ldots\ldots\ 3.8$$

The units for P and E will be the same. For NE 102A Evans and Bellamy[44] have shown that a value of $kB = 1.0 \times 10^{-2}$ g cm^{-2} Mev^{-1} gives the best agreement between theoretical and experimental results.

The energy loss values for protons in carbon and hydrogen were considered in section 2.3.1 and these were combined by applying Bragg's law to give the energy loss values of protons in CH, in this case:-

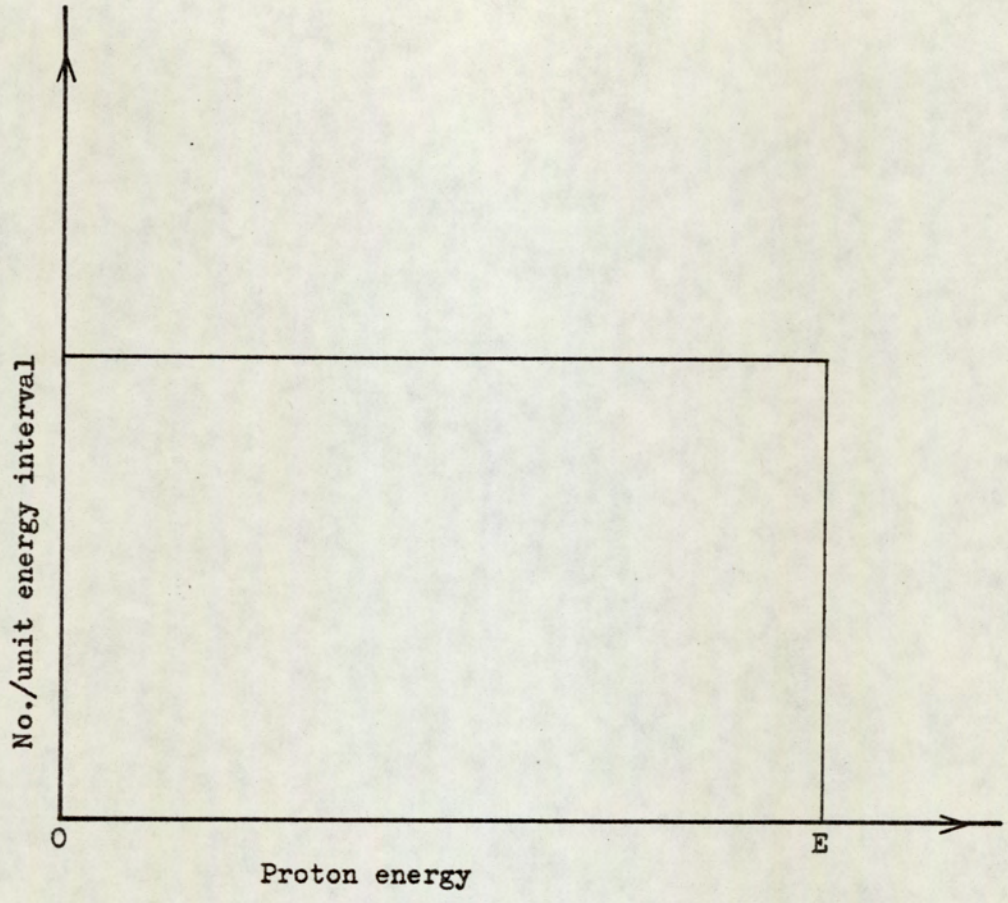

Figure 3.2 Recoil proton energy spectrum

$$\left(\frac{dE}{dx}\right)_{CH} = 0.923 \left(\frac{dE}{dx}\right)_{C} + 0.077 \left(\frac{dE}{dx}\right)_{H} \quad \ldots\ldots 3.9$$

It was assumed the energy loss of protons in NE 102A was the same as protons in CH. Equation 3.8 was evaluated to obtain values of dP/dE as a function of proton energy, the results are shown in figure 3.3. The pulse height (luminous output) due to a proton of energy Ep was then obtained by numerical integration of this dP/dE v.s. Ep curve from E = 0 to E = Ep, the results are shown in figure 3.4.

If N(P) is the number of pulses with pulse heights between P and P + dP, then the recoil proton energy spectrum is related to the pulse height spectrum by:-

$$N(E)\, dE = N(P)\, dP \quad \ldots\ldots 3.10$$

This relationship results from the requirement that the area under the two spectra be the same. For convenience N(E) was taken as unity, therefore:-

$$N(P) = \frac{dE}{dP} \quad \ldots\ldots 3.11$$

The pulse height spectrum and energy spectrum for 3 Mev neutrons are shown in figure 3.5. In practice because of statistical fluctuations in the scintillator and photomultiplier outputs the pulse height spectrum will appear distorted, this is shown in figure 3.5 as the dashed line. The area under the curve will still remain the same, therefore the efficiency calculations will not be affected.

3.3 Detector Efficiency with Discrimination

A discriminator level was selected which although rejecting pulses due to low energy neutrons, γ -rays and photomultiplier noise, did not result in a large decrease in the overall detection efficiency.

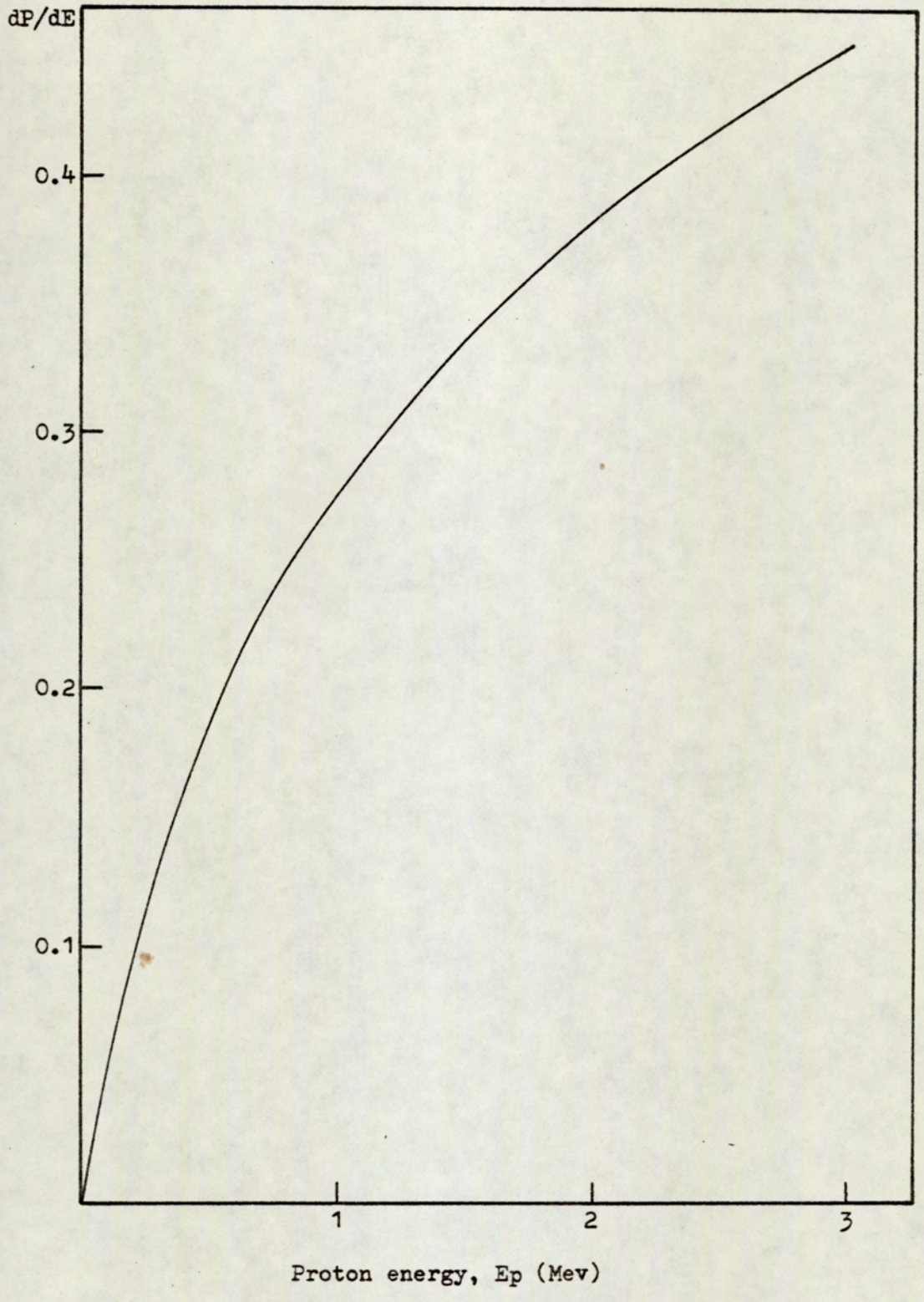

Figure 3.3 dP/dE as a function of E_p for protons in NE102A

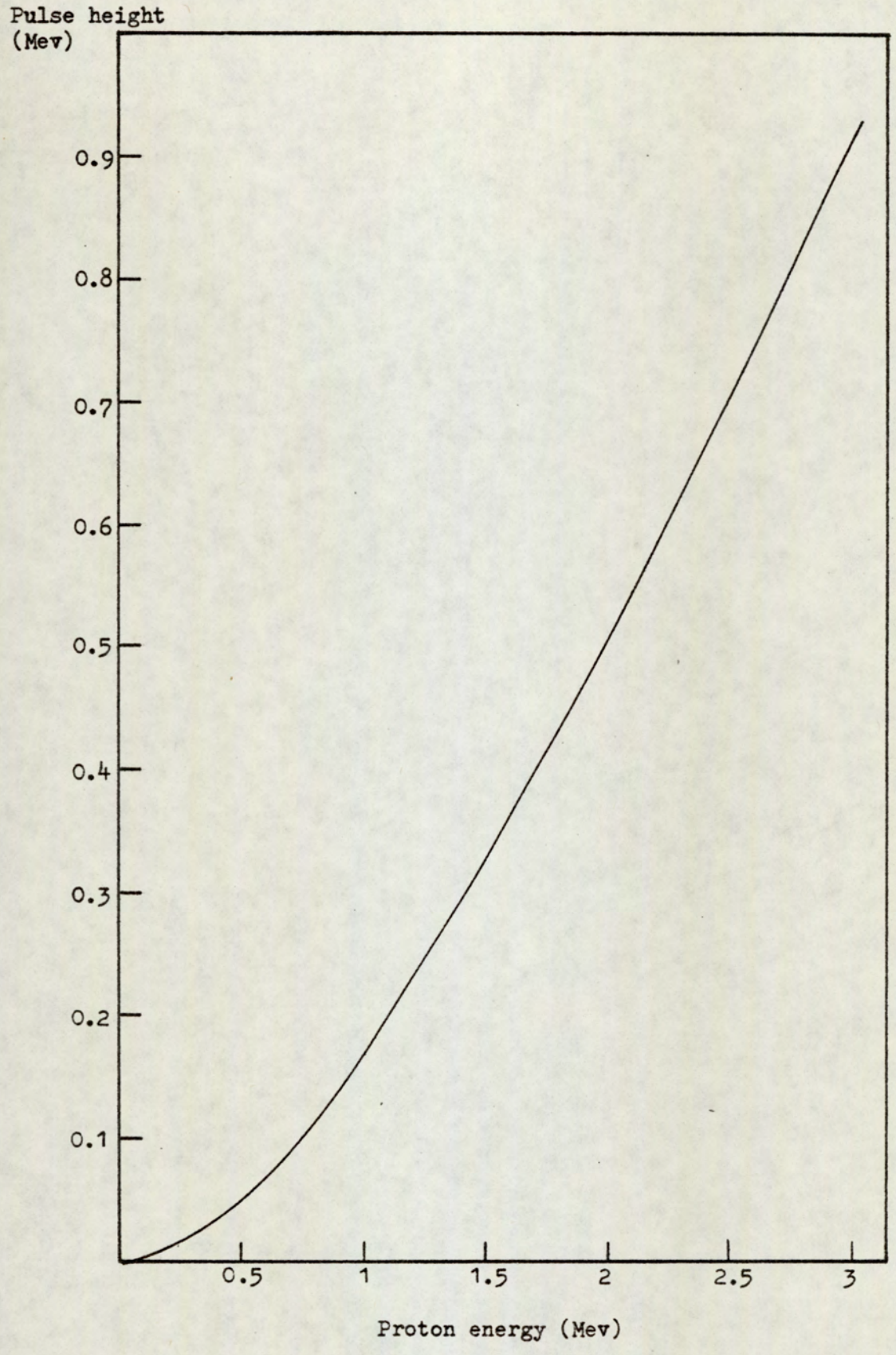

Figure 3.4 Pulse heights of protons in NE102A

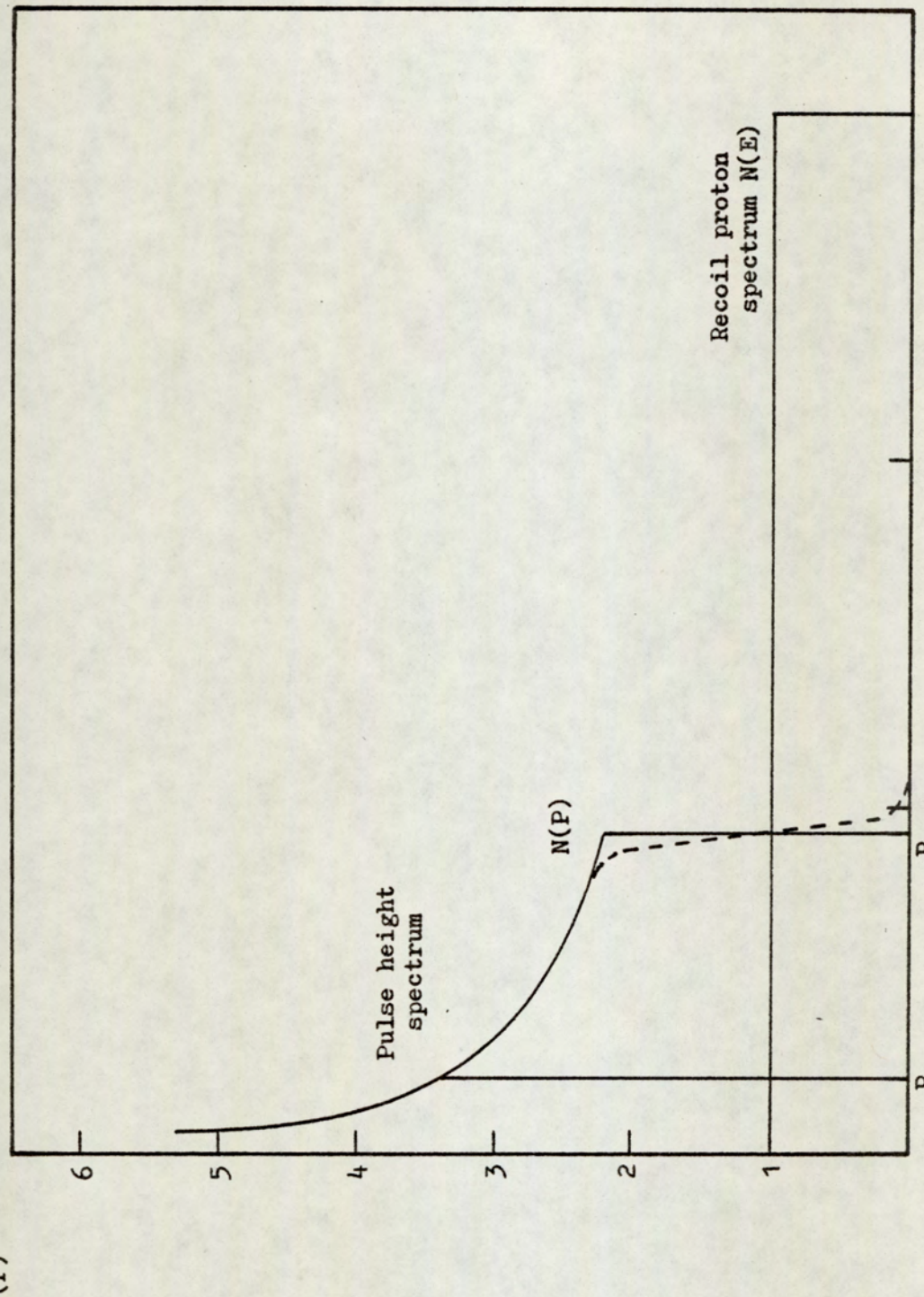

Figure 3.5 Calculated pulse height spectrum for 3 Mev neutrons in NE102A scintillator

With a discriminator designed to reject all pulses below P_D (in figure 3.5), the efficiency for 3 Mev neutrons was:-

$$\varepsilon(3) = \varepsilon_1(3) \times \left(\frac{A_3 - A_D}{A_T}\right) \quad \ldots\ldots 3.12$$

where $\varepsilon_1(3)$ = 3 Mev efficiency with no discrimination

$A_3 - A_D$ = area under pulse height spectrum between ordinates P_D and P_3 (figure 3.5)

P_D = discriminator level

P_3 = pulse height due to 3 Mev protons

A_T = total area under pulse height spectrum

From the same pulse height spectrum the efficiency for neutrons of energy E was then:-

$$\varepsilon(E) = \varepsilon_1(E) \times \left(\frac{A_E - A_D}{A_T}\right) \times \frac{3}{E} \quad \ldots\ldots 3.13$$

The discrimination level chosen had to be easily reproducible and this was accomplished by setting the discriminator to reject pulses from a γ-ray source of known energy. The γ-ray source used was ^{133}Ba which emits a 0.36 Mev γ-ray. In this energy range γ-rays interact with the plastic scintillator to produce Compton electrons. A 0.36 Mev γ-ray will produce a Compton electron with a maximum energy of 0.21 Mev. The pulse height corresponding to this can be obtained by considering equation 3.8. The energy loss of the electrons in the plastic is small, therefore kB dE/dx can be neglected. The pulse height due to electrons of energy Ee is given by:-

$$P = Ee \quad \ldots\ldots 3.14$$

Referring to figure 3.4 a pulse of amplitude P = 0.21 Mev corresponds to a proton energy of 1.12 Mev. Setting up the discriminator with ^{133}Ba as a reference is equivalent to setting a level to reject pulses due to neutrons with an energy below 1.12 Mev. With the discriminator level established the resulting efficiency was calculated by applying equation 3.13 to figure 3.5, the resulting efficiency curve is shown in figure 3.6, curve (a) assumes no multiple scattering. Curve (b) is the resulting efficiency assuming double scattering from carbon and hydrogen. It has been found in many cases that good agreement can be obtained between experimental and theoretical efficiencies by assuming that the carbon does not scatter neutrons at all[39][45]. The efficiency $\varepsilon_1(E)$ in equation 3.13 is then given by:-

$$\varepsilon_1(E) = (1 - e^{-n_H \sigma_H x}) \qquad \ldots\ldots 3.15$$

The dashed curve (c) in figure 3.6 was calculated on this assumption and differs by 3% from the curve assuming double scattering by carbon and hydrogen.

The effects of multiple scattering were assumed not to alter the shape of the pulse height spectrum, since scattering from carbon and hydrogen enhances the low energy region, while double scattering from hydrogen shifts counts towards the high energy region.

Possible effects due to the loss of protons from the sides of the scintillator were neglected as the scintillator size was much greater than the range of the recoil protons produced. Also the production of a recoil carbon nucleus produces a pulse of very small pulse height in the scintillator and therefore this effect was neglected.

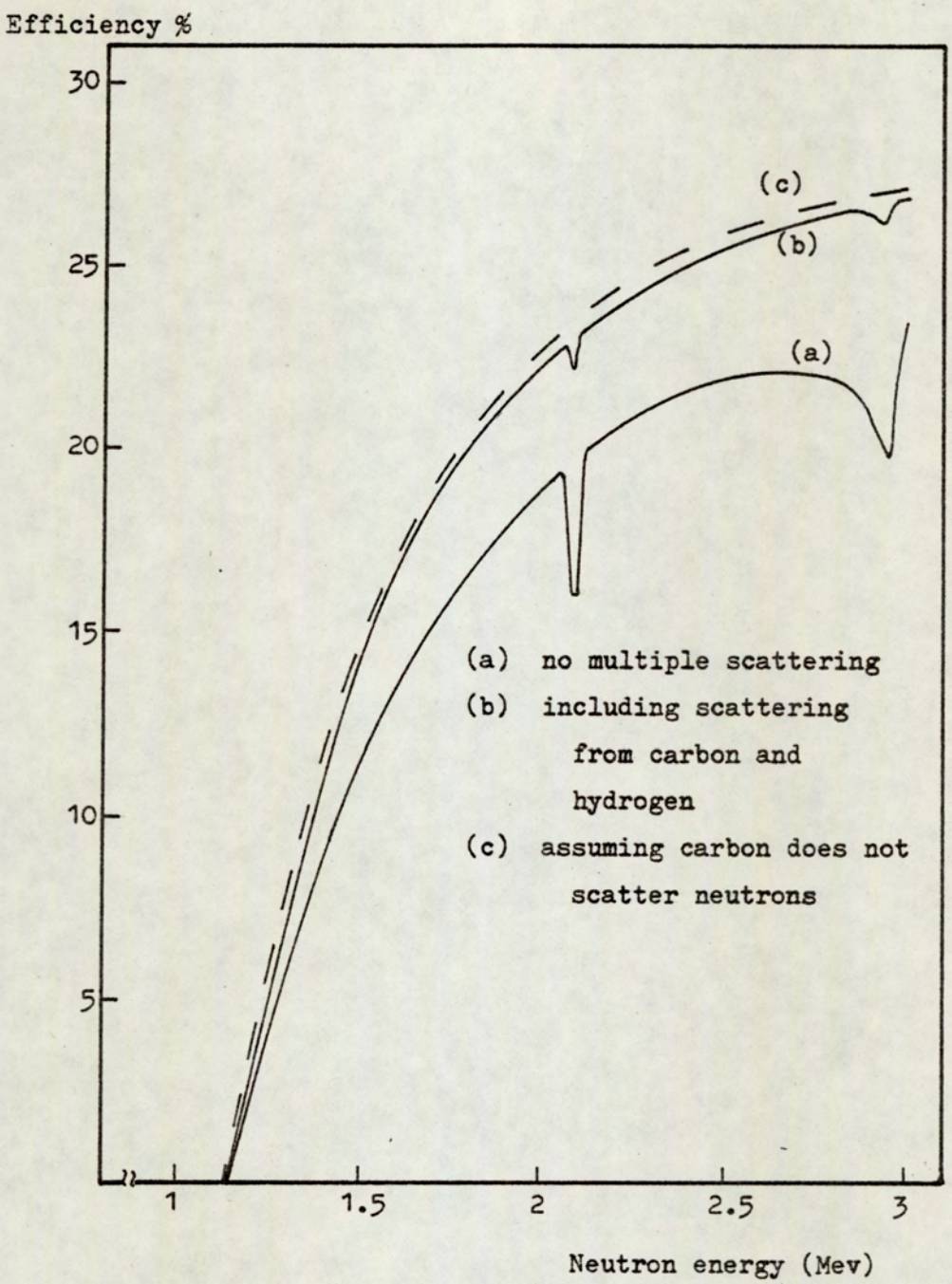

Figure 3.6 Calculated efficiency of 5 cm NE102A scintillator with a discriminator level of 1.12 Mev.

3.4 Detection System

The design and construction of the detection system has been reported elsewhere for the detection of 14 Mev neutrons[18], no modifications were found necessary for the detection of neutrons with energies between 2 Mev and 3 Mev. A description of the system is included for completeness.

The scintillator which had a diameter of 10 cm was connected to the 5 cm diameter photomultiplier by a perspex light pipe. Optical cement was used to connect the light pipe to the scintillator, optical contact between the light pipe and photomultiplier tube was obtained by using a non-drying immersion oil and spring loading the tube.

In order to reduce time uncertainties in the detection process a suitable photomultiplier tube must have a fast transit time with good time resolution. To meet these requirements a Phillips 56 AVP photomultiplier tube was used which gave an electron transit time spread of 0.5 ns at f.w.h.m. The photomultiplier had 14 stages of amplification which gave a gain of approximately 10^8 when operated at 2 Kv.

The resistance chain used to supply the voltages to the dynode stages of the photomultiplier is shown in figure 3.7. The D.C. current through the dynode chain was 2.3 mA at the operating voltage of 2 Kv. The last dynodes of the tube are decoupled by means of capacitors to avoid fluctuations in the dynode potentials.

A Mu-metal shield was placed around the photomultiplier tube to prevent the electron trajectories between dynodes being affected by the earth's magnetic field. The complete neutron detector and housing is shown in figure 3.8.

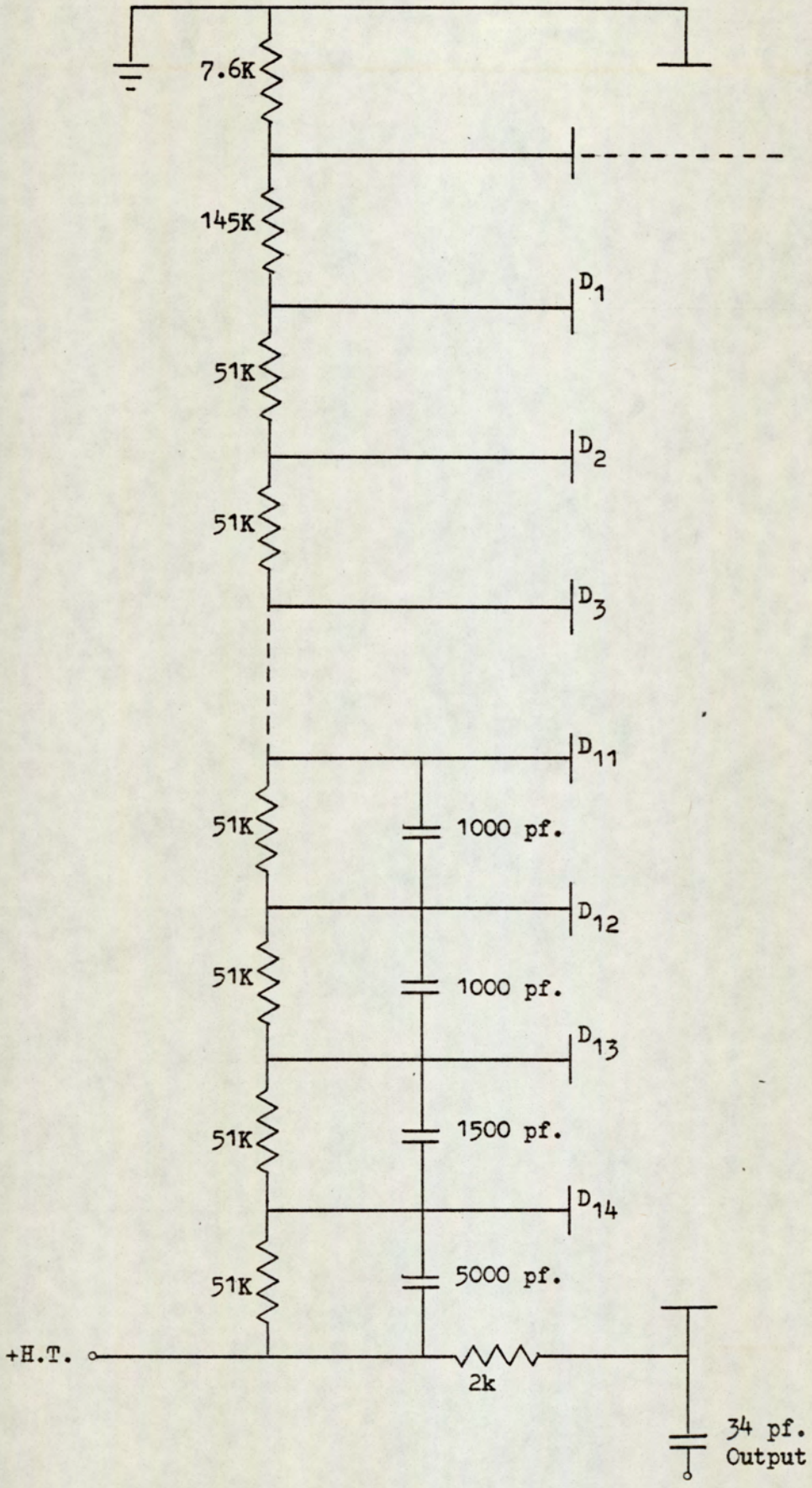

Figure 3.7 Dynode resistor chain

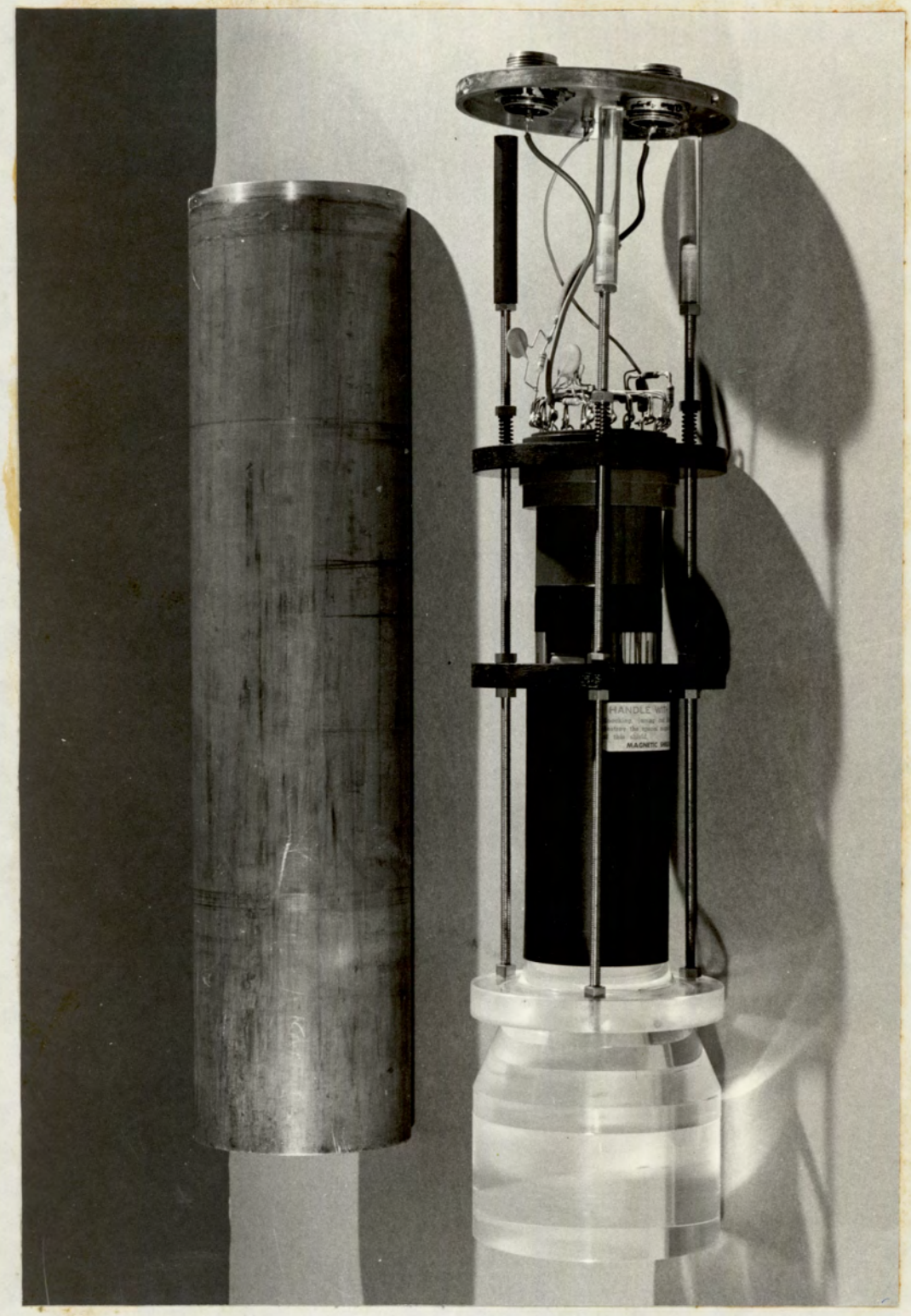

Figure 3.8 The Neutron detector assembly

3.5 Detector Shielding

In order to reduce the number of background neutrons and γ -rays entering the neutron detector, shielding was employed in the form of a shadow bar and a collimator surrounding the detector. The shadow bar was used to shield the detector from the direct neutron source.

The neutron detector and shielding had to be easily positioned before each experimental run, the selection of shielding material was chosen as a compromise between weight, size and the efficiency of the material. Also because of the nature of the beam room no permanent system could be established.

Hopkins et al[46] have shown that the most efficient shielding material for neutrons of energies below 3 Mev is hydrogen. This was readily available in the form of paraffin wax. However, neutrons thermalized by this process may give rise to γ -rays with an energy of 2.2 Mev produced in the ${}_1^1H(n,\gamma){}_2^1H$ reaction. It is possible to reduce the γ-ray production by loading the paraffin wax with a slow neutron absorbing material. Suitable materials are lithium carbonate or a similar boron compound, the former is more favourable as with the capture of slow neutrons by boron γ -rays with an energy of 0.48 Mev are emitted by the ${}^{10}B(n,\alpha){}^{7}Li$ reaction. Ashe et al[47] used a 50% mixture of paraffin wax and $Li\,CO_3$ to reduce the γ -ray yield, however this added greatly to the shield size and weight. In the consideration of the size, weight and efficiency of the shield, lithium carbonate was not included in the shield. A cross-section of the detector shield is shown in figure 3.9.

For ease of construction the shield surrounding the detector was made from paraffin wax slabs which had a thickness of about 3.8 cm each. The annular collimator in front of the detector was moulded in one piece.

The shadow bar was also constructed from paraffin wax. The

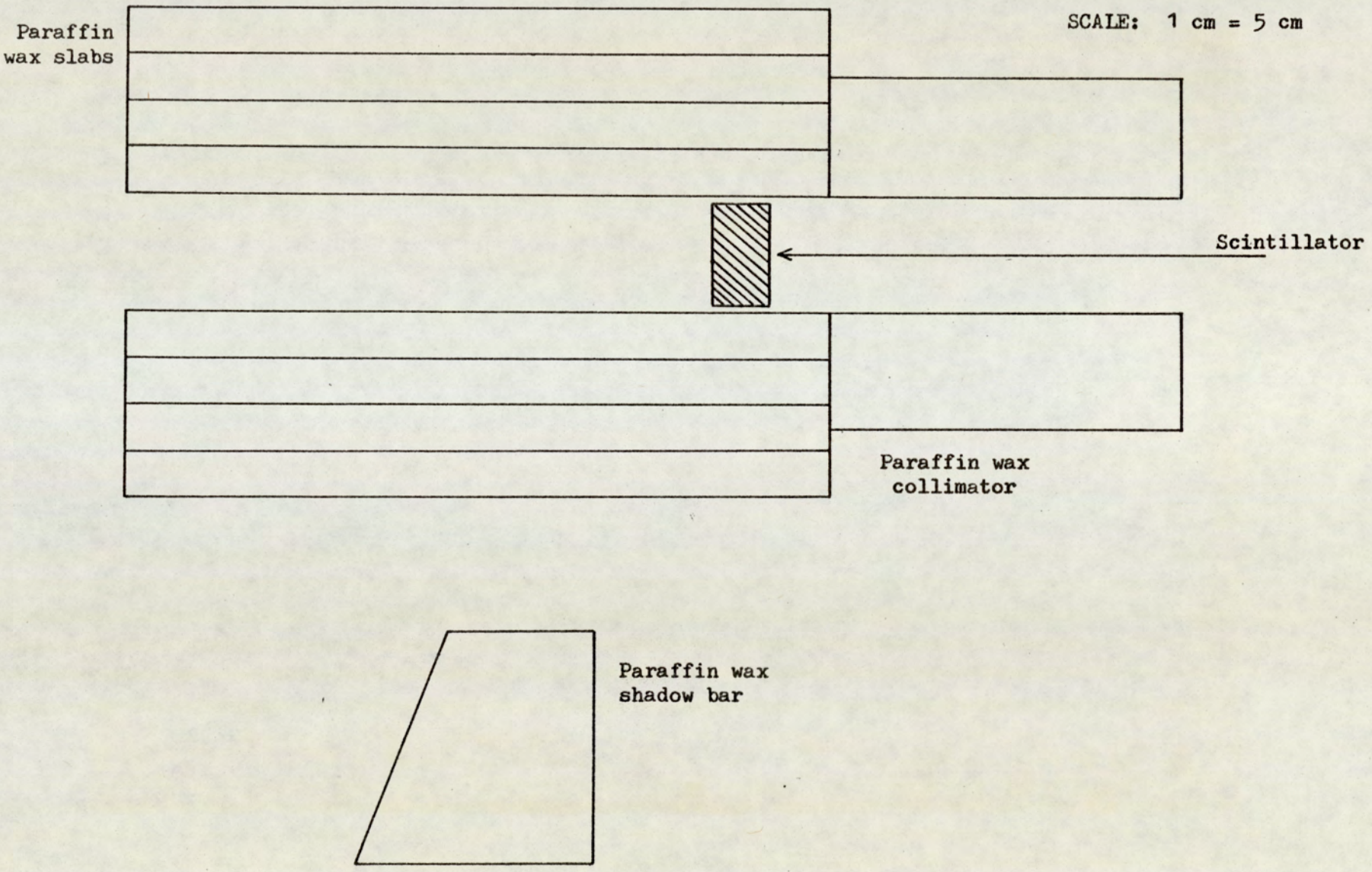

Figure 3.9 Plan view of neutron detector shield and shadow bar

efficiency of the shadow bar was measured using the time-of-flight spectrometer. The neutron detector was positioned in the direct beam of neutrons and the number of coincidences for a given neutron yield noted. The shadow bar was then placed in the direct beam between the source and detector and the experiment repeated, the result is shown in figure 3.10. The shadow bar reduced the direct flux to about 2% of its initial value.

In measuring differential cross-sections the position of the shadow bar was important. In addition to shielding the detector from the direct neutron beam, it also prevents neutrons generated at the target reaching the detector.

3.6 Charged Particle Detection

An ORTEC silicon surface barrier detector was used for charged particle detection. This type of detector was chosen because of its good energy resolution, linearity of response for different particle types and energies, fast response and ability to handle high counting rates. The detector used had a sensitive depth of 100 μm and a 0.3 cm diameter stainless steel collimator limited the active area exposed to the charged particles to 0.0706 cm^2. The front electrode was a thin 40 $\mu g\ cm^{-2}$ window of gold which had negligible effect on the energies of the particles being detected. The detector and holder could be rotated manually about the target centre. The detector was used in conjunction with an ORTEC 125 charge sensitive preamplifier which provides two isolated outputs. The output pulse had a rise time of about 20 ns and the pulse height was 10 mV per Mev deposited. An output of the preamplifier was connected to a spectroscopic amplifier (ORTEC 485) the resulting pulse heights were analysed on an ADC operating in the PHA mode.

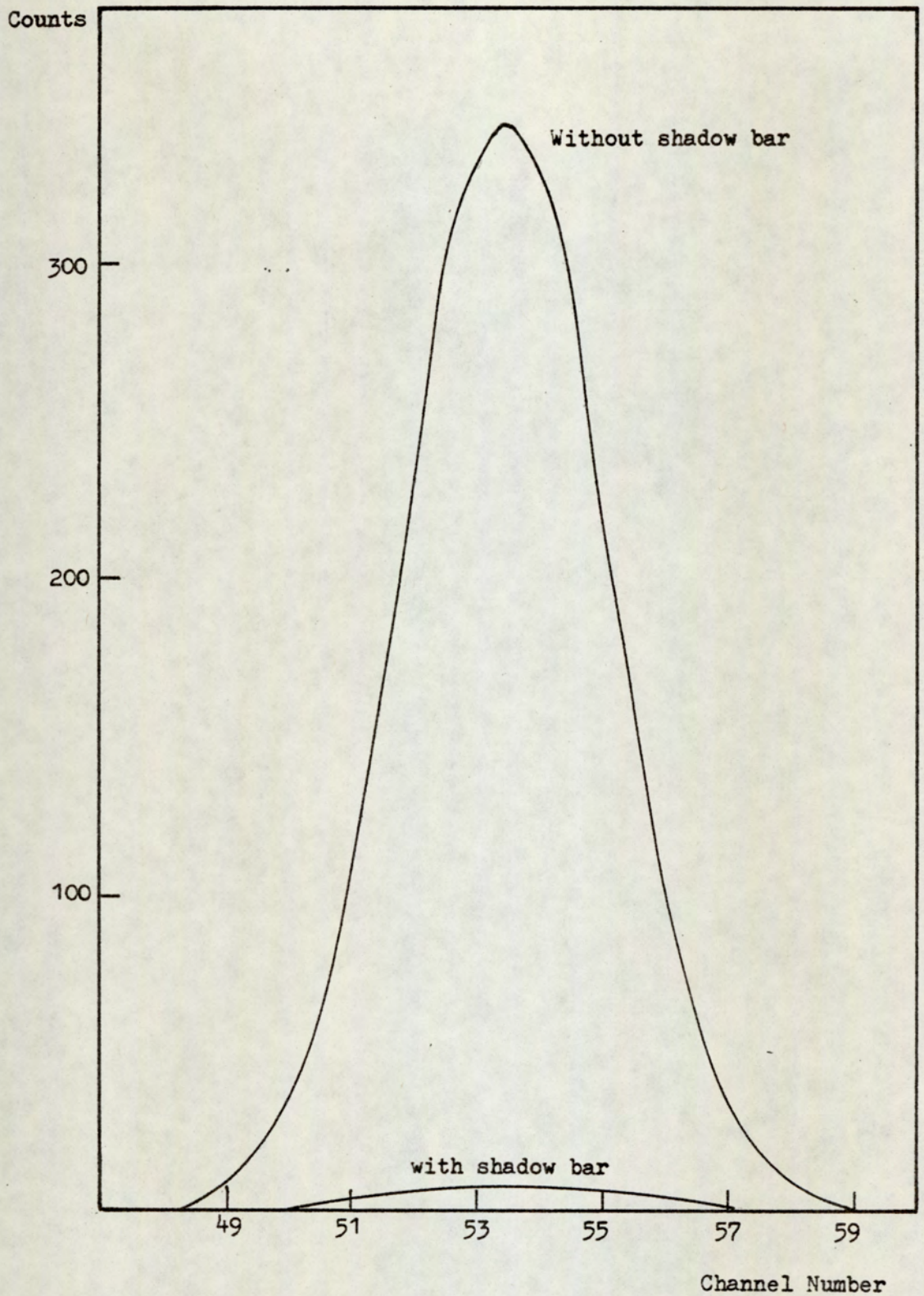

Figure 3.10 Efficiency of the shadow bar.

3.6.1 Energy Spectrum from CD_2 Targets

The energy spectrum obtained at 61.3°, with respect to the incident deuteron direction, for a 1 Mev deuteron incident on a 1.5 μm thick deuterated polyethylene target is shown in figure 3.11.

Analysis of the spectrum shows two high energy peaks. The 4.0 Mev peak is due to the detection of the proton from the $^{2}H(d,p)^{3}H$ reaction and the 3.4 Mev peak is due to a proton produced from deuteron interaction with carbon, $^{2}H(^{12}C,p)^{13}C$. In the lower energy group the triton peak is resolved, however the ^{3}He peak is situated on one of the high intensity peaks. This appears to be in contradiction to the energy spreads previously calculated for a 1.5μm target in section 2.4. However, no account was taken of the variation of ^{3}He energy with angle. The effect of this is to broaden the ^{3}He energy spread in figure 2.20 obtained as a result of the spread in energies of the interacting deuteron due to a finite target thickness.

Analysis of the low energy, high intensity region shows the presence of three resolvable peaks. The 0.18 Mev and 0.79 Mev peaks are due to deuterons elastically scattered from deuterium and carbon in the target. The peak at 0.41 Mev is attributed to the elastic scattering of a 0.5 Mev proton from carbon. The conditions required to transport a beam of 1 Mev mass I deuterons ($^{2}_{1}H^{+}$) are very similar to those for 1 Mev mass II proton ($^{2}_{2}H^{+}$) transport. A small amount of separation is achieved through the main accelerator bending magnets, but not sufficient to completely resolve the two beams at the target. A mass II proton undergoes dissociation in the thin target to form two mass I ($^{1}_{1}H^{+}$) protons which share the initial incident energy. The protons can then collide elastically with the carbon and deuterium content of the target, only the carbon

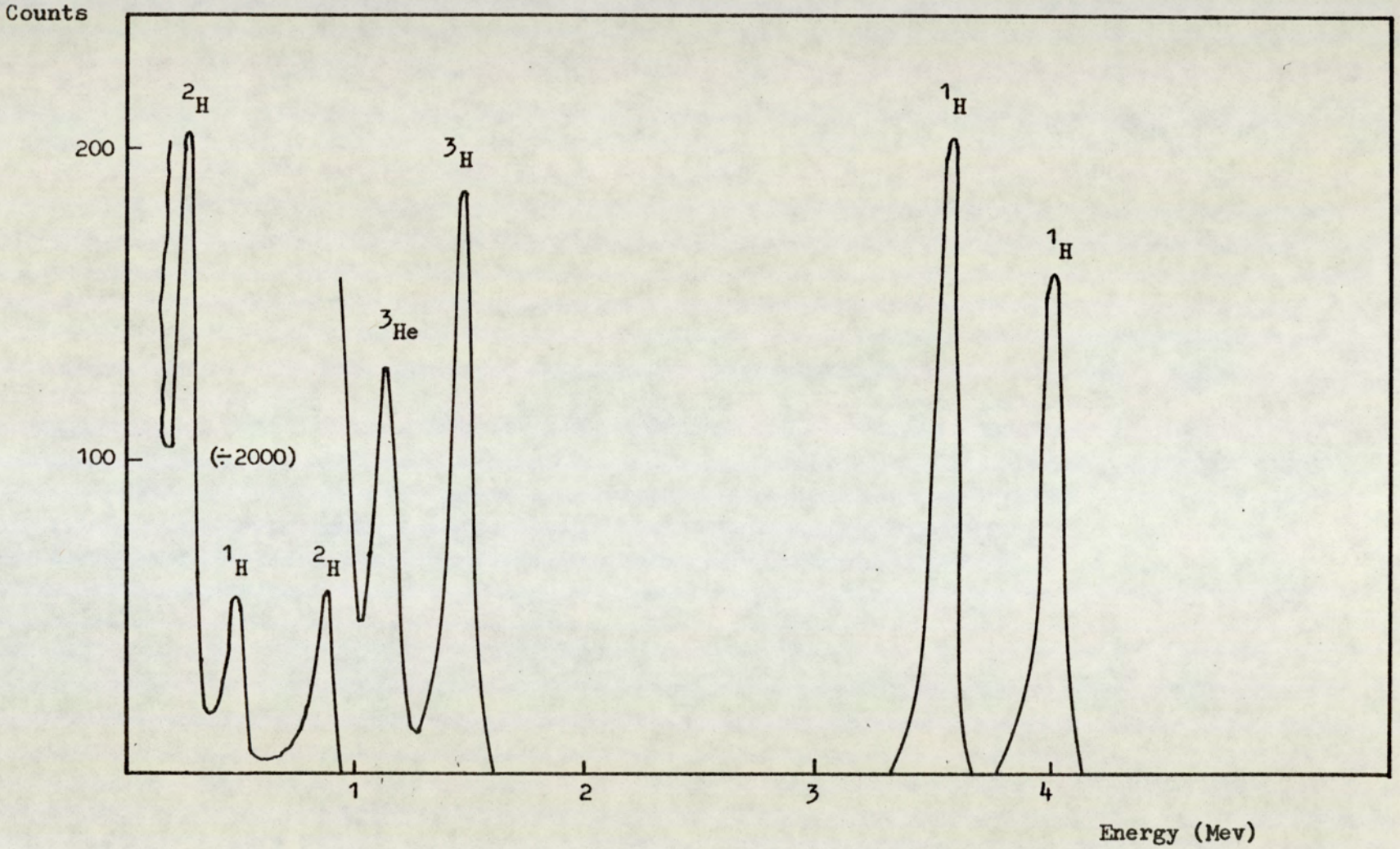

Figure 3.11 Energy spectrum for charged particle detection at 61.3°.

collisions are observed as elastic scattering with deuterium yields a low energy proton, which is unresolvable from electronic noise. The peak at 0.41 Mev is usually very prominent if the source has just been switched on indicating a high level of hydrogen impurity. The current monitored on the Faraday cup was the integrated sum of both the deuteron and proton contents of the incident beam, this therefore gave a false reading of the actual deuteron current. It was noted that the ratio of protons to deuterons decreased with increasing time the source was left on. This was attributed to the gradual removal of the hydrogen impurity in the extracted beam.

Figure 3.12 shows the energy spectrum obtained for charged particle detection at 31.2°, the incident beam energy was 1 Mev. The peaks exhibit the expected shift due to the different kinematic conditions. The ^{3}He peak due to its high energy (2.1 Mev) is shown to be well resolved from the low energy scattered deuteron peaks.

The resolution of the ^{3}He peak was important so that the pulses derived from the detection system could be used directly, to monitor the neutron yield and for timing purposes.

3.7 Neutron Yield Monitoring

As the charged particle detector is 100% efficient, for charged particle detection at 31.2° the number of ^{3}He ions detected gave the neutron yield incident onto the scattering sample. However, analysis of the energy spectrum obtained at a charged particle detector position of 61.3° (figure 3.11) shows the ^{3}He peak situated on a large deuteron background. As no discrimination against these deuterons was possible they were recorded as part of the count rate for the associated particles, this gives rise to an error in the neutron yield. Estimating and removing this deuteron background would produce a high uncertainty in the yield value. In order to

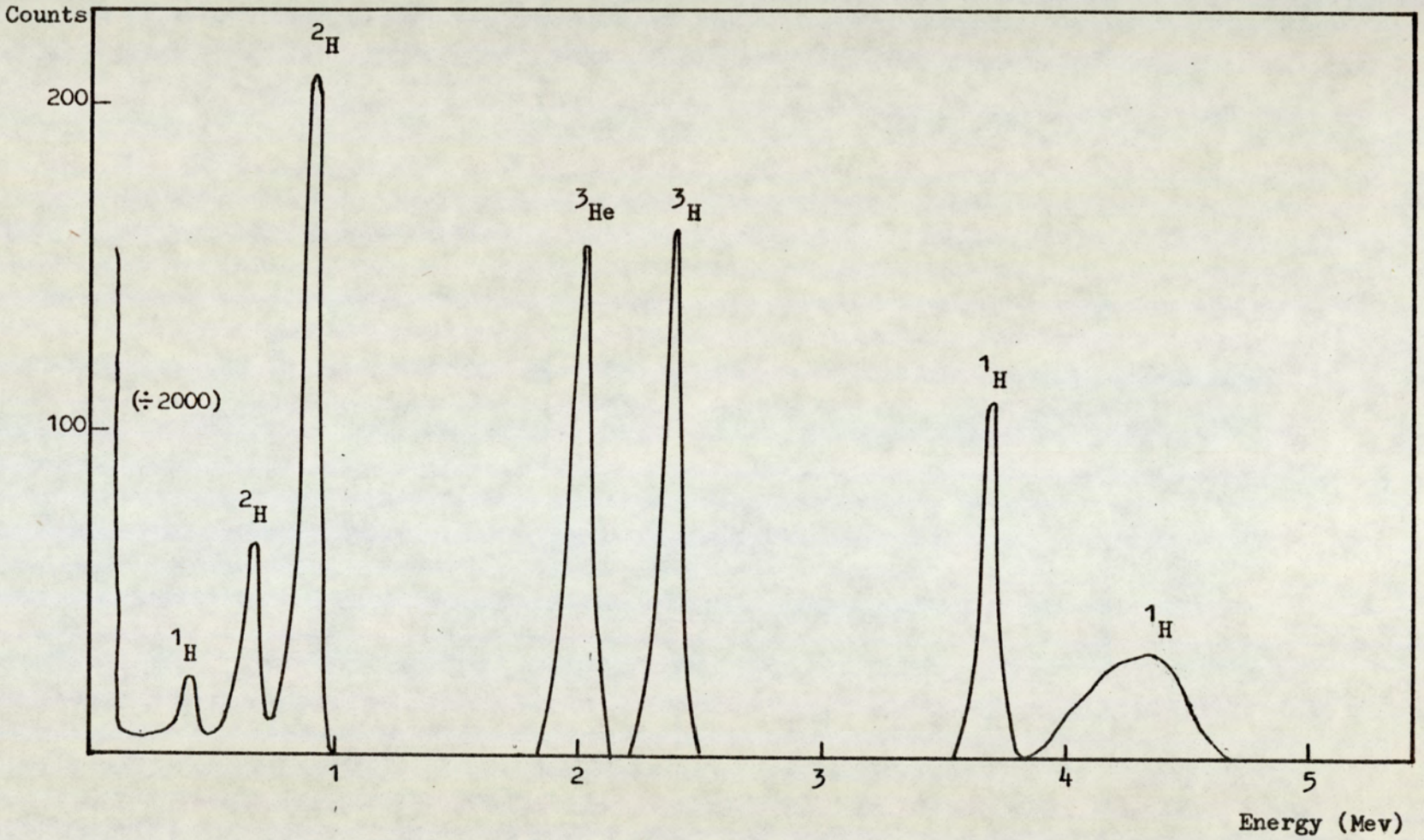

Figure 3.12 Energy spectrum for charged particle detection at 31.2°.

resolve completely the ^{3}He peak the target thickness or charged particle detector collimation would have to be reduced, the neutron yield would therefore be correspondingly smaller.

An alternative method for determining the integrated ^{3}He count unambiguously is to consider the competing ^{2}H(d,p)^{3}H reaction. Here the proton is of higher energy and is easily resolved from other neighbouring peaks. Knowledge of the respective reaction cross-sections enabled the proton yield to be related to the ^{3}He yield. This is considered in the next section.

3.7.1 Proton and ^{3}He Yields

The number of reactions N in the laboratory system per unit solid angle due to a deuteron which can interact between the energy of E and E + dE is given by:-

$$N(E)\,dE = n_t\,dx \left(\frac{d\sigma}{dw}\right)(E,w) \qquad \ldots\ldots 3.16$$

where n_t is the number of deuterium nuclei per cm^3 in the target and $d\sigma/dw$ is the laboratory differential cross-section which is a function of deuteron energy E and laboratory angle w.

Considering the number of reactions in the solid angle between w and w + dw subtended by the detector and rewriting equation 3.16, the yield at an energy E can be expressed as:-

$$N(E)\,dw = n_t \left[\frac{d\sigma}{dw}(E,w) \Big/ \frac{dE}{dx}(E) \right] dw \qquad \ldots\ldots 3.17$$

The ratio of the number of protons detected to ^{3}He particles at an energy E is given by:-

$$\frac{Np(E)dwp}{N_{^3He}(E)dw_{^3He}} = \frac{n_t\,[(d\sigma/dw)p(E,w)/(dE/dx)(E)]\,dwp}{n_t\,[(d\sigma/dw)_{^3He}(E,w)/(dE/dx)(E)]dw_{^3He}} \qquad \ldots\ldots 3.18$$

As the ^{3}He and protons are recorded in the same detector it is seen that:-

$$dwp = dw_{^{3}He} = dw \qquad \ldots\ldots 3.19$$

The ratio for the yields per deuteron between the energy range of E and E+dE and over the angular range of w and w+dw is given by:-

$$\frac{Y_p}{Y_{^{3}He}} = \frac{\int_{E}^{E+dE}\int_{w}^{w+dw}\left[\left(\frac{d\sigma}{dw}\right)_p (E,w) \Big/ \frac{dE}{dx}(E)\right] dw\,dE}{\int_{E}^{E+dE}\int_{w}^{w+dw}\left[\left(\frac{d\sigma}{dw}\right)_{^{3}He} (E,w) \Big/ \frac{dE}{dx}(E)\right] dw\,dE} \qquad \ldots\ldots 3.20$$

The centre of mass differential cross-sections for the $^{2}H(d,n)^{3}He$ reaction were obtained by substituting total cross-section and Legendre coefficient values from figures 2.11 and 2.12 into equation 2.11. The calculation was performed for the charged particle detector angle of $61.3^{o} \pm 5^{o}$ between the incident deuteron energy limits of 1 Mev and 0.87 Mev.

For the $^{2}H(d,p)^{3}H$ reaction no complete data sets were available, analysis of published values showed an absence of data over the energy range of 1 Mev to 0.87 Mev for the incident deuteron. Figure 3.13 shows the legendre coefficients obtained by Theus et al[48], Schulte et al[49], Brolley et al[50] and Wenzel et al[51]. In figure 3.14 the total cross-sections measurements of Tuck[52], Preston et al[53] and Ganeev et al[54] are shown. Intermediate values around 1 Mev were obtained from the curves drawn through the data points. The centre of mass differential cross-sections were calculated using the method described for the $^{2}H(d,n)^{3}He$ reaction. The centre of mass values for both reactions were converted to the laboratory system.

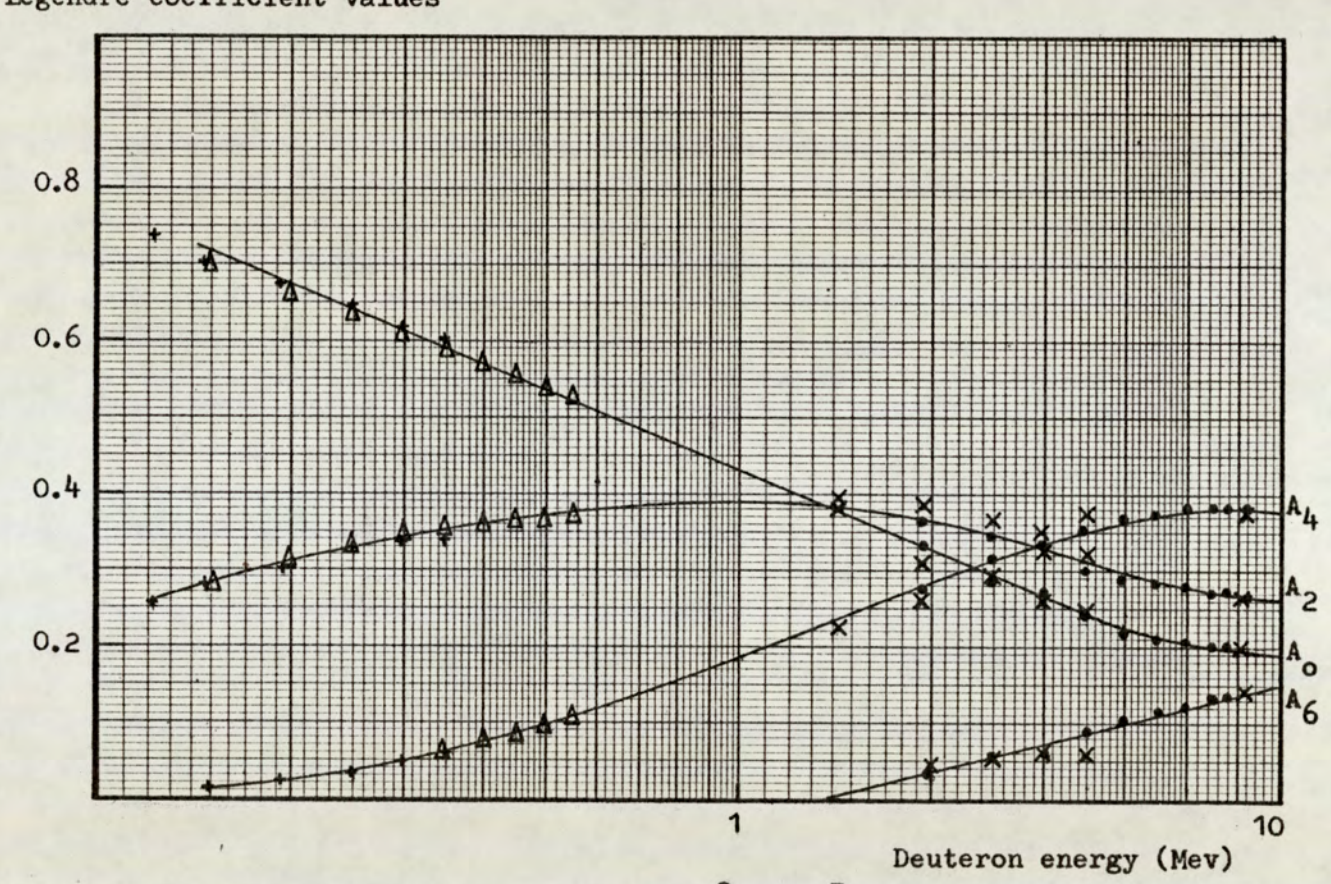

Figure 3.13 Legendre coefficients for the $^{2}H(d,p)^{3}H$ reaction.

References for experimental points: + (48); • (49); × (50); Δ (51)

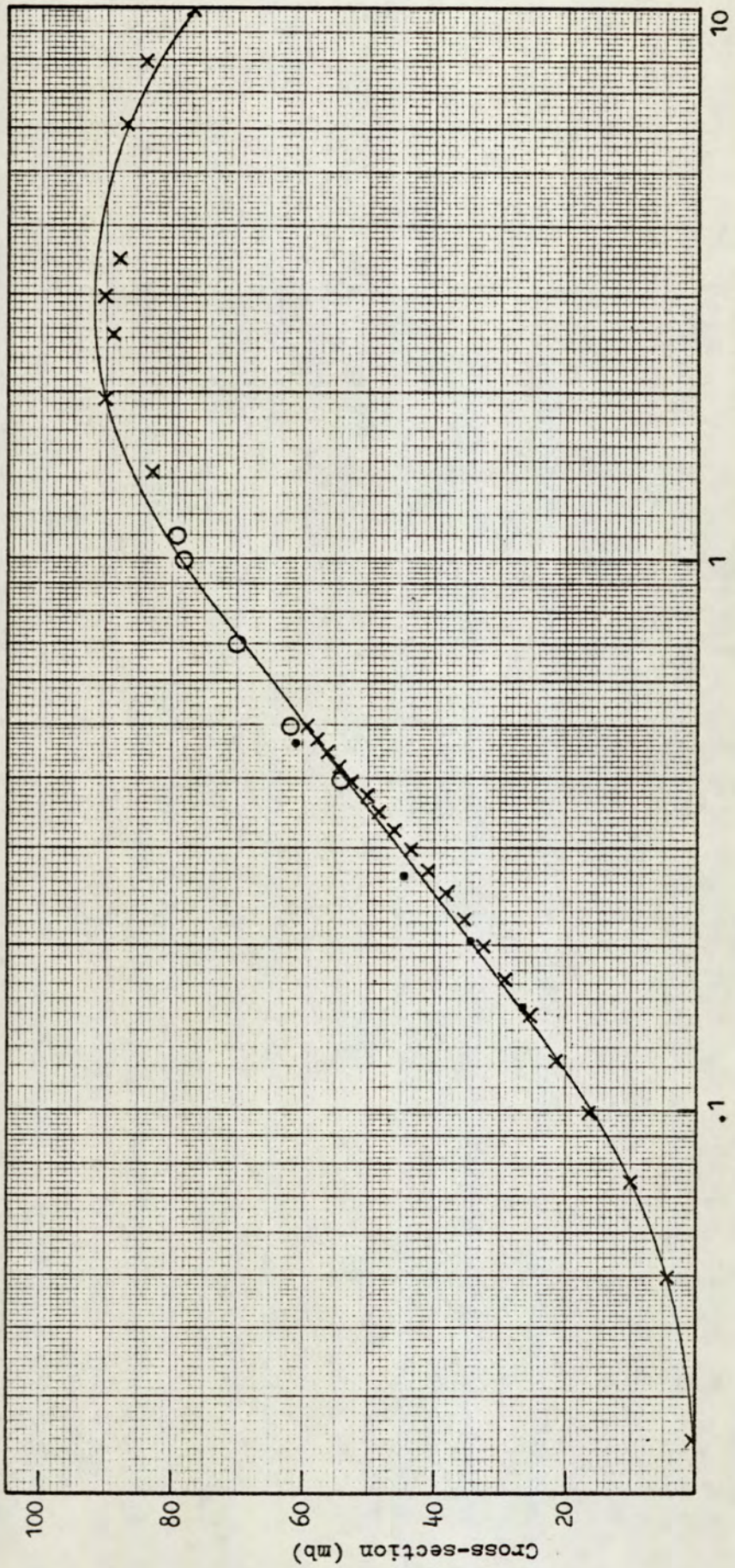

Figure 3.14 Total cross-section for the $^{2}H(d,p)^{3}H$ reaction.
References for experimental points: × (52); • (53); O (54)

The double integral in equation 3.20 was solved numerically. The function was integrated first over the angular range, the integration was repeated for different energy values, dE/dx is only a function of energy and was therefore constant for each energy considered. The values obtained were then integrated with respect to energy to give the yield value for the appropriate reaction and angular range.

For neutron production at 75°, with respect to the incident deuteron direction, the yield of ^{3}He was obtained from proton data by the relation:-

$$K = \frac{Y_p}{Y_{^3He}} = 0.711 \pm .004 \qquad \ldots\ldots 3.21$$

By using this relationship the monitored proton count can be used to measure the neutron yield produced.

CHAPTER 4

TIME-OF-FLIGHT ELECTRONICS

In order to measure the neutron flight times two timing signals are required, these relate to the instants of neutron production and detection. The instant of neutron production, "the zero time signal", is obtained when the associated ^{3}He particle is detected. The methods used for neutron and ^{3}He detection have been considered previously, the modes of obtaining the time signal from the resulting pulses are now discussed.

4.1 ^{3}He Electronics

The output pulses of the preamplifier, due to their low amplitude are unsuitable for directly using in either energy or timing applications and must be amplified and shaped for either application. For timing considerations a fast amplifier is preferable as this amplifies the signal and still retains the fast pulse rise time. An ORTEC 454 timing filter amplifier was used for this purpose.

The timing filter amplifier incorporated a variable gain control which ranged from x 2 to x 200. Also included were separately selectable integrate and differentiate time constants, the former was variable between 2 ns and 200 ns and the latter between 5 ns and 5 μs. In the present work the timing filter amplifier was operated on maximum gain, an integrate time constant of 2 ns was used as recommended for fast timing applications[55]. The differentiate time constant was set at 5μs as a compromise between the gain and signal to background ratio. The output was a negative pulse with a rise time $\leq$ 4.5 ns. A time signal was then obtained from these

pulses by employing a time pick-off system.

The type of time pick-off method in the present work was limited due to the high intensity of particles incident on the charged particle detector. Although thin targets enabled the detector to be exposed directly to the particles coming from the target, the resulting count rate was typically 10^6 - 10^7 counts/second for a beam current of 20 nA (as measured on a Faraday cup). The electronics used in measuring the flight times would accept a maximum count rate of about 10^5 counts/second. This criteria could be met by reducing the target current until the particle count rate was at an acceptable level but this would be at the expense of the neutron yield. A time pick-off system was investigated where the count rate could be reduced to the required level.

As the energy of the high intensity scattered deuteron particles are lower than the ^{3}He a discriminator can be employed such that only pulses with an amplitude over a certain level will generate a timing signal. The two basic types of discriminators considered, which provide timing signals from this method, were leading edge discriminators and constant fraction discriminators.

In leading edge discriminators a trigger circuit is operated when the front edge of anamplified detector signal reaches a predetermined level. A timing signal is generated only when a pulse has an amplitude higher than this level.

The problem inherent in using leading edge discriminators for time pick-off is that an electronic timing error known as "time walk" is introduced. This is due to the difference in triggering times caused by different amplitude pulses. Figure 4.1 illustrates this problem for leading edge pick-off.

This problem is particularly apparent when using signals which exhibit a large pulse height variation. To achieve satisfactory

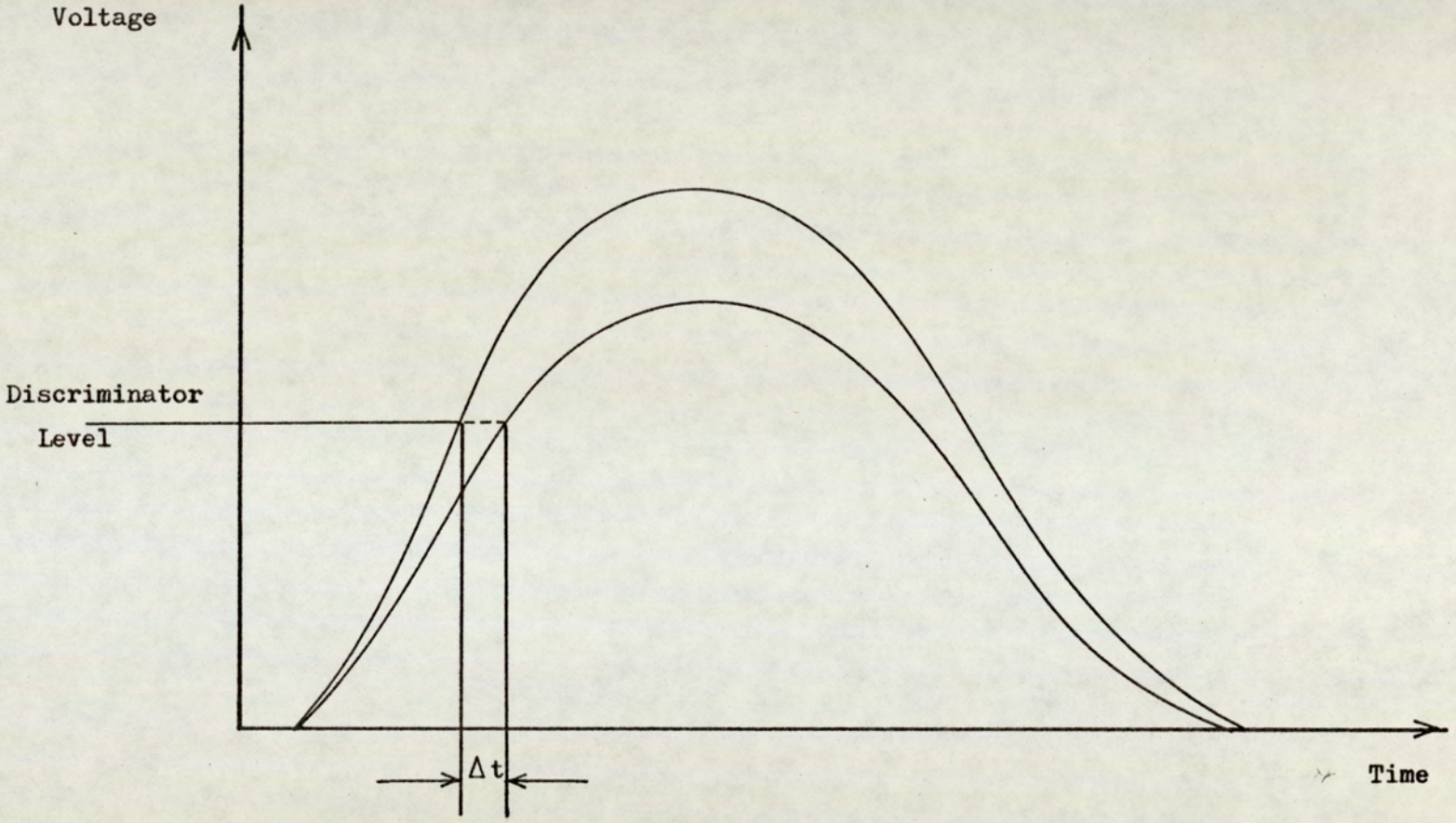

Figure 4.1 Illustration of "time walk"

timing, leading edge discriminators must be set to a very low level so that the walk is kept to a minimum. If the discriminator is set too low the discriminator will trigger on noise.

Constant fraction discrimination automatically corrects for the effects of signal amplitude variation and better time resolution has been achieved using this method in comparison to leading edge discrimination[56][57][58]. In this type of time pick-off system the input signal is divided into two, one of the signals is then delayed, attenuated and inverted. This signal is then added to the original input signal and at the point of zero cross-over a time signal is generated. The zero cross-over point is ideally independent of pulse amplitude.

In the present system an ORTEC 463 constant fraction discriminator was used due to the better timing properties offered by this system. The module incorporated a lower level discriminator which was used to reject pulses below a certain amplitude. The unit furnished three output pulses; two of these were fast negative logic signals with an amplitude of - 0.8v into 50 Ω cable; the third was a slow positive logic signal with an amplitude of +5v, and was compatible with the input of most scalers.

4.2 Neutron Electronics

The output pulse from the anode of the neutron detector photomultiplier was connected to the screened coaxial signal cable through an emitter follower, this provided suitable current drive and matching into the 50 ohm coaxial line. The resulting output was then fed into an ORTEC 436 100 MHz discriminator which provided two fast negative logic signals. The module incorporated a discriminator.

The discriminator level was set by observing the count rate in the neutron line from a ^{133}Ba gamma ray source as a function of

discriminator level, the differential count rate was then obtained by calculating the difference in count rate between each discriminator setting. The discriminator level corresponding to the Compton edge was taken as the point at which the differential count rate fell to half its value[59].

4.3 Time Measurements

Time measurements in the nano-second region are normally accomplished by converting the elapsed time into a voltage. The amplitude of the voltage pulse is then a direct measure of the elapsed time. The voltage is then analysed using a multi-channel pulse height analyser and the elapsed time measured in terms of time/analyser channel. A N.E. 4670 time to amplitude converter was used to generate a pulse whose amplitude was proportional to the time delay between the START and STOP pulses. The two pulses required were supplied by the fast timing logic signals obtained from the neutron and ^{3}He electronics. The N.E. 4670 manufactured by Nuclear Enterprises had variable time conversion ranges which could be varied between 0-50 ns to 0-200 μs, the output provided ranged from 0 to $\pm$ 10v (depending on output polarity required).

Once the time converter is initiated by a START pulse the system is busy and cannot respond to further input pulses. The system remains busy until either a STOP pulse is received or the elapsed time exceeds the time converter range. The dead time of the converter for the latter case is equivalent to the range limit plus the output pulse width i.e. 5 μs. Typically, for a 2 μs conversion range the maximum dead time will be 7 μs, which is consistent with a maximum count rate of 1.4×10^{5} counts/second.

To limit the dead time of the converter the channel with the lowest count rate was used as the START input, this corresponded to

the neutron signal (200 counts/second). The timing signal generated by the constant fraction discriminator was used as the STOP input. A block diagram of the electronics is shown in figure 4.2.

An important feature in the time-of-flight studies is the linearity of the time converter. The most useful linearity test is that of the differential linearity. This was accomplished by providing two randomly related time events to the neutron and ^{3}He electronics. The two random time events were simulated by pulsing the timing filter amplifier with a suitably shaped pulse from an ORTEC 448 research pulser, this provided a signal frequency of 200 Hz. An Am/Be neutron source was used to generate random time signals from the neutron detector, the source was placed at a distance from the detector in order to limit the count rate. Since the two signals are randomly related in time an equal number of counts are expected in each analyser channel. The differential linearity is then given by $\Delta N/N \times 100\%$ where N is the average counts per channel and ΔN is the fluctuation (other than statistical) about the mean. The differential linearity was tested on the 0-1 μs, 0-2 μs and 0-5 μs ranges and was found to be $< \pm 5\%$ on these ranges. This was considered acceptable for the present work.

4.4 ^{3}He Discrimination Level

In setting a discrimination level on the constant fraction discriminator to reject most of the deuteron pulses extreme difficulty was encountered. A discrimination level was required which would eliminate the deuteron pulses, hence reduce the count rate into the STOP input of the time converter, yet still allow the ^{3}He pulses to generate a time signal.

In the timing filter amplifier the fast pulse rise time was obtained at the expense of the gain. The resulting pulses had a very

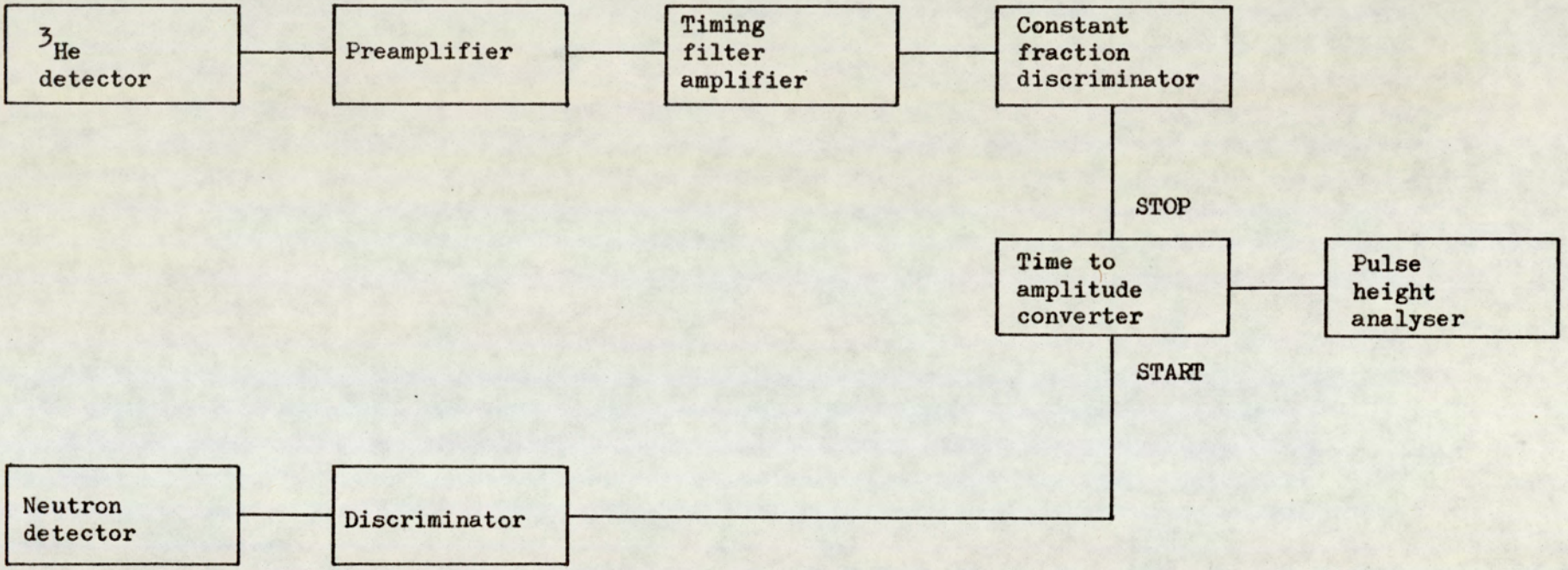

Figure 4.2 Block diagram of time-of-flight electronics employing constant fraction discrimination.

low amplitude and therefore there was poor amplitude resolution between the ^{3}He and deuteron pulses. It was found that in order to allow all time signals generated by the ^{3}He pulses into the time converter the resulting count rate in the STOP channel was about 10^5 counts/second. Any attempt to observe the time spectrum on a pulse height analyser resulted in a random time spectrum. The random electronic coincidence between pulses produced in the neutron detector due to background and events in the charged particle electronics outnumbered the true electronic coincidences between neutrons and associated ^{3}He particles.

For a system employing two detectors the random coincidence rate per analyser channel is:-

$$C = N_1 N_2 t$$

where N_1 = count rate in neutron detector

N_2 = count rate in ^{3}He detector

t = resolving time/analyser channel

The differential linearity was studied when a signal frequency of 0.1 MHz was applied to the STOP input of the time converter through the timing filter amplifier. A neutron count rate of 150 - 200 counts/second was maintained in the START input. The resulting linearity was found to be $> \pm$ 25%.

In an attempt to reduce the count rate in the charged particle electronics leading edge discrimination was investigated.

4.5 Leading Edge Discrimination

To overcome the problem of poor amplitude resolution a spectroscopic amplifier (ORTEC 485) was used in conjunction with the timing filter amplifier. The latter was used to extend the gain of the preamplifier and still retain the fast pulse rise time to limit

"time walk", the resulting pulses were amplified further by the spectroscopic amplifier. The ORTEC 485 module, which can be used with either negative or positive input pulses has a variable gain, ranging from x6 to x640, and either bipolar or unipolar output pulses can be selected. In the present work the bipolar output mode was used and it was possible to observe the pulse height spectrum on a multi-channel pulse height analyser. The gain of the spectroscopic amplifier was adjusted until the ^{3}He and ^{3}H pulses were resolved, the ^{3}He peak was then partially resolved from the overlapping deuteron peak. A timing single channel analyser (ORTEC 420A) was used to set an electronic window across the ^{3}He peak.

A pulse generator was connected to the input of the timing filter amplifier, replacing the preamplifier input. By observing the position of the pulser peak superimposed on the energy spectrum the voltage level for the upper limit of the discrimination level was obtained. For charged particle detection at 61.3°, with respect to the incident beam direction, the lower discrimination level was estimated. By using this method the count rate in the ^{3}He channel was limited to about 150 counts/second. For charged particle detection at 31.2° the lower level of the discriminator could be easily measured as the ^{3}He peak was well resolved from the scattered deuterons. The count rate for this angle was about 10 counts/second in the ^{3}He channel. Due to this lower count rate for both angles of charged particle detection, the ^{3}He channel was used as the START input of the time converter. The START input was derived from the fast negative logic pulse generated by the timing single channel analyser, a slow positive logic pulse was also generated at the same time. A delay was incorporated into the neutron line to allow the neutron time signals to arrive within the time converter output range, this was necessary because of the large delay introduced in

the ^{3}He electronics by the spectroscopic amplifier. A block diagram of the electronics is shown in figure 4.3.

The relevant neutron yield monitoring systems are also shown in figure 4.3. For charged particle detection at 31.2° the positive output pulses from the timing single channel analyser were counted on a scalar, this was then used as a measure of the neutron yield. For charged particle detection at 61.3° the ^{3}He peak was only partially resolved and the protons from the ^{2}H(d,p)^{3}H reaction were used to monitor the neutron yield. To achieve this a separate output was used from the preamplifier and the pulses amplified using an ORTEC 485 spectroscopic amplifier the gain of which was adjusted until the two high energy proton peaks were resolved. A timing single channel analyser was used to set an electronic window across the appropriate proton peak, the positive output pulses were counted on a scaler.

4.6 Spectrometer Performance

The absolute time resolution of the spectrometer was tested by observing the direct neutron beams at 75° and 120°, with respect to the incident deuteron beam direction. The time spectra obtained for these two neutron production angles are shown in figures 4.4 and 4.5. The f.w.h.m. of the spectra are 65 ns at 75° and 31.4 ns for 120°

The ideal time spectrum should be a line spectrum, but because of timing uncertainties introduced in the detecting and production processes the spectrum will consist of several sources of time uncertainties folded together. For neutron emission at 75° the ^{3}He particles can have energies between 1.4 Mev and 0.75 Mev, this spread is introduced due to the angular acceptance of the charged particle detector and the production of ^{3}He particles by interacting deuterons with energies between 1 Mev and 0.87 Mev.

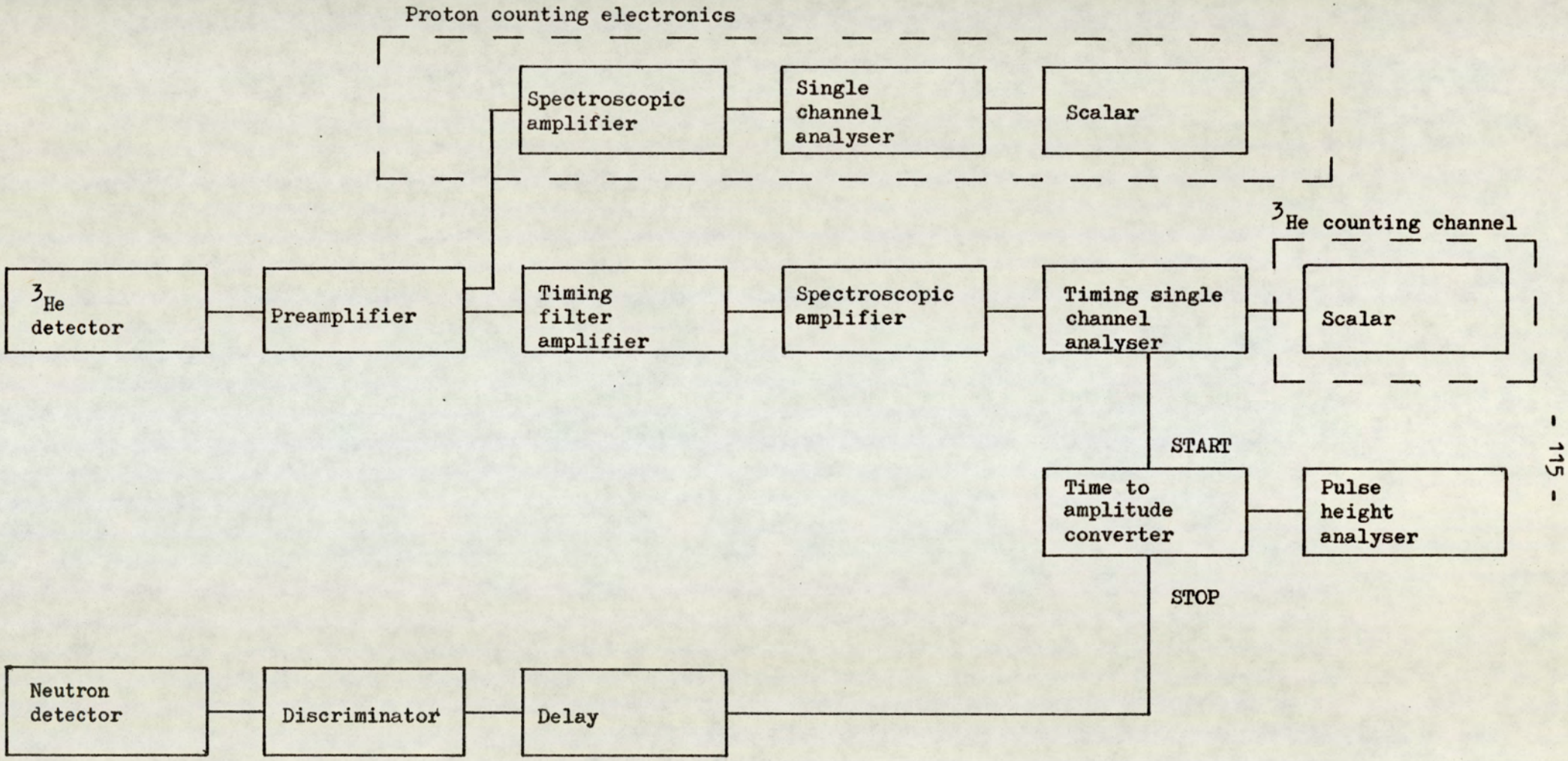

Figure 4.3 Block diagram of time-of-flight electronics employing leading edge time pick-off.

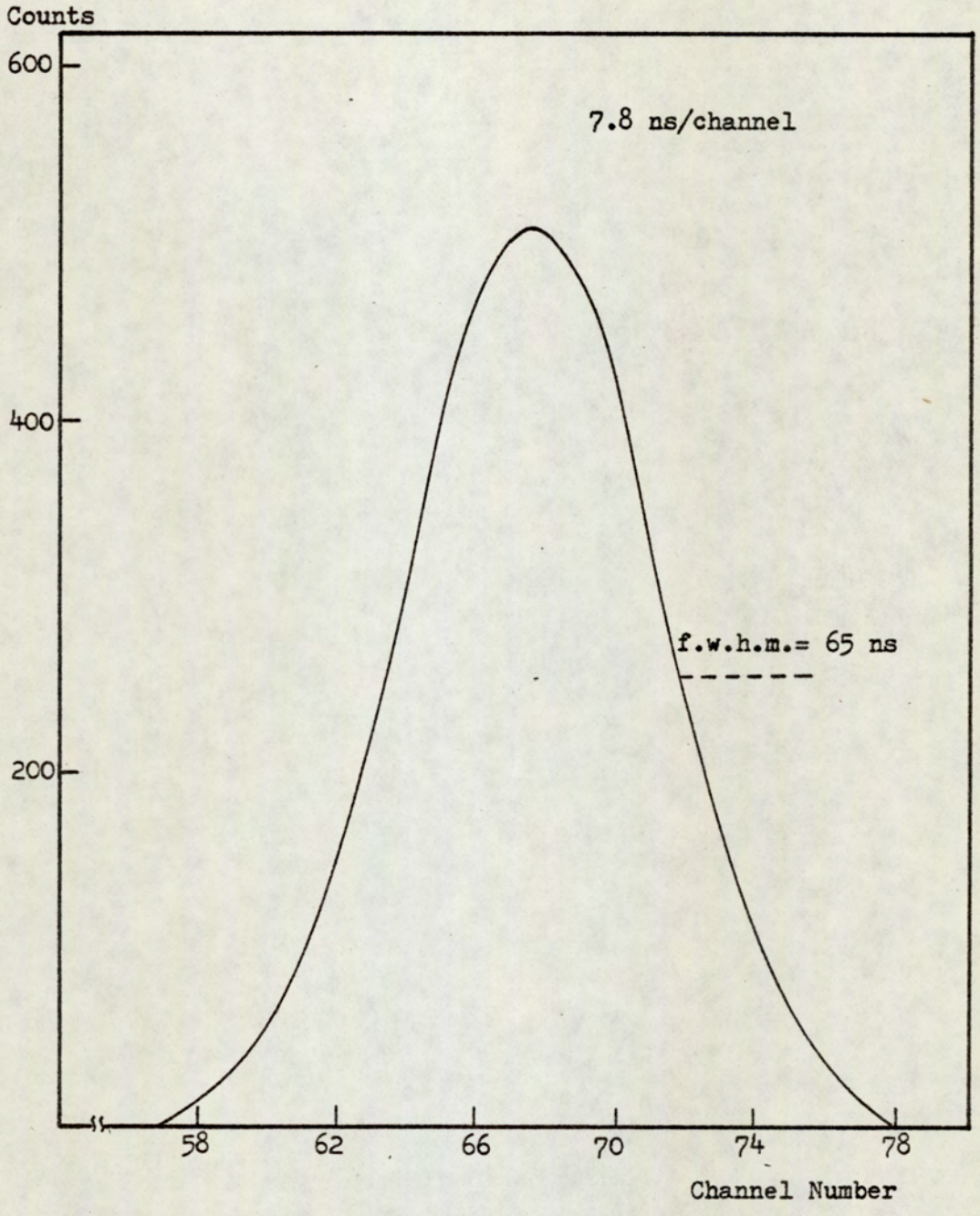

Figure 4.4 Spectrometer resolution for neutron production at 75°.

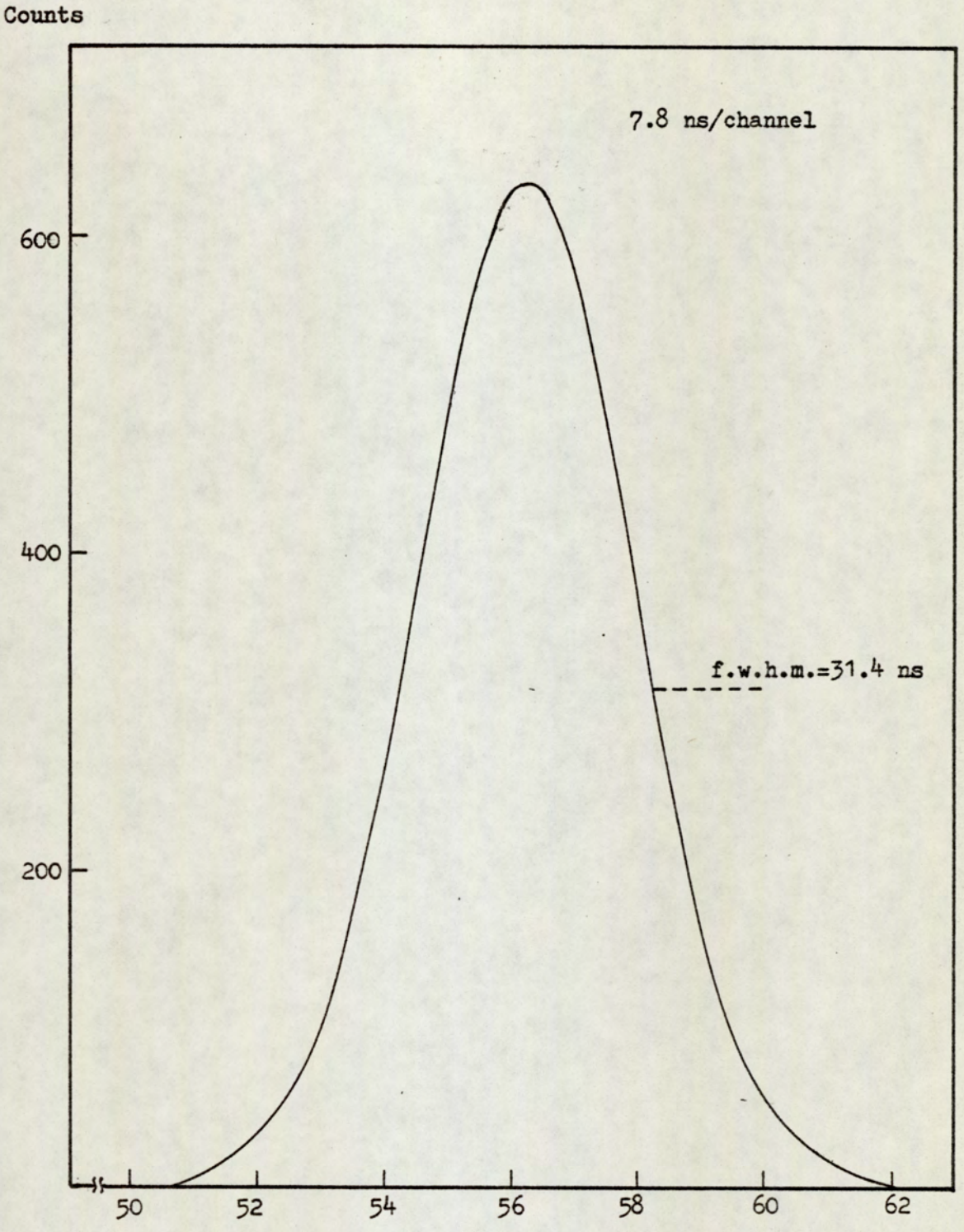

Figure 4.5 Spectrometer resolution for neutron production at 120°.

The energy spread of the ^{3}He particles contributes a transit time spread of 2.2 ns. The transit time spread due to the neutron energy spread is 2 ns. The time uncertainties introduced by the 5 cm thick scintillator and photomultiplier tube used for neutron detection are 2.5 ns and 0.5 ns respectively. In the silicon surface barrier detector the collection time for the charged carriers is dependent on their velocity in the detecting medium i.e. about 10^{7} cm/sec in the present case, for a 100 μm depletion depth this corresponds to a maximum collection time of 1 ns.

The resolving time expressed as f.w.h.m. (full width at half maximum) is given by the square root of the sum of the squares of the individual timing uncertainties. For neutron production at 75^{o} the theoretical resolution (f.w.h.m.) is 5 ns. The difference between the measured and calculated resolution of the time spectrum was attributed to "time walk" introduced in using the leading edge time pick-off technique.

CHAPTER 5

ASSOCIATED PARTICLE TIME-OF-FLIGHT SYSTEM AT INCIDENT DEUTERON ENERGIES OF 130 Kev

A study was carried out to determine the feasibility of establishing a time-of-flight system using the associated particle technique for the $^{2}H(d,n)^{3}He$ reaction at lower incident deuteron energies. Deuterons of 130 Kev were obtained from a S.A.M.E.S. type 'J' accelerator which was located at the University of Aston in Birmingham.

5.1 The S.A.M.E.S. Accelerator

The voltage to accelerate the deuteron beam was furnished by an electrostatic generator hermetically sealed in an hydrogen atmosphere. The accelerating voltage was continuously variable from 0-160 Kv and a voltage stability of better than $\pm$ 1% at 150 Kv was quoted by the manufacturers. The ion source, excited by a 100 MHz oscillator was supplied with deuterium through a thermally activated palladium leak. The ions were extracted by a potential variable from 0 to + 6 Kv and the maximum output current from the ion source was 600 μA. An oil-immersed Cockroft-Walton generator supplied a 0-45 Kv focussing potential. The accelerator is shown in figure 5.1.

After acceleration the deuterons passed down a 5m long beam tube, this required an additional pumping stage to maintain a pressure of less than 10^{-5} torr at the target assembly. Additional beam focussing was required due to the length of the beam tube. This was accomplished by a pair of electrostatic quadrupole lenses[18].

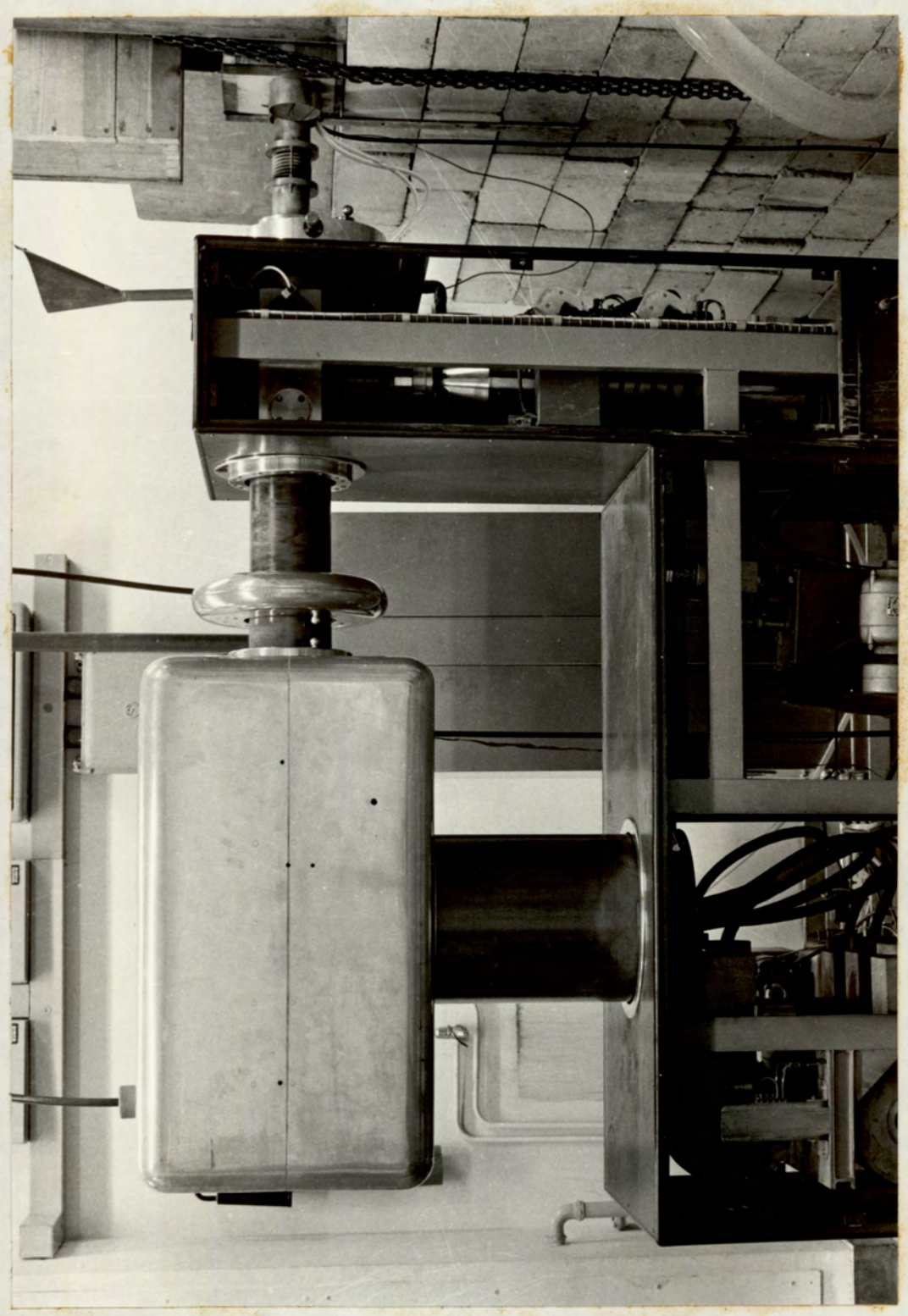

Figure 5.1 The S.A.M.E.S. Accelerator

5.2 Target Considerations

As considered in Section 2.2, in applying the $^{2}H(d,n)^{3}He$ reaction at lower deuteron energies (< 300 Kev) the energy of the ^{3}He produced is higher than the maximum energy of the scattered deuteron. However, the problem of a high intensity of scattered deuterons produced at the target is still apparent. The cross-sections for the $^{2}H(d,n)^{3}He$ and $^{2}H(d,p)^{3}H$ reactions are comparable, as was the case for 1 Mev incident deuterons, also the energy of the ^{3}He and ^{3}H particles are similar.

The method employed in the present work to reduce the scattered deuteron intensity was to use low mass targets. Deuterated polyethylene targets were used for this purpose. It has also been found that at these lower deuteron energies the scattered deuteron intensity can be reduced further by detecting the ^{3}He particles at backward angles[23] i.e. angles greater than 90° with respect to the incident deuteron direction. The detection of the ^{3}He at backward angles is possible as the ^{3}He energy does not decrease as rapidly with increasing detection angle as at higher deuteron energies (>1 Mev), this is shown in figures 2.3 and 2.4. At backward angles the ^{3}He energy is still higher than the maximum energy of the scattered deuteron. Also for the specific case of deuteron-deuterium elastic scattering no deuterons can be scattered beyond 90°.

Due to limitations on the physical geometry of the system the detection of the charged particles was limited to angles $\leqslant 125^{\circ}$. In the present work the charged particles were detected at 125° with respect to the incident deuteron direction.

In order to minimise the distance traversed by the incident deuteron beam and charged particles produced in the target, the target surface should be normal to both incident beam and detector positions, however this cannot be realised experimentally.

Considering limitations imposed on the experimental system the target assembly was mounted at 68^{o} with respect to the incident beam direction, the target surface was then at 57^{o} to the charged particle detector position. The charged particles were detected on the same side of the target as the impinging incident deuteron beam. Figure 5.2 is a schematic representation of the detection of charged particles at 125^{o}.

With reference to figure 5.2 and considering a thin target element of thickness b, an incident deuteron of initial energy E_D after losing energy in traversing a distance x can interact with an energy E_D^1. The energy of the products at this point can be found from the kinematic relationships for an interacting deuteron energy of E_D^1. The charged particles produced will lose energy in traversing the target thickness r, and emerge with an energy E^1_{OUT}. The limits of the energy spread of charged particles are governed by E^1_{OUT} and E_{OUT}, where E_{OUT} is the energy of the charged particle produced by an interacting deuteron of energy E_D on the target surface.

The energy loss of deuterons, ^3He and ^3H in deuterated polyethylene have been considered in section 2.4 and their respective emergent energies were calculated for a thin target element. Figure 5.3 shows the resulting energy spreads of the ^3H, ^3He and scattered deuterons from carbon, in emerging from a target of increasing thickness. An incident deuteron of 130 Kev will lose all its energy in traversing a distance where x is $2\mu m$, this corresponds to a thickness of $1.85\mu m$. From figure 5.3 the ^3He and ^3H particles should be well resolved, for a target thick to the incident beam some of the ^3He particles will overlap in energy with scattered deuterons. Due to the requirement of high neutron yields thick targets were employed.

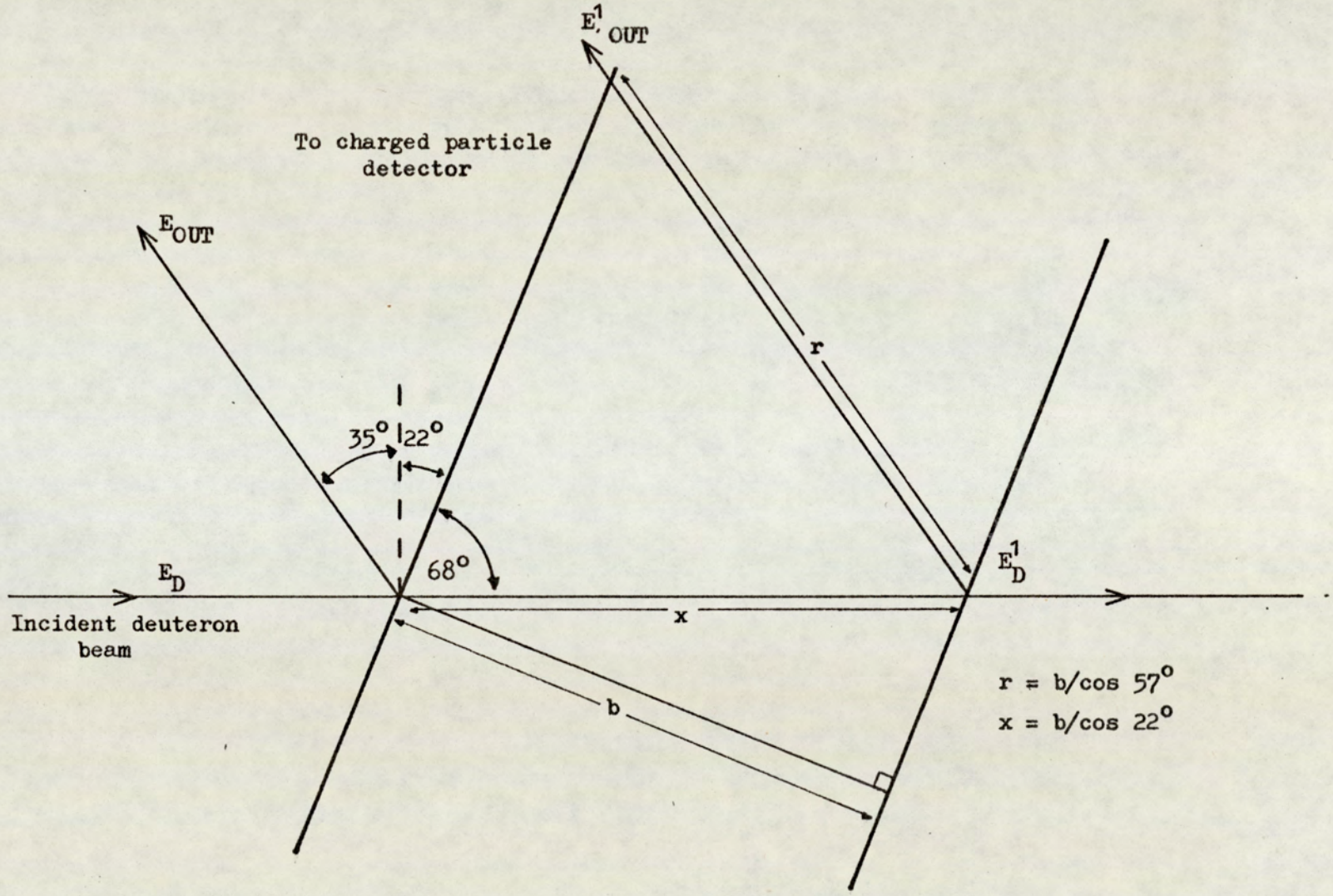

Figure 5.2 Schematic representation of charged particle detection at 125°.

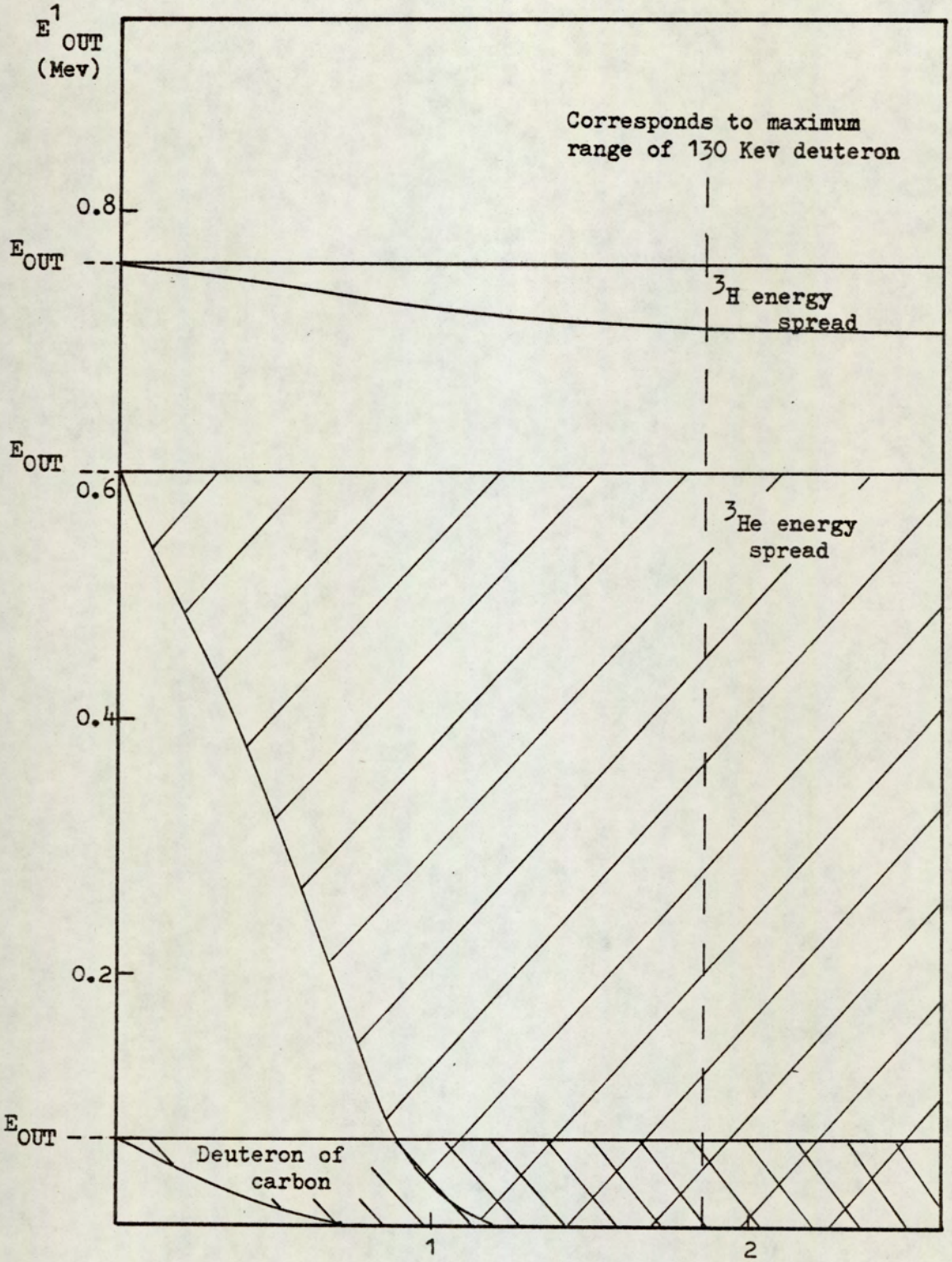

Figure 5.3 Energy spreads of ^3He, ^3H and deuterons scattered from carbon.

5.3 Angular Divergence of Neutron Beam

The relationship between the neutron and ^3He angles is shown in figure 5.4 for interacting deuteron energies between 130 Kev and 0 Kev. For the special case of E_D = 0 Kev the ^3He angle ζ and the neutron emission angle Ψ are related by:-

$$\zeta = 180 - \Psi \qquad \ldots\ldots 5.1$$

where the angles ζ and Ψ (laboratory system) are in degrees.

In the experimental arrangement the charged particle detector was collimated with a 7 mm circular aperature which was located 5 cm from the target centre, the angular divergence was $\pm 4^\circ$. From figure 5.4 a ^3He angle of $125 \pm 4^\circ$ defines a neutron angular spread extending from 37.4° to 59°.

In view of the variation of the cross-section of the $^2H(d,n)^3He$ reaction with incident deuteron energy, this is shown in figure 2.1 , the neutron yield will not be uniform over the angular range defined by the ^3He particle detector. This is illustrated in figure 5.4, i.e. at a neutron angle of 38.5° only neutrons with associated ^3He particles are produced by deuterons interacting with an energy between 130 Kev and 110 Kev while at 47° neutrons with associated ^3He particles are produced by dueterons interacting between 80 Kev and 10 Kev. In order to calculate the relative neutron yield over this defined angular range, 37.4° to 59°, the neutron yield was calculated as a function of incident deuteron energy.

5.4 Neutron Yield

For a target thick to the incident deuteron beam, the yield of neutrons per steradian per incident deuteron at a specific neutron angle Ψ is given by:-

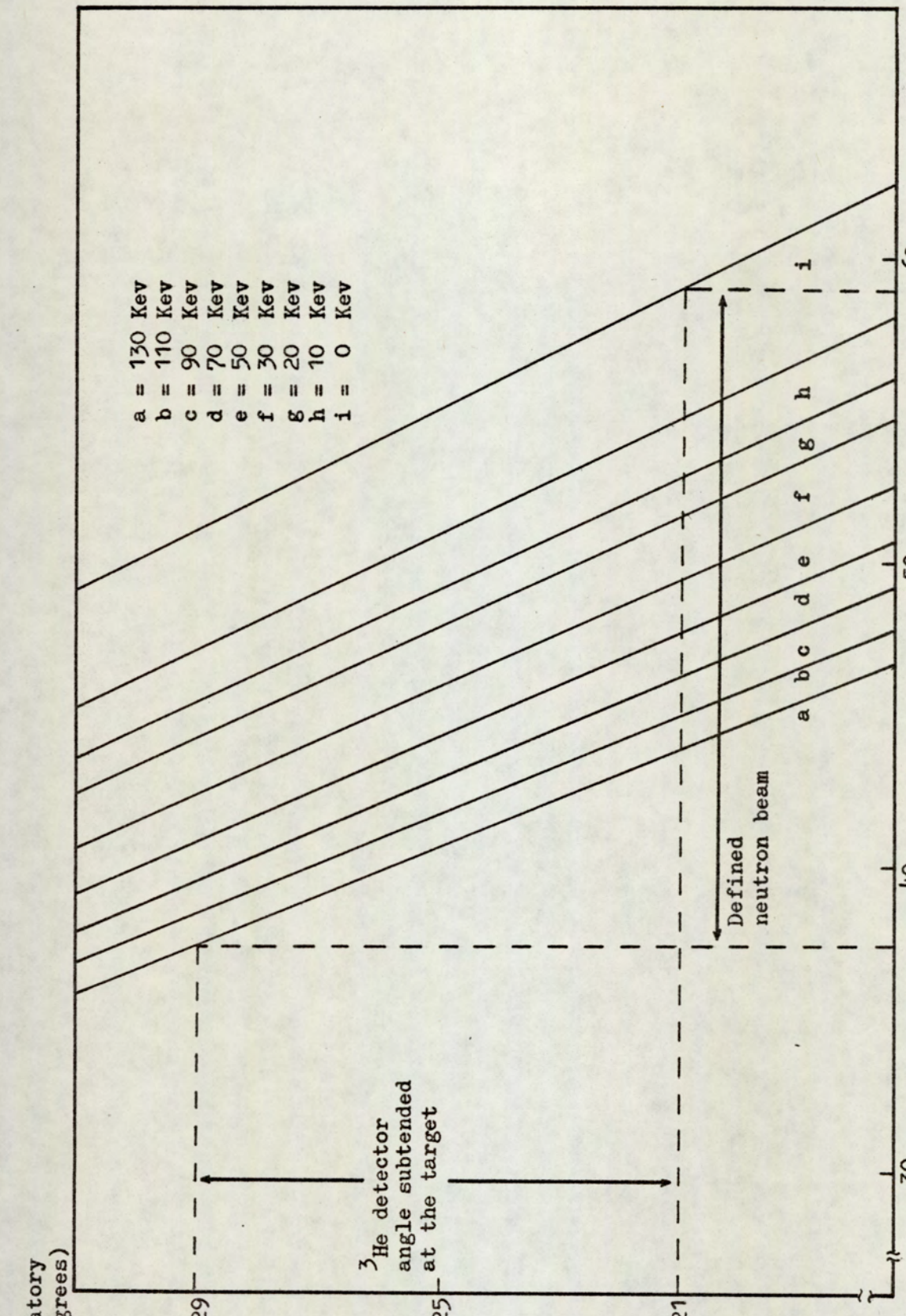

Figure 5.4 Related neutron and ^{3}He angles of emission.

$$Y = \frac{nd}{\rho} \int_{0}^{E_D} \frac{d\sigma/dw(E)}{dE/dx\,(E)}\, dE \qquad \ldots\ldots 5.2$$

where nd is the number of deuterium atoms per cm^3 in a target, ρ is the target density ($g\ cm^{-3}$), dE/dx is the energy loss in Mev $g^{-1}\ cm^2$ and $d\sigma/dw$ is the differential cross-section in units of barns/steradian.

The neutron yield was calculated for the mean neutron angle of the defined angular range i.e. 48°. The values under the integral were calculated for deuteron energies between 130 Kev and 0 Kev in 10 Kev steps, the results are shown in figure 5.5. This curve was then integrated from 0 Kev to 130 Kev to give the total neutron yield curve, figure 5.6.

By comparison of this neutron yield curve with that obtained for a 1 Mev incident deuteron energy, figures 2.15 and 2.16, the main disadvantage of operating at low incident deuteron energies can be realised. For a 130 Kev deuteron losing all its energy in the target the resulting neutron yield is typically 10 times lower than a 1 Mev deuteron interacting in a 2μm thin target.

5.5 Neutron Beam Profile

The neutron beam profile was calculated by considering the relative neutron yield at each neutron angle, Ψ. This was obtained by considering figures 5.4 and 5.5. From figure 5.4 it can be seen that at a neutron angle of 38.5° the emitted neutrons having detected ^{3}He particles are produced only by deuterons with an energy between 130 Kev to 110 Kev. From figure 5.5 the area under the curve in this energy interval i.e. 130 Kev to 110 Kev, is proportional to the neutron yield. This calculation was performed over the defined neutron angular range and this yielded the neutron

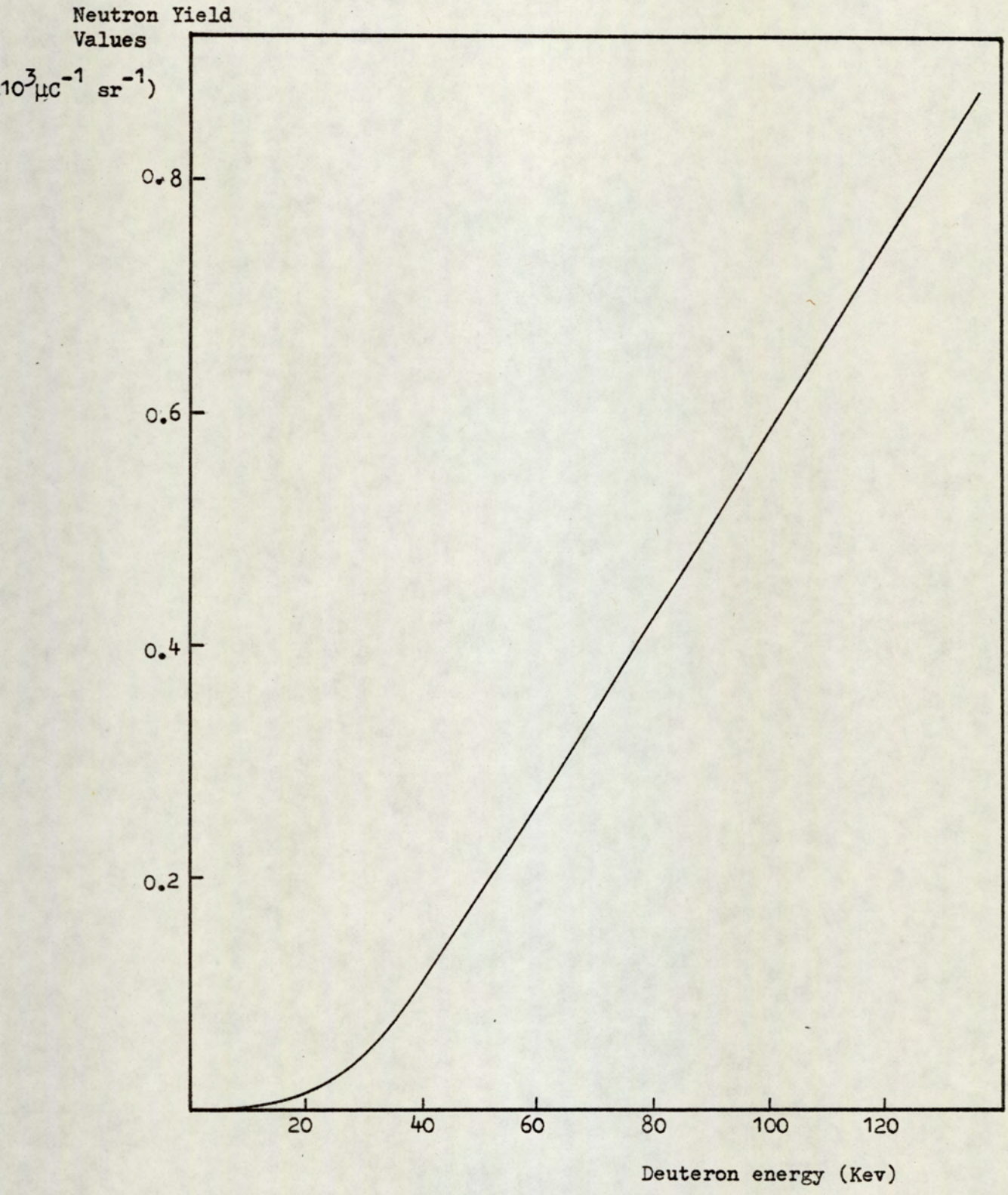

Figure 5.5 Neutron yield values v.s. deuteron energy.

- Thick target

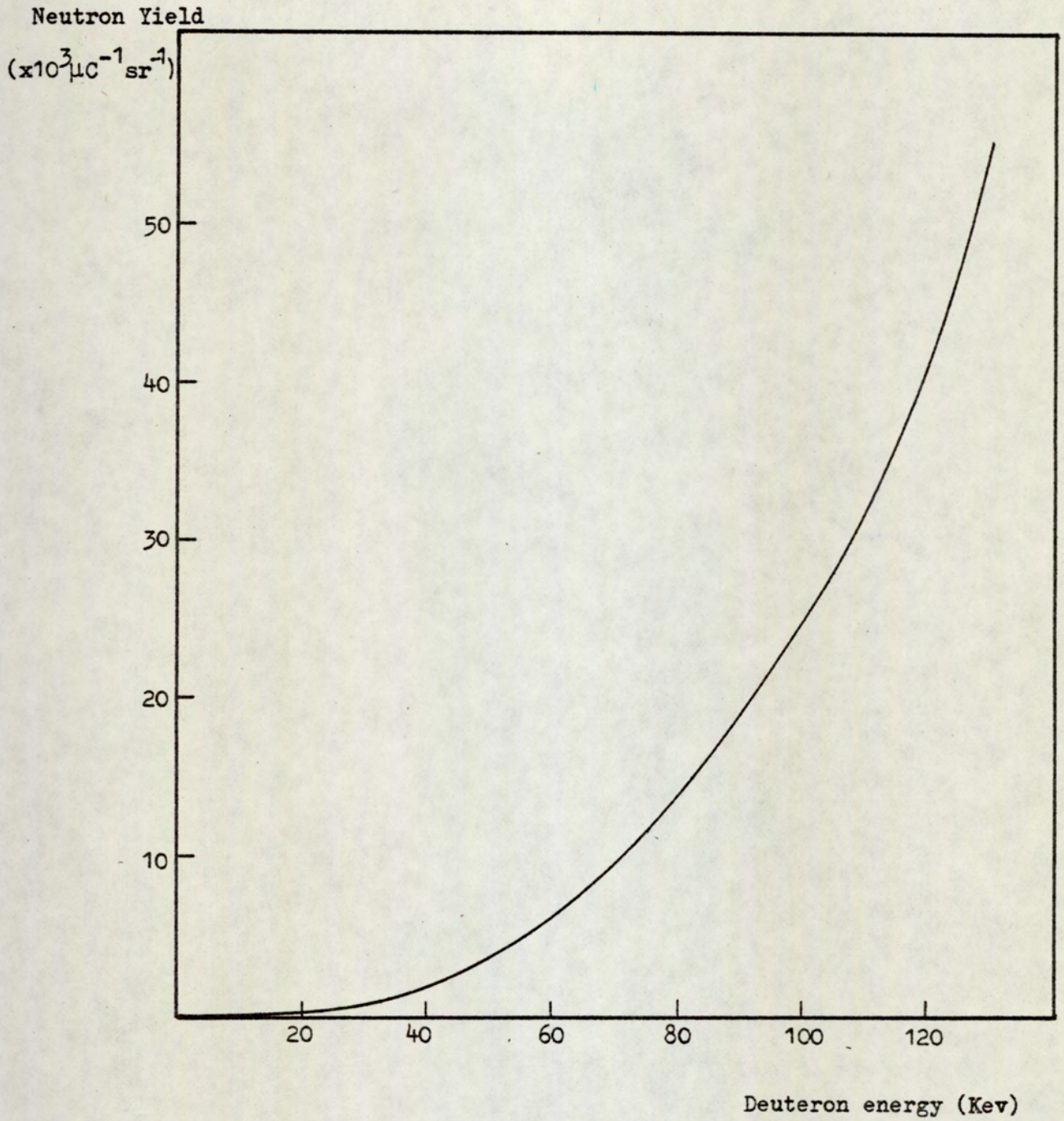

Figure 5.6 Calculated neutron yield as a function of deuteron energy. - Thick target

beam profile shown in figure 5.7, the neutron beam is centred at 44°. The neutrons produced with angles between 51° and 59° only have associated ^{3}He particles for incident deuteron energies which interact with energies less than 35 Kev, the relative yield of these neutrons in comparison to the yields at smaller angles is relatively small.

In calculating the neutron beam profile it was assumed that the target could be considered as a point source, also that the variation of $d\sigma/dw$ with neutron angle was constant. The error introduced by this latter consideration was less than 6% over the defined angular range.

5.6 Experimental System

The self supporting deuterated polyethylene films of thickness 2 μm were rotated in the vacuum system to prolong the target lifetimes. The rotating target assembly and charged particle detector were housed in a target chamber which had an internal diameter of 30.5 cm. The main body of the chamber was constructed from 1.27 cm thick stainless steel, a 1 mm thick brass window was located at 45° to the incident beam direction. The window, which was 5.1 cm in diameter, attenuated the neutron beam by 0.98 of its initial intensity.

A rotating O-ring vacuum seal was located in the side of the chamber at 135° with respect to the incident deuteron direction. Annular rings with an internal diameter of 2.5 cm were used to hold the self supporting films of polyethylene. Target rotation was achieved by mounting the annular rings onto the inner ring of a ball-race of internal diameter of 3.2 cm. The outer, non-rotating, ring of the ball-race was mounted in the chamber, the target surface defined an angle of 68° to the incident beam. The inner ring of the

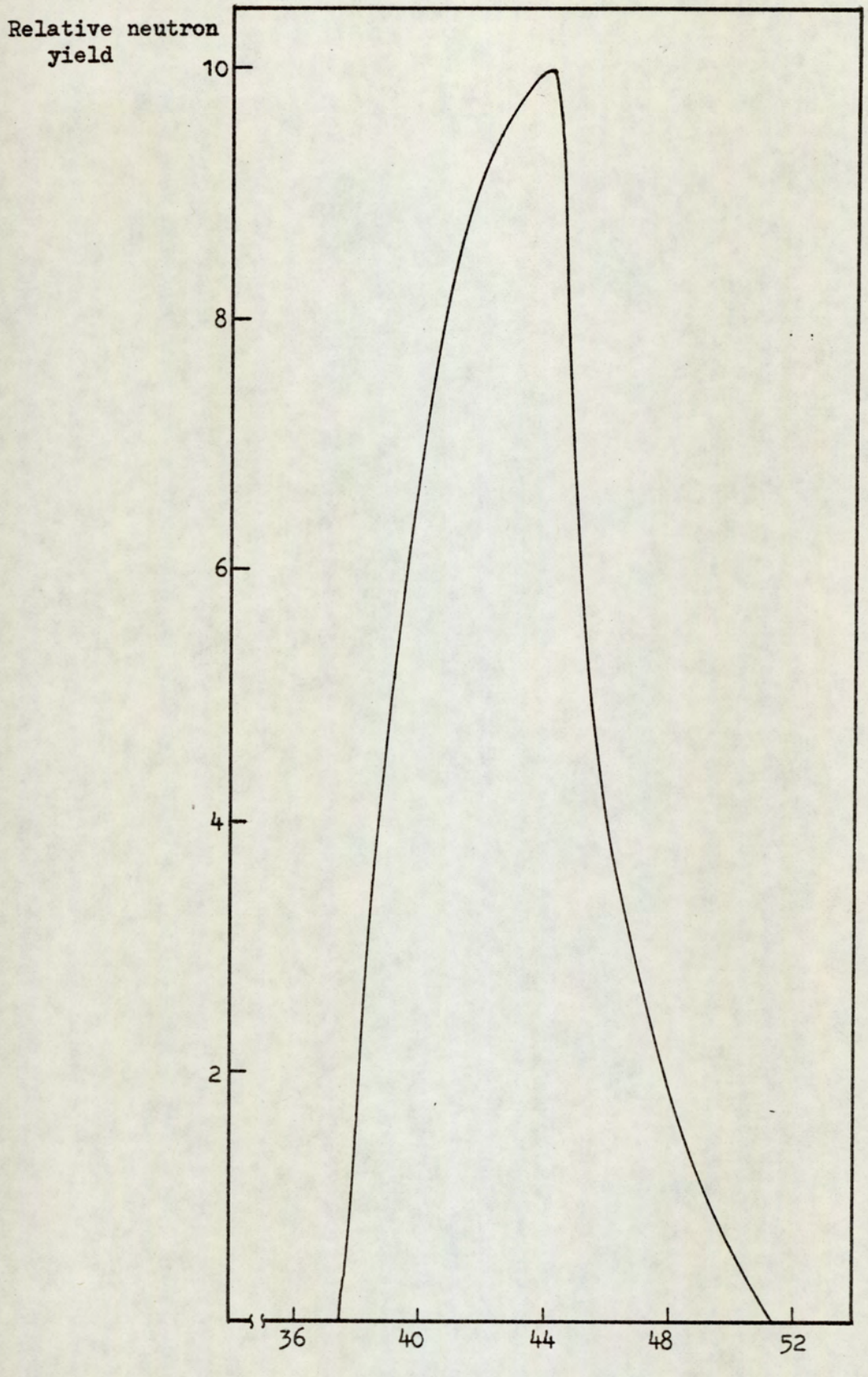

Figure 5.7 Calculated neutron yield profile.

ball-race was driven by a friction drive mounted in the horizontal plane. The friction drive consisted of a rubber O-ring pushed onto a pulley, this was located so that the O-ring edge was in contact with the inner ring of the ball-race. A gear was fixed on the vertical rotating shaft of the friction drive to allow the horizontal rotating drive shaft, connecting to the external drive through the vacuum seal, to convert this rotation to the pulley mounted on the vertical drive shaft. The rotating target assembly is shown in figure 5.8. A 12v D.C. motor supplied the external drive motion, the ball-race rotated at 1 Hz.

The area of the target under bombardment by the deuteron beam was restricted by a rectangular collimator defining a line source 10 mm in the vertical plane and 1 mm in the horizontal plane, approximating to a point source in the horizontal plane. The collimator was in two parts to enable efficient pumping of the target, the aperature was water cooled. The main beam tube and collimator flange were insulated by araldite spacing flanges.

The charged particle detector was mounted in an aluminium holder which could be rotated manually about the target centre. The detector and holder were electrically insulated from the target chamber to prevent r.f. pick-up. Figure 5.9 shows the experimental system.

5.7 Charged Particle Detection

An ORTEC silicon surface barrier detector was used for charged particle detection and the detector had a sensitive depth of 100 μm. The output of the detector was taken out of the vacuum system via vacuum tight insulated connectors mounted in the base of the target chamber. The output of the detector was then taken from these and fed into an ORTEC 125 charge sensitive preamplifier, the output

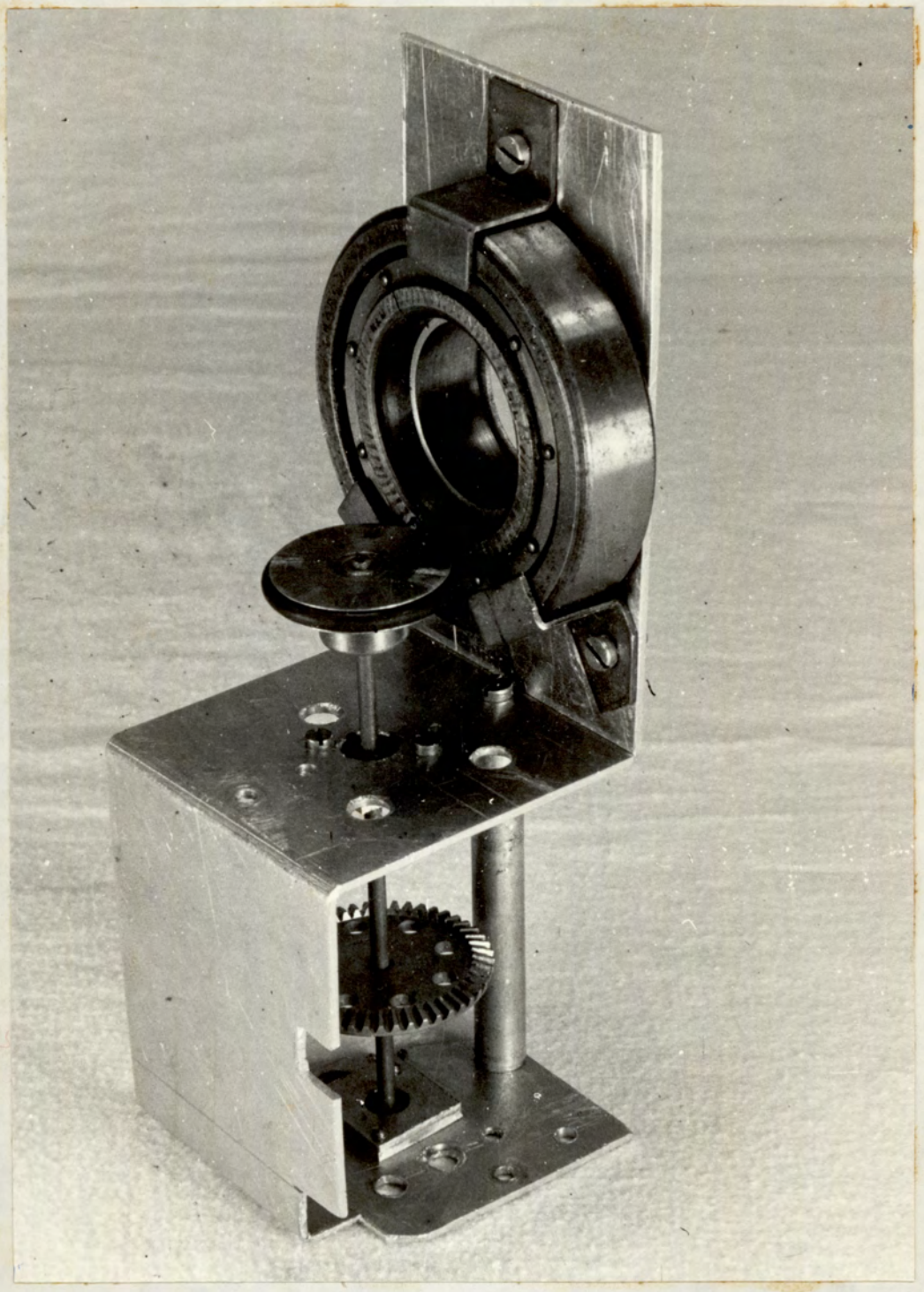

Figure 5.8 Rotating target assembly

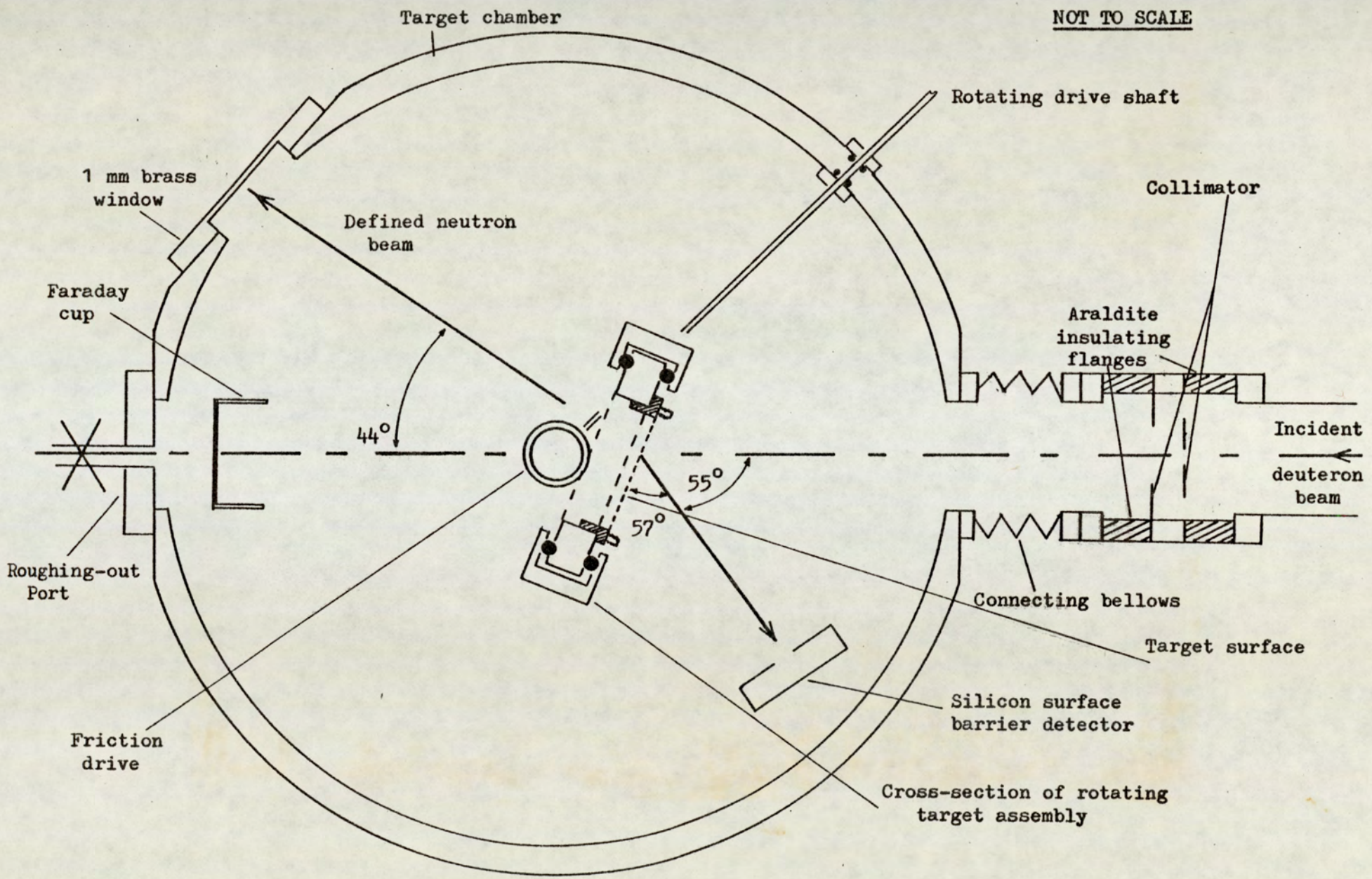

Figure 5.9 Target chamber

pulses from this had an amplitude of about 5 mV for every 0.5 Mev deposited in the detector. An ORTEC 485 spectroscopic amplifier was used to amplify the signals from the preamplifier and analyse the pulse height spectrum of the particles emitted from the target. The signal cable from the preamplifier was about 15 m long and was terminated with a 50 ohm resistor when connected to the main amplifier. The output of the amplifier was anlysed on a RIDL pulse height analyser operating on 400 channels output. The pulse height spectrum of the charged particles produced at 125^{o} by the deuteron bombardment of the target is shown in figure 5.10.

Analysis of the spectrum in figure 5.10 shows that the ^{3}H, ^{3}He and proton peaks are well resolved. The protons are produced from the $^{2}H(d,p)^{3}H$ reaction. The ^{3}He peak exhibits a low energy tail due to the formation of ^{3}He particles with energies from 0.65 Mev to 0 Mev. The maximum ^{3}He energy detected was found to be larger than that calculated, this was attributed to the variation of ^{3}He energy over the angular range of the detector.

5.8 Thin Targets

The polyethylene targets have a very low electrical conductivity and therefore are good insulators. This presented a problem in locating and measuring the beam current on the target. To overcome this problem thin targets were employed and the current of the incident beam monitored by a Faraday cup which was located at the back of the target chamber in line with the incident beam, this is shown in figure 5.9. The Faraday cup was electrically insulated from the chamber and the output was taken out via a vacuum tight insulated connection, the current was monitored to assist in beam transportation and also provide a measure of the beam current.

A target thickness was chosen which although being partially transparent to the incident beam would not affect the neutron yield

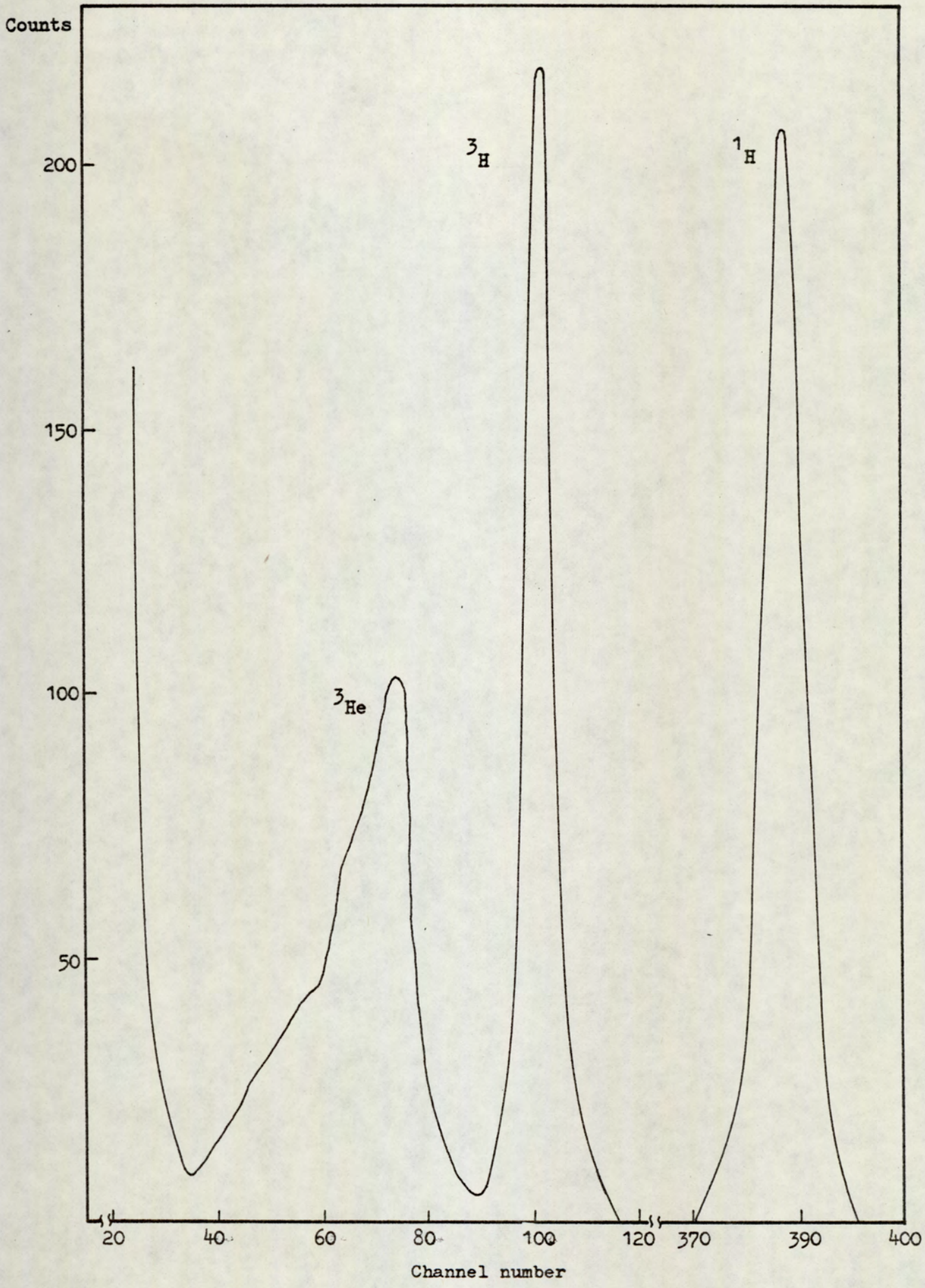

Figure 5.10 Charged particle energy spectrum at 125° for an incident deuteron energy of 130 Kev on a CD_2 target

significantly. A target thickness of 1 μm was employed, the resulting deuterons could interact with an energy between 130 Kev and 35 Kev. The contribution to the neutron yield for deuteron energies below 35 Kev was shown in section 5.5 to be small, the reduction in the neutron yield was considered acceptable. The resulting neutron angular spread, from figure 5.4, ranged from 37.4° to 52.2°, which compares with the angular range of the neutron beam profile calculated for a thick target in figure 5.7. The neutron beam profile was assumed to be unaltered.

The defined neutron beam had an energy spread between 2.8 Mev and 2.68 Mev.

5.9 Time-of-flight Measurements and Spectrometer Performance

The electronics used to measure the flight times were the same as those used in Chapter 4, for leading edge timing considerations, the block diagram of the electronics is shown in figure 4.3. As the ^{3}He peak was well resolved it was used to monitor the neutron yield, the positive output of the timing single channel analyser was recorded on a scalar for this purpose. An electronic window was set across the ^{3}He peak using the timing single channel analyser.

The neutron detector was placed at 45° with respect to the incident deuteron beam direction, corresponding to ^{3}He detection at 125°. The neutron flight path from the source to the detector was fixed at 1.5m. The observed time spectrum is shown in figure 5.11, the f.w.h.m. was 114 ns. This spectrometer resolution is obtained as a result of the contributions from time uncertainties in the production and detection processes. The ^{3}He energy spread is from 0.65 Mev to 0.035 Mev which results in a time spread of 25.4 ns for the 0.05 m flight path. The energy spread of the neutron beam contributes a further 2 ns to the overall time uncertainty. Other

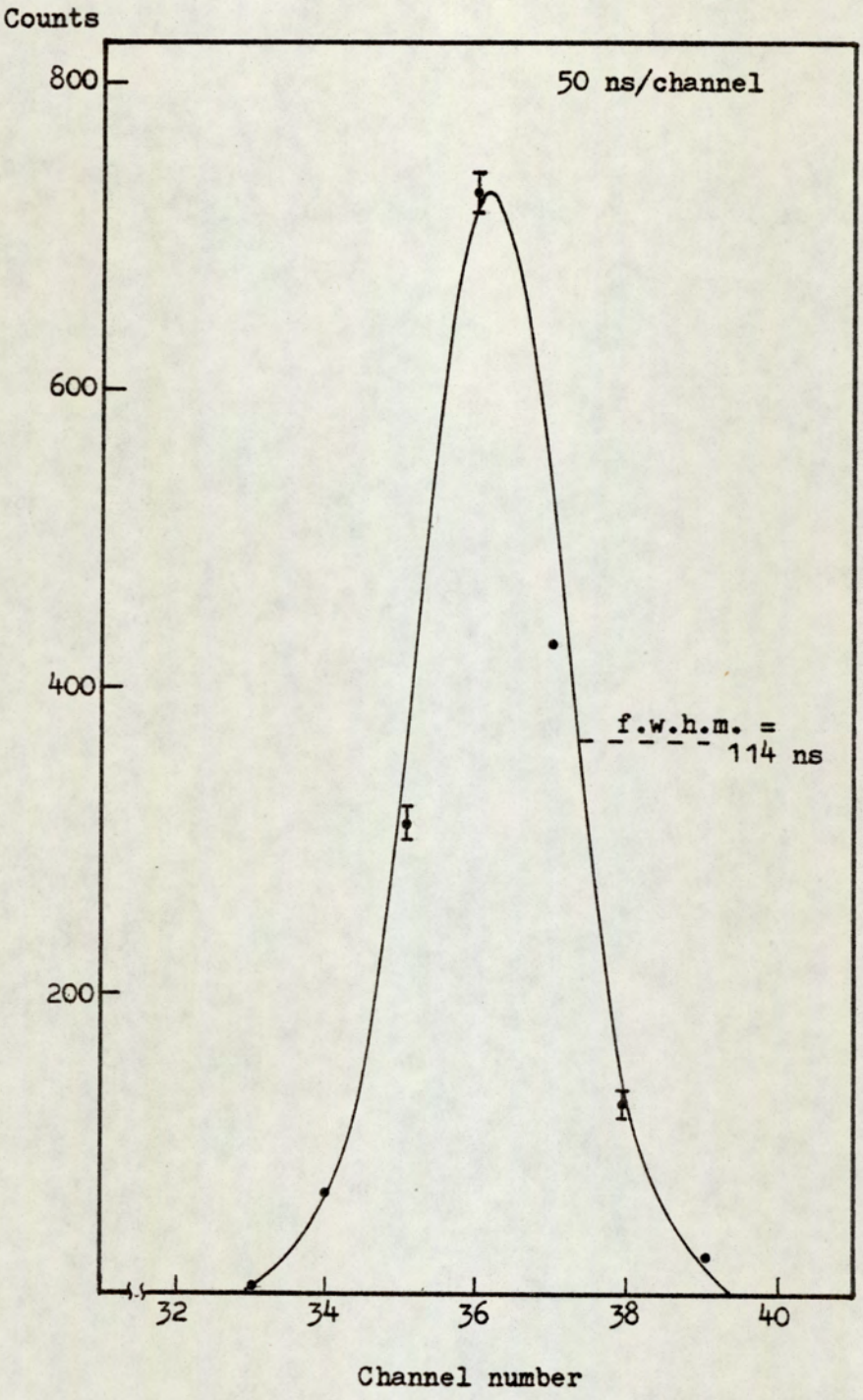

Figure 5.11 Spectrometer resolution obtained with a deuterated polyethylene target.

sources of time uncertainty were discussed in section 4.6. The main degrading effect on the spectrometer resolution was attributed to the time uncertainty introduced through "time walk".

When obtaining a time spectrum for a constant target current, difficultywas encountered in maintaining a stable neutron yield over a period of time sufficient to make measurements. When operating on the minimum possible current ($\sim 0.5\mu A$) the targets had a maximum life time of 1.5 hours. During this time the targets showed a marked reduction in neutron yields before they eventually punctured, this necessitated frequent target changes.

The energy deposited in the target by the incident deuteron beam was manifested in the form of heat. Because of the low thermal conductivity of the targets the heat was dissipated over a large surface area by rotating the targets.

The use of targets with a high thermal conductivity was investigated with the object of dissipating more efficiently by conduction, the deposited energy. This aspect is considered in the next section.

5.10 Titanium Deuteride Targets

A circular titanium deuteride target was employed, the target was copper backed and was 2.5 cm in diameter. The target was mounted stationary in the centre of the chamber and was electrically insulated from the rest of the system. To prevent electrons ejected from the target under deuteron bombardment reaching the surface barrier detector an electron suppressor was mounted around the target. An aluminium cylinder with entrance and exit holes for the incident deuterons and emitted charged particles was placed around the target assembly. The cylinder was isolated from the target and chamber and was maintained at a potential of - 200 volts.

5.10.1 Spectrometer Performance

The resulting energy spectrum obtained showed the ^{3}He peak to be unresolved, while the ^{3}H peak remained partially resolved. Difficulty was encountered in estimating the position of the ^{3}He peak in the energy spectrum, the voltage levels for the upper and lower discriminator levels for the timing single channel analyser were set at the values obtained for the ^{3}He peak position obtained with the plastic targets. Due to the high count rate, about 10^{4} counts/second, obtained from the timing single channel analyser output, the negative timing signal generated was used for the STOP input of the time converter. This was to limit the converter dead time and the random coincidence count rate.

The time spectrum obtained as a result of the electronic coincidence between neutrons and associated ^{3}He is shown in figure 5.12. The spectrum was obtained for a target current of $3\mu A$ operating at an incident deuteron energy of 130 Kev, the neutrons were detected at 45° and the resulting f.w.h.m. of the time spectrum is 508 ns. The resolution obtained in the present work compares with that obtained by Monier et al[23], the resolution obtained was 10 μs for deuterons of 50 Kev incident on a solid ice target with a solid state detector situated at an angle of 105° with respect to the incident beam direction. Bell et al[20] working at an incident energy of 100 Kev on a gold drive in target obtained a resolution of 400 ns and Naggier et al[60] using energies of 100 Kev obtained a resolution of $1\mu s$.

By using the titanium deuteride targets stable conditions could be maintained over a longer period of time in comparison to the deuterated polyethylene targets. In this respect the titanium targets were superior in providing a constant neutron yield. One of the main disadvantages of the metal targets was that the random

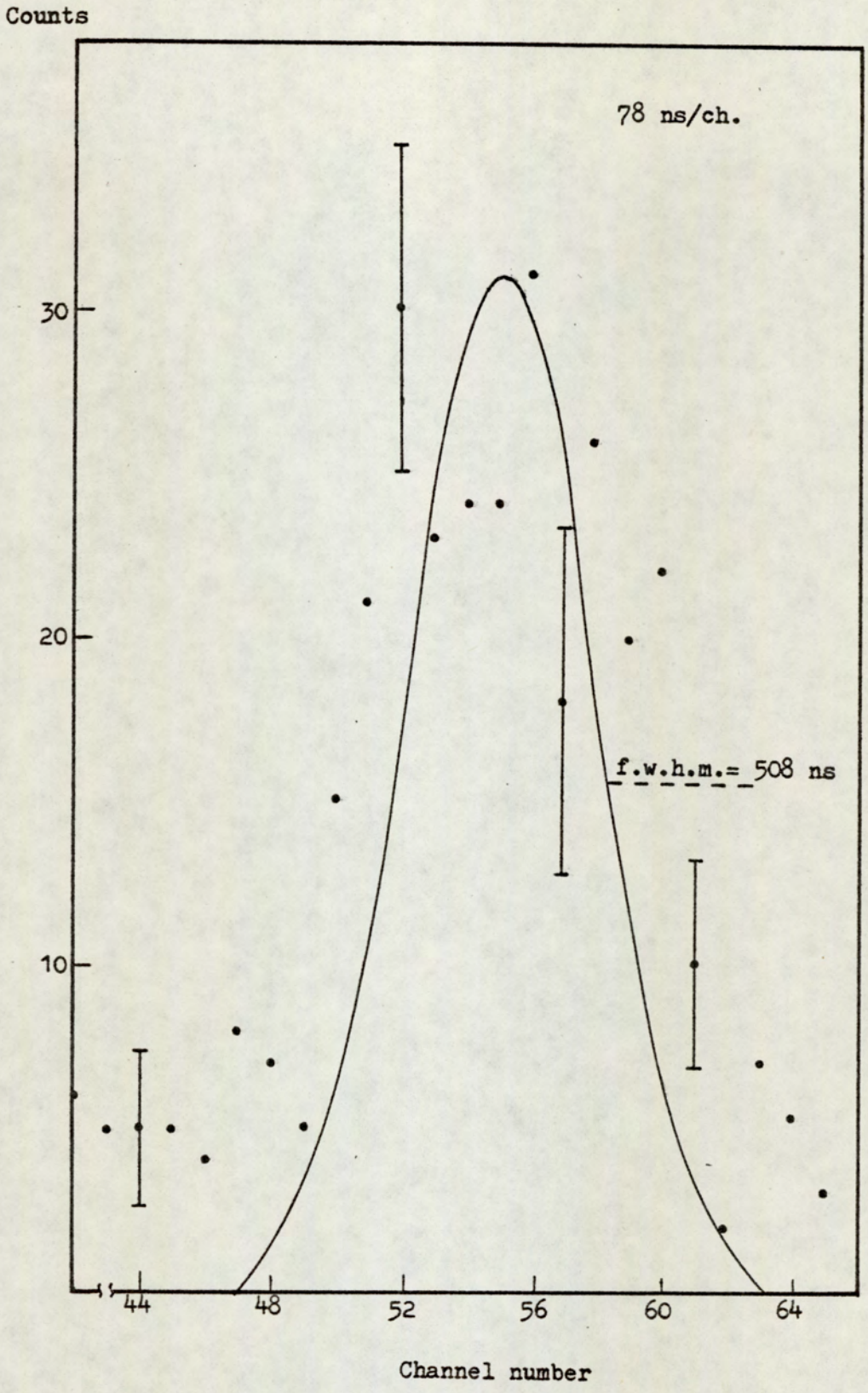

Figure 5.12 Spectrometer resolution obtained with a titanium deuteride target.

coincidence rate was much higher. The γ -rays produced by bombardment of the metal target gave a high background in the neutron detector, these pulses produced random coincidences with the high number of background events in the charged particle electronics. As the ^{3}He peak was unresolved the positive output of the timing single channel analyser could no longer be used to monitor the neutron yield.

Thus the use of the time-of-flight technique for the $^{2}H(d,n)^{3}He$ reaction is shown to be feasible for the low energy accelerator, however due to the low neutron yields this will lead to measurements of cross-sections taking considerable time. Hence the Dynamitron facility was used to take measurements because of its ability to produce higher neutron yields.

CHAPTER 6

DIFFERENTIAL CROSS-SECTION MEASUREMENTS

6.1 Sample Geometry

In neutron differential cross-section measurements the shape of the source, scattering sample material, detector and shielding are chosen as a compromise between the need to increase the signal to background signal ratio and the need to reduce the magnitude and complexity of the corrections which must be made to the data. The three most commonly used arrangements, the ring geometry, cylindrical geometry and flat plate geometry are shown in figures 6.1(a), 6.1(b) and 6.1(c).

In the ring geometry, figure 6.1(a), the scattering sample is presented to the neutron flux in the form of a ring. The scattering material is placed with its axis on the line passing through both the source and the detector, a shadow shield is placed along this line to remove the direct flux. The scattering angle is varied either by moving the scatterer or detector along the axis or by employing rings with different diameters. The main advantage of this geometry is that for a given angular resolution and thickness of scatterer more material can be used and hence a greater scattered intensity can be obtained than with any other arrangement, however the angular resolution for this geometry is generally poor. The ring geometry is mainly limited to pulsed beam spectrometers, where time-related neutrons are produced in all directions.

The cylindrical and flat plate geometry can be used with the associated particle time-of-flight technique, figures 6.1(b) and 6.1(c). With the cylindrical geometry where the scatterer is a cylinder and the flat plate geometry where the scatterer is a thin

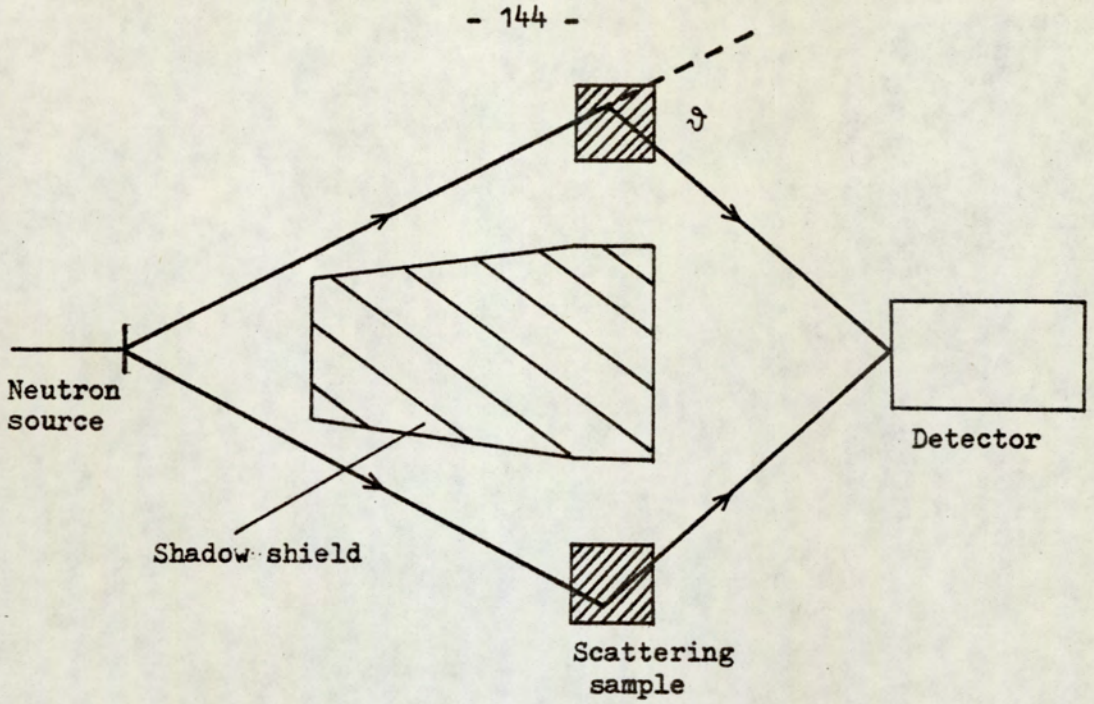

Figure 6.1(a) Ring geometry

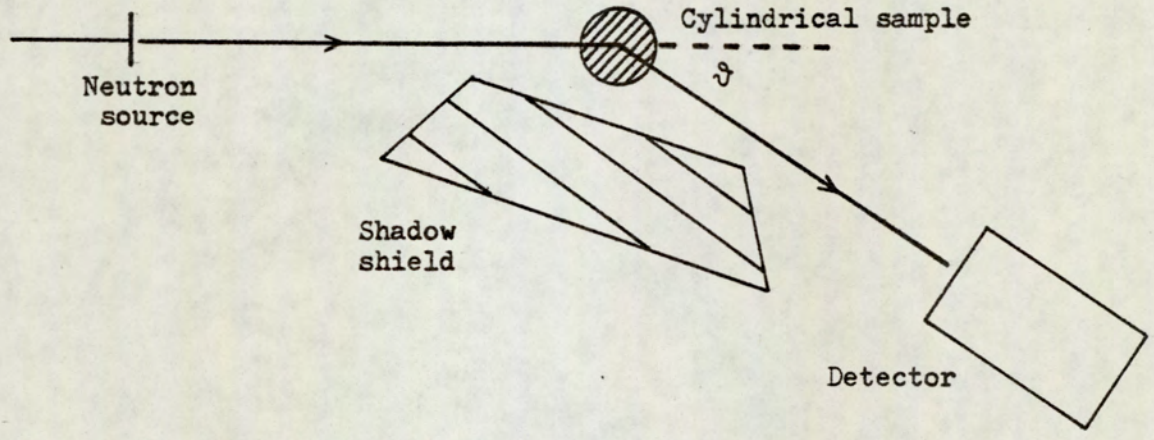

Figure 6.1(b) Cylindrical geometry

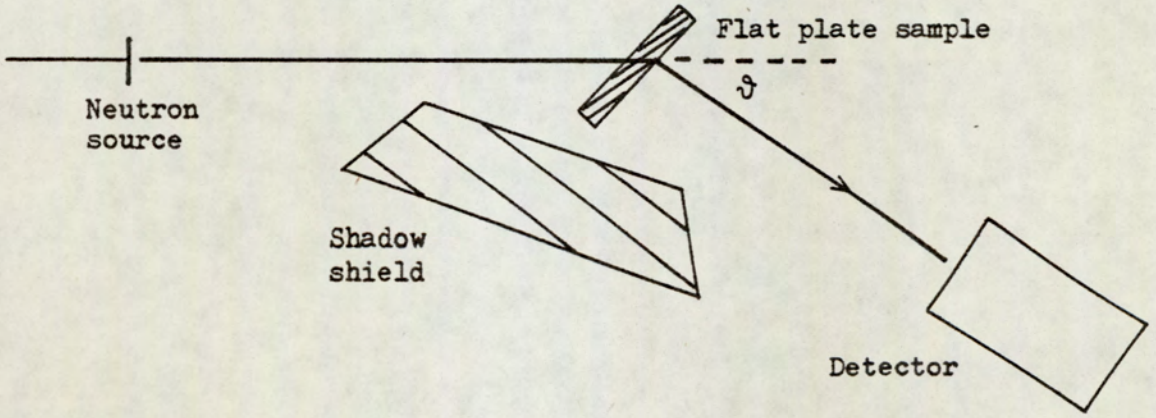

Figure 6.1(c) Flat Plate geometry

rectangular slab of material the detector is rotated around the scatterer which is placed in the direct neutron beam. Good angular resolution can be attained with the cylindrical and flat plate geometry.

The flat plate geometry was used in the present work as this results in a simplification of the equations relating the scattered neutron intensity to the differential scattering cross-section. The sample size was chosen such that it completely intercepted the defined neutron cone. The monitored charged particle count was used as a measure of the neutron flux incident on the sample. The equation relating the scattered neutron intensity to the differential elastic cross-section is now considered.

6.2 Differential Cross-section for Elastic Scattering

If a flux of ϕ' neutrons per second per unit area is incident onto a sample containing n' nuclei, and N_s neutrons are elastically scattered per second into unit solid angle centred at an angle ϑ to the direct neutron beam, the differential cross-section per unit solid angle at an angle ϑ can be expressed as:-

$$\frac{d\sigma}{dw}(\vartheta) = \frac{N_s(\vartheta)}{n' \phi'} \qquad \ldots\ldots 6.1$$

The differential cross-section will be in units of area per solid angle which is usually expressed as barns/steradian.

By examination of the time-of-flight spectra obtained at various angles around a sample which intercepts the defined neutron cone, the number of neutrons detected at an angle ϑ can be obtained by summing the counts in the peak of the time-of-flight spectrum obtained at this angle. To relate the number of neutrons N detected to those actually scattered the integrated counts obtained must be

corrected for the neutron detector efficiency. The neutron detector will also define a solid angle Δw at the sample, equation 6.1 can be rewritten as:-

$$\frac{d\sigma}{dw}(\vartheta) = \frac{N(\vartheta)}{n'(\emptyset/A)\,\Delta w\,\varepsilon(E_n)} \qquad \ldots\ldots 6.2$$

where $\varepsilon(E_n)$ is the neutron detector efficiency for a neutron of energy E_n, A is the area of the sample face on which the neutron beam is incident and $\emptyset$ is the number of neutrons incident on the scattering sample. The factor n'/A in equation 6.2 can be expressed as nx where n is the number of nuclei per unit volume and x is the target thickness. The value of n is given by:-

$$n = \frac{\rho\, N_o}{A\ wt} \qquad \ldots\ldots 6.3$$

where N_o is Avogadro's number, ρ is the density of the sample and A wt is the atomic weight.

Factors which affect the accuracy of equation 6.2 will be discussed in the subsequent sections.

6.3 Neutron Flux

In the associated particle system the number of neutrons incident on the sample is determined directly from the monitored ^{3}He count. For neutron emission centred at 120°, with respect to the incident deuteron direction, the associated ^{3}He particles were well resolved from the scattered deuterons therefore the ^{3}He count was monitored directly. The error in the neutron flux thus measured was due to the statistical error in the integrated ^{3}He count.

For neutron emission centred at 75° the ^{3}He peak overlapped the scattered deuteron peak and here the protons produced from the ^{2}H(d,p)^{3}H reaction were monitored to provide a measure of the neutron

flux. For this case, if K is the ratio of the yield of protons to ^{3}He calculated in section 3.7.1, equation 6.2 becomes:-

$$\frac{d\sigma}{dw}(\vartheta) = \frac{N(\vartheta)}{nx\,(\phi_p/K)\,\Delta w\,\varepsilon(E_n)} \qquad \ldots\ldots 6.4$$

where ϕ_p is the proton yield.

In addition to the error in the integrated proton count an error of 0.6% is introduced into the neutron flux due to the uncertainty in K.

6.4 Neutron Absorption

The neutrons produced at the target had to penetrate a 1 mm thick stainless steel window before reaching the scattering sample. The number of neutrons reaching the sample was therefore reduced due to absorption and scattering processes in the stainless steel. The stainless steel had a composition of 74% iron, 18% chromium and 8% nickel. The fraction of neutrons escaping the vacuum system was then given by:-

$$C = \exp - (\mu_{Fe} + \mu_{Cr} + \mu_{Ni})\,x \qquad \ldots\ldots 6.5$$

In the expression x is the thickness traversed i.e. 1 mm and μ is the linear attenuation coefficient of the material under consideration and can be found from:-

$$\mu = n\sigma_T \qquad \ldots\ldots 6.6$$

where n is the number of nuclei per cm^3 and σ_T is the total cross-section for the material under consideration. The linear attenuation coefficients in equation 6.6 were calculated with values of σ_T taken from Hughes et al[61]. The fraction of source neutrons escaping the stainless steel window was calculated at 0.97 $\pm$ 0.02. By considering

this factor the fraction of neutrons attenuated will be slightly over estimated as the neutron elastic scattering is forward peaked, so that a fraction of the neutrons elastically scattered by the window will still pass through the sample.

6.5 Beam Attenuation and Multiple Scattering

In passing through the sample the neutron flux would be expected to decrease in intensity with increasing penetration. If the initial flux is ϕ_o then the reduced flux at a distance x inside the sample is given by:-

$$\phi(x) = \phi_o \exp - (\mu x) \qquad \ldots\ldots 6.7$$

where μ has been defined previously in equation 6.6.

In the attenuation process neutrons are considered to be removed from the incident flux by scattering and absorption processes in the sample. In equation 6.7, if a neutron is scattered out of the direct neutron beam it is assumed to be removed and unable to undergo further interactions. However, the scattered neutrons are still available to undergo further collisions, due to this multiple scattering process equation 6.7 under estimates the neutron flux present in the sample. A Monte Carlo type calculation should be performed to estimate the contribution to the neutron flux of these multiple scattered neutrons.

However, Day[62] has shown that for samples which have a neutron transmission greater than or equal to 70% the effects of multiple scattering cancel the neutron attenuation and the neutron flux is constant through the sample. This approximation has been checked experimentally[63][64] and has been found to introduce less error than that due to experimental uncertainties. This criteria was applied in the present work.

6.6 Weighted Sample Thickness

The neutron beam profiles (figures 2.29 and 2.30) show that the neutron beam incident onto the scattering sample will be a diverging beam and that the intensity will vary with neutron angle. The width of the sample traversed by the neutron beam will therefore vary with the neutron angle, figure 6.2 shows the dependence of the sample thickness on neutron angle for a sample positioned at 45° to the incident neutron beam centred at 75° with respect to the incident deuteron direction. As the intensity is angular dependent it is necessary to calculate the weighted sample thickness $\bar{x}$, defined by:-

$$\bar{x} = \frac{\sum_i f_i x_i}{\sum_i f_i} \qquad \ldots\ldots 6.8$$

In the expression the value of i defines the neutron angle. The weighing fraction f_i is proportional to the area under the beam profile curve calculated in 1° intervals from Ψ_1 to Ψ_2, where Ψ_1 and Ψ_2 define the maximum and minimum limits of the neutron beam profile. The value of x_i corresponding to a neutron angle of Ψ_i, for neutron emission at 75°, is given by:-

$$x_i = \frac{b}{\sin (120^{\circ} - \Psi_i)} \qquad \ldots\ldots 6.9$$

where b denotes the sample thickness. The weighted sample distance for neutron emission at 75° was calculated at:-

$$\bar{x} = (1.42 \pm 0.06)\ b$$

When in addition the different neutron angular spread and beam profile shape produced for neutron emission at 120° were taken into account the expression becomes:-

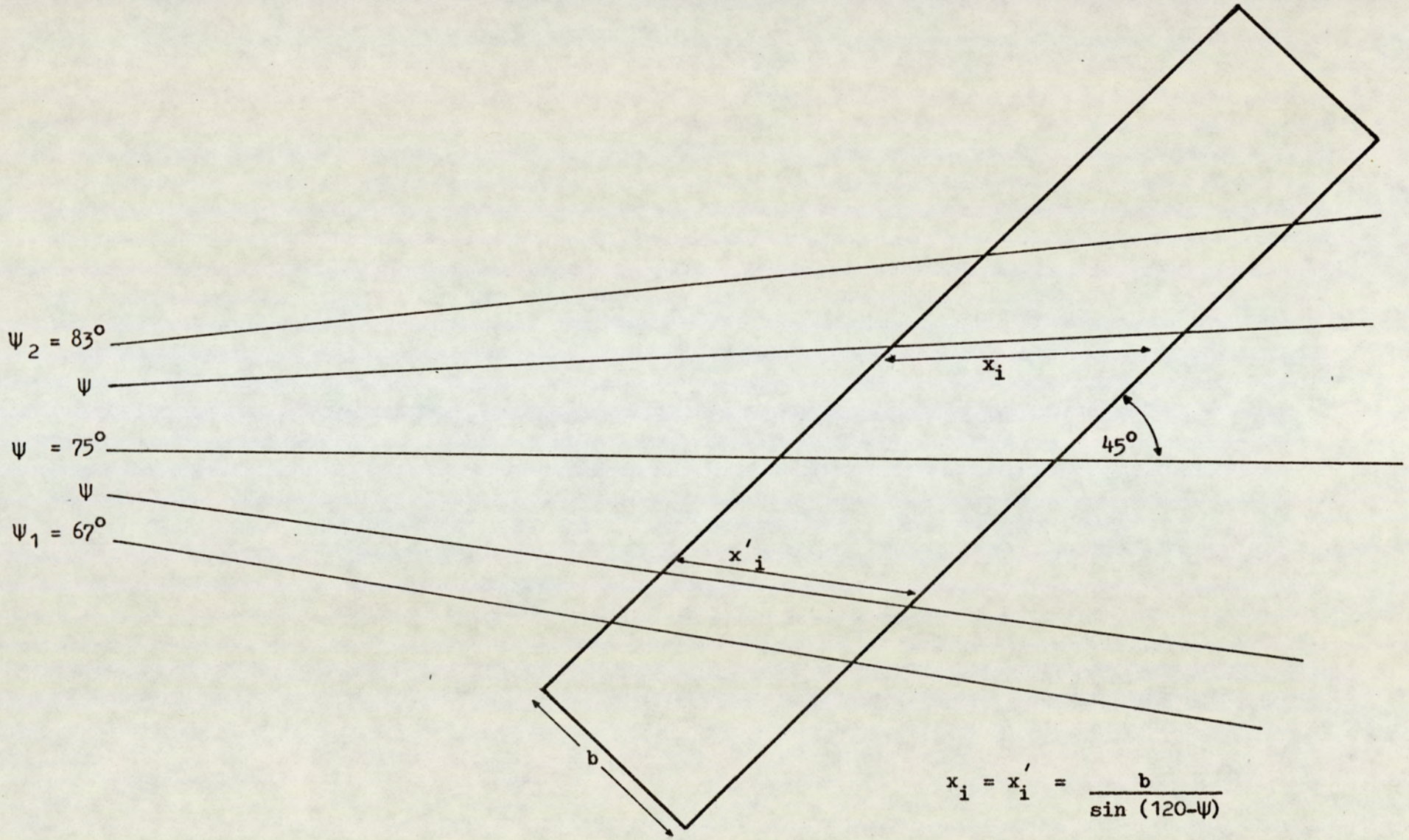

Figure 6.2 Calculation of the weighted sample thickness

$$\bar{x} = (1.44 \pm 0.06)b$$

Experimentally the sample could be positioned to within 1°, thus introducing an error of 2% in the sample thickness. A further error of 2% was attributed to the uncertainty in the neutron beam profile shape.

6.7 Neutron Detector Efficiency Measurements

The two neutron production angles of 75° and 120°, with respect to the incident beam direction, allowed absolute measurements of the neutron detector efficiencies for the neutron energies of 2.99 Mev and 2.18 Mev. For both neutron production angles the neutron detector was placed 0.3m from the target centre, thus ensuring that the detector encompassed the defined neutron cones completely. For the two measurements the count rates in the ^{3}He and proton counting channels were maintained at about 10 counts/second. Ten coincidence spectra were taken at each energy. The absolute efficiency for 2.99 Mev neutrons was calculated from the relation:-

$$\varepsilon(2.99) = \frac{N}{(\phi_p/K)} \qquad \ldots\ldots 6.10$$

where N is the total number of coincidences, ϕ_p is the integrated proton count and K is the ratio of the proton to ^{3}He yield.

For 2.18 Mev neutrons where the ^{3}He count was monitored directly the efficiency was found from:-

$$\varepsilon(2.18) = \frac{N}{\phi_{^3He}} \qquad \ldots\ldots 6.11$$

The measured absolute efficiencies where 27.01% ± 0.68% for 2.99 Mev neutrons and 25.45% ± 0.64% for 2.18 Mev neutrons. A

comparison between the measured values and the theoretical values is shown in figure 6.3.

The theoretical values were considered accurate to within ± 6%, the uncertainty being introduced by errors in the energy loss values of protons in the NE/02A and errors in the total neutron scattering cross-sections for carbon and hydrogen. Considering these uncertainties and errors in the measured values the measured efficiencies were in good agreement with the theoretical values.

6.8 Neutron Detector Solid Angle

Here the scattering sample was assumed to be a point source, the solid angle subtended by the detector at the scatterer can therefore be found from the expression:-

$$\Delta w = \frac{A^1}{r^2} \qquad \ldots\ldots 6.12$$

where A^1 is the area of the detector face and r is the separation of the detector from the sample. The detector position could be measured to within 0.5 cm, this introduced an error of 1% in the solid angle calculated in equation 6.12.

6.9 Analysis of Data

The differential cross-section per nucleus for elastic scattering of neutrons was derived using the formula:-

$$\frac{d\sigma}{dw}(\vartheta) = \frac{N(\vartheta)}{n \bar{x} \phi \Delta w \varepsilon(E_n) C} \qquad \ldots\ldots 6.13$$

where all terms have previously been defined.

The number of neutrons, N scattered at an angle ϑ was obtained by summing the counts in the peak of the time-of-flight spectrum obtained for an incident neutron flux of ϕ counts. A

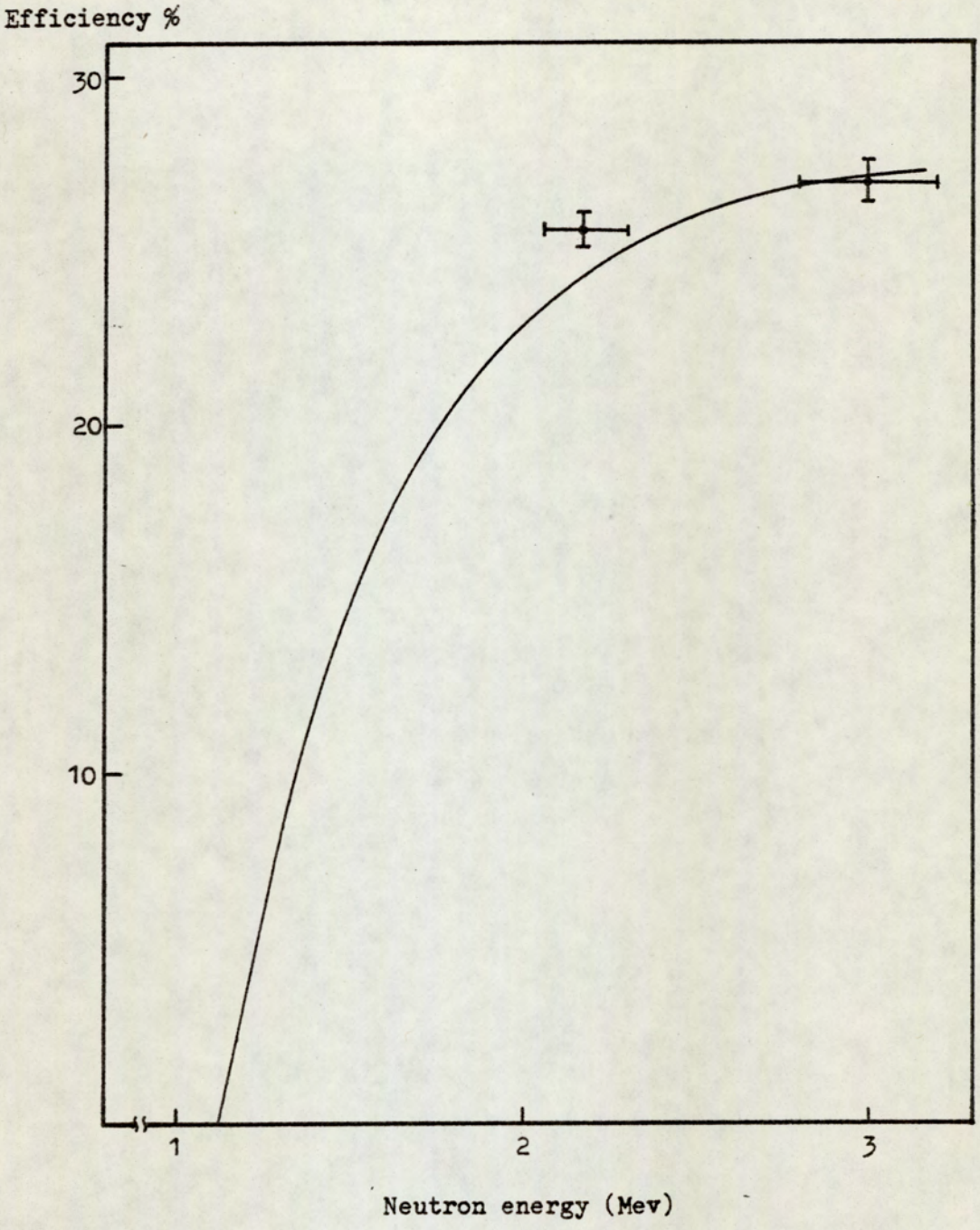

Figure 6.3 Measured efficiencies of the neutron detector: the theoretical curve was calculated assuming the carbon did not scatter neutrons.

time-of-flight spectrum was obtained by making alternate runs; a spectrum was first accumulated with the scattering sample in the direct neutron beam for a specific charged particle count (^{3}He or proton), the sample was then removed and a background spectrum accumulated for the same integrated charged particle count. The number of neutrons scattered, per analyser channel, by the sample was obtained by subtracting the background spectrum from the spectrum obtained with the sample in the direct beam. If C_i counts were added in the i^{th} channel and B_i the background counts subtracted from the i^{th} channel, then the error in C_i was given by:-

$$e_i = (C_i + B_i)^{\frac{1}{2}}$$

The total error on the integrated peak count was then $(\Sigma e_i^2)^{\frac{1}{2}}$.

6.10 Centre of Mass Frame of Reference

The differential cross-section measurements and calculations were all performed in the laboratory frame of reference. However, most theoretical calculations are performed in the centre of mass system to eliminate the complication of a moving centre of mass. In order to compare the results obtained with the optical model predictions it was necessary to convert all measurements to the centre of mass system.

The angular distribution $d\sigma/dw$ observed in the laboratory system is related to the centre of mass angular distribution $d\sigma/dw'$ by the equation[65]:-

$$\frac{d\sigma}{dw}(\vartheta) = \frac{(1 + 2\gamma\cos\vartheta + \gamma^2)^{3/2}}{1 + \gamma\cos\vartheta} \frac{d\sigma}{dw'}(\phi) \qquad \ldots\ldots 6.14$$

here $\gamma = M_1/M_2$, M_1 is the neutron mass and M_2 the mass of the target nuclei.

The laboratory angle ϑ is related to the centre of mass angle

ϕ by[66]:-

$$\phi = \vartheta + \sin^{-1}(\gamma \sin\vartheta) \qquad \ldots\ldots 6.15$$

6.11 The Scattering Samples

The calcium sample consisted of calcium granules compressed into a metal container. To prevent oxidation of the calcium the top of the sample was sealed by a layer of paraffin wax. The sample thickness was chosen so that the neutron transmission through the sample was 70%. In order to achieve this a sample thickness of 5 cm was used. The sample container had the internal dimensions of 5 cm x 13 cm x 18 cm and an X-ray radiograph was made of the sample to test the uniformity throughout the sample. An identical metal can was made which was used as a dummy sample when the background was subtracted.

The density of the calcium was measured and found to be 1.0 ($\pm$ 0.02) g cm^{-3}. Then by applying equation 6.3 the value of n was calculated at 1.5×10^{22} ($\pm$ 2%) nuclei cm^{-3}.

The sulphur due to its low melting point (113° - 119°) was able to be moulded into a block measuring 2.8 cm x 12.5 cm x 9.5 cm. The sample thickness, 2.8 cm was chosen on the same criteria as the calcium sample thickness. The density of the sulphur was measured at 1.91 ($\pm$ .04) g cm^{-3} and the number of nuclei cm^{-3} was calculated to be 3.58×10^{22} ($\pm$ 2%).

In both cases the sample was positioned 30 cm from the target centre, thus ensuring that all the defined neutron cone would pass through the sample, at an angle of 45° to the defined cone. The neutron detector was placed at 50 cm from the centre of the sample face and could be rotated around the sample, figure 6.4 shows the experimental configuration with the shadow bar in position.

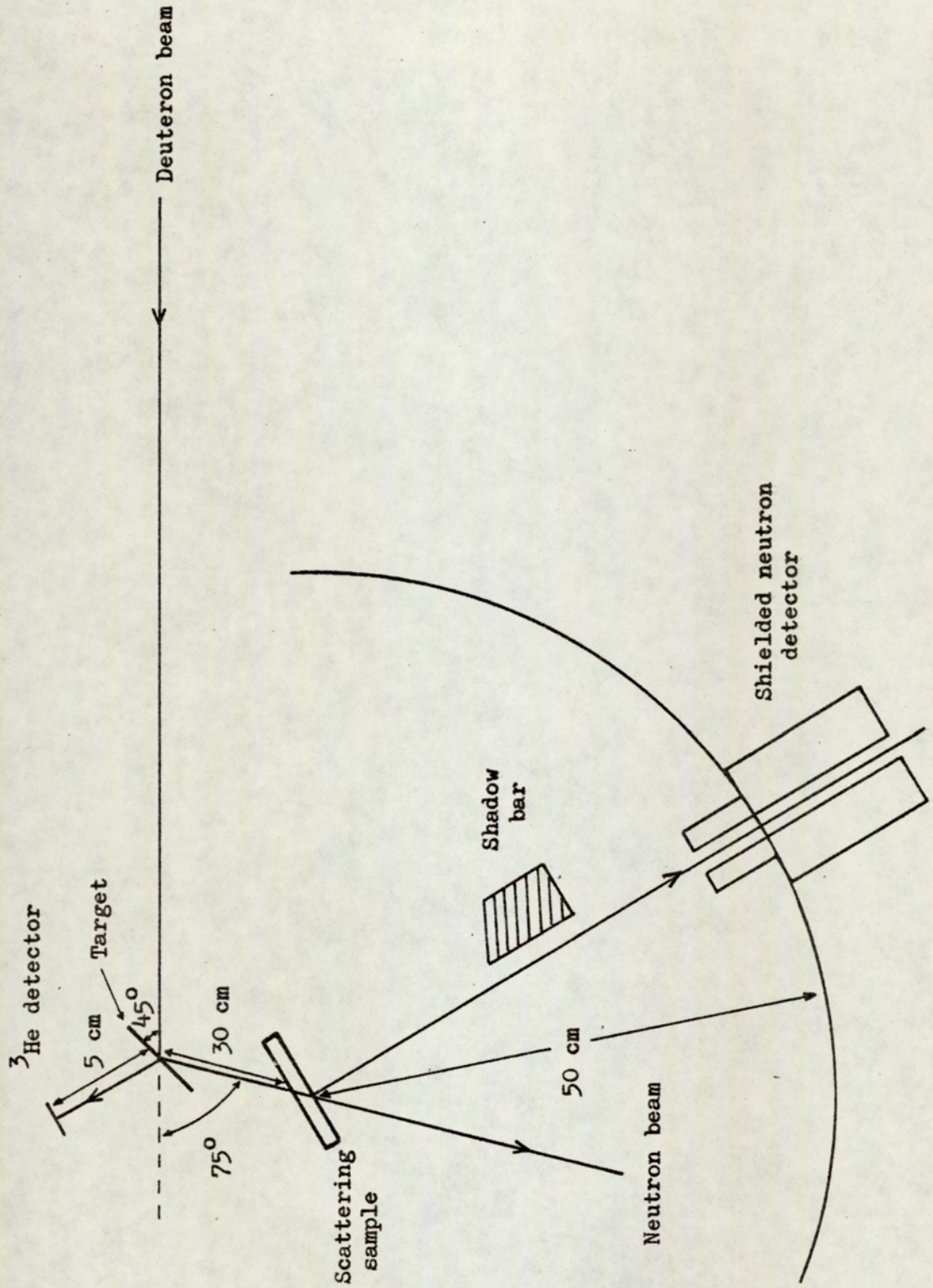

Figure 6.4 Plan view of the experimental configuration for scattering of 2.99 Mev neutrons.

6.12 Calcium Differential Elastic Scattering Cross-section Measurements for 2.99 Mev Neutrons

Prior to making any experimental measurements the electronics, set up as described in Chapter 4 for leading edge timing, were switched on for three hours to allow the system to stabilize. With the sample positioned as described in section 6.11, time-of-flight spectra were obtained at laboratory angles of 20°, 40°, 45°, 60° and 80°.

The time-of-flight spectra were accumulated by making alternate runs with the calcium sample in the direct beam (the add mode) and with the empty metal container (the subtract mode). Typical spectra obtained are shown in figures 6.5, 6.6 and 6.7. Each time-of-flight spectra was fitted with a normal error curve, the method used to do this is given in Appendix II.

The main isotope present in the calcium sample was $^{40}_{20}Ca$ which has an isotopic abundance of 96.95%[67]. The first excitable state of this isotope is 3.74 Mev[68], as the incident neutron energy is 2.99 Mev there will be no inelastic reactions produced. The time-of-flight spectra were therefore assumed to consist entirely of elastically scattered neutrons.

The differential elastic scattering cross-sections were evaluated using the equation:-

$$\frac{d\sigma}{dw}(\vartheta) = \frac{N(\vartheta)}{n\bar{x}\,(\phi_p/K)\,\Delta w\,\varepsilon(E_n)C} \qquad \ldots\ldots 6.16$$

6.12.1 Experimental Errors

The experimental errors relevant to equation 6.16 have been considered previously but are tabulated for completeness:-

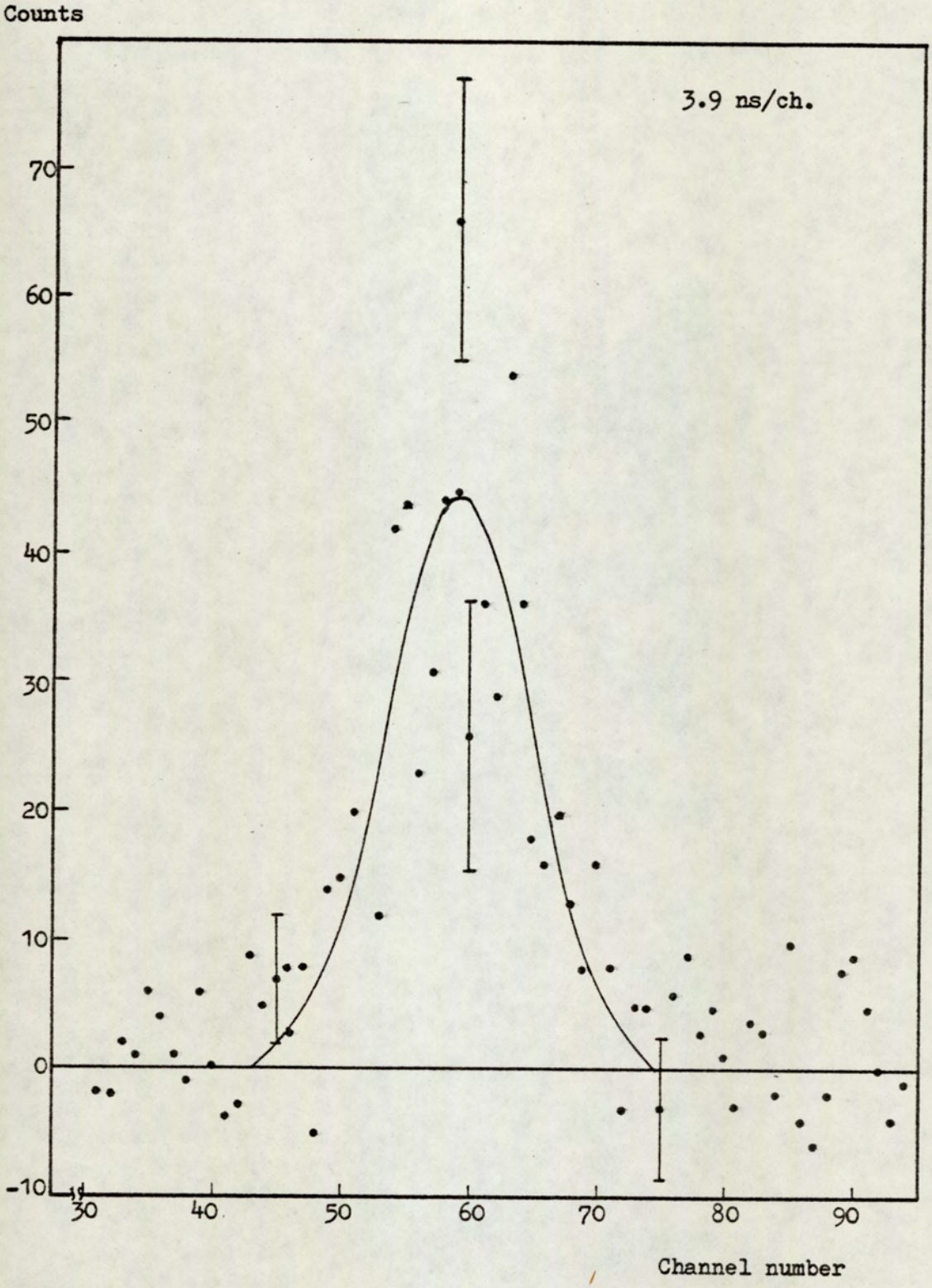

Figure 6.5 Time-of-flight spectrum for scattering from calcium at 20^{o} in the laboratory system

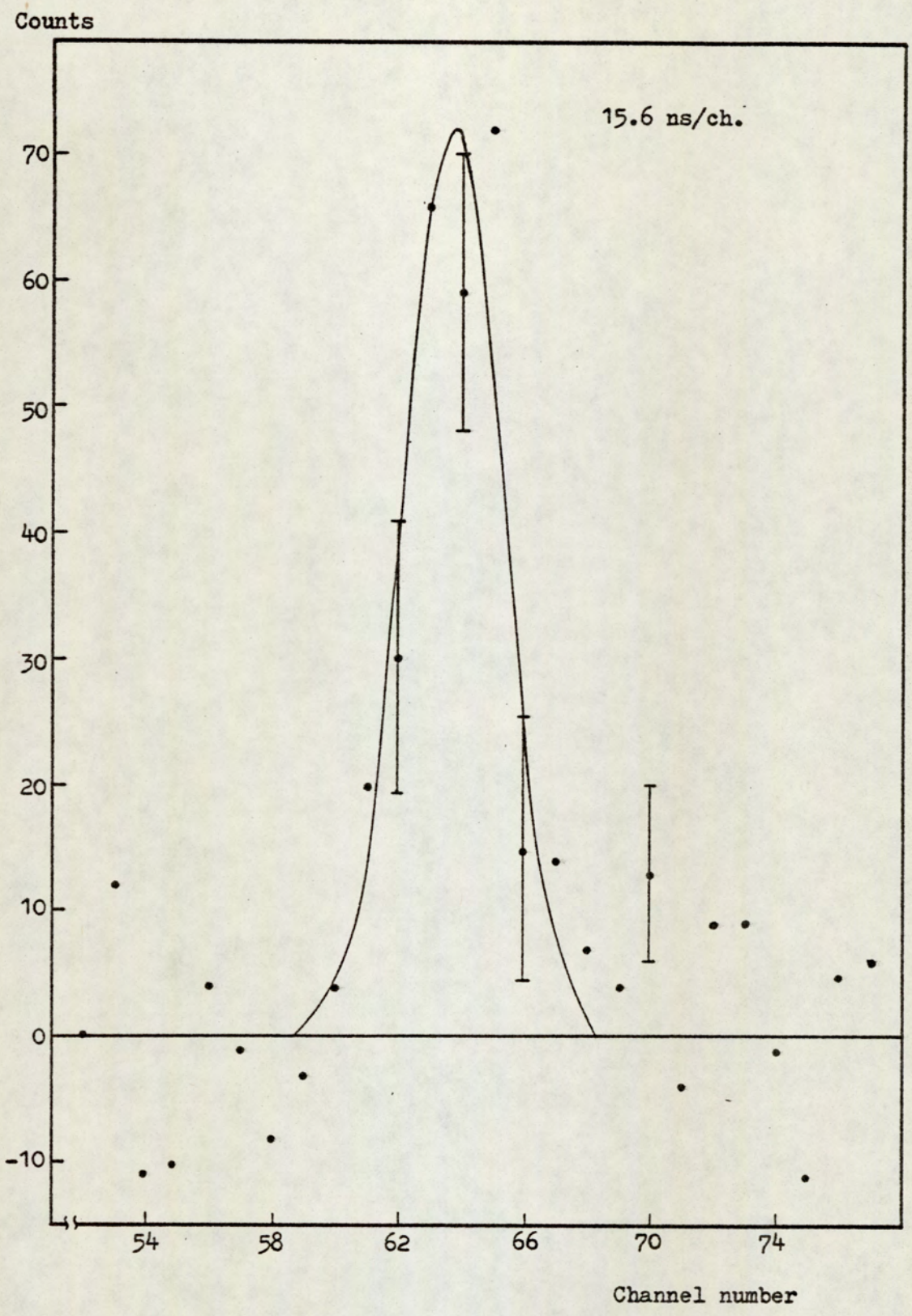

Figure 6.6 Time-of-flight spectrum for scattering from calcium at 40° in the laboratory system.

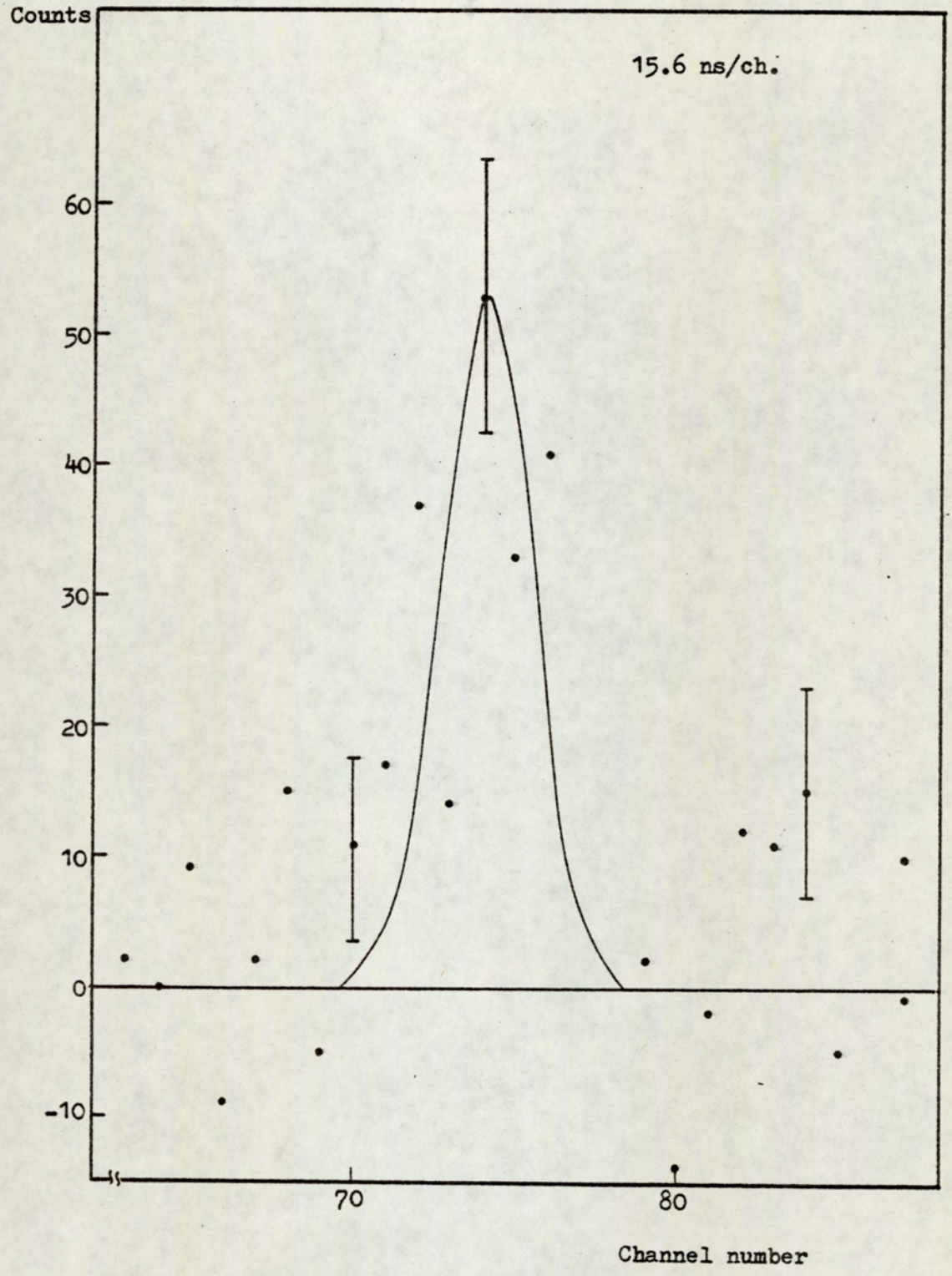

Figure 6.7 Time-of-flight spectrum for scattering from calcium at 60° in the laboratory system.

Term	Percentage error
$N(\vartheta)$	$(\Sigma e_i^2)^{\frac{1}{2}}$
n	2%
$\bar{x}$	4%
ϕ_p	< 1%
K	0.6%
Δw	1%
$\varepsilon(E_n)$	6%
C	2%

The experimental error in a differential cross-section was obtained by adding these errors in quadrature. Each experimental point was also subject to an angular uncertainty of $\pm 8^{\circ}$ due to the angular acceptance of the neutron detector and also due to the finite size of the neutron beam incident onto the scattering sample.

6.12.2 Angular Distribution

The calculated cross-sections were plotted as a function of the cosine of the centre of mass angle and are shown in figure 6.8, the errors on each point represent the experimental uncertainties mentioned in section 6.12.1. The results are also presented in table 6.1.

No previously published information could be found on the measurements of differential elastic scattering cross-sections for 2.99 Mev or 3 Mev neutrons on calcium. Differential cross-section measurements on calcium reported by Abramson et al[10] for a neutron energy of 2.83 Mev and Reber and Brandenburger[11] working at a neutron energy of 3.29 Mev are also shown in figure 6.8. The measurements at the latter energy were obtained using a cylindrical scattering sample. Subsequent corrections were made to the data for neutron multiple scattering and attenuation. The data was also

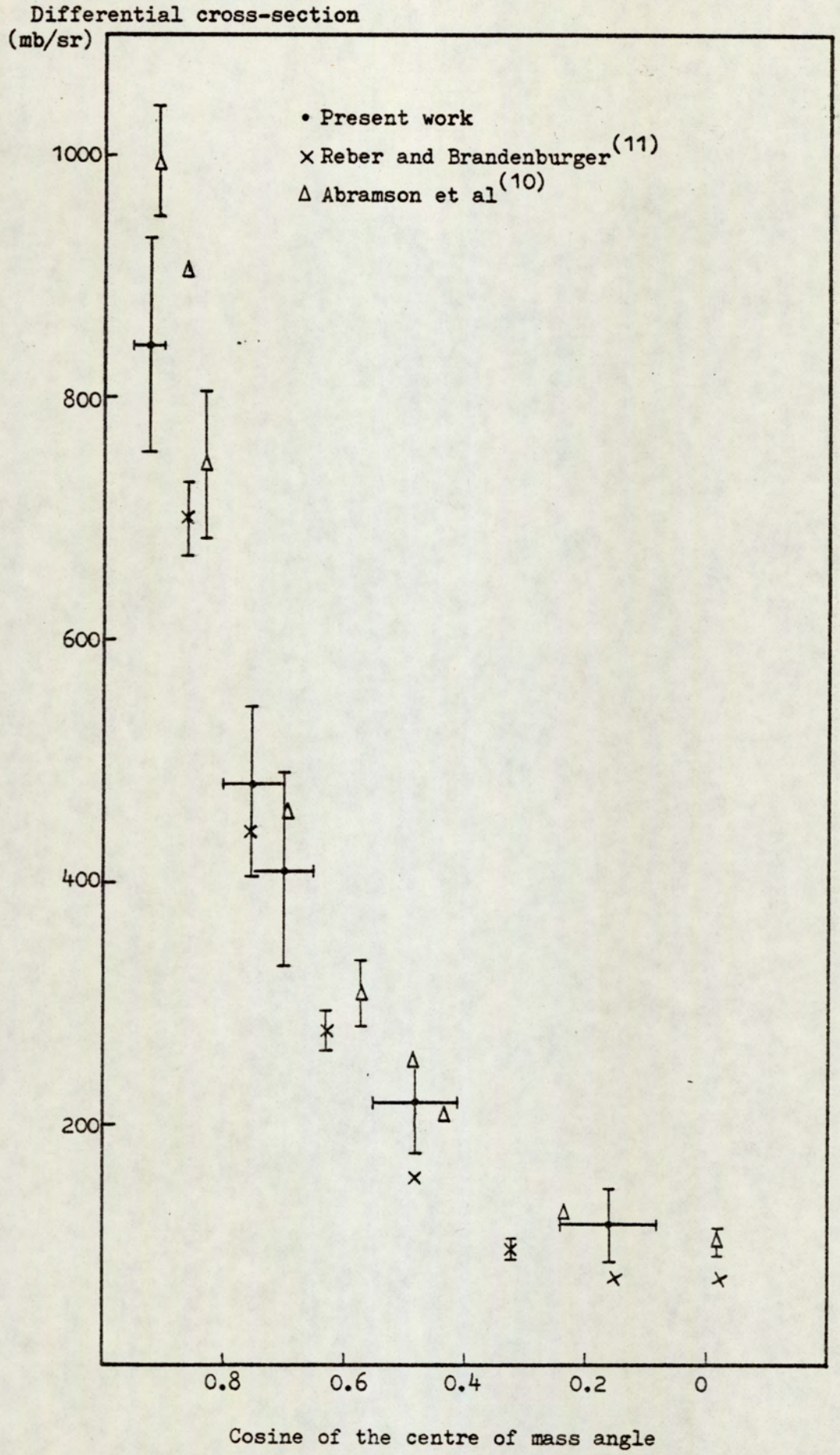

Figure 6.8 Comparison of the measurements of the differential elastic scattering cross-section for calcium.

TABLE 6.1

CALCIUM DIFFERENTIAL ELASTIC SCATTERING CROSS-SECTION DATA

Centre of Mass Scattering Angle (degrees)	Cosine value of scattering angle	Differential cross-section (mb/sr)	Experimental Error (mb/sr)
20.49	0.937	841	97
40.93	0.756	477	64
46.02	0.694	409	80
61.25	0.481	216	41
81.42	0.149	113	30

corrected for the angular resolution of the detector, this being $\pm$ 7.6° which compares with the angular resolution in the present work of $\pm$ 8°. The data obtained at 2.83 Mev was corrected for absorption and multiple scattering, the angular resolution was not given. The measurements in the present work fall between the measurements at 2.83 Mev and 3.29 Mev.

A comparison of the present measurements with the optical model predictions is discussed in Chapter 7.

6.13 Sulphur Differential Elastic Scattering Cross-section Measurements for 2.18 Mev Neutrons

Time-of-flight spectra were accumulated at laboratory angles of 20°, 40°, 60°, 80° and 100°. Typical spectra obtained are shown in figures 6.9, 6.10 and 6.11.

The main isotope in the sulphur sample was $^{32}_{16}S$ which has an isotropic abundance of 95.0%[67]. The first excited state of this isotope is 2.23 Mev[68] above the ground state, on excitation to this level it can decay by γ -ray emission back to the ground state. Although the mean neutron energy is 2.18 Mev the defined neutron beam considered in section 2.10 was shown to have an energy spread from 2.06 Mev to 2.3 Mev. A fraction of the neutron beam can therefore produce inelastic collisions in the sulphur. Due to the resolution of the time-of-flight spectrometer and the distance of the neutron detector from the sample, the γ -rays and elastically scattered neutrons cannot be resolved. Typically, the γ -rays will take 2 ns to reach the neutron detector at 50 cm from the sample, while the neutrons will take 24 ns. To completely resolve the γ -rays from the elastically scattered neutrons the neutron detector should be moved to about 1.5 m from the sample. This was considered undesirable as the neutron flux intensity is inversely proportional

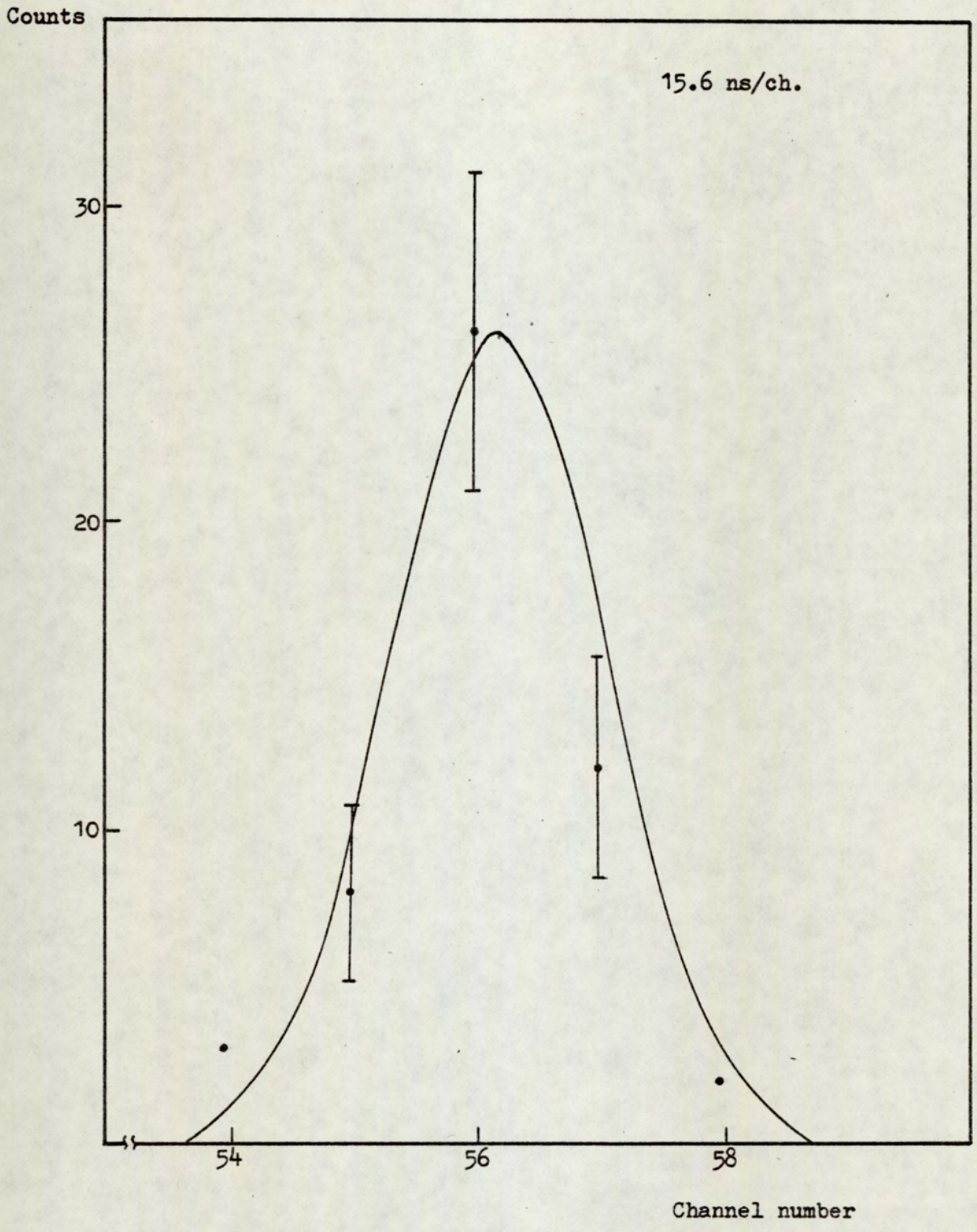

Figure 6.9 Time-of-flight spectrum for scattering from sulphur at 20° in the laboratory system.

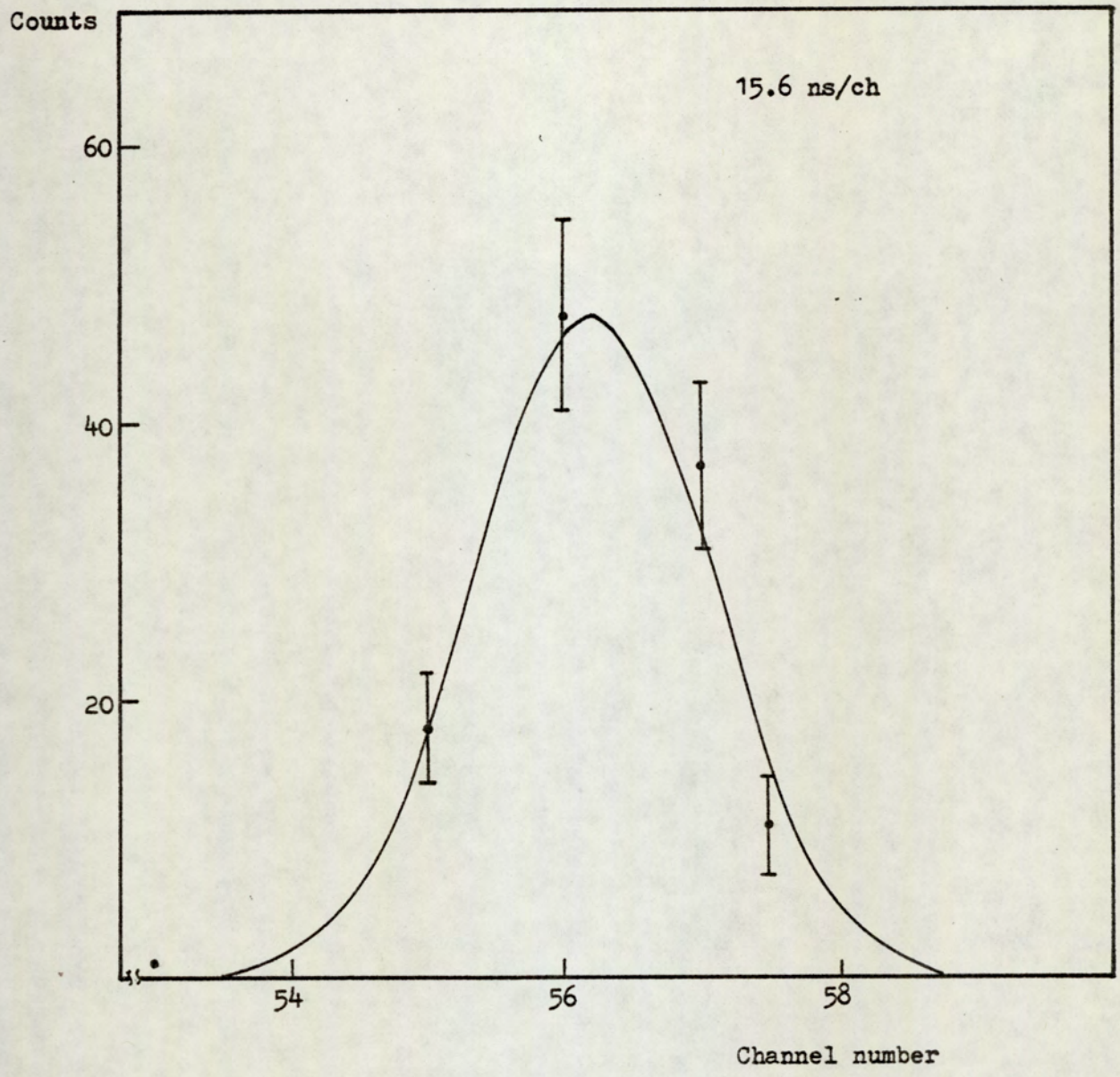

Figure 6.10 Time-of-flight spectrum for scattering from sulphur at 40° in the laboratory system.

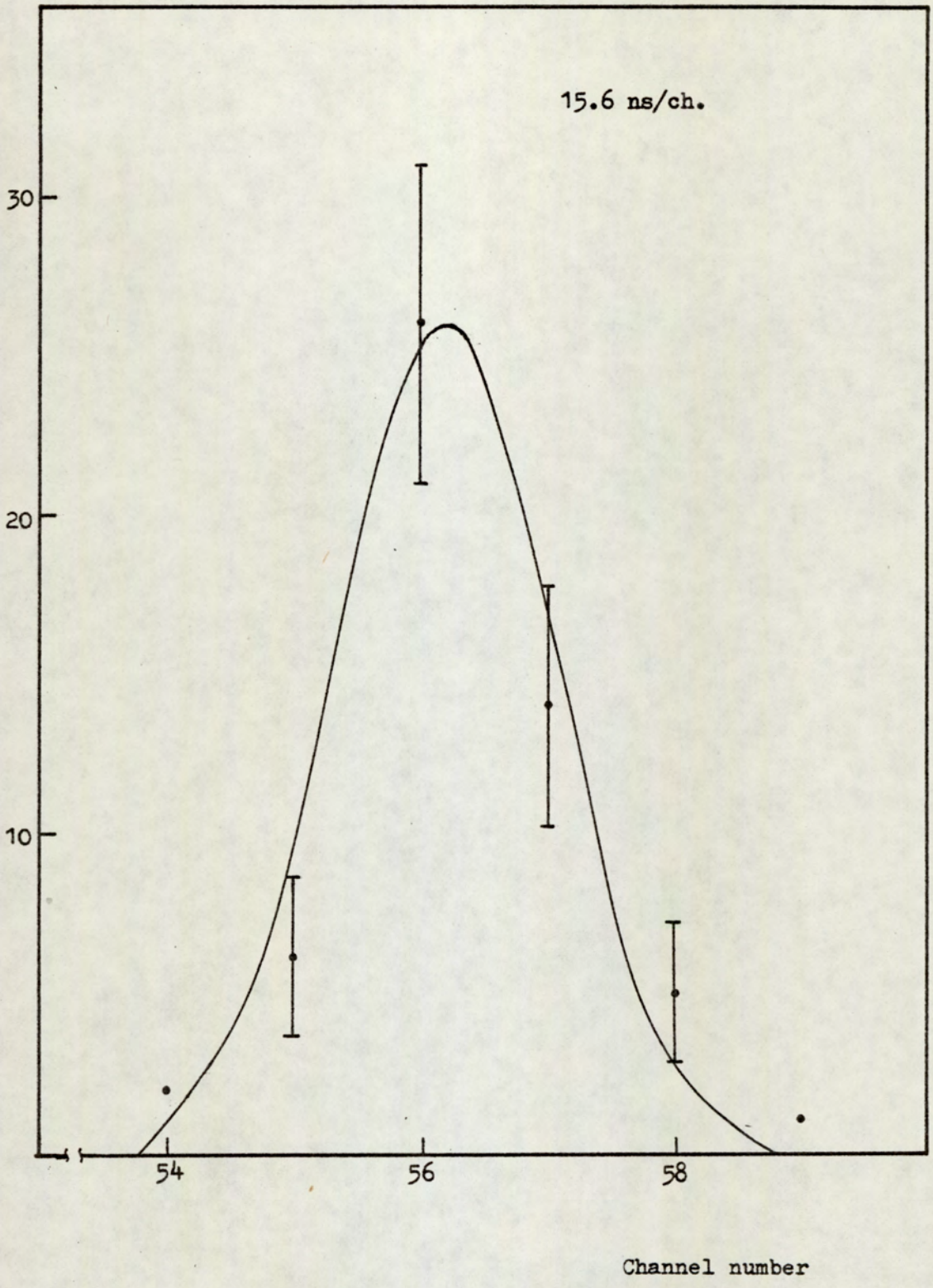

Figure 6.11 Time-of-flight spectrum for scattering from sulphur at 60° in the laboratory system.

to the square of the separation between the source and detector, moving the detector further away would lead to a significant reduction in the scattered neutron intensity reaching the detector. In section 2.10 the relative neutron yield was calculated as a function of the neutron energy thus giving the neutron line shape for the particular neutron production angle, this is shown in figure 2.33 for a neutron production angle of 120° with respect to the incident deuteron direction.

The fraction of neutrons of the defined beam with an energy over 2.23 Mev was found from figure 2.33. The percentage of neutrons capable of producing inelastic collisions was calculated at 10.3%. Day[62] has obtained the differential cross-section for the inelastic scattering of 2.56 Mev neutrons from sulphur. The measured differential cross-section was isotropic to within $\pm$ 5% and had a value of 173 $\pm$ 16 mb/steradian. As only 10.3% of the neutrons in the present work could interact to produce γ -rays, the effective contribution to each measured differential elastic scattering cross-section was 17.3 mb/steradian ($\pm$ 15%). The neutron line shape curve was assumed to be accurate to 5%, also it was assumed that the value of the differential cross-section for inelastic scattering at 2.56 Mev was the same for the neutron energies under consideration in the present work.

In view of larger experimental uncertainties introduced elsewhere the γ -ray contribution in the time spectra was considered negligible.

As the ^{3}He counts were monitored directly the differential elastic scattering cross-sections were evaluated using the equation:-

$$\frac{d\sigma}{dw}(\vartheta) = \frac{N(\vartheta)}{n\bar{x}(\phi_{^{3}He})\,\Delta w\;\varepsilon(E_n)C} \qquad \ldots\ldots 6.17$$

6.13.1 Experimental Errors

The experimental errors, listed below, were essentially the same as those given in section 6.12.1.

Term	Percentage error
$N(\vartheta)$	$(\Sigma e_i^2)^{\frac{1}{2}}$
n	2%
$\bar{x}$	4%
$\phi_{^3He}$	< 1%
Δw	1%
$\varepsilon(E_n)$	6%
C	2%

Again each experimental point was subject to an angular uncertainty of $\pm 8^{\circ}$.

6.13.2 Angular Distribution

The calculated cross-sections were plotted as a function of the cosine of the centre of mass angle and are shown in figure 6.12. The results are also presented in table 6.2. No published experimental values could be found for a neutron energy of 2.18 Mev and the results of Holmqvist and Wiedling[69] obtained at a neutron energy of 2.47 Mev are shown in figure 6.12 for comparison. The differential elastic scattering cross-sections obtained at 2.47 Mev were measured relative to the neutron-proton cross-sections. Corrections were made for neutron multiple scattering and attenuation in the cylindrical scattering sample.

A comparison of the present measurements with the optical model predictions is discussed in Chapter 7.

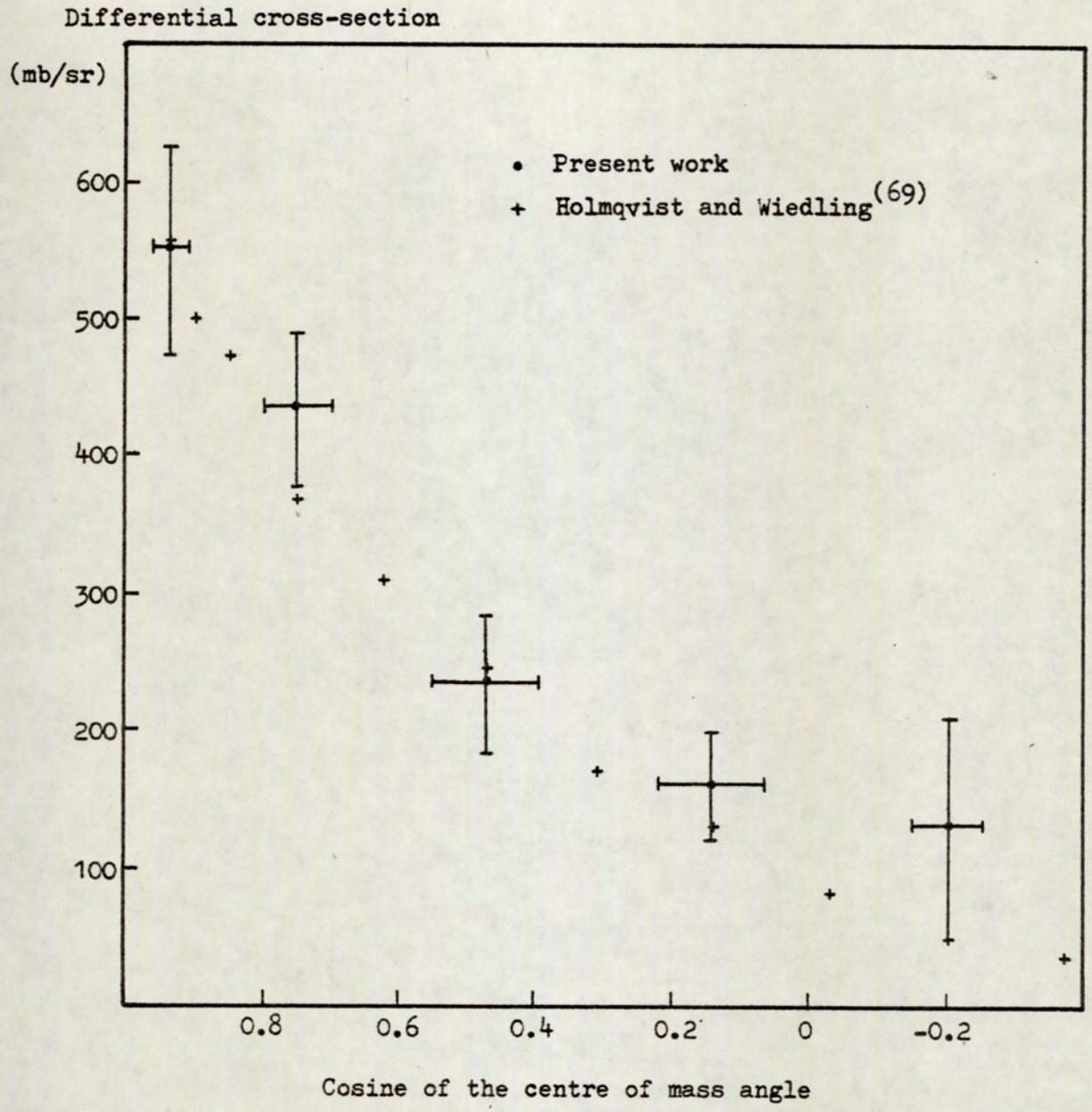

Figure 6.12 Comparison of the measurements of the differential elastic scattering cross-sections for sulphur.

TABLE 6.2

SULPHUR DIFFERENTIAL ELASTIC SCATTERING CROSS-SECTION DATA

Centre of Mass Scattering Angle (degrees)	Cosine value of scattering angle	Differential cross-section (mb/sr)	Experimental Error (mb/sr)
20.62	0.936	552	77
41.16	0.753	435	56
61.57	0.476	235	49
81.78	0.143	162	40
101.78	-0.204	126	80

6.14 Background Considerations

In obtaining the time-of-flight spectra at a neutron energy of 2.18 Mev it was observed that the background due to random coincidences was significantly reduced in comparison to measurements for 2.99 Mev neutrons.

For the production of 2.18 Mev neutrons the angle of emission was 120° with respect to the incident deuteron direction. The associated ^{3}He particles were detected at 31.2°, and the charged particle energy spectrum, figure 3.12, showed the ^{3}He peak well resolved. An electronic window across the ^{3}He peak allowed only these events to operate the time converter.

For the production of 2.99 Mev neutrons the emission angle was 75°, this corresponds to an associated ^{3}He angle of 61.3°. The energy spectrum, figure 3.11, showed the ^{3}He peak situated on a large deuteron background, an electronic window across the ^{3}He peak also allowed unrelated deuteron pulses to operate the time converter. In this situation the time converter was operated not only by true ^{3}He pulses, as was the case for 2.18 Mev neutrons, but also by the deuteron background. This background, if operating the time converter could produce random coincidences with neutron and γ-ray background detected in the neutron detector. Thus an increase in the random coincidence background could be expected in comparison to when only true ^{3}He events operate the time converter.

CHAPTER 7

OPTICAL MODEL ANALYSIS OF THE EXPERIMENTAL RESULTS

7.1 Optical Model Analysis

The optical model has been used very successfully in the analysis of elastic scattering of neutrons by medium and heavy weight nuclei, as these approach the limit of uniform nuclear matter. Many investigations have shown that neutron elastic scattering cross-sections can be well represented by the optical model with a complex potential with suitably adjusted parameters.

The optical model analysis was performed using the computer search code RAROMP (Regular and Reformulated Optical Model Programme) at the Rutherford High Energy laboratory . The present section gives a brief description of the mathematical formulation and method of solution used in the computer code.

The optical potential $U_{OP}(r)$ can be written as:-

$$U_{OP}(r) = U_R(r) + iW_I(r) + U_S(r) \qquad \ldots\ldots 7.1$$

where r is the separation of the target nucleus and the incident neutron, U_R and W_I are the real and imaginary parts of the central potential and U_S is the spin-orbit potential.

To calculate the cross-sections for two particles interacting through the potential in equation 7.1 Shrödinger's equation is applied to the whole system, viz:-

$$\frac{\hbar^2}{2m}\nabla^2\psi + (E - U_{OP})\psi = 0 \qquad \ldots\ldots 7.2$$

where U_{OP} is defined in equation 7.1, E is the centre of mass energy, $\hbar = h/2\pi$ here h is Plancks constant, ψ is the wave function and m is the reduced mass, given by:-

$$m = \frac{M_1 M_2}{M_1 + M_2} \qquad \ldots\ldots 7.3$$

where M_1 and M_2 are the neutron and target nuclei masses.

The separation of the radial and angular parts leads to the radial Shrödinger equation:-

$$\left[\frac{d^2}{dr^2} - \frac{l(l+1)}{r^2} + k^2 - \frac{2m}{\hbar^2} U_{OP}(r)\right] \psi_l^{\pm}(r) = 0 \qquad \ldots\ldots 7.4$$

where the superscripts + or - denotes the solutions for total angular momentum $j = l + {}^1/2$ or $l - {}^1/2$, respectively. The wave number k is found from:-

$$k = (2mE/\hbar^2)^{\frac{1}{2}} \qquad \ldots\ldots 7.5$$

The solution of equation 7.4 has both real and imaginary components as the potential U_{OP} is complex. Within the nuclear potential the solution of equation 7.4 is obtained by step-by-step numerical integration from the origin to a point R, where the nuclear field is negligible. Beyond this point $U_{OP}(r)$ may be omitted from equation 7.4 and the remaining equation can be solved analytically to give the asymtotic form of the radial wave function as a combination of spherical Bessel functions, this is then matched to the numerical solution to give:-

$$\psi_l^{\pm}(R) \sim F_l(R) + iG_l(R) + S_l^{\pm}[F_l(R) - iG_l(R)] \qquad \ldots\ldots 7.5$$

where $F_l(R)$ and $G_l(R)$ are Bessel functions, and the coefficients $S_l^{\pm}$ are related to the nuclear phase shifts, $\delta_l^{\pm}$ by:-

$$S_l^{\pm} = \exp(2i\delta_l^{\pm}) \qquad \ldots\ldots 7.6$$

With the phase shifts thus calculated the various cross-sections can be evaluated.

Considering the specific case where both the incident particles and the nucleus are without spin, a free particle moving with energy E parallel to the Z-axis, with respect to a scattering centre, can be represented by a plane wave:-

$$\psi_{inc} = e^{ikz} \qquad \ldots\ldots 7.7$$

Expressing z as a function of r and ϑ by the relation $z = r\cos\vartheta$, the plane wave can be expanded in a series of spherical harmonics viz:-

$$e^{ikz} = \sum_{l=0}^{\infty} i^l \frac{2l+1}{2} \left[h_l^*(kr) + h_l(kr) \right] P_l(\cos\vartheta) \qquad \ldots\ldots 7.8$$

where $P_l(\cos\vartheta)$ is a Legendre polynomial and h^* and h are Hankel functions which represent an incoming and outgoing wave respectively. The total wave function, considering axial symmetry, shows the effect of the potential of the nucleus on the incident wave:-

$$\psi_{tot}(r,\vartheta) = \sum_{l=0}^{\infty} i^l \frac{2l+1}{2} \left[h_l^*(kr) + S_l h_l(kr) \right] P_l(\cos\vartheta) \qquad \ldots\ldots 7.9$$

where S_l previously defined is related to the nuclear phase shifts. The scattered wave is then given by:-

$$\psi_{scat}(r,\vartheta) = \psi_{tot}(r,\vartheta) - e^{ikz} \qquad \ldots\ldots 7.10$$

For incident neutrons which have a spin $^1/_2$, the plane wave which describes the free particles has the form:-

$$\psi_{inc} = e^{ikz} \chi_{inc} \qquad \ldots\ldots 7.11$$

where χ_{inc} describes the spin wave function of the neutron. In the presence of a nuclear potential the asymptotic form of the wave function of the neutron is given by the general solution of equation 7.2, viz:-

$$\psi_{tot} \sim \psi_{inc} + \frac{1}{r} e^{ikr} F(\vartheta) \chi_{inc} \qquad \ldots\ldots 7.12$$

where $F(\vartheta)$ is a scattering matrix which describes the amplitude of the wave for a particular spin orientated scattering mode, i.e. spin parallel or anti-parallel to angular momentum, and has the form:-

$$F(\vartheta) = A(\vartheta) + B(\vartheta) \qquad \ldots\ldots 7.13$$

The scattering amplitudes A and B are then evaluated by substituting the forms of ψ_{tot} and ψ_{inc} into equation 7.12. The total wave function, which has the form described by equation 7.9, will also include the spin wave function of the neutron. At a point far from the scattering centre the asymptotic forms of the Hankel functions can be used, i.e.:-

$$h^{*}_{l} \sim \frac{1}{kr} \exp\left(-i\left[kr-(l+1)\pi/2\right]\right) \qquad \ldots\ldots 7.14$$

and

$$h_{l} \sim \frac{1}{kr} \exp\left(i\left[kr-(l+1)\pi/2\right]\right) \qquad \ldots\ldots 7.15$$

The relevant equations for the scattering amplitudes obtained are given by:-

$$A(\vartheta) = \frac{1}{2ik} \sum_{l=0}^{\infty} \left[(l+1)\,(S_l^{+}-1)+l(S_l^{-}-1)\right] P_l(\cos\vartheta) \qquad \ldots\ldots 7.16$$

and

$$B(\vartheta) = \frac{1}{2k} \sum_{l=0}^{\infty} (S_l^+ - S_l^-) P_l^1 (\cos\vartheta) \qquad \ldots\ldots 7.17$$

where $P_l^1 (\cos\vartheta)$ is a Legendre function.

The differential shape elastic scattering cross-section for an unpolarised beam is obtained from:-

$$\sigma_{SE} (\vartheta) = |A|^2 + |B|^2 \qquad \ldots\ldots 7.18$$

In order to predict the theoretical cross-section values, forms are required for the various potentials defined in equation 7.1, this aspect is considered in the next section.

7.2 The Potential Forms

The optical potential usedwas a combination of Woods-Saxon volume and surface derivative forms. From equation 7.1 the optical potential is given by:-

$$U_{OP} (r) = U_R (r) + i W_I (r) + U_S (r)$$

where $U_R(r)$ is the real central potential expressed as:-

$$U_R (r) = -V_R f(r, R_R, a_R) \qquad \ldots\ldots 7.19$$

The form factor for the potential is that of Woods-Saxon type represented by:-

$$f(r,R,a) = \left[1 + \exp\frac{(r - R)}{a} \right]^{-1} \qquad \ldots\ldots 7.20$$

where R is the nuclear radius and a is the diffuseness parameter.

The real potential is responsible for the shape elastic scattering. The imaginary potential $iW_I(r)$ which accounts for the absorption process consists of surface W_d and volume W_v absorption potentials, and is given by:-

$$iW_I(r) = -W_v\, f(r,R_I^{1},a_I^{1}) + 4a_I\, W_d \frac{d}{dr} f(r,R_I,a_I) \qquad \ldots\ldots 7.21$$

The imaginary volume has the same potential form as the real central potential, described by equation 7.20, while the surface absorption has a Woods-Saxon derivative form.

The spin orbital potential was assumed to have the usual Thomas form:-

$$U_S(r) = -(V_S+i\,W_S)\left(\frac{\hbar}{m_\pi c}\right)^2 \frac{1}{r}\frac{d}{dr} f(r,R_S,a_S)\, \bar{l}.\,\bar{\sigma} \qquad \ldots\ldots 7.22$$

where the coefficient $(h/m_\pi c)^2$ is the square of half the pion Compton wavelength introduced to keep the dimensions of $U_S(r)$ correct, here m_π is the pion mass, c is the velocity of light and $\hbar = h/2\pi$. In equation 7.22 $\bar{l}$ is the orbital angular momentum of the neutron and $\bar{\sigma}$ is the Pauli spin operator. The spin orbital potential $U_S(r)$ is normally taken to be purely real i.e. $W_S = 0$, this criteria was applied in the present analysis.

The radius parameter in equation 7.20 is assumed to have an $A^{\frac{1}{3}}$ variation for all the radii, i.e. $R_R = r_R A^{\frac{1}{3}}$, where A is the mass number of the nuclei. By using the form factor of equation 7.20 in equations 7.19, 7.21 and 7.22 the radii for the real, imaginary and spin orbital potentials have the forms:-

$$\begin{aligned} R_R &= r_R A^{\frac{1}{3}} \\ R_S &= r_S A^{\frac{1}{3}} \\ R_I^{1} &= r_I^{1} A^{\frac{1}{3}} \\ R_I &= r_I A^{\frac{1}{3}} \end{aligned}$$

The strength and geometry of the optical potential is thus determined by V_R, r_R, a_R for the real central potential; V_S, r_S, a_S for the spin orbit potential; W_v, r_I^{1}, a_I^{1} for the imaginary volume and;

W_d, r_I, a_I for the imaginary surface.

7.3 Optical Model Parameters

Optical model studies have been carried out in order to determine "average sets" of optical model parameters applicable over a certain range of energies and mass numbers[8][9][70][71]. Due to inherent parameter ambiguities in the optical model it has been found best in analysing individual data sets to use parameter sets which have been determined systematically over the range of energies and mass numbers in the region of interest, rather than use ambiguous best-fit parameters to a single distribution. Parameters obtained from a single angular distribution may be strongly affected by systematic experimental errors and particular reaction mechanisms occurring at that energy of the nucleus.

In the present analysis the values for the optical model parameters obtained by Becchetti and Greenlees[71] for mass numbers > 40 and energies < 50 Mev were used as initial values to predict differential cross-section values for calcium and sulphur. Subsequent adjustments were made to the parameters to obtain the "best-fit" between the experimental and theoretical values.

Initial values used to predict theoretical differential cross-section data, taken from Becchetti and Greenlees[71] were:-

$$V_R = 56.3 - 0.32E - 24.0\,(N-Z)/A \qquad - 7.23$$

$$r_R = 1.17 \qquad - 7.24$$

$$a_R = 0.75 \qquad - 7.25$$

$$W_v = 0.22\text{-}1.56 \text{ or zero whichever is greater} \qquad - 7.26$$

$$W_d = 13.0\text{-}0.25E\text{-}12(N-Z)/A \text{ or zero whichever is greater} \qquad - 7.27$$

$$r_I = r_I^{\,1} = 1.26 \qquad - 7.28$$

$$a_I = a_I^{\,1} = 0.58 \qquad - 7.29$$

$V_S = 6.2$ - 7.30

$r_S = 1.01$ - 7.31

$a_S = 0.75$ - 7.32

where all the potential strengths are in Mev, E is the neutron energy in Mev in the laboratory system, and the geometric parameters are in femtometers (fm).

The value of the imaginary volume potential W_v in equation 7.26 is zero for all incident energies below 7.1 Mev. For energies below 20 Mev it has been found that the data can be satisfactorily represented using only a pure surface form for the imaginary part of the potential[70][72][73]. In addition the spin orbit potential V_S does not greatly affect the calculated cross-section at forward angles, it does however modify them at backward angles[73]. In the present analysis the values of the spin orbit terms were kept constant.

The parameters which were varied in order to obtain agreement between theoretical values and experimental data were V_R, r_R, a_R, W_d, a_I and r_I.

7.4 Fitting Procedure

The criteria most widely used to compare theoretical and experimental quantities is that of determining the quantity χ^2 [74][75][76]. In the present analysis the quantity χ^2/point was used for the comparison, where:-

$$\chi^2/\text{point} = \frac{1}{N_d} \sum_{i}^{N_d} \left\{ \frac{\sigma_{th}(\vartheta_i) - \sigma_{ex}(\vartheta_i)}{\Delta \sigma_{ex}(\vartheta_i)} \right\}^2 \qquad \ldots\ldots 7.33$$

where $\sigma_{ex}(\vartheta_i)$ is the measured experimental differential cross-section with an associated error of $\pm \Delta \sigma_{ex}(\vartheta_i)$ at a centre of mass angle ϑ_i, and $\sigma_{th}(\vartheta_i)$ is the differential cross-section

predicted by the optical model, the summation runs over all the N_d experimental points. Thus the lower χ^2 the better the fit.

In the iteration procedure in the computer programme the value of the parameters under investigation are systematically varied until the minimum value of χ^2 is found.

7.5 Averaging Option

Due to the finite angular resolution of the neutron detector the measured differential cross-sections are subject to appreciable experimental averaging. In the computer programme the theoretical quantities can be averaged over the experimental angular resolution before making the χ^2 comparison, i.e.:-

$$\bar{\sigma}(\vartheta) = \int_{-\Delta\vartheta}^{\Delta\vartheta} \sigma(\vartheta)\, d\vartheta \qquad \ldots\ldots 7.34$$

where $\pm \Delta\vartheta$ is the experimental angular resolution.

This option was used in the present analysis to average the theoretical values over the detector angular resolution of $\pm 8^{\circ}$.

7.6 Compound Elastic Scattering Considerations

At low energies < 6 Mev the differential elastic cross-sections predicted by the optical model should be less than the experimental values due to the presence of compound elastic scattering. As the optical model programme used predicts shape elastic scattering only, an estimate must be made of the compound elastic scattering.

Perey and Buck[8] have fitted neutron elastic scattering data from 4 Mev to 24 Mev for a range of nuclei by a single energy independent non-local optical potential. The potential obtained gave a good fit to cross-sections in the range of nuclei and energies considered and was used to predict reaction cross-sections and differential elastic cross-sections at energies between 1 Mev and

6 Mev. The theoretical reaction cross-sections at these energies were higher than experimental non-elastic cross-sections as the theoretical values consisted of the sum of the compound elastic cross-section σ_{CE} and the true reaction or non-elastic cross-section σ_{NE}, viz:-

$$\sigma_R = \sigma_{CE} + \sigma_{NE} \qquad \ldots\ldots 7.35$$

Experimental values were available for σ_{NE} on the elements and energies chosen for the analysis, hence σ_{CE} could be deduced. For energies where compound elastic scattering was negligible, the predicted reaction cross-sections were in agreement with experimentally determined non-elastic cross-sections. When this was not the case, the experimental angular distributions were corrected by assuming the compound elastic scattering to be isotropic, hence:-

$$\frac{d\sigma}{dw}_{CE} = \frac{\sigma_{CE}}{4\pi} \qquad \ldots\ldots 7.36$$

The corrected angular distributions gave good agreement with the theoretical predictions.

This method was used by Wilmore and Hodgson[9] in fitting an equivalent local potential to various elements including calcium and sulphur for neutron energies between 1 Mev and 15 Mev. Again good agreement was obtained between theoretical and experimental values for energies where compound elastic scattering was negligible. The model was then used to predict values for the differential elastic and reaction cross-sections for energies where compound elastic scattering was not negligible. For energies where published values were available on the non-elastic cross-sections, the values of the compound elastic cross-section were calculated from equation 7.35. For energies where no published values of σ_{NE} were available, the

values of σ_{CE} were obtained by assuming that the compound elastic cross-sections vary smoothly with energy and fall rapidly to zero at energies where the number of inelastic channels becomes large. The differential cross-sections were again calculated from equation 7.36.

Values for the differential compound elastic cross-sections obtained by Wilmore and Hodgson[9], for the energies under consideration in the present work, were 84 mb/steradian for calcium and 50 mb/steradian for sulphur. These values were used in the present analysis.

The optical model analysis of each element was carried out in two parts. The data was first fitted uncorrected for compound elastic scattering, the experimental data was then corrected by subtracting the compound elastic contribution and the best-fit obtained.

7.7 Optical Model Analysis of $^{40}_{20}Ca$

As a first step, an initial comparison was made between the experimental data (uncorrected for compound elastic scattering) and the theoretical predictions of the optical model using the values of Becchetti and Greenlees[71] indicated in equations 7.23 to 7.32. The values of the real central and imaginary surface potentials for 2.99 Mev neutrons were calculated from equations 7.23 and 7.27, giving:-

$$V_R = 55.34 \text{ Mev} \qquad - 7.37$$

$$W_d = 12.25 \text{ Mev} \qquad - 7.38$$

A comparison between the theoretical angular distribution and the experimental points is shown in figure 7.1. As expected the agreement is poor and is typical of optical model predictions at low

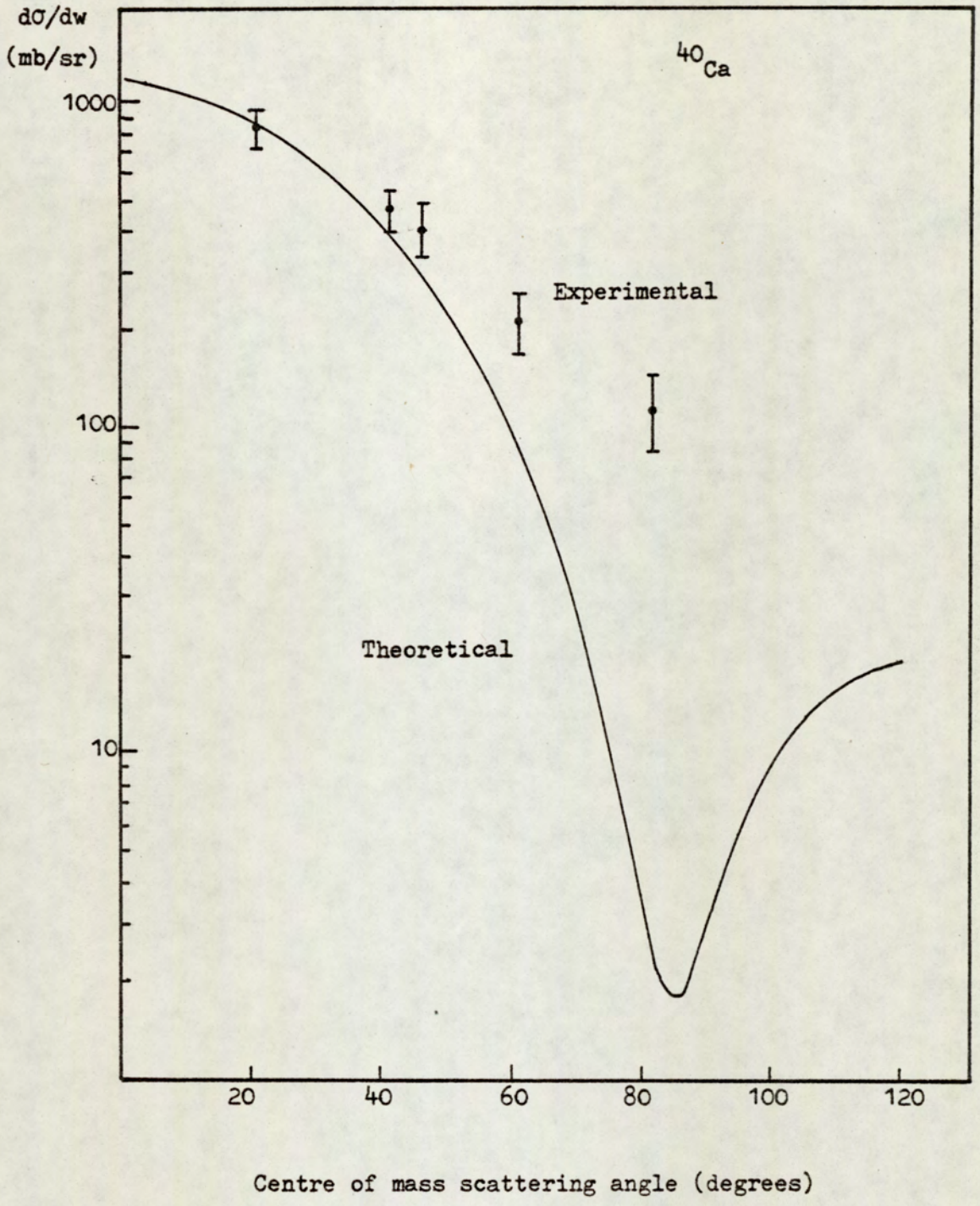

Figure 7.1 Optical model predictions for calcium with the parameters of Beechetti and Greenlees - data not corrected for compound elastic scattering.

energies (< 6 Mev)[8][9]. The value of χ^2/point for this fit was 5.98. Better agreement was achieved by varying the values of the parameters for V_R, r_R, a_R, W_d, r_I and a_I.

Initially the two potentials were optimised by searching on V_R and W_d, the geometric terms were kept constant. After twenty-four iterations the values of the two potentials and χ^2/point remained constant indicating that the potentials had been optimised, the values obtained were:-

$$V_R = 38.68 \text{ Mev} \qquad - 7.39$$

$$W_d = 1.04 \text{ Mev} \qquad - 7.40$$

$$\chi^2/\text{point} = 0.085 \qquad - 7.41$$

The lower value of χ^2/point indicated that there was an overall improvement of the fit.

The next stage of the analysis investigated the effect on the fit of optimising the radius term r_I. A search was performed on the values of V_R, W_d and r_I, the optimum values of the potentials in equations 7.39 and 7.40 were used as starting values. The value of χ^2/point remained constant, after three iterations, at a value of 0.066. By comparison to the value of χ^2/point in equation 7.41, the optimisation of r_I gave theoretical values which were in better agreement with the experimental cross-sections.

By increasing the extent of the search to incorporate the diffuseness parameters a_R and a_I the overall fit was improved further. Initially a search was performed on the parameters V_R, a_R, W_d, r_I where the optimum values of V_R, W_d and r_I obtained from the previous search were used as starting values, six iterations were required to optimise the parameters. In the next stage of the analysis difficulty was encountered in searching on five parameters i.e. a search on V_R, a_R, W_d, r_I, a_I. In order to optimise the value

of the diffuseness term, a_I the parameters V_R, a_R, W_d and r_I were fixed at the optimum values obtained from the previous search. A separate search was then performed on a_I, after two iterations the value of a_I remained constant at 0.55 fm, the value of χ^2/point was 0.063. This optimum value of a_I was then substituted in the two searches of V_R, W_d, r_I and V_R, a_R, W_d, r_I and improved fits were obtained. By fixing the parameters at the optimum values a further search was then performed on a_I and the final value of χ^2/point was 0.025.

As yet, the real radius parameter r_R has not been included in any of the searches undertaken. This was because of the well-known $V_R r_R$ ambiguity[77]. If both V_R and r_R are allowed to vary there is a large range of values over which $V_R r_R$ is constant and giving only a small change in the value of χ^2. To determine the optimum value of the real radius parameter the parameters V_R, a_R, W_d, r_I and a_I were kept fixed at the optimum values previously obtained. A search was then performed on r_R. However, no iterations were executed which indicated that the value of r_R given by Becchetti and Greenlees[71] of 1.17 fm was the optimum. The validity of this value in describing the optimum value of r_R is investigated in section 7.7.1.

The theoretical predictions for the angular distribution which gave the best fit to the experimental data which consisted of shape and compound elastic scattering is shown in figure 7.2, the value of χ^2/point for the final fit was 0.025.

In subtracting the estimated compound elastic scattering contribution of 84 mb/steradian from the experimental points, the optical model predictions obtained using the starting values of Becchetti and Greenlees were still low in comparison to the experimental data. The value of χ^2/point for the initial comparison was 3.46. Again, better agreement was obtained between

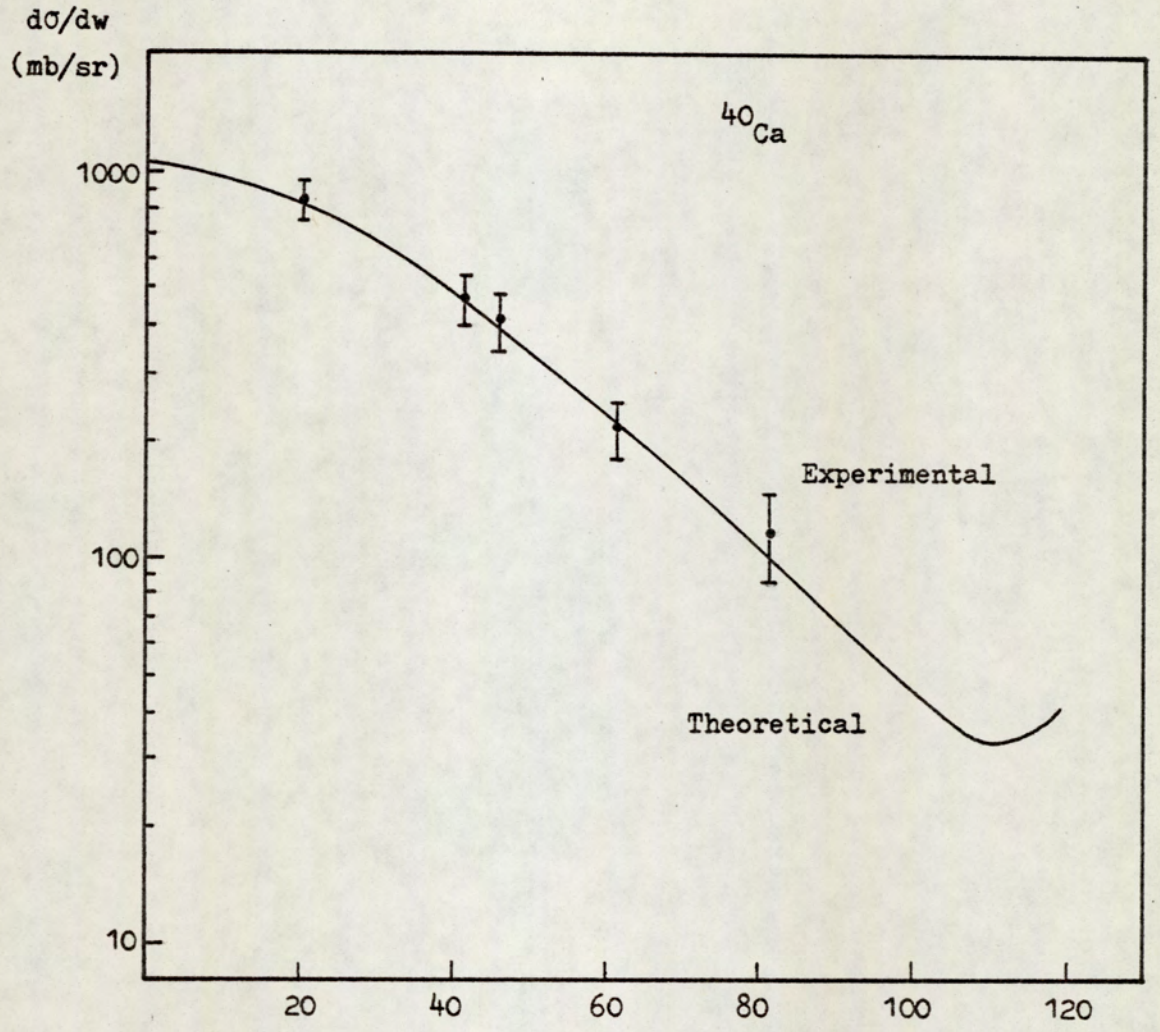

Figure 7.2 Best fit obtained between optical model predictions and experimental data not corrected for compound elastic scattering.

the theoretical differential cross-sections and the corrected experimental data by searching on the values of the parameters V_R, r_R, a_R, W_d, r_I and a_I. Initially the two potentials were searched on and eleven iterations were required to optimise the values, giving:-

$$V_R = 41.43 \text{ Mev} \qquad -7.42$$
$$W_d = 10.31 \text{ Mev} \qquad -7.43$$

the value of χ^2/point was 0.01. The technique used to obtain optimum values of the parameters was the same as the procedure employed in fitting the experimental data which was uncorrected for compound elastic scattering. Searches were performed on V_R, W_d, r_I and V_R, a_R, W_d, r_I and in both instances better overall fits were obtained. With the optimum values obtained a search was made on a_I, the value of χ^2/point for this fit was 0.0065. A search was then executed on V_R, a_R, W_d, r_I and the optimum values were then used in a further search on a_I. The final value of χ^2/point was 0.006. A separate search on the real radius parameter, r_R showed that the value given by Becchetti and Greenlees was the optimum value.

The experimental values corrected for compound elastic scattering and the optical model predictions (obtained with the optimised parameters) are shown in figure 7.3.

7.7.1 Optical Model Parameters

The optimised optical model parameters determined for calcium by the two analysis are given in table 7.1, also shown are the optical model results obtained by Reber and Brandenburger[11] for 3.29 Mev neutrons. In this latter analysis the experimental data was corrected for compound elastic scattering and only the potentials V_R, W_d and V_S were searched on in order to obtain an

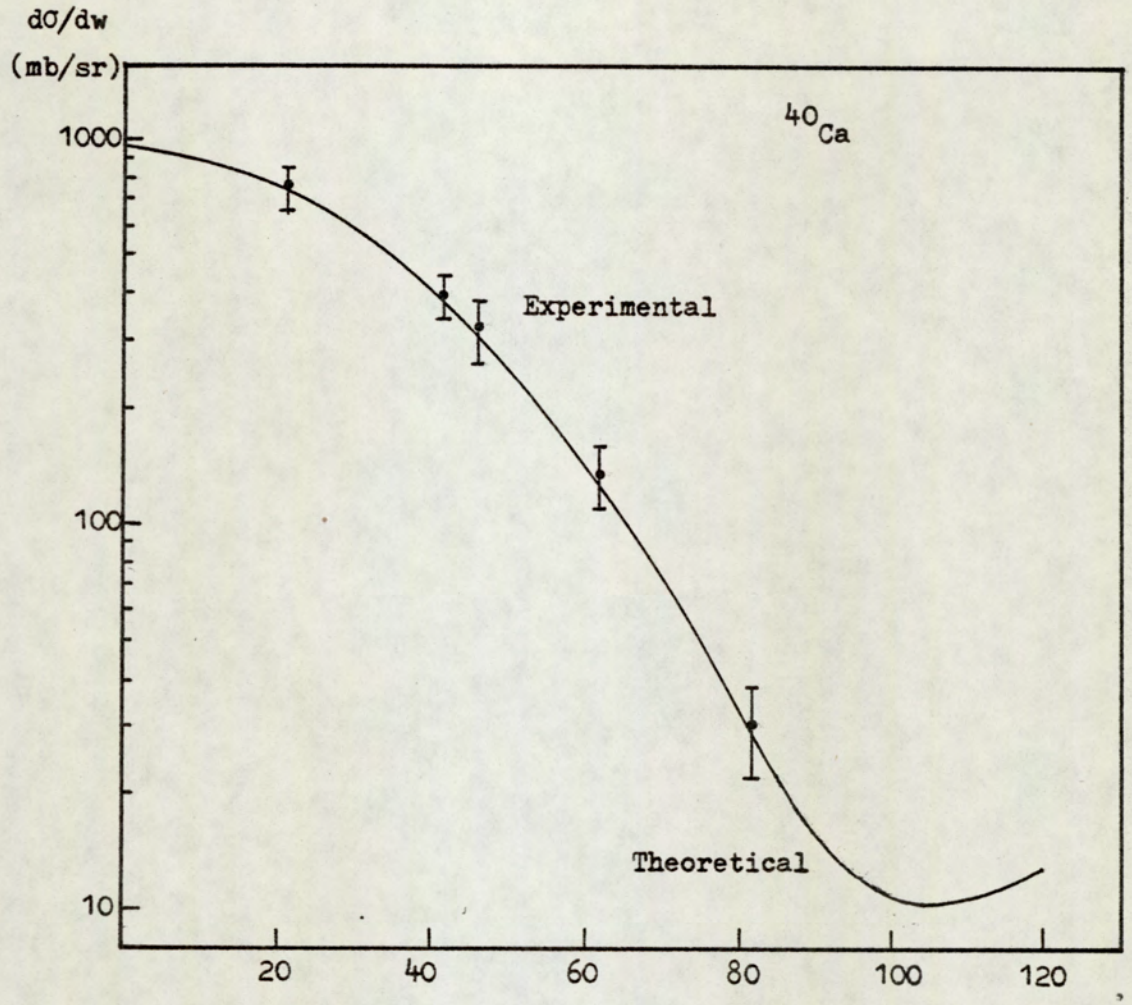

Figure 7.3 Best fit obtained between optical model predictions and experimental points corrected for compound elastic scattering.

TABLE 7.1

Optical Model Parameters obtained from the optimum fit to Calcium Elastic Scattering Data

Parameter	Data corrected for Compound Elastic Scattering	Data not corrected for Compound Elastic Scattering	Reber and Brandenburger
V_R (Mev)	45.94	38.66	51
r_R (fm)	1.17	1.17	1.25
a_R (fm)	0.55	0.73	0.65
W_d (Mev)	14.02	0.93	6.0
r_I (fm)	1.25	1.39	1.3
a_I (fm)	0.58	0.51	0.47
V_S (Mev)	6.2	6.2	2.0
r_S (fm)	1.01	1.01	1.25
a_S (fm)	0.75	0.75	0.65
σ_R (mb)	1485	892	-
χ^2/point	0.006	0.025	15.12

optimum fit. The value of χ^2/point for the best fit between experimental and theoretical values was 15.12 compared to a value of 0.006 in the present analysis when V_R, r_R, a_R, W_d, r_I and a_I were all optimised. The present analysis gave a better overall fit to the experimental data.

In the present analysis, the optimum value obtained for the imaginary surface potential for the experimental data, corrected for compound elastic scattering, was much higher than the value obtained when the uncorrected data was fitted. The higher absorption potential was in accordance with the higher predicted reaction cross-section which consisted of both compound elastic and non-elastic cross-sections.

When the experimental data was corrected for compound elastic scattering the optical model gave a better overall fit to the data, the value of χ^2/point was 0.006 in comparison to 0.025 for the optimum fit on the uncorrected data.

The sensitivity of the fit to the optical model parameters was investigated, i.e. the extent that χ^2/point changed when the value of a parameter was altered from the optimum value. The analysis was performed by initially fixing all the optical model parameters at the optimum values obtained previously, shown in table 7.1. The value of the parameter under investigation was then altered in steps either side of the optimum value, the values of the remaining parameters were kept fixed, the value of χ^2/point obtained at each step was then plotted against the parameter value.

Using this method the sensitivity of the fit to the geometric parameters r_R, a_R, r_I and a_I was investigated first. Figure 7.4 shows the sensitivity of the fit to the parameters obtained from the optimum fit on the experimental data containing compound elastic scattering. The fit is shown to be dependent mainly on the

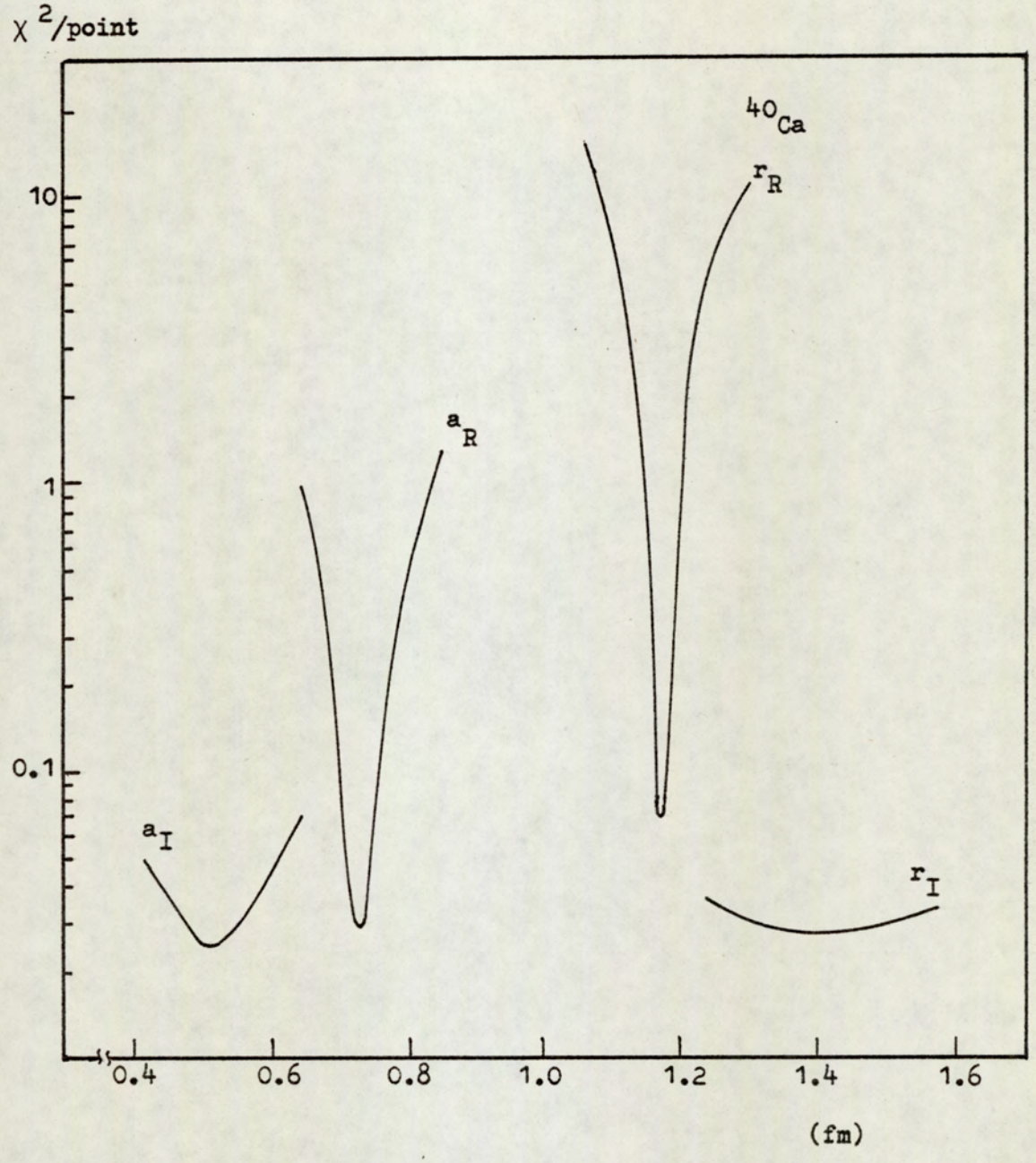

Figure 7.4 Effect on χ^2/point to variations in the geometric parameters

- data not corrected for compound elastic scattering.

geometry of the real central potential i.e. r_R and a_R. The optimum values of a_I and r_I are not so well defined. An 8% change in the value of r_I produced no noticeable change in χ^2, whereas the same percentage change in the optimum value of r_R increases the value of χ^2/point from 0.062 to about 4.0.

Figure 7.5 shows the effect on χ^2/point of varying the geometric parameters obtained from the optimum fit to the experimental data corrected for compound elastic scattering. The values of r_R, a_R, r_I and a_I are well defined in producing a minimum value of χ^2.

The optimum value of r_R, for both analysis, is shown to be well defined at the value obtained by Becchetti and Greenlees[71] of 1.17 fm.

Next, the effect on the value of χ^2 by varying the real and imaginary surface potentials was investigated. Figures 7.6 and 7.7 show the sensitivity of χ^2/point to variations in W_d and V_R for the cases where the experimental data was fitted with and without compound elastic corrections. In the case where the data was uncorrected the optimum values of V_R and W_d appear to be better defined than in the case where only the estimated shape elastic data was fitted.

7.8 Optical Model Analysis of $^{32}_{16}S$

The procedure for the analysis of the sulphur differential cross-section data was exactly the same as that for calcium. The values of the real central and imaginary surface potentials were evaluated for the incident neutron energy of 2.18 Mev from equations 7.23 and 7.27, giving:-

$$V_R = 55.6 \text{ Mev} \qquad - 7.44$$

$$W_d = 12.5 \text{ Mev} \qquad - 7.45$$

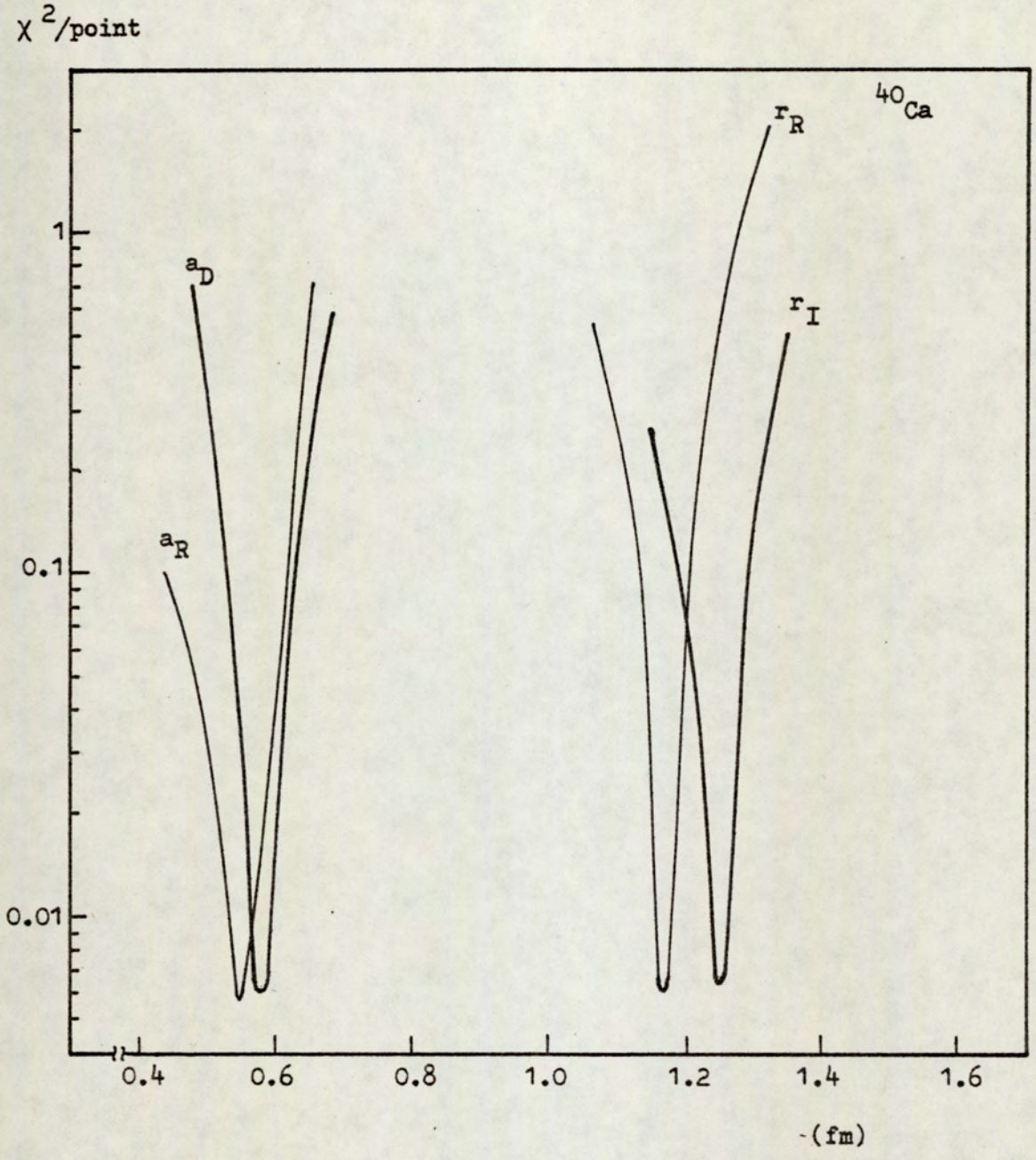

Figure 7.5 Effect on χ^2/point to variations in the geometric parameters

- data corrected for compound elastic scattering.

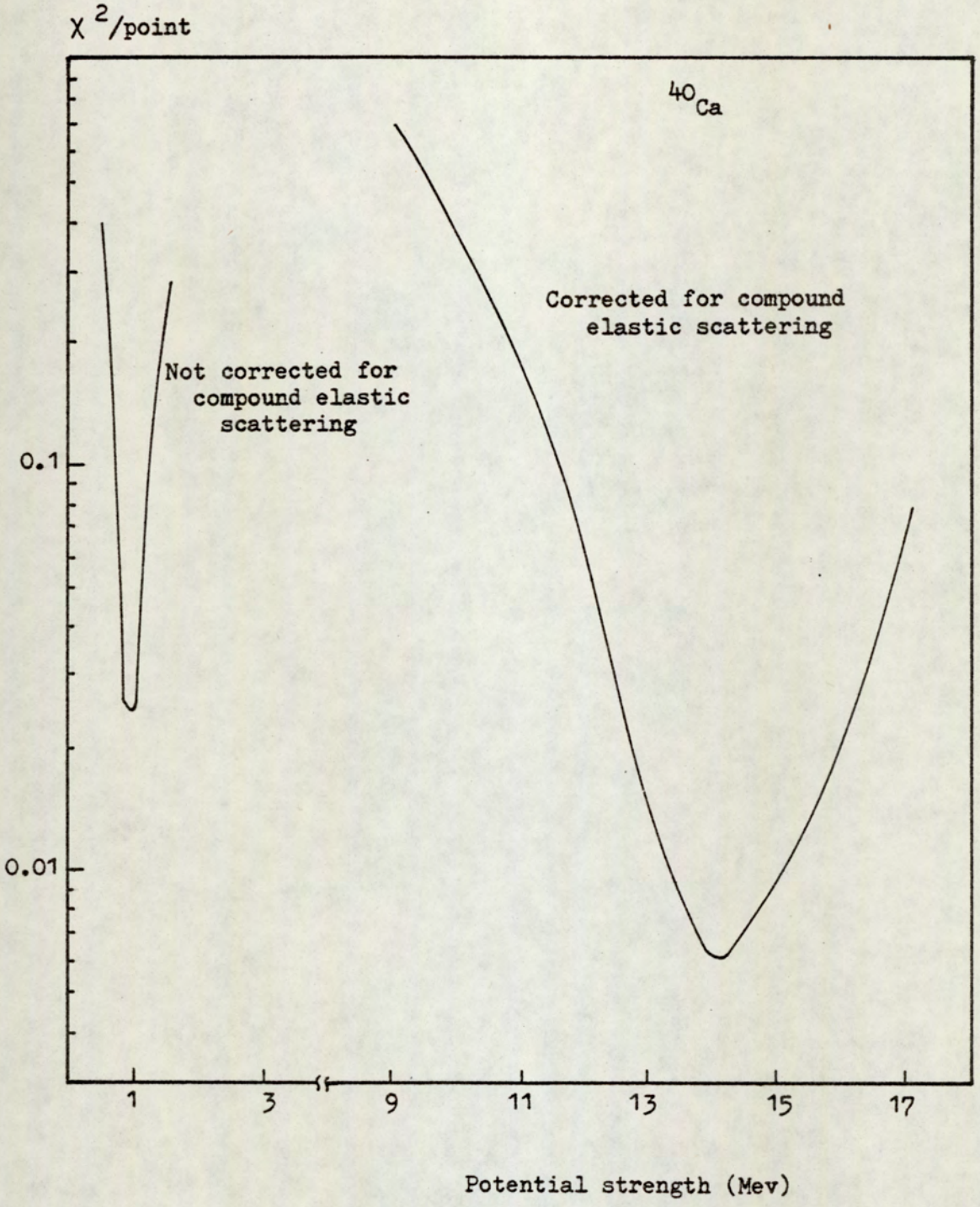

Figure 7.6 Effect on χ^2/point to variations in W_d

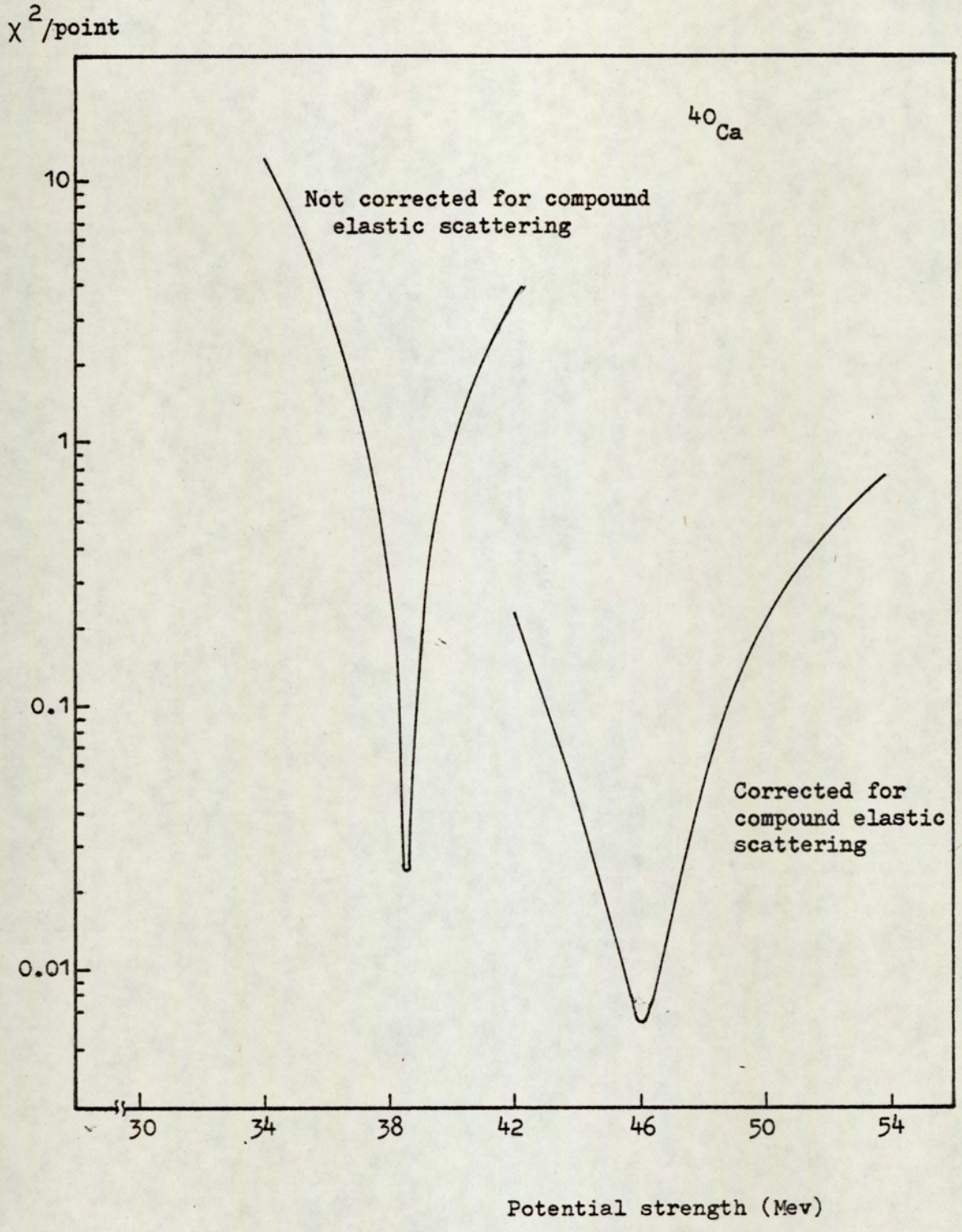

Figure 7.7 Effect on χ^2/point to variations in V_R

As an initial step, a comparison was made between the theoretical angular distributions obtained with the starting values of Becchetti and Greenlees and the experimental data not corrected for compound elastic scattering. The fit obtained is shown in figure 7.8 and the value of χ^2/point was 3.25, as expected the fit was poor.

As was the case with calcium better agreement was achieved by searching on the values of the parameters V_R, r_R, a_R, W_d, r_I and a_I. Initially a search was performed on the potentials V_R and W_d, after twenty-four iterations the values were optimised, giving:-

V_R	= 40.57 Mev	- 7.46
W_d	= 0.67	- 7.47
χ^2/point	= 0.26	- 7.48

Improvements in the fit were obtained by searching on V_R, W_d, r_I and V_R, a_R, W_d, r_I. The optimised values obtained from a fit were used as the starting values of the subsequent search. A search was then executed on a_I, here the optimised values obtained for the other parameters were kept fixed. The last two searches were repeated, i.e. searches on V_R, a_R, W_d, r_I and on a_I, the value of χ^2/point for the final fit was 0.22. A separate search on the real radius parameter, r_R showed that the value obtained by Becchetti and Greenlees[71], was again the optimum value. The optical model prediction for the angular distribution which gave the best agreement with the experimental data containing both shape and compound elastic contributions is shown in figure 7.9.

The predictions of the optical model, using the initial values of Becchetti and Greenlees, gave better agreement when the estimated differential compound elastic cross-section of 50 mb/steradian was subtracted from each experimental point, i.e. the value of χ^2/point for the initial comparison was 2.84. However, better agreement was

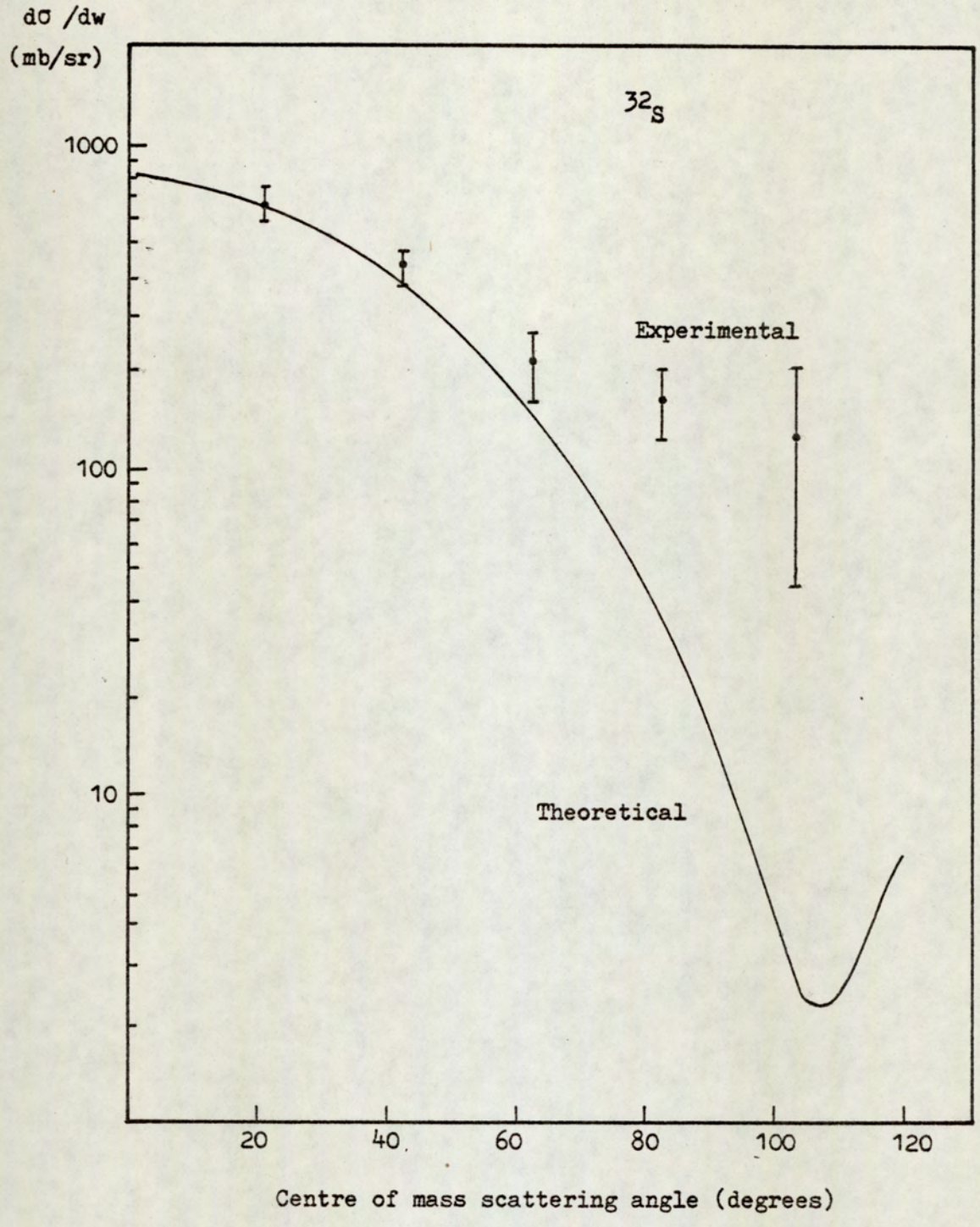

Figure 7.8 Optical model predictions with the parameters of Becchetti and Greenlees
- data not corrected for compound elastic scattering

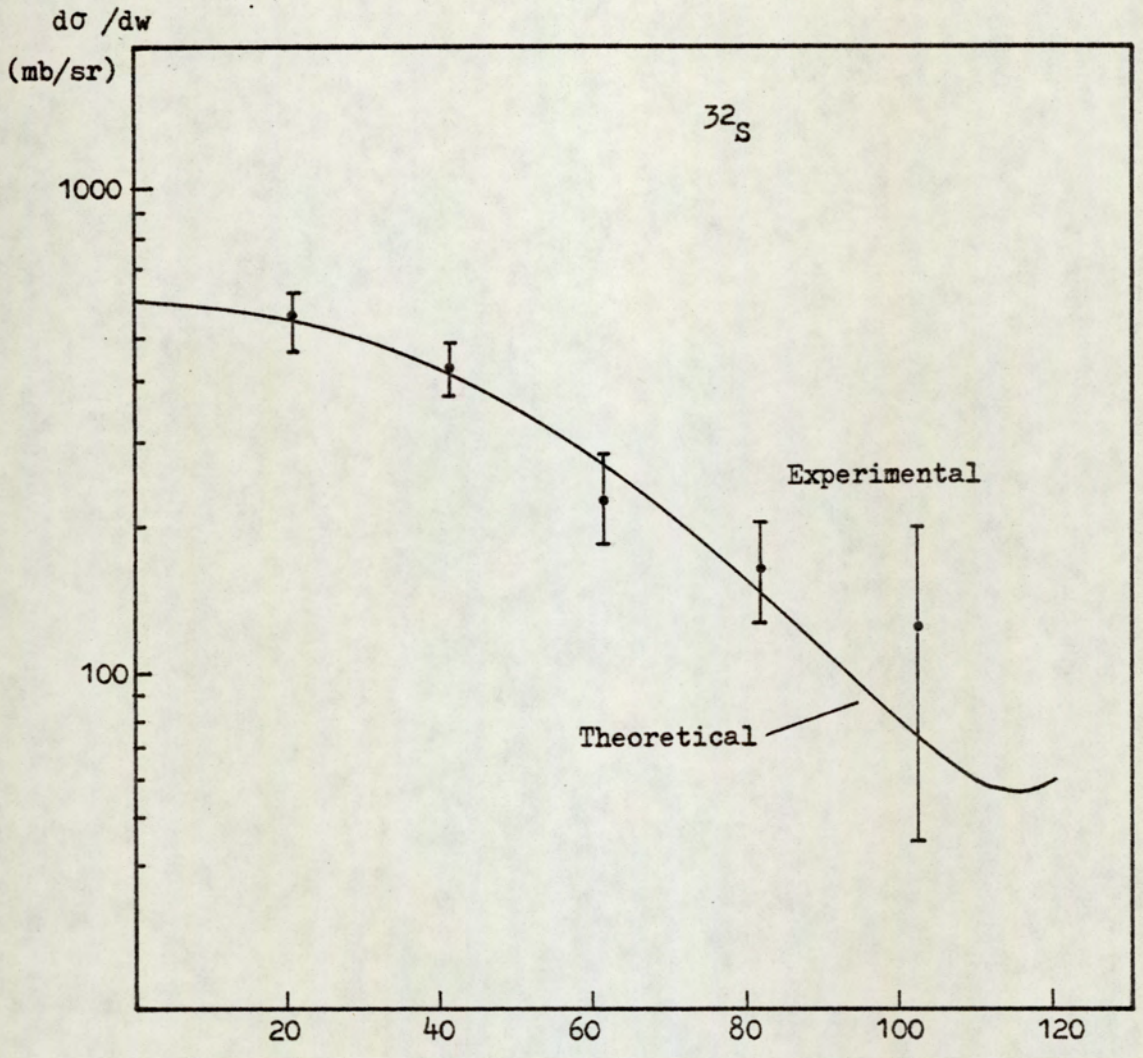

Figure 7.9 Best fit obtained between optical model predictions and experimental data
- data not corrected for compound elastic scattering

again achieved by searching on the parameters V_R, a_R, W_d, r_I, a_I. The same search procedure as used previously was adopted to optimise the parameters. A separate search on r_R showed that the optimum value was 1.17 fm. The theoretical angular distribution which gave the best fit to the data is shown in figure 7.10 and the value of χ^2/point for the final fit was 0.15.

7.8.1 Optical Model Parameters

The optimum values of the optical model parameters obtained from the two analysis are presented in table 7.2. The optimum value of W_d obtained for the fitting of the corrected experimental data is higher than that obtained for the fit on the data not corrected for compound elastic scattering. As was the case with calcium, the fit which predicts the higher value of W_d also predicts a higher theoretical reaction cross-section.

In comparing the parameters in table 7.1 and 7.2 obtained for calcium and sulphur, the values of W_d are very similar for both elements in the fits obtained on the experimental data uncorrected for compound elastic scattering. However, the values of W_d differ markedly for the fits on the corrected data from 14 Mev for calcium to 1.5 Mev for sulphur. Although W_d should vary smoothly with energy and (N-Z)/A, other discrepancies have been found in comparing the imaginary potential for other elements and incident energies[78][79]. The weakest point in optical model predictions has been found to be the imaginary potential which appears to exhibit, for all incident particles, the greatest amount of variation in comparing angular distributions.

In considering the analysis performed, in the present work it has been shown that the value of W_d, and to some extent V_R, depend on the way in which the compound and shape elastic contributions

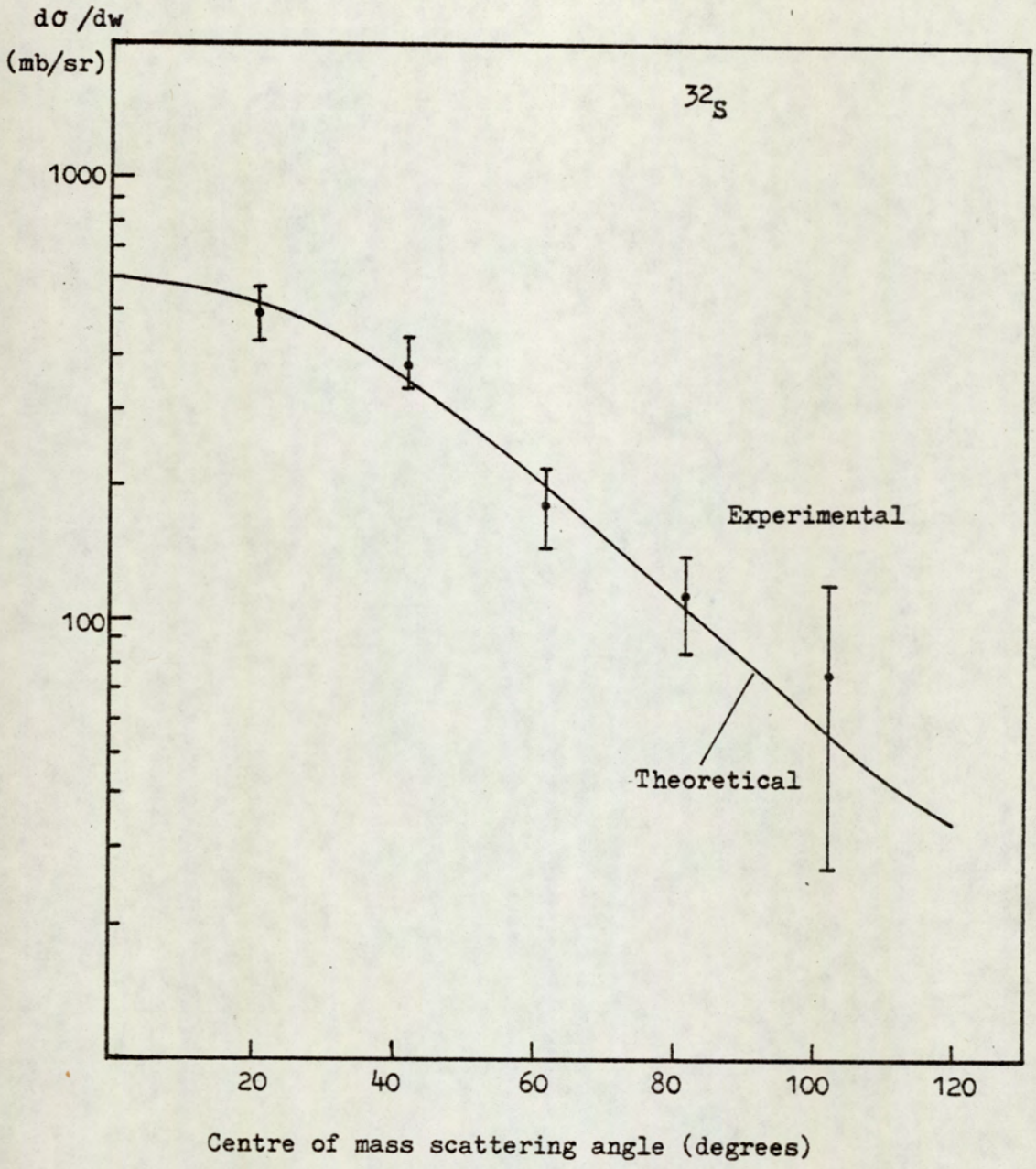

Figure 7.10 Best fit obtained between optical model predictions and experimental data corrected for compound elastic scattering

TABLE 7.2

Optical Model Parameters obtained from the optimum fit to Sulphur Elastic Scattering Data

Parameter		Data corrected for Compound Elastic Scattering	Data not corrected for Compound Elastic Scattering
V_R	(Mev)	36.35	43.24
r_R	(fm)	1.17	1.17
a_R	(fm)	0.919	0.611
W_d	(Mev)	1.51	1.00
r_I	(fm)	1.503	0.97
a_I	(fm)	0.53	0.38
V_S	(Mev)	6.2	6.2
r_S	(fm)	1.01	1.01
a_S	(fm)	0.75	0.75
σ_R	(mb)	982	265
χ^2/point		0.15	0.22

of the experimental data are treated in the analysis.

The sensitivity of the fits obtained for the two analyses on sulphur were investigated with variations in the geometric parameters (i.e. r_R, a_R, r_I, a_I). Figure 7.11 shows the effect on χ^2/point of varying the values of the geometric parameters from the optimum values obtained for the fit on the data containing compound elastic scattering. The sensitivity of χ^2/point for the parameters obtained for the fit on the corrected data is shown in figure 7.12. In both cases the optimum values of a_R and r_R are well defined, a small change in the value of the parameter gives a large change in χ^2/point. The value of r_R is shown to be well defined at the value obtained by Becchetti and Greenlees[71]. The fits on sulphur appear to be insensitive to changes in r_I and a_I, this is particularly apparent for r_I in figure 7.11, where a $\pm$ 15% change in the value of the parameter gives no appreciable change in the value of χ^2.

The effect on χ^2 to variations in the real central and imaginary surface potentials are shown in figures 7.13 and 7.14 respectively. The optimum values of the real potential are well defined, but the imaginary surface potentials do not exhibit the same rapid convergence.

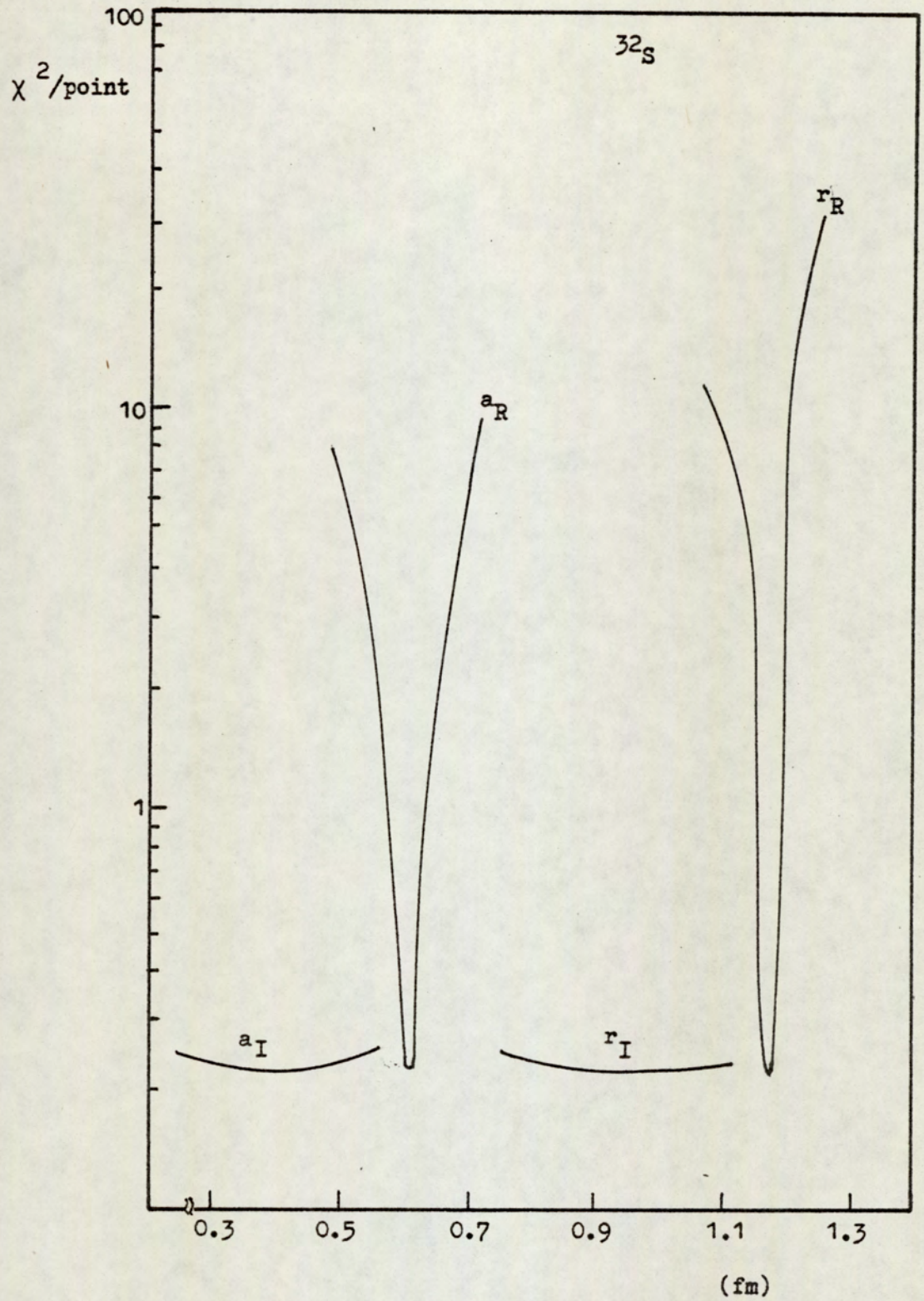

Figure 7.11 Effect on χ^2/point to variations in the geometric parameters

- data not corrected for compound elastic scattering

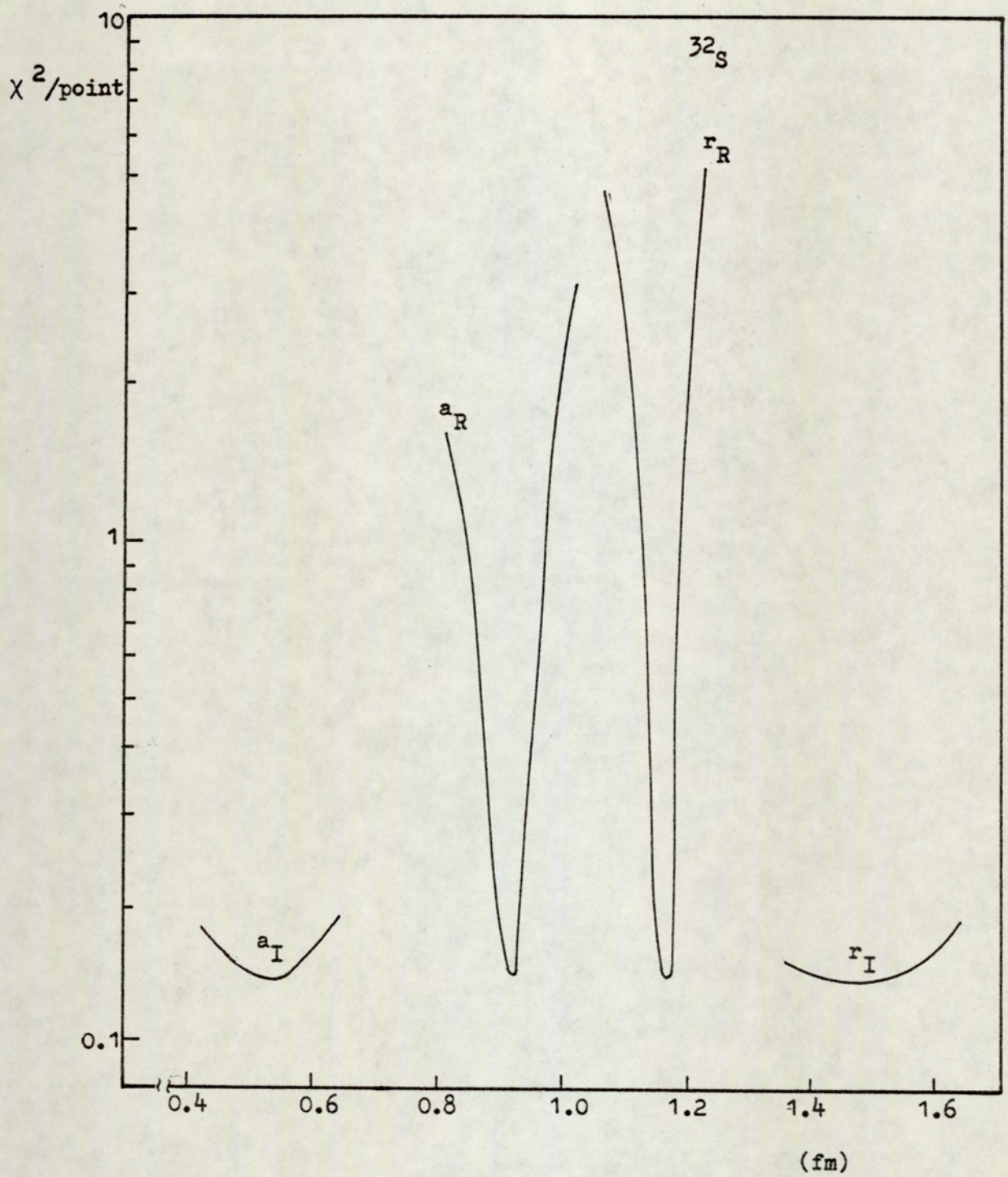

Figure 7.12 Effect on χ^2/point to variations in the geometric parameters

- data corrected for compound elastic scattering

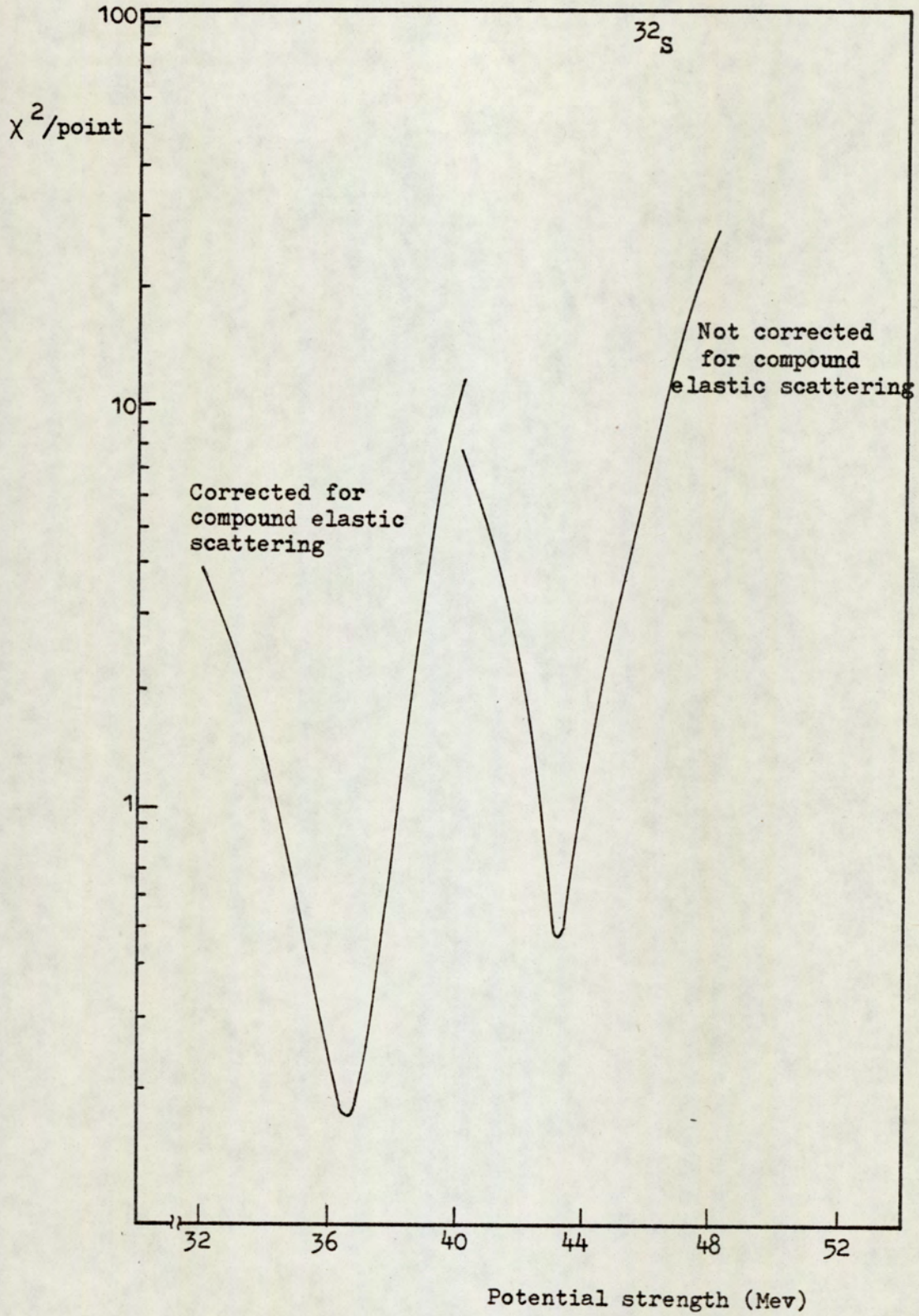

Figure 7.13 Effect on χ^2/point to variations in W_d

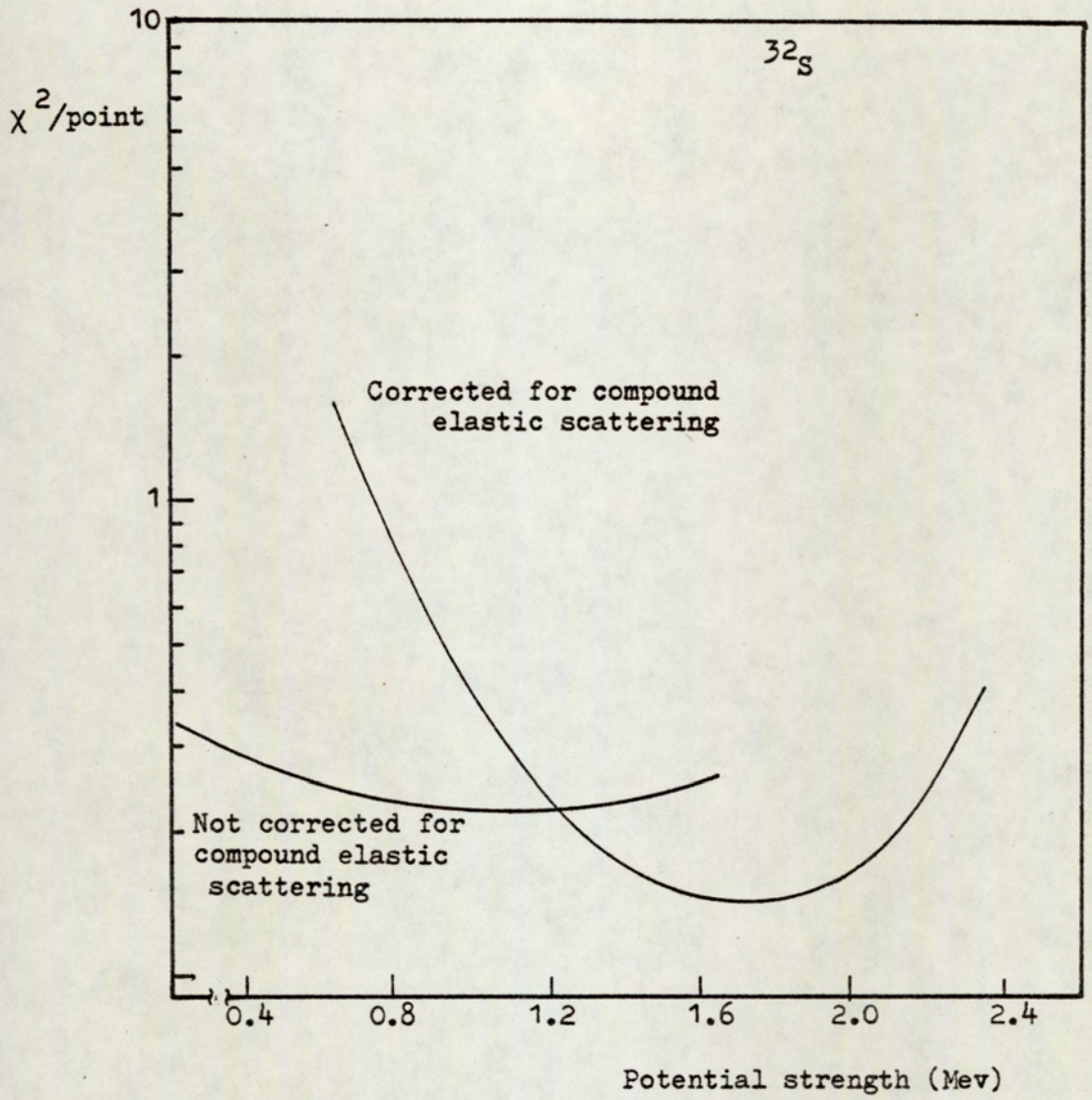

Figure 7.14 Effect on χ^2/point to variations in V_R

CHAPTER 8

CONCLUSIONS

For incident deuteron energies of 1 Mev supplied by the Dynamitron accelerator it has been shown that the time-of-flight technique can be applied successfully to the $^{2}H(d,n)^{3}He$ reaction. The use of thin deuterated polyethylene targets enabled the intensity of scattered deuterons incident onto the charged particle detector to be reduced sufficiently to enable the ^{3}He particles to be completely resolved, for sulphur, and used directly for timing purposes. For the case of calcium where the ^{3}He particles were only partially resolved, the count rate in the associated electronics allowed the pulses to be used for timing applications. The problem of obtaining the neutron yield was overcome by monitoring the proton yield from the competing $^{2}H(d,p)^{3}H$ reaction. The resolution of the spectrometer was 31.4 ns (f.w.h.m.) for the production of 2.18 Mev neutrons and 65 ns (f.w.h.m.) for 2.99 Mev neutrons.

The background levels determined the minimum differential cross-section measurable for the 2.99 Mev neutrons at about 20 mb/steradian. For measurements of differential cross-sections below this, the scattered neutron intensity would be indistinguishable from the background. At a neutron energy of 2.18 Mev no limit could be determined because of the apparent absence of background present. The limiting criteria, in this case, would be the time available for the accumulation of the cross-section data. To obtain a statistical accuracy of $\pm$ 10% in a differential elastic scattering cross-section measurement of 100 mb/steradian about 20 hours at each angle would be required. This estimate is based on

a deuteron content of 80% or greater in the accelerated beam.

In order to reduce the time required to measure an angular distribution a battery of counters could be employed. Here, detectors would be arranged at intervals around a sample and the number of scattered neutrons at these angles measured simultaneously. These facilities were not available for the present research programme.

In the present work the neutron detector was placed 0.5 m from the sample. At this distance inelastic and elastic contributions were not resolved. However, the problem of inelastic contributions in the time spectra was overcome in the present study by choosing the neutron energy appropriately. In the case of calcium the neutron energy was 2.99 Mev which was chosen to be below the first excited state at 3.74 Mev. With sulphur the estimated contribution due to inelastic scattering was considered to be negligible compared with the other experimental errors.

In future studies it would be helpful to be able to resolve the elastic and inelastic components of a scattered neutron beam. A further improvement would be the ability to resolve gamma rays and elastically scattered neutrons in the time spectra. At an incident neutron energy of 2.18 Mev, the detector would have to be placed at about 1.5 m from the sample to achieve this. At a neutron energy of 2.99 Mev the separation would have to be increased to about 3 m because of the poorer spectrometer resolution obtained at this energy. The increased sample-detector distance would inevitably lead to longer accumulation times. These times could be reduced either by improvements in the spectrometer resolution or by increased neutron yields from the target. The former would allow the detector to be moved closer to the sample, while the latter would enable the detector to be moved further away and still retain

the present spectrometer resolution. However, it is difficult to envisage how the resolution could be improved further. The difference between the theoretically determined and experimentally measured resolutions indicated that a source of timing uncertainty was present, which was introduced through the time-of-flight electronics. This uncertainty was attributed to "time walk" introduced in using leading edge time pick-off. If this was the case, then the resolution could be improved by employing a constant fraction technique to obtain a time signal. One solution would be to use a fast amplifier of higher gain than used in the present work, allowing better pulse amplitude resolution between the ^{3}He and scattered deuteron pulses.

Other authors[24][25] working with $(C_2D_4)_n$ targets have shown that by increasing the target rotation increased beam currents are attainable without damage to the targets. Tripard et al[24] using a rotation of 4 Hz obtained a target current of 1.5 μA for 2 Mev deuterons on targets of 1 μm thickness. Schuster[25] obtained 0.5 μA of 10 Mev deuterons on 13 μm targets with a target rotation of 2 Hz. In the present system if the target current could be increased to 1 μA then the estimated neutron yield would be about 10^5 neutrons/steradian. In the present work the design of the target assembly was limited due to restrictions on materials permitted in the Dynamitron system. The assembly was constructed from stainless steel and slow rotation was favoured to reduce friction between the moving parts.

The possibility of employing the associated particle technique to produce neutrons with an energy between 2-3 Mev has been shown possible for 130 Kev incident deuterons. With deuterated polyethylene targets the neutron yields were lower by a factor of ten in comparison to yields for 1 Mev deuterons. The peak to

background ratios obtained for the time spectra were comparable for both incident energies, therefore the measurements of comparable cross-sections with the same statistical accuracy would take about ten times as long at the lower deuteron energy. Because of the length of time involved for one measurement of a differential cross-section of an element at the lower deuteron energy, the use of solid targets would be favoured in terms of time economy and in keeping the neutron yield stable throughout the measurement. However, these targets produce time spectra with a peak to background ratio of about 3 to 1 in comparison to a ratio of 700 to 1 for $(C_2D_4)_n$ targets. This decrease in the peak to background ratio obtained with solid targets will increase the minimum cross-section that can be measured.

The decrease in the peak to background ratio was due to a large number of events other than ^3He entering the charged particle detector thus leaving the ^3He particles unresolved. This problem could be overcome by using a technique which employs discrimination before the particles reach the detector, thus allowing only ^3He particles to be detected i.e. electrostatic or electromagnetic analysis. By using this technique higher target currents would be possible without the problem of a high scattered deuteron flux. Because of the higher and more stable neutron yields and hence reduced time factors involved, measurements of differential elastic scattering cross-sections were made on the Dynamitron facility.

The differential elastic scattering cross-section measurements obtained on calcium fall between the results of Abramson et al[10] and Reber and Brandenburger[11]. The optical model analysis performed in the present work showed a disparity with the results obtained by Reber and Brandenburger[11]. However, the optimised optical model parameters in the present analysis predicted theoretical

differential cross-sections which were in better agreement with the experimental results corrected for compound elastic scattering (χ^2/point = 0.006).

The differential elastic scattering cross-sections for sulphur were comparable to those of Holmqvist and Wiedling[69] for a neutron energy of 2.47 Mev. In the present work the optical model gave good agreement (χ^2/point = 0.15) between theoretical predictions and experimental values corrected for compound elastic scattering.

In the optical model analysis on both calcium and sulphur better agreement was achieved between theoretical predictions and experimental values when the data was corrected for compound elastic scattering.

The agreement achieved between the theoretical angular distributions and experimental data indicates that the optical model can be used to describe elastic scattering at energies where compound elastic scattering is present. However, the present analysis has shown that both experimental data corrected and uncorrected for compound elastic scattering can be represented by the optical model with suitably adjusted parameters. Therefore to obtain meaningful parameters for the optical model potentials it is necessary to correct experimental data for the compound elastic contribution.

Complete unambiguity cannot, therefore, be claimed in the present analysis as the compound elastic scattering cross-sections were estimated from the difference in theoretical and experimental data[9]. Ideally the compound elastic contribution should be determined independently of parameters generated by the optical model, however in the present analysis no independent method could be determined.

For future work the use of the spectrometer, with suitable modifications, could be extended to study inelastic scattering and

complementing such results by studying the gamma rays emitted during the inelastic studies. Also by using extended scattering samples, where the sample thickness is chosen deliberately to induce multiple scattering, the behaviour of neutrons could be investigated in materials significant to fission and fusion reactor design.

APPENDIX I

Kinematic Relationships for a Nuclear Reaction

The nonrelativistic equation for the energy of the light particle, E_3 is given by[66]:-

$$E_3 = \frac{M_1 M_3 E_1}{(M_3+M_4)^2} \left\{ 2\cos^2\psi + \frac{M_4(M_3+M_4)}{M_1 M_3} \left(\frac{Q}{E_1} - \frac{M_1}{M_4} + 1 \right) \right.$$

$$\left. \pm 2\cos\psi \left[\cos^2\psi + \frac{M_4(M_3+M_4)}{M_1 M_3} \left(\frac{Q}{E_1} - \frac{M_1}{M_4} + 1 \right) \right]^{\frac{1}{2}} \right\} \quad \ldots \text{ A1.1}$$

where

M_1 = mass of incident particle

M_2 = mass of target

M_3 = mass of light product

M_4 = mass of heavy product

E_1 = energy associated with M_1

ψ = laboratory angle of light product

Q = energy released in reaction

Defining the quantities:-

$$A = \frac{M_1 M_4}{(M_1+M_2)(M_3+M_4)} \frac{E_1}{E_T}$$

$$B = \frac{M_1 M_3}{(M_1+M_2)(M_3+M_4)} \frac{E_1}{E_T}$$

$$C = \frac{M_2 M_3}{(M_1+M_2)(M_3+M_4)} \left[1 + \frac{M_1}{M_2} \frac{Q}{E_T} \right]$$

$$D = \frac{M_2 M_4}{(M_1+M_2)(M_3+M_4)} \left[1 + \frac{M_1}{M_2} \frac{Q}{E_T} \right]$$

where

$$E_T = E_1 + Q$$

By rewriting equation A1.1, the energy of the light particle E_3 can be found from:-

$$E_3 = E_T B \left[\cos\Psi + (D/B - \sin^2\Psi)^{\frac{1}{2}}\right]^2 \qquad \text{.....A1.2}$$

Considering the centre of mass angle of production, ϑ the energy E_3 can also be written as:-

$$E_3 = E_T (B+D+ [2AC]^{\frac{1}{2}} \cos\vartheta) \qquad \text{.....A1.3}$$

Similarly the energy of the heavy product, E_4 in the laboratory is given by:-

$$E_4 = E_T (A + C + [2AC]^{\frac{1}{2}} \cos\phi) \qquad \text{.....A1.4}$$

and $$E_4 = E_T A\left[\cos\zeta + (C/A - \sin^2\zeta)^{\frac{1}{2}}\right]^2 \qquad \text{.....A1.5}$$

where the angles ϕ and ζ are the centre of mass and laboratory angles of the heavy product.

The laboratory angle of the heavy product can be found from the relation:-

$$\sin\zeta = \left(\frac{M_3}{M_4} \frac{E_3}{E_4}\right)^{\frac{1}{2}} \sin\Psi \qquad \text{.....A1.6}$$

The centre of mass and laboratory angles of the light product are related by:-

$$\sin\vartheta = \left(\frac{E_3}{E_T D}\right)^{\frac{1}{2}} \sin\Psi \qquad \ldots\ldots \text{A1.7}$$

APPENDIX II

THE NORMAL ERROR DISTRIBUTION

The normal error or Gaussian distribution can be represented by the function:-

$$y(x) = \frac{A}{\sigma(2\pi)^{\frac{1}{2}}} \exp\left[\frac{-(x-x_o)^2}{2\sigma^2}\right] \quad \ldots\ldots \text{A2.1}$$

where A is the total number of counts in the distribution, x_o is the mean of the distribution, σ is the standard deviation and y(x) the ordinate value at a channel number x.

Using the property of the Gaussian function:-

$$Q(x) = \frac{y(x-1)}{y(x+1)} \quad \ldots\ldots \text{A2.2}$$

$$= \exp\left[2(x-x_o)/\sigma^2\right] \quad \ldots\ldots \text{A2.3}$$

where y(x-1) and y(x+1) are the counts in the channels either side of channel number x. Equation A2.3 can be rewritten as:-

$$\ln Q(x) = 2(x-x_o)/\sigma^2 \quad \ldots\ldots \text{A2.4}$$

This quantity is a linear function of x, therefore the ln Q(x) values defined by the y(x) data, i.e. $\ln[y(x-1)/y(x+1)]$ can be fitted to a straight line. In practice the ln Q(x) values were plotted as a function of x on graph paper. From the straight line obtained, which had a slope of $2/\sigma^2$, the value of x_o was taken at the point where the line crossed the x-axis (channel number).

With the values of σ and x_o determined the distribution was calculated using equation A2.1.

APPENDIX III

LIMITATIONS OF THE OPTICAL MODEL ANALYSIS

The extent to which the optical model can be used to describe experimental measurements of cross-sections where resonances occur is limited. The optical model cannot describe the resonances exhibited, for example, by low energy neutrons. In these areas, therefore, it predicts average cross-section only. To be able to compare theoretical cross-sections predicted by the optical model and experimental measurements, the latter values must also represent energy averaged values. For the experimental values and the theoretical predictions to be comparable the energy spread of the incident neutron beam must be sufficiently large to encompass the many resonances which may be present hence assuring that the experimental measurements also represent energy averaged values. This enables theory and experiment to be compared meaningfully. In the present work the energy spreads of the defined neutron beams were 0.19Mev (f.w.h.m.) for the study of elastic scattering from calcium and 0.14MeV (f.w.h.m.) for sulphur. In both cases these spreads were considered sufficiently large to ensure that the experimental results represented a reasonable average over the resonances present.

In the present work another difficulty arises in that the optical model parameters found from the theoretical analysis are seen not to be unique because of the limitation of the experimental data. Experimental measurements were limited to scattering angles up to 80° for calcium and 100° for sulphur, and in addition lengthy accumulation times meant that the experimental inaccuracies were relatively large.

In the computer search code R.A.R.O.M.P. account is taken of the experimental errors in comparing the theoretical and experimental cross-section values. The minimum value of x^2/points used for the comparison is dependent on the experimental error. Because of the relatively few experimental points obtained and the large errors associated with them, several sets of optical model parameters obtained from the analysis of the data, corrected for compound elastic scattering,would produce an equally good fit. This ambiguity is further emphasized in the present work as the experimental data uncorrected for compound elastic scattering can also be fitted using the optical model, with suitably adjusted parameters, to give reasonable agreement between the theory and experiment, although this is no more than a curve fitting exercise.

Comparison of the predictions of the optical model using the optical parameters of Becchetti and Greenlees show that an adequate fit can be obtained for the experimental data after it has been corrected for compound elastic scattering. It is felt that these values of Becchetti and Greenlees have the most physical significance as they were obtained from fits on a large number of elements over a large energy range.

REFERENCES

1. H.A. BETHE, Phys.Rev., 47 (1935) 747
2. N. BOHR, Nature, 137 (1936) 344
3. S. FERNBACH, R. SERBER and T.B. TAYLOR, Phys.Rev., 75 (1949) 1352
4. H. FESHBACH, C.E.PORTER and V.F. WEISSKOPF, Phys.Rev., 96 (1954) 448
5. J.R. BEYSTER, M. WALT and E.W. SALMI, Phys.Rev., 104 (1956) 1319
6. P.L. OKHUYSEN and J.T. PRUD'HOMME, Phys.Rev., 116 (1959) 986
7. R.S. CASWELL, Journal of research of the National Bureau of Standards, 66A (1962) 389
8. F. PEREY and B. BUCK, Nucl.Phys., 32 (1962) 353
9. D. WILMORE and P.E. HODGSON, Nucl.Phys., 55 (1964) 673
10. D. ABRAMSON et al, EANDC(E)-149 (1971)
11. J.D. REBER and J.B. BRANDENBURGER, Phys. Rev., 163 (1967) 1077
12. L. CRANBERG and J.S. LEVIN, Phys.Rev., 100 (1955) 435
13. P.J. SCANLON, G.H. STAFFORD, J.J. THRISHER and P.H. BOWEN, Rev.Sci.Instr., 28 (1957) 749
14. H.W. LEFEVRE, R.R. BORCHERS and C.H. POPPE, Rev.Sci.Inst., 33 (1962) 1231
15. C.A. BAKER et al., Nucl.Inst. and Methods, 85 (1970) 259
16. G.K. O'NEILL, Phys.Rev., 95 (1954) 1235
17. G.C. NEILSON and D.B. JAMES, Rev.Sci.Instr., 26 (1955) 1018

18. D.E. BAYNHAM, Ph.D. Thesis, University of Aston in Birmingham (1971)

19. W.R. DIXON and J.H. AITKEN, Nucl.Phys., 24 (1961) 456

20. R.A.I. BELL, N.G. CHAPMAN and P.B. JOHNSON, Nucl.Inst. and Methods, 33 (1965) 13

21. W. FRANZEN, P. HUBER and L. SCHELLENBERG, Z. Naturforsch, 10a (1955) 820

22. L.W. PUT et al, Physica, 32 (1966) 1397

23. L.F.C. MONIER, G.E.TRIPARD and B.L. WHITE, Nucl.Inst. and Methods, 45 (1966) 282

24. G.E. TRIPARD et al, Nucl.Inst. and Methods, 66 (1968) 261

25. D.G. SCHUSTER, Nucl.Inst. and Methods, 76 (1969) 35

26. T.B. RYVES and D. SHARMA, Nucl.Inst. and Methods, 128 (1975) 455

27. M. RICH and R. MADEY, UCRL - 2301 (1954)

28. S. GORODETZKY et al, Nucl.Phys., A91 (1967) 133

29. J.H. ORMROD and H.E. DUCKWORTH, Can.Jour.Phys., 41 (1963) 1424

30. H.K. REYNOLDS et al, Phys.Rev., 92 (1953) 742

31. P.K. WEYL, Phys.Rev., 91 (1953) 289

32. A. DALGARNO and G.W. GRIFFING, Proc.Roy.Soc., 232 (1955) 423

33. PLATZMAN, Symposium on Radiobiology, National Research Council (1952). Edited by J.J. Nickson

34. H. LISKIEN and A. PAULSEN, Nucl.Data Tables, A11 (1973) 618

35. M. WHITE, Vacuum, 15 (1965) 449

36. G.T.J. ARNISON, Nucl.Inst. and Methods, 40 (1966) 359

37. G.E. TRIPARD and B.L. WHITE, Rev.Sci.Instr., 38 (1967) 435

38. C.M. BARTLE and H.O. MEYER, Nucl.Inst. and Methods, 112 (1973) 615

39. C.D. SWARTZ and G.E. OWEN, "Fast Neutron Physics, Part I". J.B. Marion and J.L. Fowler, Interscience Publishers

40. M.E. TOMS, Nucl.Inst. and Methods, 92 (1971) 61

41. J.C. HOPKINS and G. BREIT, Nucl.Data Tables, A9 (1971) 137

42. H.H. BARSHALL and M.H. KANNER, Phys.Rev., 58 (1940) 590

43. J.B. BIRKS, Proc.Phys.Soc., 64A (1951) 874

44. H.C. EVANS and E.H. BELLAMY, Proc.Phys.Soc., 74 (1959) 483

45. E. FINCKH, "Nuclear Spectroscopy and Reactions", Part B, Edited by J. Cerny

46. J.C. HOPKINS et al, Nucl.Instr. and Methods, 56 (1967) 175

47. J.B. ASHE, J.D. HALL and I.L. MORGAN, Rev.Sci.Instr., 37 (1966) 1559

48. R.B. THEUS, W.I.McGARRY and L.A. BEACH, Nucl.Phys., 80 (1966) 273

49. R.L. SCHULTE et al, Nucl.Phys., A192 (1972) 609

50. J.E. BROLLEY, T.M. PUTNAM and L. ROSEN, Phys.Rev., 107 (1957) 820

51. W.A. WENZEL and W. WHALING, Phys.Rev., 88 (1952) 1149

52. J.L. TUCK, LA-1190 (1957)

53. G. PRESTON, P.F.D. SHAW and S.A. YOUNG, Proc.Roy.Soc., 226 (1954) 206

54. A.S. GANEEV et al, SOVIET Jour.Atomic Energy Suppl. (English Trans.), 5 (1957) 21

55. ORTEC Limited, Technical Data

56. D. GEDCKE and W. McDONALD, Nucl.Inst. and Methods, 58 (1968) 253

57. R.L. CHASE, Rev.Sci.Instr., 39 (1968) 1318

58. K. ALLENBY, Ph.D. Thesis, University of Aston in Birmingham (1974)

59. K.F. FLYNN et al, Nucl.Inst. and Methods, 27 (1964) 13

60. V. NAGGIAR, L. LAFAYE and P. BREONCE, Nucl.Inst. and Methods, 41 (1966) 77

61. D.J. HUGHES et al, BNL - 325 (1958)

62. R.B. DAY, Phys.Rev., 102 (1956) 767

63. D.T. STEWART and P.W. MARTIN, Nucl.Phys., 60 (1964) 349

64. K. NISHIMURA, Nucl.Phys., 70 (1965) 421

65. W.E. BURCHAM, "Nuclear Physics - an Introduction", Longman (1973)

66. J.B. MARION and F.C. YOUNG, "Nuclear Reaction Analysis", North-Holland Publishing Co. (1968)

67. Handbook of Chemistry and Physics, 54th edition (1973), The Chemical Rubber Co.

68. P.M. ENDT and C. VAN DER LEUN, Nucl.Phys., A214 (1973) 1

69. B. HOLMQVIST and T. WIEDLING, AE-366 (1969)

70. F. BJORKLUND and S. FERNBACH, Phys.Rev., 109 (1958) 1296

71. F.D. BECCHETTI and G.W. GREENLEES, Phys.Rev., 182 (1969) 1190

72. G.J. PYLE and G.W. GREENLEES, Phys.Rev., 181 (1969) 144

73. F.G. PEREY, Phys.Rev., 131 (1963) 745

74. J.S. NODVIK, C.B. DUKE and M.A. MELKANOFF, Phys.Rev., 125 (1962) 975

75. P.K. BINDAL et al, Phys.Rev., C9 (1974) 2154

76. G.W. GREENLEES et al, Phys.Rev., C6 (1972) 2057

77. P.E.HODGSON, "The Optical Model of Elastic Scattering", Oxford (1963)

78. R.L. CASSOLA and R.D. KOSHEL, Nouvo Cimento, 53B (1968) 363

79. C.M. PEREY and F.G. PEREY, Atomic Data and Nucl.Data Tables, 13 (1974) 293